Reaction Mechanisms for Low Temperature Plasma Interactions with Complex Surfaces and Molecules

by

Jordyn Polito

A dissertation submitted in partial fulfillment
of the requirements for the degree of
Doctor of Philosophy
(Chemical Engineering)
in the University of Michigan
2024

Doctoral Committee:

Professor Mark J. Kushner, Chair
Associate Professor Bryan R. Goldsmith
Professor Eric Johnsen
Professor Nicholas A. Kotov

Jordyn Polito

jopolito@umich.edu

ORCID iD: 0000-0003-3409-6007

Dedication

To Cyndi, David, and Lauryn. Thank you for always supporting my crazy dreams and never trying to clip my wings, even when they carry me far away from you.

In memory of Juliusz A. Kruszelnicki. Thanks for everything. I'll miss you forever my dude.

Acknowledgements

A PhD is definitely not something you can do on your own and I have been incredibly lucky to have had the support of more people than I can ever begin to thank during my time at Michigan. The first of many people to whom I owe my extreme gratitude is my advisor, Mark Kushner. Mark – thanks for taking a chance on a random chemical engineer who showed up in your office with no clue what she wanted to do with her life and no idea what a plasma was. I could not have asked for a better advisor or mentor throughout my time here. Thank you for patience with me as I learned and for sharing with me your wealth of knowledge, not only about plasma physics, but life as well. Your dedication to the field and to every person who works for you is an inspiration. I'll carry the memories of our ongoing airline debate and your storytelling with me throughout the rest of my life.

If the pandemic taught me anything, it's that an office without the people who work in it is just oversized computer storage. To my groupmates past and present, Amanda Lietz, Juliusz Kruszelnicki, Shuo Huang, Guy Parsey, Eve Lanham, Chenhui Qu, Mackenzie Meyer, Florian Krüger, Evan Litch, Yifan Gui, Kseniia Konina, Tugba Piskin, Sanjana Kerketta, Scott Doyle, Chenyao Huang, Yeon Geun Yook, and Jisu Jeon – I can honestly say I have learned something different from every single one of you. Thank you for the insightful conversations, the lunch buddies, and the office shenanigans. I would also like to thank our lovely office assistant Julia Falkovitch-Khain for all of her help with travel, reimbursements, and room bookings, and for

always being available for a chat. I would not have been able to go half the places I've gone without you.

This dissertation would not have been possible without my collaborators in industry and at other institutions. I would like to thank Mark Denning at Agilent Technologies and Professor Elijah Thimsen and Dr. Eric Husmann from Washington University in St. Louis for their interest in my ideas and providing me with opportunities for collaboration. I would also like to thank Professor Katharina Stapelmann and María Herrera-Quesada at North Carolina State University. I have learned so much from the two of you. Thank you for sharing your knowledge of experimental plasma physics and plasma medicine with me and for trusting in me and my models. I have thoroughly enjoyed the last few years of working with you. Each of you are a huge inspiration to women in plasma physics.

My PhD experience would not have been complete without the support of my community outside of plasma physics. There have been so many of you that have played huge roles in supporting me throughout my time in Ann Arbor. Anna Kopp, Misché Hubbard, Ray Asare, Harrison Ball, Anna Nelson, Danielle Richards, Greg Smail, and Issy Gapp are just a few of the many grad school friends I would like to thank here. Thanks for always being there for ice cream, a bottle of wine, late-night life chats, or a fun road trip. I also would have been completely lost without the support of Autonomous women's club ultimate frisbee team. All of you are so special to me. I never thought that playing ultimate for 8+ hours in a day would be something I would look forward to doing with my weekends. Thank you especially to Anna Kilbourn, Becca Ostman, Jordan Hudgins, Jordan Rose-Figura, Yewande Taiwo, Kelly Jones, and Lauren Quiroga. All of you have bought me a meal at some point during the summer so that I could afford to play club ultimate and be a grad student at the same time.

Finally, thank you to my family. I know all of you thought I was crazy when I said I was going to grad school. You thought I was even crazier when I said I was moving to Michigan, but you never failed to support me through it all. I am especially grateful to my parents Cyndi and David. You always raised me telling me that I was going to college. You probably never dreamed that I would be the first doctor in the family. Thanks for never being further than a phone call away and for being willing to drive across the country and fly across the ocean for me. And to my sister Lauryn – thank you so much for always being willing to listen to me complain, for sending me random fun packages, and for always being there when I needed you. I couldn't have done this without any of you.

Table of Contents

List of Tables

List of Figures

Abstract

Low temperature plasmas (LTPs) can be used as sources of reactive chemistry for various existing and emerging commercial applications. These applications include but are not limited to synthesis of nanoparticles for optoelectronic devices, improvement to adhesive properties of bulk commodity polymers, produce disinfection, medical instrument sterilization, and therapeutic treatments for wounds and various cancers. In each of these applications, reactive plasma species interact with a target molecule or surface to add commercial value or induce modifications that promote a desired effect, such as cell death. In many of these applications, the target molecule or surface for plasma treatment consists of complex metallic or organic molecules. Improving and optimizing these systems relies on understanding the mechanisms through which reactive species interact with these complex molecules, however these mechanisms are often unclear. In this dissertation, reaction mechanisms for several commercially relevant systems are developed and used in a 0-dimensional plasma chemistry model to better understand how LTPs interact with complex surfaces and molecules.

In some instances, algorithms were added to the 0D model to provide new capability. An algorithm for describing nanoparticle nucleation and growth was developed by the author to predict the average mass density and size of silicon nanoparticles formed in a low-pressure flowing plasma. The model was used together with experiments to provide insights into how changing plasma operating conditions such as inlet gas composition, pressure, and reactor diameter effect the growth regime (onset of nucleation or growth by coagulation) of the silicon nanoparticles.

Nucleation of silicon nanoparticles was shown to be sensitive to the reactor radius and flow rate. Recommendations for operating conditions that can promote or suppress particle growth are suggested.

A reaction mechanism was developed to predict the addition of O-functionality to the surface of polystyrene (PS) by an atmospheric pressure plasma jet (APPJ). The addition of O functionality to polystyrene increases the wettability of the polystyrene and is desired in the production of biocompatible well-plates and petri dishes. The reaction mechanism was validated by comparison to experimental data. Results indicated that O-occupancy on the PS surface is highly sensitive to the flux of O-atoms delivered to the surface by the plasma. Operating conditions that achieve optimum O-occupancy were identified.

Plasma interactions with organic molecules in liquid are inherent to plasma medical applications. A reaction mechanism for the APPJ treatment of cysteine in solution was developed and validated against experimental data. The model elucidated reaction pathways responsible for the addition of O or NO functionality to the cysteine molecule as a result of plasma exposure. Results showed that cysteine oxidation production formation can be adjusted by changing plasma operating conditions such as distance from the substrate and inlet gas composition.

The cysteine reaction mechanism was extended to produce a hierarchal model for bacterial inactivation by APPJ treatment. The model enabled comparison of time to cell death between dissimilar plasma devices which is difficult to achieve experimentally. Results indicated that plasma systems that can produce reactive nitrogen species are most efficient at bacterial inactivation.

Modelling approaches and mechanisms in this dissertation can be extended to studies of plasma interactions with similar complex targets. Increased understanding of plasma interactions

that add value or induce modifications to a target molecule were demonstrated and recommendations to improve or optimize the efficiency of existing or emerging plasma systems were identified.

Chapter 1 Introduction

Plasma, or the fourth state of matter, is a collection of electrons, ions, and heavy particles created by the application of an electrostatic or electromagnetic field to an atomic or molecular gas. One subclass of plasmas, low temperature plasmas (LTPs), has been widely studied and is currently used in many commercial applications such as semiconductor processing [1], synthesis of optically diverse nanoparticles [2–4], modification of commodity polymers [5–7], produce disinfection [8], medical instrument sterilization [9,10], wound healing [11–13], and cancer therapy [14–16], among many others.

Computational modelling can serve as a low-cost, efficient tool for the design and optimization of the plasma sources for many of these applications, though there are still challenges to overcome. Plasma models are often limited by the development of reaction mechanisms as substrates become increasingly complex. However, the development of validated reaction mechanisms for plasma interactions with complex substrates is necessary for increasing understanding of the basic phenomena that govern plasma interactions with these substrates. Computational models that include validated mechanisms can enable more efficient design of application-specific plasma tools.

In this chapter an overview of low temperature plasmas is discussed (Section 1.1). Discussion of plasma-liquid interactions, which are important in many plasma medical applications and key to later chapters of this work, follows in Section 1.2. In Section 1.3, a few LTP applications that are relevant to this dissertation are discussed, including plasma assisted nanoparticle growth (1.3.1), plasma functionalization of commodity polymers (1.3.2), and plasma

medical applications (1.3.3). The Motivation for this work and the Scope of the Dissertation are discussed in Sections 1.4 and 1.5, respectively.

1.1 Low Temperature Plasmas

Though rare on earth, plasmas are believed to make up most of the matter of the universe [1]. Plasmas are typically classified by their electron number density and temperature (Figure 1.1). A wide range of plasma classes exist, from low density (10^4 – 10^8 cm^{-3}), low temperature (0.1 – 1 eV) space plasmas, to high density (10^{14} – 10^{20} cm^{-3}), high temperature (10^3 – 10^4 eV) fusion plasmas [2]. One subclass of plasmas, low temperature plasmas (LTPs), sits in the middle of these two extreme regimes. LTPs are typically formed at low (1 mTorr – 1 Torr) or atmospheric pressure. They have electron densities on the order of 10^8 – 10^{13} cm^{-3} and electron temperatures of a few eV (1 – 10 eV) [3]. LTPs are easily formed in a laboratory by application of radio frequency (RF) or DC power to electrodes or antennae.

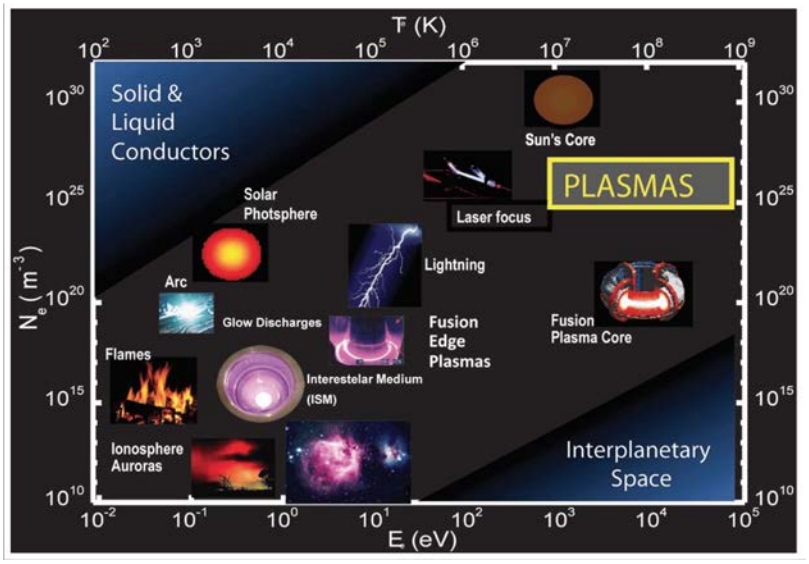

Figure 1.1. Examples of common plasmas as a function of electron number density and electron temperature [18].

LTPs are also called nonequilibrium plasmas, as the heavy particles (ions, neutrals, and radical atoms and molecules derived from the background gas) and electrons are not in thermal

equilibrium. LTPs are characterized as having background gas temperatures that are near ambient (300 – 400 K) while electron collisions with heavy particles result in electron temperatures that are on the order of 1,000 – 10,000 K (1 – 10 eV). The unique nonequilibrium nature of LTPs makes them valuable for a wide range of processing applications, especially when the substrate is thermally sensitive or substrate heating is otherwise undesired.

Though LTPs contain charged species, they are considered to be quasineutral. That is, the positive charge is equal in magnitude to the negative charge. The charge density can oscillate and break charge neutrality over small time and length scales. The time over which a plasma can be non-neutral is determined by the frequency with which electrons displaced from ions by electrostatic oscillations are restored by the Coulomb force. The plasma frequency is given by

$$\omega_p = \sqrt{\frac{e^2 n_e}{\varepsilon_0 m_e}} \tag{1.1}$$

where e is the fundamental charge of an electron, n_e is the electron density, ε_0 is the permittivity of free space, and m_e is the mass of an electron. The distance over which the plasma can be non-neutral is the Debye Length, λ_D,

$$\lambda_D = \sqrt{\frac{\varepsilon_0 k_b T_e}{e^2 n_e}} \tag{1.2}$$

where k_b is the Boltzmann's constant and T_e is the electron temperature.

A plasma is formed by electron collisions with atoms and molecules. Electron impact processes include ionization, attachment, recombination, dissociation, electronic excitation, vibrational excitation, rotational excitation, and elastic processes. The probability that an electron with electron energy ε will produce an electron impact event is called a cross section. The

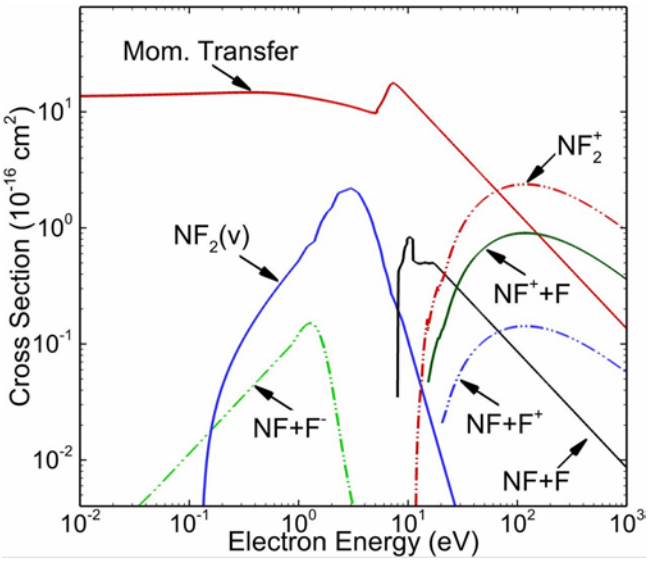

Figure 1.2. Example cross sections for momentum transfer, vibrational excitation, and dissociation of an NF_2 molecule. Adapted from Bartschat and Kushner [20].

threshold energy and shape of the cross section required for a particular event to occur differs by event and by atom or molecule [4]. An example of cross sections for several electron impact events on NF_2 is depicted in Figure 1.2. The electron energy is commonly represented by the electron temperature (eV) in the plasma community. Momentum transfer, or the transfer of energy from a free electron to an electron in the outer shell of an atom or molecule, is often the most likely electron impact process to occur at low electron energies (electron temperatures). As more power is deposited into the plasma by the electric field, electrons gain energy and can reach or surpass the critical (threshold) energy required to produce ionization or dissociation events.

The reactivity of a plasma is largely driven by electron impact events (e.g., $e + O_2 \rightarrow O + O + e$). Reactive species formed by electron impact processes can continue to react with heavy particles to create more reactivity (e.g., $O + O_2 + M \rightarrow O_3 + M$). The reactive species that are formed in a plasma depend on the inlet gas, which usually consists of a noble gas with impurities (e.g., H_2O, O_2, N_2, SiH_4). Impurities included in the inlet gas mixture are application dependent.

Often, the inlet gas composition can be used as a control to fine-tune reactions at the substrate to more effectively produce desired results. Reactive oxygen and nitrogen species (RONS) such as OH, O, NO, NO_2, and NO_3 are commonly desired plasma products, especially in the fields of polymer processing and plasma medicine. RONS are readily formed in LTPs when impurities of H_2O, O_2, and N_2 are included in the gas inlet, or when humid air is used as the inlet gas.

LTPs for semiconductor processing applications are generally formed under low pressure (10s of mTorr to a few hundred mTorr), however many other applications (e.g., bulk processing of commodity polymers, large-scale disinfection, plasma wound healing) utilize plasmas formed at atmospheric pressure. As the pressure increases, the plasma density, and therefore the number of collisions between particles, increases. In plasmas, the average distance which an atom or molecule must travel to have a collision is the mean free path λ_{mfp},

$$\lambda_{mfp} = \frac{1}{n\sigma} \tag{1.3}$$

where n is the number density and σ is the collision cross-section. In low pressure plasmas, low number density leads to a large λ_{mfp}. Ions, which gain energy from the externally applied electric field, do not lose energy in collisions and are delivered to the substrate surface with high energy. High energy ions are typically desired in semiconductor processing applications, particularly when substrate etching is desired. In atmospheric pressure plasmas λ_{mfp} is small and collisionality is high. Ions that reach the substrate are low in energy and reactivity can be delivered to the target without inducing damage or heating.

1.2 Plasma-Liquid Interactions

In many applications, especially in the fields of plasma agriculture and plasma medicine, the substrate (target for plasma treatment) is covered by or contained in a liquid. These liquids

range from pure water (e.g., large-scale produce disinfection [5]) to solutions that may contain salts, vitamins, proteins or other organic matter (e.g., cell media in experimental conditions, fluid produced by the host organism in wound treatment [6]). Therefore, interphase transport and liquid-phase reactions must be considered when designing devices intended to deliver plasma-produced species to the target in these systems.

Many device configurations have been used to study plasma-liquid interactions. These configurations can be classified as direct liquid-phase discharges, gas-phase plasmas that come in contact with liquid (direct gas-phase treatment), gas-phase plasmas whose plasma effluent comes in contact with the liquid (indirect gas-phase treatment), and multi-phase plasmas [7]. Direct liquid-phase discharges are generated by applying a high voltage pulse to a pin electrode submerged in liquid [8]. Direct liquid-phase discharges are most applicable to environmental applications, such as wastewater treatment, as they can offer higher efficiency than traditional chemical treatment methods and are more easily scalable than gas-phase discharges [9]. Direct gas-phase plasmas generally consist of a radio-frequency (rf) powered pin electrode and use the liquid as ground. These devices are commonly used for plasma medical applications such as wound treatment and sterilization [10]. Indirect gas-phase devices usually consist of two parallel plate electrodes, one grounded and one powered, that plasma forms between. Since power is not extended to the liquid surface, the plasma effluent (a collection of plasma-produced radical species that does not include electrons or ions) comes into contact with the liquid surface rather than the plasma. Indirect gas-phase configurations are also used for plasma medical applications [11]. Multi-phase plasmas devices may consist of bubblers, which inject gas into a liquid. The bubbles formed by the gas can act as an electrode and when a sufficiently high voltage is applied to the system, plasma forms inside of the bubbles [12]. Examples of multi-phase plasmas include

electrosprays used in electrospray ionization mass spectrometry [13]. Configurations of the some of the many devices used to expose a plasma to liquid are shown in Figure 1.3.

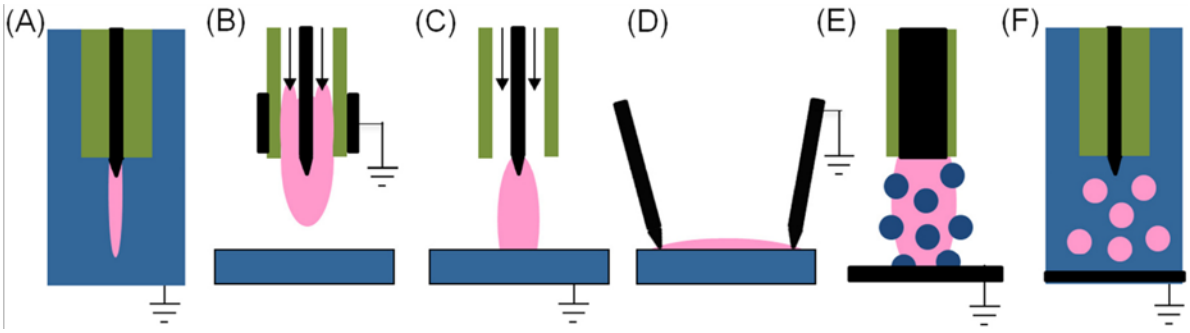

Figure 1.3. Common device configurations used to expose a liquid to plasma. Blue = water, pink = plasma, black = metal electrode, green = dielectric [23].

Many applications, especially in the field of plasma medicine, require plasma devices to operate at atmospheric pressure, rather than at low pressure. Atmospheric pressure plasma devices are generally smaller than low pressure devices and can be designed to be portable since they do not require vacuum equipment. Therefore, atmospheric pressure plasma interaction with liquid for plasma medical applications is an active and ongoing area of research [7,14,15]. Atmospheric pressure plasmas are efficient at producing RONS, which can solvate into a solution and generate reactivity through liquid-phase reactions. A schematic of plasma-liquid processes is shown in Figure 1.4. RONS are considered either short-lived or long-lived. Short-lived species such as OH_{aq} react on short timescales (microseconds) to form other ROS_{aq} and must be replenished by the plasma source through constant exposure or on a pulse-by-pulse basis [16]. Long-lived species include H_2O_{2aq}, O_{3aq}, $NO_2^-{}_{aq}$, $NO_3^-{}_{aq}$, HNO_{2aq}, and HNO_{3aq}. These species persist in solution over long timescales (seconds to minutes), as their production and loss processes are partially dependent upon short-lived species [17]. Plasma treated liquids are typically acidic, as HNO_{xaq} hydrolyzes to $H_3O^+_{aq}$ in solution. The reactivity generated by liquid exposure to plasma has been used to

degrade volatile organic compounds [18], kill cancer cells in solution [19,20], and inactivate bacteria [21,22].

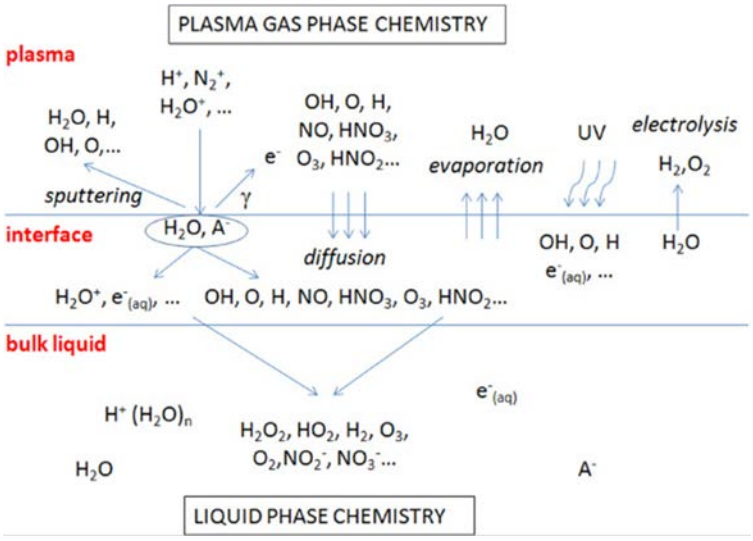

Figure 1.4. Overview of important processes at a plasma-liquid interface [23].

1.3 LTP Applications

LTP has been used for a wide array of commercial applications ranging from feature-scale device processing to wound treatment. This section discusses the LTP applications which are most relevant to this dissertation. In Section 1.3.1, nanoparticle synthesis in low pressure plasmas is discussed. In Section 1.3.2, an overview of the field of commodity polymer processing by atmospheric pressure plasmas is given. In Section 1.3.3, LTP applications to the field of plasma medicine, including several common plasma device configurations, are discussed.

1.3.1 Plasma Assisted Nanoparticle Growth

LTPs offer several advantages over traditional methods of liquid and gas-phase nanoparticle synthesis. Plasmas do not require dangerous solvents or ligands; nanoparticles in a plasma can reach crystallization temperatures independent of the background gas; and plasma operating parameters such as gas composition, gas flowrate, and power deposition can offer control over nanoparticle composition and size distributions [23,24]. Nanoparticles synthesized in plasmas include group III- V semiconducting materials [25,26], metal oxides [27,28], and, more recently, core-shell particles (for example, a particle consisting of a Ge core and a Si shell) [29,30]. Nanoparticles produced in plasmas have also been shown to have unique optical and physical properties, such as extended plasmonic range [31]. Low pressure (100s of mTorr to a few Torr) flowing plasmas are being investigated to better understand control of plasma-assisted nanoparticle synthesis. Typically, these plasmas consist of a rare gas with a small fraction of the feedstock gas (e.g. SiH_4, GeH_4, B_2H_6). An example of a flowing plasma that has been investigated for silicon nanoparticle growth is shown in Figure 1.5.

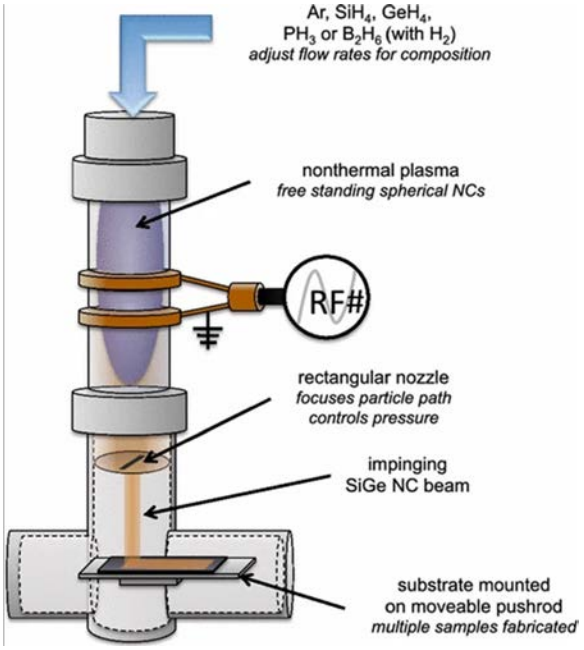

Figure 1.5. Typical configuration of a low-pressure flowing plasma reactor used for nanoparticle synthesis [38].

The size distribution of nanoparticles grown in plasmas can be controlled through tuning plasma operating parameters such as power, gas flow rate, and pulse repetition rate [32–34]. Nanoparticles in a plasma collect charge as a result of collisions with gas phase ions and electrons,

which leads to the particles being trapped in the region of highest plasma potential. Particle trapping allows particles to grow by surface deposition of radical species until the particles are large enough that fluid drag overcomes electrostatic forces and carries the particle downstream out of the reactor.

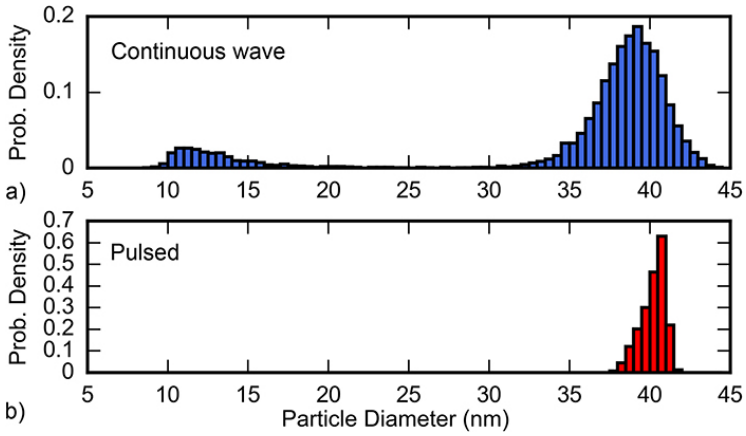

Figure 1.6. Silicon nanoparticle size distributions for (a) continuous wave power and (b) pulsed power in a 1 Torr inductively coupled flowing plasma [46].

The nanoparticle charging process is stochastic in nature and particles experience charge fluctuations over their lifetime in the plasma. The charge distribution of small nanoparticles (less than a few nms) has been shown to be Gaussian in nature [35]. As particles increase in size, charge fluctuations become negligible and the average particle charge can be calculated as a function of nanoparticle radius. In general, larger particles collect more elementary charges (a 10 nm silicon nanoparticle can collect between 30 – 50 elementary charges) [36].

Particle size distributions can therefore be tuned by controlling the time that a particle is trapped by the plasma electrostatic potential. For example, Lanham et. al showed that using pulsed power in a low pressure inductively coupled flowing plasma leads to more monodisperse nanoparticle size distributions compared to using continuous waveform power [32]. Furthermore, adjusting the pulse repetition frequency and duty cycle resulted in finer control of the average particle size. An example of the calculated nanoparticle size distributions is shown in Figure 1.6. Controlling nanoparticle size distributions is particularly important as dimensions of semiconductor devices decreases. Particles below about 10 nm are considered to be killer defects

which can irreparably damage feature scale devices [37]. Plasma produced particles with monodisperse size distributions are desired for easier particle collection in semiconductor processing and for uniformity in novel materials applications.

Models for plasma synthesis of nanoparticles are challenged by several factors including the stochastic nature of particle charging, physical property dependences on particle size, and spatial-temporal differences in particle properties and growth rates that are functions of plasma dynamics. Many models have used a sectional growth approach for predicting nanoparticle size and charge distributions in plasmas [38–40]. These models divide particle sizes into bins and a population balance equation is solved for each bin. Because sectional models require large numbers of equations to resolve the system, they are computationally expensive and are often limited to 0D or 1D models. Monte Carlo (MC) methods have also been used to describe particle growth in plasmas [41]. These models predict particle size and charge distributions that are in good agreement with experiment, but they often assume plasma properties rather than solving the plasma physics equations. To increase both computational efficiency and physical accuracy, kinetic models (such as MC) can be coupled to plasma hydrodynamics models [32,34,42]. The plasma properties such as species densities, electron temperature, and electric field are calculated in the 2D model and passed to the kinetic model, which resolves the forces on a particle, particle charge, and particle size that are functions of the plasma parameters. The local values of particle charge and particle density that will change the plasma properties are fed back to the 2D model periodically to update the plasma properties. In Chapter 3, methods for incorporating particle growth in a 0D plasma chemistry model are discussed. This method greatly increases computational efficiency while simultaneously resolving important plasma dynamics to predict and elucidate particle growth trends observed in experiments.

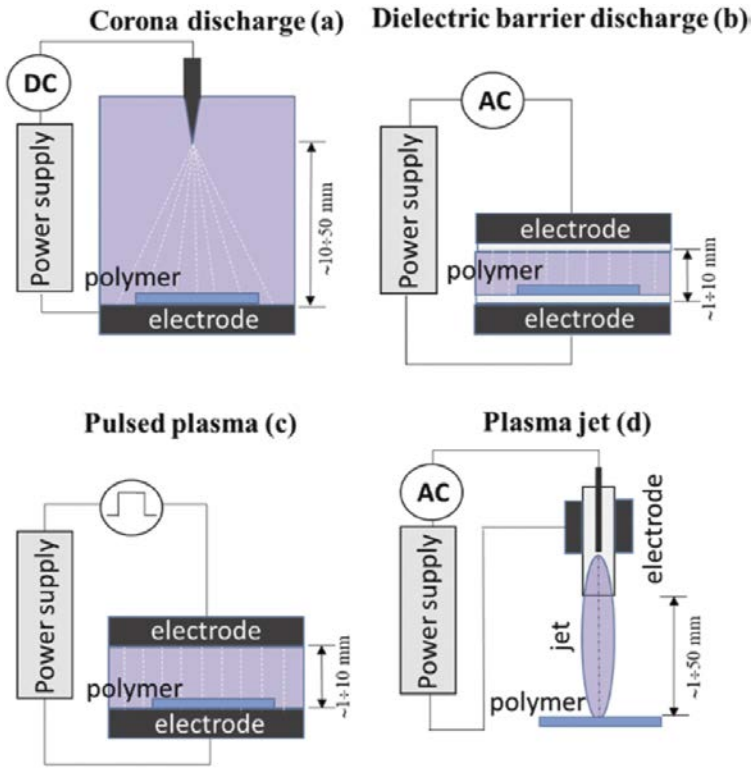

Figure 1.7. Common atmospheric pressure plasma devices used for polymer functionalization [57].

1.3.2 Plasma Functionalization of Polymers

Commodity polymers such as polystyrene (PS), polypropylene (PP), and polycarbonate (PC) are present in almost every area of daily life. Polymers are cheap, easy to manufacture, and are desired in many applications for their mechanical versatility and chemical stability at low temperatures. However, the surface properties of manufactured polymers are often inadequate for the intended application and require some form of post-treatment. The wettability of a polymer, or the ability of a liquid to wet the polymer surface, is one of the most important surface characteristics. Polymer wettability is closely related to its surface energy – low surface energy equates to low wettability. Polymers generally consist of hydrophobic functional groups that are organized in such a way as to minimize surface energy, and so inherently have low wettability. Polymers that are used as spray coatings, adhesives, or for biomedical applications must be made wettable by increasing the surface energy, often by the addition of hydrophilic O-containing functionality.

LTPs, specifically oxygen-containing atmospheric pressure plasmas, are widely used to alter the surface functionality of polymers [43,44]. Atmospheric pressure plasma configurations

used to functionalize polymers include corona discharges [45,46], dielectric barrier discharges (DBDs) [47,48], pulsed plasmas [49], and atmospheric pressure plasma jets [50,51]. Examples of these common plasma device configurations are shown in Figure 1.7. The addition of functional groups to a polymer surface by plasma treatment is considered to be a three-step process: (1) a plasma-produced radical abstracts a hydrogen atom from the polymer backbone to create a surface radical site, (2) other plasma-produced radicals react with the newly created surface radical site to create a different radical site or a terminal functional group, (3) reactions continue until all surface radical sites are terminated, either by surface cross-linking or by the addition of functional groups.

X-ray photoelectron spectroscopy is commonly used to characterize the surface of atmospheric pressure plasma treated polymers. Studies have shown that hydroxyl (C-OH), peroxy (C-O-O), carbonyl (C=O), carboxyl (O=C-OH), and carbonate (O-C-O-O) groups can be added to the polymer surface as a result of treatment with oxygen-containing atmospheric pressure plasmas [52,53]. The type of O-containing functionality that can be added to the polymer surface is largely dependent on the plasma gas composition.

Models have been used to predict the surface composition of polymers with simple monomer units, such as PP. Modelling approaches that have been used include regressive models capable of predicting the percentage of O atoms on the PP surface [54] and more robust methods, such as coupling plasma chemistry models for predicting gas-phase fluxes to the surface with surface site balance models for predicting the evolution of surface properties [55–57]. These types of models can be extended to polymers with more complex monomer units, such as PS and PC (the monomer units of PP, PS, and PC are shown in Figure 1.8). However, mechanisms for functionalization of these polymers are complicated by the presence of aromatic rings and embedded O-functionality. Mechanisms can be approximated by using analog reactions of gas-

phase species with long-chain alkanes and validated by comparison to experimental data. This method of reaction mechanism development is discussed in detail in Chapter 4, where it is used to develop a reaction mechanism for the atmospheric pressure plasma functionalization of PS.

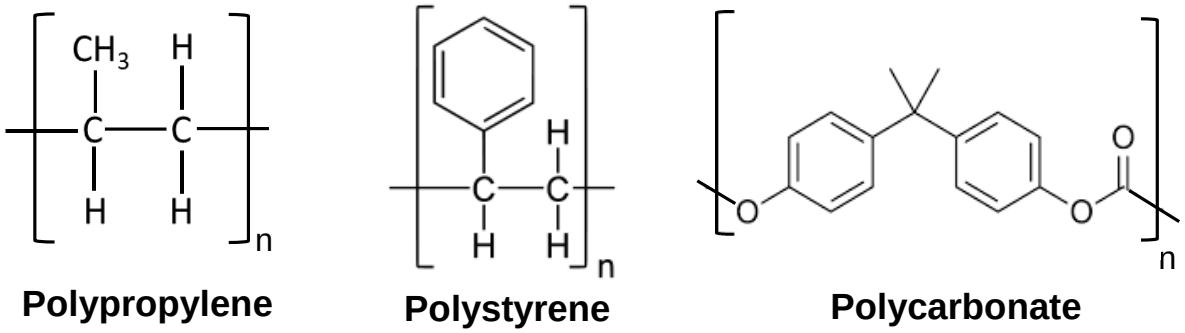

Figure 1.8. Monomer units of common commodity polymers.

1.3.3 Plasma Medical Applications

Atmospheric pressure plasmas have been investigated for therapeutic purposes and biological decontamination [72]. Reactive oxygen and nitrogen species (RONS) produced by atmospheric pressure plasmas interact with the liquid environment of cells to induce bacterial inactivation, stimulation of cell proliferation and tissue regeneration, or, as plasma treatment time is increased, cell death by apoptosis. Plasmas are under investigation as therapeutic options for several types of cancer, burn and wound healing, skin treatments, and root canal treatments as they are nontoxic and can deliver RONS that induce desired effects in a target area without damaging the surrounding environment. The study of plasma interactions with biological targets and solutions is collectively referred to as plasma medicine.

Atmospheric pressure plasmas can be applied to a target directly or indirectly to induce desired biological effects. Direct plasma treatment consists of exposing the biological target directly to an electrical discharge. Direct treatment involves using the target as the grounded electrode, such that electrons, ions, and photons are delivered to the target surface. Plasma devices

such as plasma jets and dielectric barrier discharges have been studied as direct treatment devices. One common direct plasma device is the kINPen [26,73], which is shown in Figure 1.9. The kINPen consists of a pin electrode in a cylindrical dielectric housing. The pin electrode is powered by a few hundred milliwatts of rf power and the target acts as ground such that plasma is formed in the gap between the tip of the pin electrode and the surface of the target. The plasma is typically formed in argon or helium with impurities of nitrogen, oxygen or water [74,75]. The kINPen has been extensively characterized and has served as the basis for the standardization of direct plasma medical devices in Germany [76].

Figure 1.9. Schematic and example use of the kINPen. Adapted from [26].

Indirect plasma treatment consists of exposing the biological target to the plasma effluent (the collection of neutral radicals produced by the plasma when the applied power is turned off) or exposing a solution to the plasma. Plasma activated water (PAW), plasma activated solutions (PAS), or plasma activated cell media (PAM) are commonly used to transport RONS produced by the plasma to a biological target [77,78]. Plasma activated liquids have been shown to be inhibitive to a variety of cancer and tumor cell lines including brain [79], lung [80], and pancreatic [81,82] cancers. Atmospheric pressure plasma jet (APPJ) configurations in which the discharge is formed between two electrodes rather than between an electrode and the biological target are also

Figure 1.10. The COST Reference Microplasma Jet (COST-jet) [85].

considered to be indirect treatment methods. Indirect APPJs have been shown to be effective in inhibiting cancer cell growth and promoting cancer and bacterial cell death [37,83,84].

The COST Reference Microplasma Jet (COST-jet), shown in Figure 1.10, is one APPJ configuration that is used to study indirect plasma treatment of biological targets [85]. The COST-jet consists of two parallel plate electrode that are 3 cm long by 1 mm wide housed in a rectangular casing. A few (0.75 to 2) watts of rf power are applied to one electrode while the opposite electrode is grounded. The plasma discharge is formed vertically along the length of the electrodes. The plasma effluent comes into contact with ambient air at the exit of the reactor such that the concentration of RONS that reach the biological target is a function of the inlet gas composition and the length of the air gap between the reactor outlet and the substrate.

Both direct and indirect plasma treatment methods are effective at generating the RONS that are responsible for inducing desired biological effects. Plasma-produced RONS can react with cell membranes by altering the functionality of organic molecules on the cell membrane surface to interrupt vital cell signaling pathways, resulting in excessive uptake of RONS and apoptosis due to oxidative stress. By changing the concentrations of RONS delivered to the target, plasma treatment can also assist in wound healing. Plasma-produced RNS such as NO and NO_2 stimulate natural immune responses and play key roles in regulation of blood flow and blood circulation [86].

Plasma treatment is promising for many medical applications, however commercialization and federal approvals for plasma therapeutic devices are challenged by the complexity of biological targets that are under investigation for plasma treatment. Mechanisms for plasma interactions with large organic molecules such as those that make up cell membranes are unclear and are further complicated by the presence of liquids in many applications. Furthermore, plasma treatments that are effective for one type of cell may be less effective for others [87]. Models that include validated reaction mechanisms can begin to elucidate the reaction pathways that play key roles in plasma medicine applications. Development of reaction mechanisms relevant to plasma medical applications are discussed in Chapters 5 and 6.

1.4 Motivation

LTPs represent a safe, non-toxic source of reactive chemistry that can be utilized to add value or functionality to commercial products (such as nanoparticles or polymers), or as disinfectants or therapeutics for wound healing and cancer therapy. LTP applications in the fields of materials processing and plasma medicine involve plasma interactions with complex surfaces and molecules such as metallic nanoparticles, polymers, proteins, and cell membranes. Modelling of systems in these areas can increase understanding of relationships between the reactivity delivered by the plasma and the resulting modifications of the target exposed to the plasma. LTP modelling also benefits the plasma community by increasing understanding of the relationship between plasma operating conditions (power, pressure, temperature, gas flow, etc.) and production of the reactive species needed to produce the desired modifications of these complex targets. LTP models can provide a cost-effective method to improve and optimize device design to more efficiently achieve desired outcomes. However, LTP models for plasma interactions with complex surfaces and molecules are limited by the availability of validated reaction mechanisms.

This dissertation focuses on the development of reaction mechanisms for plasma interactions with several complex surfaces and molecules that are of interest to existing or emerging commercial systems. A mechanism and computationally efficient algorithm for silicon nanoparticle growth is developed to help identify how nanoparticle nucleation and growth can be promoted or suppressed through tuning of plasma operating conditions. Identification of the operating regimes in which silicon nanoparticle growth can suppressed is of interest to the field of semiconductor processing, as nanoparticle below a critical size can poison feature scale devices. A reaction mechanism for the APPJ treatment of dry PS is developed and validated to describe the addition of O-functionality to the PS surface. The addition of O-functionality to polymers promotes cell adhesion and growth on their surfaces and is desired by manufacturers of petri dishes and well plates. A reaction mechanism for the APPJ assisted modification of cysteine in solution is developed and validated to identify reaction pathways that play major roles in oxidation or nitrosylation of the cysteine molecule. The knowledge gained from the cysteine study is applicable to the field of plasma medicine and can begin to elucidate plasma-produced species and reaction pathways that are responsible for inducing cell death or wound healing as a result of plasma treatment. The cysteine mechanism is also extended to produce a hierarchal model for bacterial inactivation in solution. Complete models that consider plasma dynamics as well as plasma interactions at the cell membrane are unavailable, but would be valuable in elucidating relationships between plasma operating conditions and their effects on the biological target that are necessary for acquiring federal approval of plasma devices for clinical use.

All of the reaction mechanisms developed in this dissertation are used in a 0-dimensional (0D) plasma chemistry model to provide insight into relationships between plasma operating conditions (e.g., inlet gas composition, pressure, and reactor configuration) and the final

composition of the target surface or molecule. Configurations which are optimum to achieving the desired outcomes and that can be implemented in real-world systems will be identified.

0D plasma chemistry models, or global models, assume that the plasma is a well-stirred reactor. Global models provide plasma properties such as species densities and electron temperature as a function of time. Plug-flow approaches can also be used to provide a quasi-1D spatial description of the plasma properties. Fluxes of plasma-produced species provided by the global model can be coupled to surface site balance models or liquid models to predict the evolution of a surface or solution in time. Global models make many assumptions, but simulations can be performed in seconds or minutes, rather than hours or days. Global models are preferred for detailed plasma chemistry studies, especially when long time-scale chemistry (minutes) is of interest.

While the reaction mechanisms in this dissertation are developed for use in a 0D global model, they are not exclusive to 0D models. These mechanisms can be extended to any 2D or 3D model with capability to predict the evolution of plasma species densities over time and will aid in the design and optimization of plasma devices for materials processing and plasma medical applications.

1.5 Scope of this Dissertation

The models used in this dissertation are described in Chapter 2. The *0D* plasma chemistry model, *GlobalKin*, was used predominantly to validate reaction mechanisms proposed by the author. An algorithm to track nanoparticle nucleation and growth in a low temperature plasma was also developed by the author and implemented in *GlobalKin.*

The nanoparticle algorithm is used in Chapter 3 to model nanoparticle nucleation and growth in a low-pressure plasma formed in a cylindrical quartz tube reactor. A computationally

efficient reaction mechanism for silicon nanoparticle growth in plasmas is also discussed. Modeling results are compared with experiments to identify plasma operating parameters that can be tuned to promote suppression or growth of nanoparticles in the system. Trends between the model and experiments were in good agreement and effects of plasma operating conditions leading to changes in transport regimes that affect mechanisms of nanoparticle growth are discussed.

In Chapter 4, a reaction mechanism is developed to describe the atmospheric pressure plasma treatment of dry polystyrene. *GlobalKin* was used to predict fluxes of plasma-produced gas-phase species incident onto a flat polystyrene surface. Changes in the O/C ratio as a result of plasma treatment predicted by the model were found to be in good agreement with experimental XPS measurements. Plasma operating conditions that can be changed to tune the degree of functionalization of the PS surface are discussed.

In Chapter 5, the mechanism from Chapter 4 is modified and extended to the small organic molecule cysteine to describe plasma modification of cysteine in solution. The cysteine reaction mechanism is validated against experimental data and trends agree well. Reactions that are important in the modification of cysteine, and therefore may be important in plasma medical applications, are discussed in detail. Plasma operating conditions that may promote or demote these reactions are also discussed.

In Chapter 6, the cysteine mechanism is extended to a hierarchical model for planktonic cell death in solution. The model and mechanism are implemented in *GlobalKin* to describe cell death as a result of exposure to different types and source configurations of atmospheric pressure plasma jets. Results are compared to the literature to provide proof of concept and motivate discussion on target-specific plasma medical device design.

A summary of the work presented in this dissertation is in Chapter 7. Future work and possible studies to extend the work in this dissertation are also discussed.

1.6 References

[1] G. S. Oehrlein and S. Hamaguchi, Plasma Sources Sci. Technol. **27,** 23001 (2018).

[2] L. Mangolini, E. Thimsen and U. Kortshagen, Nano Lett. **5,** 655 (2005).

[3] A. Alvarez Barragan, N. V. Ilawe, L. Zhong, B. M. Wong and L. Mangolini, J. Phys. Chem. C **121,** 2316 (2017).

[4] D. J. Rowe, J. S. Jeong, K. A. Mkhoyan and U. R. Kortshagen, Nano Lett. **13,** 1317 (2013).

[5] J. M. Grace and L. J. Gerenser, J. Dispers. Sci. Technol. **24,** 305 (2003).

[6] E. M. Liston, L. Martinu and M. R. Wertheimer, J. Adhes. Sci. Technol. **7,** 1091 (1993).

[7] Y. Kusano, J. Adhes. **90,** 755 (2014).

[8] V. Scholtz, J. Pazlarova, H. Souskova, J. Khun and J. Julak, Biotechnol. Adv. **33,** 1108 (2015).

[9] N. Kaushik, S. Mitra, E. J. Baek, L. N. Nguyen, P. Bhartiya, J. H. Kim, E. H. Choi and N. K. Kaushik, J. Adv. Res. **43,** 59 (2023).

[10] A. Sakudo, Y. Yagyu and T. Onodera, Int. J. Mol. Sci. **20,** 5216 (2019).

[11] B. Boekema, M. Stoop, M. Vlig, J. van Liempt, A. Sobota, M. Ulrich and E. Middelkoop, Appl. Microbiol. Biotechnol. **105,** 2057 (2021).

[12] M. A. Oliver, L. K. Hussein, E. A. Molina, J. W. Keyloun, S. M. McKnight, L. M. Jimenez, L. T. Moffatt, J. W. Shupp and B. C. Carney, Burns (2024).

[13] S. Arndt, P. Unger, E. Wacker, T. Shimizu, J. Heinlin, Y. F. Li, H. M. Thomas, G. E. Morfill, J. L. Zimmermann, A. K. Bosserhoff and S. Karrer, PLoS One **8,** 1 (2013).

[14] D. B. Graves, Plasma Process. Polym. **11,** 1120 (2014).

[15] M. Keidar, A. Shashurin, O. Volotskova, M. Ann Stepp, P. Srinivasan, A. Sandler and B.

Trink, Phys. Plasmas **20,** (2013).

[16] J. Schlegel, J. Köritzer and V. Boxhammer, Clin. Plasma Med. **1,** 2 (2013).

[17] F. F. Chen, *Introduction to Plasma Physics and Controlled Fusion*, Springer (2006).

[18] F. L. Tabares and I. Junkar, Molecules **26,** 1903 (2021).

[19] M. A. Lieberman and A. J. Lichtenberg, *Principles of Plasma Discharges and Materials Processing: Second Edition*, John Wiley and Sons (2005).

[20] K. Bartschat and M. J. Kushner, Proc. Natl. Acad. Sci. **113,** 7026 (2016).

[21] S. Perinban, V. Orsat and V. Raghavan, Compr. Rev. Food Sci. Food Saf. **18,** 1985 (2019).

[22] H. Jablonowski and T. von Woedtke, Clin. Plasma Med. **3,** 42 (2015).

[23] P. J. Bruggeman, M. J. Kushner, B. R. Locke, J. G. E. Gardeniers, W. G. Graham, D. B. Graves, R. C. H. M. Hofman-Caris, D. Maric, J. P. Reid, E. Ceriani, D. Fernandez Rivas, J. E. Foster, S. C. Garrick, Y. Gorbanev, S. Hamaguchi, F. Iza, H. Jablonowski, E. Klimova, J. Kolb, F. Krcma, P. Lukes, Z. Machala, I. Marinov, D. Mariotti, S. Mededovic Thagard, D. Minakata, E. C. Neyts, J. Pawlat, Z. L. Petrovic, R. Pflieger, S. Reuter, D. C. Schram, S. Schröter, M. Shiraiwa, B. Tarabová, P. A. Tsai, J. R. R. Verlet, T. von Woedtke, K. R. Wilson, K. Yasui and G. Zvereva, Plasma Sources Sci. Technol. **25,** 053002 (2016).

[24] A. Starikovskiy, Y. Yang, Y. I. Cho and A. Fridman, Plasma Sources Sci. Technol. **20,** 024003 (2011).

[25] S.-C. Kim, Y.-K. Park and S.-C. Jung, Korean J. Chem. Eng. **38,** 885 (2021).

[26] S. Bekeschus, A. Schmidt, K. D. Weltmann and T. von Woedtke, Clin. Plasma Med. **4,** 19 (2016).

[27] J. Golda, F. Kogelheide, P. Awakowicz and V. S. Von Der Gathen, Plasma Sources Sci. Technol. **28,** (2019).

[28] K. Tachibana, Y. Takekata, Y. Mizumoto, H. Motomura and M. Jinno, Plasma Sources Sci. Technol. **20,** 034005 (2011).

[29] D. D. Ebeling, M. S. Westphall, M. Scalf and L. M. Smith, Anal. Chem. **72,** 5158 (2000).

[30] I. Adamovich, S. D. Baalrud, A. Bogaerts, P. J. Bruggeman, M. Cappelli, V. Colombo, U. Czarnetzki, U. Ebert, J. G. Eden, P. Favia, D. B. Graves, S. Hamaguchi, G. Hieftje, M. Hori, I. D. Kaganovich, U. Kortshagen, M. J. Kushner, N. J. Mason, S. Mazouffre, S. M. Thagard, H. R. Metelmann, A. Mizuno, E. Moreau, A. B. Murphy, B. A. Niemira, G. S. Oehrlein, Z. L. Petrovic, L. C. Pitchford, Y. K. Pu, S. Rauf, O. Sakai, S. Samukawa, S. Starikovskaia, J. Tennyson, K. Terashima, M. M. Turner, M. C. M. Van De Sanden and A. Vardelle, J. Phys. D. Appl. Phys. **50,** (2017).

[31] P. J. Bruggeman, A. Bogaerts, J. M. Pouvesle, E. Robert and E. J. Szili, J. Appl. Phys. **130,** (2021).

[32] A. M. Lietz and M. J. Kushner, J. Phys. D. Appl. Phys. **49,** (2016).

[33] P. Heirman, W. Van Boxem and A. Bogaerts, Phys. Chem. Chem. Phys. **21,** 12881 (2019).

[34] J. Jose and L. Philip, J. Environ. Manage. **286,** 112202 (2021).

[35] H. Tanaka, S. Bekeschus, D. Yan, M. Hori, M. Keidar and M. Laroussi, Cancers (Basel). **13,** 1737 (2021).

[36] J. Tornin, C. Labay, F. Tampieri, M.-P. Ginebra and C. Canal, Nat. Protoc. **16,** 2826 (2021).

[37] C. A. J. Van Gils, S. Hofmann, B. K. H. L. Boekema, R. Brandenburg and P. J.

Bruggeman, J. Phys. D. Appl. Phys. **46,** (2013).

[38] U. Kortshagen, Plasma Chem. Plasma Process. **36,** 73 (2016).

[39] U. R. Kortshagen, R. M. Sankaran, R. N. Pereira, S. L. Girshick, J. J. Wu and E. S. Aydil, Chem. Rev. **116,** 11061 (2016).

[40] M. Shimada, Y. Azuma, K. Okuyama, Y. Hayashi and E. Tanabe, Jpn. J. Appl. Phys. **45,** 328 (2006).

[41] K. H. You, J. H. Kim, S. J. You, H. C. Lee, H. Ruh and D. J. Seong, Curr. Appl. Phys. **18,** 1553 (2018).

[42] Z. Li, P. R. Wray, M. P. Su, Q. Tu, H. P. Andaraarachchi, Y. J. Jeong, H. A. Atwater and U. R. Kortshagen, ACS Omega **5,** 24754 (2020).

[43] A. Nikiforov, X. Deng, Q. Xiong, U. Cvelbar, N. DeGeyter, R. Morent and C. Leys, J. Phys. D. Appl. Phys. **49,** 204002 (2016).

[44] K. I. Hunter, J. T. Held, K. A. Mkhoyan and U. R. Kortshagen, ACS Appl. Mater. Interfaces **9,** 8263 (2017).

[45] O. H. Asnaz, J. Drewes, M. Elis, T. Strunskus, F. Greiner, O. Polonskyi, F. Faupel, L. Kienle, A. Vahl and J. Benedikt, Nanoscale Adv. **5,** 1115 (2023).

[46] S. J. Lanham, J. Polito, Z. Xiong, U. R. Kortshagen and M. J. Kushner, J. Appl. Phys. **132,** (2022).

[47] C. Xu, H. P. Andaraarachchi, Z. Xiong, M. A. Eslamisaray, M. J. Kushner and U. R. Kortshagen, J. Phys. D. Appl. Phys. **56,** 015201 (2023).

[48] Z. Xiong, S. Lanham, E. Husmann, G. Nelson, M. A. Eslamisaray, J. Polito, Y. Liu, J. Goree, E. Thimsen, M. J. Kushner and U. R. Kortshagen, J. Phys. D. Appl. Phys. **55,** 235202 (2022).

[49] T. Matsoukas, M. Russell and M. Smith, J. Vac. Sci. Technol. A Vacuum, Surfaces, Film. **14,** 624 (1996).

[50] T. Matsoukas and M. Russell, J. Appl. Phys. **77,** 4285 (1995).

[51] M. P. Herrling and P. Rychen, Ultrapure Micro **1,** 34 (2017).

[52] P. Agarwal and S. L. Girshick, Plasma Chem. Plasma Process. **34,** 489 (2014).

[53] P. Agarwal and S. L. Girshick, Plasma Sources Sci. Technol. **21,** 055023 (2012).

[54] U. Kortshagen and U. Bhandarkar, Phys. Rev. E - Stat. Physics, Plasmas, Fluids, Relat. Interdiscip. Top. **60,** 887 (1999).

[55] X. Chen and C. J. Hogan, Chem. Eng. J. **411,** 128383 (2021).

[56] S. J. Lanham, J. Polito, X. Shi, P. Elvati, A. Violi and M. J. Kushner, J. Appl. Phys. **130,** (2021).

[57] J.-P. Booth, M. Mozetič, A. Nikiforov and C. Oehr, Plasma Sources Sci. Technol. **31,** 103001 (2022).

[58] A. Vesel and M. Mozetic, J. Phys. D. Appl. Phys. **50,** 293001 (2017).

[59] I. Novák, V. Pollák and I. Chodák, Plasma Process. Polym. **3,** 355 (2006).

[60] Leon-Garzon, Dotelli, Tommasini, Bianchi, Pirola, Villa, Lucotti, Sacchi and Barbieri, Polymers (Basel). **11,** 1646 (2019).

[61] C. Liu, N. Cui, N. M. D. Brown and B. J. Meenan, Surf. Coatings Technol. **185,** 311 (2004).

[62] C.-S. Ren, K. Wang, Q.-Y. Nie, D.-Z. Wang and S.-H. Guo, Appl. Surf. Sci. **255,** 3421 (2008).

[63] K. Narushima, Y. Tsutsui, K. Kasukabe, N. Inagaki, Y. Isono and M. R. Islam, Jpn. J. Appl. Phys. **46,** 4246 (2007).

[64] M. Noeske, J. Degenhardt, S. Strudthoff and U. Lommatzsch, Int. J. Adhes. Adhes. **24,** 171 (2004).

[65] A. Van Deynse, P. Cools, C. Leys, R. Morent and N. De Geyter, Surf. Coatings Technol. **276,** 384 (2015).

[66] A. Vesel, Surf. Coatings Technol. **205,** 490 (2010).

[67] A. Vesel, R. Zaplotnik, G. Primc and M. Mozetič, Polymers (Basel). **12,** (2020).

[68] C. Wang and X. He, Surf. Coatings Technol. **201,** 3377 (2006).

[69] A. N. Bhoj and M. J. Kushner, J. Phys. D. Appl. Phys. **39,** 1594 (2006).

[70] A. N. Bhoj and M. J. Kushner, J. Phys. D. Appl. Phys. **40,** 6953 (2007).

[71] R. Dorai and M. J. Kushner, J. Phys. D. Appl. Phys. **36,** 666 (2003).

[72] K.-D. Weltmann and T. von Woedtke, Plasma Phys. Control. Fusion **59,** 014031 (2017).

[73] S. Reuter, T. Von Woedtke and K. D. Weltmann, J. Phys. D. Appl. Phys. **51,** (2018).

[74] G. Bruno, T. Heusler, J. W. Lackmann, T. von Woedtke, K. D. Weltmann and K. Wende, Clin. Plasma Med. **14,** 100083 (2019).

[75] A. Schmidt-Bleker, R. Bansemer, S. Reuter and K. D. Weltmann, Plasma Process. Polym. **13,** 1118 (2016).

[76] M. S. Mann, R. Tiede, K. Gavenis, G. Daeschlein, R. Bussiahn, K.-D. Weltmann, S. Emmert, T. von Woedtke and R. Ahmed, Clin. Plasma Med. **4,** 35 (2016).

[77] N. K. Kaushik, B. Ghimire, Y. Li, M. Adhikari, M. Veerana, N. Kaushik, N. Jha, B. Adhikari, S.-J. Lee, K. Masur, T. von Woedtke, K.-D. Weltmann and E. H. Choi, Biol. Chem. **400,** 39 (2018).

[78] H. Tanaka, M. Mizuno, K. Ishikawa, H. Kondo, K. Takeda, H. Hashizume, K. Nakamura, F. Utsumi, H. Kajiyama, H. Kano, Y. Okazaki, S. Toyokuni, S. Akiyama, S. Maruyama,

S. Yamada, Y. Kodera, H. Kaneko, H. Terasaki, H. Hara, T. Adachi, M. Iida, I. Yajima, M. Kato, F. Kikkawa and M. Hori, Clin. Plasma Med. **3,** 72 (2015).

[79] H. Tanaka, M. Mizuno, K. Ishikawa, K. Nakamura, F. Utsumi, H. Kajiyama, H. Kano, S. Maruyama, F. Kikkawa and M. Hori, Plasma Med. **2,** 207 (2012).

[80] T. Adachi, H. Tanaka, S. Nonomura, H. Hara, S. Kondo and M. Hori, Free Radic. Biol. Med. **79,** 28 (2015).

[81] D. Yan, H. Cui, W. Zhu, N. Nourmohammadi, J. Milberg, L. G. Zhang, J. H. Sherman and M. Keidar, Sci. Rep. **7,** 4479 (2017).

[82] Y. Sato, S. Yamada, S. Takeda, N. Hattori, K. Nakamura, H. Tanaka, M. Mizuno, M. Hori and Y. Kodera, Ann. Surg. Oncol. **25,** 299 (2018).

[83] K. Ninomiya, T. Ishijima, M. Imamura, T. Yamahara, H. Enomoto, K. Takahashi, Y. Tanaka, Y. Uesugi and N. Shimizu, J. Phys. D. Appl. Phys. **46,** 425401 (2013).

[84] H. Min Joh, S. Ja Kim, T. H. Chung and S. H. Leem, Appl. Phys. Lett. **101,** 053703 (2012).

[85] J. Golda, J. Held, B. Redeker, M. Konkowski, P. Beijer, A. Sobota, G. Kroesen, N. S. J. Braithwaite, S. Reuter, M. M. Turner, T. Gans, D. O'Connell and V. Schulz-Von Der Gathen, J. Phys. D. Appl. Phys. **49,** (2016).

[86] C. V. Suschek and C. Opländer, Clin. Plasma Med. **4,** 1 (2016).

[87] H. Jablonowski, M. A. C. Hänsch, M. Dünnbier, K. Wende, M. U. Hammer, K.-D. Weltmann, S. Reuter and T. von Woedtke, Biointerphases **10,** (2015).

Chapter 2 Model Description

2.1 Description of *GlobalKin*

GlobalKin is a general purpose 0D plasma chemistry model with capability for addressing plasma interactions with solid and liquid-phase surfaces. *GlobalKin* has been discussed in detail previously [1,2]. *GlobalKin* solves for volume averaged species densities n_i, gas temperature T_{gas}, and electron temperature T_e as a function of time or reactor position (see Section 2.1.1).

Input to *GlobalKin* includes a namelist where system properties such as initial conditions, power profile, and reactor configuration are specified. A data file containing species and their properties (e.g., mass, charge) as well as the reaction mechanism is also included. Reaction rates are specified either in Arrhenius form (most heavy particle reactions) or from their cross-sections (most electron-impact reactions) using a Boltzmann lookup table. Electron Energy Distributions (EEDs) are generated by solving the stationary Boltzmann equation over a range of E/N (electric field/gas density) values as a function of electron temperature. Solutions to the Boltzmann equation are stored in lookup tables that are interpolated over to provide electron impact rate coefficients and transport coefficients at the appropriate electron temperature. Boltzmann tables can be updated periodically throughout the execution of *GlobalKin* to reflect changes in the gas composition.

The electron temperature is calculated by the electron energy equation

$$\frac{\partial\left(\frac{3}{2}n_e k_b T_e\right)}{\partial t} = \vec{j}\cdot\vec{E} + n_e\sum_i \Delta\varepsilon_i k_i n_i + \sum_i \Delta\varepsilon_i k_i n_i m_i - \sum_i \frac{3}{2}n_e \nu_{mi}\left(\frac{2m_e}{M_i}\right)k_b\left(T_e - T_i\right) \qquad (2.1)$$

where the electron density is n_e and k_b is Boltzmann's constant. The first term represents changes in electron temperature due to power deposition. The second term is contributions from inelastic collisions where $\Delta\varepsilon_i$ is the change in energy during a collision with species n_i in a reaction having rate coefficient k_i. The third term represents changes in electron energy due to collisions between electrons and gas-phase species n_i and m_i. The last term in the electron energy equation accounts for momentum transfer from electrons to neutral species through elastic collisions. The electron momentum transfer collision frequency is ν_{mi}, m_e is the mass of an electron, M_i is the mass of the heavy particle, and T_i is the heavy particle temperature (assumed to be the neutral gas temperature).

The neutral gas temperature is calculated using the energy equation

$$\frac{d}{dt}\left(\frac{3}{2}N_g c_p T_g\right) = P_{ion} + \sum_l \frac{3}{2} n_e \nu_{mi}\left(\frac{2m_e}{m_i}\right) k_b\left(T_e - T_i\right) + \sum_i \Delta\varepsilon_i^{fc} R_i$$
$$-\sum_i \Delta H_i R_i + \frac{1}{\tau_{flow}}\left(N_{g0} c_{p0} T_{g0} - N_g c_p T_g\left(\frac{P}{P_0}\right)\right) - \frac{\kappa}{\Lambda^2}\left(T_g - T_w\right) \qquad (2.2)$$

where N_g is the gas density and c_p is specific heat. P_{ion} is the joule heating into ions. The second term in the equation accounts for contributions to gas-heating due to momentum-transfer collisions with electrons. The third term accounts for Franck-Condon heating, or gas heating due to dissociation reactions where $\Delta\varepsilon^{fc}$ is the energy released due to reaction i with rate R_i. The fourth term is the heating (or cooling) due to reactions with changes in enthalpy, ΔH_i. The fifth term in the energy equation accounts for changes in gas heating due to fluid flow (advective heating or cooling) where τ_{flow} is the average gas residence time, P is the instantaneous pressure, and P_0 is the desired operating pressure. N_{g0}, c_{p0}, and T_{g0} are the number density, specific heat, and temperature of the inlet gas. The final term in the energy equation accounts for temperature loss to the wall where κ is the thermal conductivity of the wall material, Λ is the diffusion length, and T_w is the wall temperature.

Gas phase species densities are solved using the species continuity equation, which accounts for sources and losses due to reactions, gas flow, and diffusion to the reactor walls.

$$\frac{dn_i}{dt} = \sum_j \left(\left(a_{ij}^{(R)} - a_{ij}^{(L)} \right) k_j \prod_l n_l^{a_{ij}^{(L)}} \right) + \frac{1}{\tau_{flow}} \left(n_{i0} - n_i \left(1 + \frac{\left(P - P_0 \right)}{P_0} \right) \right) + \sum_m \left(-\frac{D_i n_i}{\Lambda^2} f_m S_{im} + \sum_k \frac{D_k n_k}{\Lambda^2} f_m S_{km} g_{ikm} \right) \tag{2.3}$$

The first term in the continuity equation represents sources and losses of species *i* as a result of reactions where $a_{ij}^{(R)}$ and $a_{ij}^{(L)}$ are the stoichiometric coefficients of species *i* on the right- and left-hand side of reaction *j*, respectively. The second term represents sources and losses due to gas flow where n_{i0} is the inlet density of species *i*. Changes in instantaneous pressure are the result of reactions that change the gas composition (dissociation) or gas temperature (gas heating). The pressure term accounts for changes in the flow speed as the gas mixture evolves. The final term in the continuity equation accounts for diffusion losses to the walls where D_i is the gas-phase diffusion coefficient and f_m is the fractional area of wall material *m* in contact with the plasma. S_{im} in the first term is the probability of reaction of species *i* on wall *m*. S_{km} in the second term is the fraction of the diffusive flux that disappears at the wall and g_{ikm} is the give fraction, or the fraction of the consumed flux of species *k* that returns as species *i*.

The diffusion coefficient, D_i, is calculated as

$$D_i = \frac{k_b T_g}{\sum_j \frac{1}{\mu_{ij}} \frac{n_j}{N_{STP}}} \tag{2.4}$$

where μ_{ij} is mobility and N_{STP} is the gas number density at standard temperature and pressure (2.5×10^{19} cm^{-3}). Neutral-species mobility is given by

$$\mu_{ij} = \sqrt{\frac{m_i m_j}{m_i + m_j}} \sqrt{\frac{\pi}{8 k_b T_g}} \frac{1}{m_i N_{STP} \sigma_{ij}} \tag{2.5}$$

where σ_{ij} is the collision cross-section

$$\sigma_{ij} = \pi \left(\frac{\sigma_i + \sigma_j}{2} \right)^2 \tag{2.6}$$

and σ_i and σ_j are the Lennard-Jones radii of species *i* and *j*.

Charged species diffusion is assumed to be ambipolar diffusion. For positive ions, the ambipolar diffusion coefficient is

$$D_{+a} = D_+ \left(1 + \frac{k_b T_e}{k_b T_{ion}} \right) \tag{2.7}$$

Where T_{ion} is the ion temperature. Negative ions are assumed to be in Boltzmann equilibrium and their ambipolar diffusion coefficient is reduced by a Boltzmann factor.

$$D_{-a} = D_- \exp\left(-\frac{V_{float}}{k_b T_g} \frac{n_e}{n_+} \right) \tag{2.8}$$

V_{float} is the plasma floating potential and n_+ is the total positive ion density. The diffusive flux of electrons, Γ_e, is then set such that the diffusive flux of positive ions, Γ_+, is equal to the diffusive flux of negative ions, Γ_-. The total flux to the surface is charge neutral.

$$\Gamma_+ = \Gamma_e + \Gamma_- \tag{2.9}$$

Mobilities for charged species are provided to *GlobalKin* based on experimental data, rather than calculated based on Lennard-Jones parameters.

The electron energy equation, gas temperature energy equation, and species continuity equation comprise a set of ordinary differential equations that are solved with the general purpose ODE solver DVODE [3] and a convergence criterion of 10^{-8}- 10^{-6}. A flow chart of *GlobalKin* is

shown in Figure 2.1.

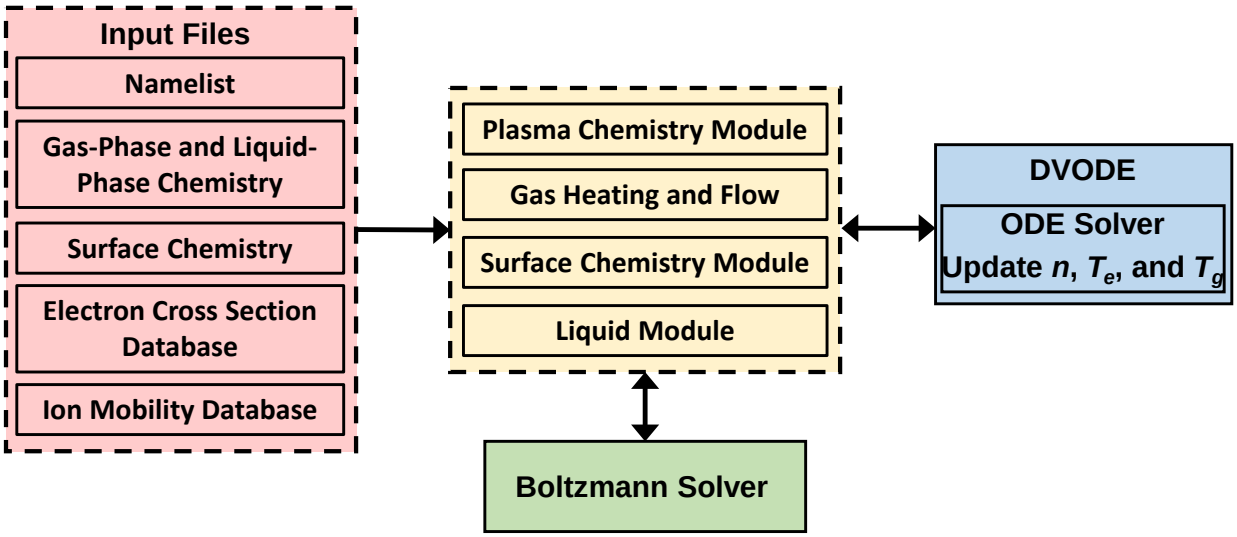

Figure 2.1. Flow chart of *GlobalKin*.

2.1.1 The Plug-Flow Approximation

In *GlobalKin*, gas-flow is advanced either in time (as residence time), or as a function of reactor position using a plug-flow approximation. The plug-flow approximation is valid in subsonic, constant pressure flow systems as long as diffusion in the flow direction is negligible. As these assumptions are applicable to the work described in later chapters of this dissertation, gas-flow is always approximated as plug-flow herein.

The plug-flow approach follows a slug of gas down the length of a reactor having a cross-sectional area $A = WD$, where W is the electrode width and D is the distance between the two electrodes. The plug speed, v, is calculated as $v = \frac{F}{A}$ where F is the volumetric flowrate. F is a function of input flowrate (sccm) and gas density. The plug speed is adjusted as the gas density changes due to dissociation reactions that increase the total inventory of atoms and molecules, or gas heating. The gas temperature is adjusted to maintain constant pressure. Transport perpendicular to the flow direction is assumed to be dominated by diffusion. Charged particle

diffusion to the walls is addressed as ambipolar diffusion while neutral particles are addressed by fundamental free-mode diffusion. The plug-speed is used to convert integration in time to integration in space along the flow direction by translating $d/dx = \left(\frac{1}{v}\right) d/dt$. The conversion of the integral from time to space provides a pseudo-1D approximation of gas-flow without the need for a spatial mesh. The species densities and electron temperature as a function of reactor length in a He/O_2 APPJ used to functionalize polystyrene are shown in Figure 2.2 as an example of the output of *GlobalKin* operated in plug flow mode.

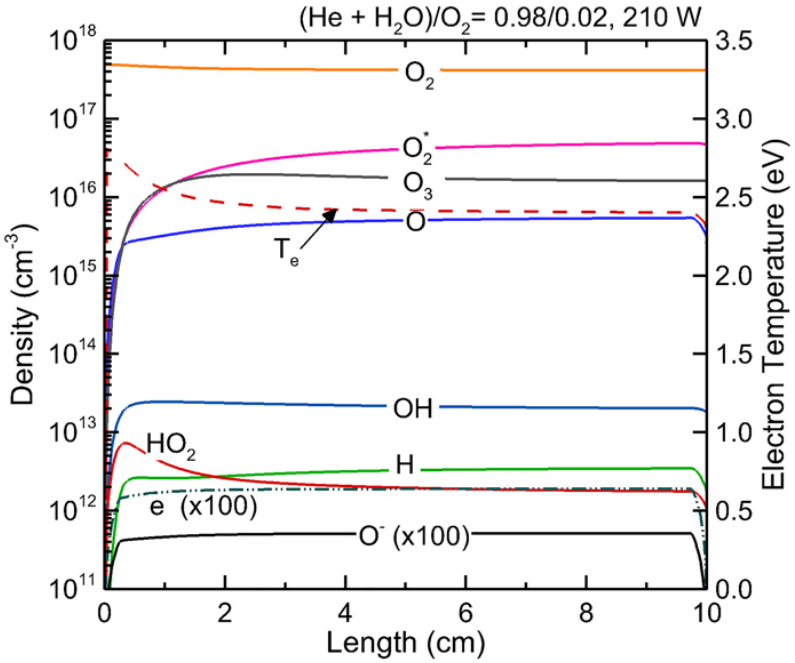

Figure 2.2. Example output of *GlobalKin* operated in plug-flow mode. Gas-phase species densities and electron temperature in a He/O_2 APPJ used in the functionalization of polystyrene.

When using the plug-flow option in *GlobalKin* total input power (W/cm^3) is specified as a function of reactor position in the flow direction. The power density profile is normalized so that the integral of the power density profile over the total reactor volume is equal to the desired

total input power. Power is constant along the length of the reactor for all of the works included in this thesis, save for a 1-2 mm ramp up distance at the top of the reactor and a 1-2 mm ramp down distance at the end of the reactor.

2.1.2 Algorithm for Describing Nanoparticle Growth[1]

Capability was added to *GlobalKin* to describe nanoparticle growth in a low-pressure, low-temperature, flowing plasma. The algorithm described in this subsection is used in Chapter 3 to provide insight into transport regimes dominating silicon nucleation and growth in a small quartz tube reactor.

The nanoparticle algorithm utilizes *GlobalKin* produced number densities and reaction rates to predict the average nanoparticle radius as a function of reactor position (when the plug-flow approximation is used). Particle growth is tracked by accounting for changes in particle mass density,

$$\frac{d\rho_m}{dt} = \sum_{i,j} n_i n_j k_{ij} \left(\pm \Delta m_{ij} \right) \tag{2.10}$$

where ρ_m is the instantaneous mass density of particle species m, k_{ij} is the reaction rate coefficient between species i and j having densities n_i and n_j. Δm_{ij} is the change in mass of the NP due to these reactions. Losses in particle mass density due to diffusion to the reactor walls are also accounted for.

The instantaneous NP mass is derived from the mass density as

$$m_i = \frac{\rho_i}{n_i} \tag{2.11}$$

[1]Portions of the text in this subsection have been previously published in E. Husmann, J. Polito, et. al. "Design Considerations for Controlling Silicon Nanoparticle Nucleation and Growth in Nonthermal Plasmas," Plasma Chemistry and Plasma Processing 43, 225-245 (2023).

where n_i is the number density of NP particle species *i*. Assuming particles are spherical, the radius of the particle scales as

$$r_i = r_0 \left(\frac{m_i}{m_0} \right)^{1/3} \tag{2.12}$$

where r_0 is the original radius of the particle species and m_0 is the original mass of the particle species.

2.1.3 Surface Kinetics Module

GlobalKin includes capability to address plasma interactions with surfaces that may result in etching, sputtering, or changes in functionalization [4]. The Surface Kinetics Module (SKM) uses fluxes of ions and neutrals from *GlobalKin* as input to predict changes in surface composition. The SKM consists of a set of rate equations for the surface density of sites (or fraction surface coverage) of surface resident species. The surface site balance accounts for rates of adsorption, abstraction, and desorption resulting from incident gas phase fluxes, and by reactions between surface species. The site balance equation is

$$\frac{\partial \theta_j}{\partial t} = -\theta_j \left(\sum_i \phi_i p_{ij} + \sum_m \theta_m p'_{jm} \right) + \sum_{i,m} \theta_m \phi_i p_{imj} + \sum_{l,m} \theta_l \theta_m p'_{lmj} \tag{2.13}$$

where θ_j is the surface site coverage of species or group *j*, ϕ_i is the incident flux of gas-phase species *i*, p_{ij} is the total reaction probability of gas phase species *i* with surface species *j*, p_{imj} is the probability of reaction between gas-phase species *i* and surface species *m* that produces surface species *j*, p'_{jm} is the total probability of reaction between surface sites *j* and *m*, and p'_{lmj} is the total probability of reaction between surface species *l* and *m* to produce surface species *j*.

In plasma applications such as polymer processing, surface exposure to the ambient air soon after plasma treatment may result in termination of radical species still present on the polymer

surface or, at longer time periods, changes to surface morphology known as aging [5,6]. Capability was added to the SKM to allow for post-exposure of a surface to a post-processing gas (or ambient atmosphere). After the specified plasma treatment time, plasma-produced gas-phase fluxes to the surface are replaced by diffusive fluxes of a user-specified gas to the surface. For example, in Chapter 4 of this dissertation, a polymer surface is exposed to ambient humid air after plasma treatment. The SKM is then executed for additional time to allow the surface to come to a near steady state.

2.1.4 Liquid Module

GlobalKin includes capability to account for the interaction of a plasma in contact with a liquid surface. The liquid module was first described in Lietz and Kushner [1]. Gas-phase fluxes from *GlobalKin* are used as a source term in the species continuity equation to predict densities of liquid species as a consequence of plasma exposure over a user-specified amount of time. Every gas-phase species has a solvated counterpart that may participate in a liquid-phase reaction. A separate liquid-phase reaction mechanism is included (with appropriate rate coefficients and cross sections) for the liquid module.

The liquid is considered as a separate well-stirred volume with its own species continuity equation for solution of species densities. The species continuity equation used in the liquid module is similar to that used in the gas-phase.

$$\frac{dn_{i,liq}}{dt} = \sum_j \left(\left(a_{ij}^{(R)} - a_{ij}^{(L)} \right) k_j \prod_l n_l^{a_{ij}^{(L)}} \right) + \frac{D_{i,gas} n_{i,gas}}{\Lambda^2} f_{liq} S_{i,liq} \frac{V_{gas}}{V_{liq}} - \max\left(0, \frac{D_{i,gas}\left(n_{i,liq} - h_i n_{i,gas} \right)}{\Lambda^2} \frac{V_{gas}}{V_{liq}} \right) \tag{2.14}$$

The first term represents sources and losses of species *i* as a result of liquid-phase reactions. The second term represents diffusion of gas-phase species into the liquid where f_{liq} is the fractional area of the liquid in contact with the plasma, V_{gas} is the gas-phase volume, and V_{liq} is the user-specified liquid volume. The sticking coefficient, $S_{i,liq}$ for a neutral gas-phase species solvating into the liquid is calculated based on Henry's law, where h_i is the Henry's law constant for species *i*.

$$S_{i,l} = \frac{h_i n_{i,gas} - n_{i,liq}}{h_i n_{i,gas}} \tag{2.15}$$

If $\frac{n_{i,l}}{n_{i,g}} < h_i$, species will solvate into the liquid. If $\frac{n_{i,l}}{n_{i,g}} > h_i$, the liquid is super-saturated and net transport of species *i* is from the liquid into the gas-phase. The third term in the species conintuity equation allows for fluxes of species *i* back to the gas-phase if the liquid is super-saturated. Charged particles solvate with unity probability (S_i = 1).

2.2 Author's Contributions

The author developed and implemented the nanoparticle growth algorithm, which provides a volume averaged estimation of nanoparticle mass density and radius based on plasma properties, into *GlobalKin*.

The author also made significant changes to the 2D Hybrid Plasma Equipment Model (HPEM) [7], which are not included in this dissertation. Changes to the HPEM included the added capability to track nanoparticle properties (mass, radius, and mass and number density) in the fluid portion of the HPEM. This added capability involved restructuring of several main subroutines (i.e., heavy particle momentum, mobility, and diffusion) to allow for species having variable mass.

The author's major contribution was in the development of several reaction mechanisms that are used as input to the *GlobalKin*. Detailed discussion of the development of the reaction

mechanisms, the reaction sets included in the mechanisms, and validation of the mechanisms, appears in later chapters.

2.3 References

[1] A. M. Lietz and M. J. Kushner, J. Phys. D. Appl. Phys. **49,** 425204 (2016).

[2] R. Dorai, K. Hassouni and M. J. Kushner, J. Appl. Phys. **88,** 6060 (2000).

[3] P. N. Brown, G. D. Byrne and A. C. Hindmarsh, SIAM J. Sci. Stat. Comput. **10,** 1038 (1989).

[4] A. N. Bhoj and M. J. Kushner, J. Phys. D. Appl. Phys. **39,** 1594 (2006).

[5] P. C. Schamberger, J. I. Abes and J. A. Gardella, Colloids Surfaces B Biointerfaces **3,** 203 (1994).

[6] N. V. Bhat and D. J. Upadhyay, J. Appl. Polym. Sci. **86,** 925 (2002).

[7] M. J. Kushner, J. Phys. D Appl. Phys. **42,** (2009).

Chapter 3 Processes Contributing to Silicon Nanoparticle Growth in Low Temperature Flowing Plasmas[2]

Controlling the nucleation and growth of nanoparticles in low temperature plasma systems is imperative for controlling nanoparticle size distributions; and for some applications such as deposition and etching in microelectronic processing, preventing particle contamination. In this work, silicon nanoparticle (NP) production from silane is used as a model system to investigate the nucleation process. Although the mechanisms responsible for silicon NP nucleation and growth have been studied, it is unclear how controllable system parameters (e.g., pressure, system geometry, and gas composition) can be used to inhibit or promote NP formation. For example, the transport of reactive silane species is expected to significantly affect the feed fraction of silane required to nucleate silicon NP (the nucleation onset fraction) due to losses at the reactor walls. In this work, NP mass density was determined as a function of system pressure, gas composition, and reactor diameter for a tubular flow-through radiofrequency (RF) plasma using $Ar/H_2/He/SiH_4$ gas mixtures. A quartz crystal microbalance (QCM) impactor was used to measure the total aerosol mass density downstream of the plasma and thereby identify the nucleation onset and its dependence on process parameters. A reaction mechanism was developed and incorporated into a global plasma chemistry model to better understand the nucleation onset and NP growth.

[22] Results discussed and portions of the text in this chapter have been previously published in E. Husmann, **J. Polito**, et. al. "Design Considerations for Controlling Silicon Nanoparticle Nucleation and Growth in Nonthermal Plasmas," Plasma Chemistry and Plasma Processing 43, 225-245 (2023).

3.1 Introduction

The promotion or suppression of silicon nanoparticle formation in dilute silane containing plasmas is a topic of interest within the nanomaterials field. Silicon nanoparticles are being investigated for their use in photocatalysis [1,2], optoelectronics [3], energy storage [4], and medicine [5,6]. Controlling the nucleation and growth rate of nanoparticles allows for increased particle mass yields, control over particle size, or even suppressed particle formation if particles are undesired. In the case of semiconductor processing, particle deposition onto microelectronics devices during fabrication steps using plasmas continues to be a source of reduced yields [7]. With device dimensions having approached nm scale, particles below 10 nm in diameter are "killer defects" [8]. The suppression of particle formation in these systems typically is accomplished by reducing plasma power, which reduces processing rates and utilization of the feedstock gases. As such, the ability to suppress particle formation while promoting film growth or etching is of great benefit.

Several methods have been reported to reduce particle contamination of thin films during plasma processing. The methods used to prevent existing particles from reaching a film surface include increasing the volumetric flowrate through the plasma reactor to sweep out particles [9] and leveraging thermophoresis to transport particles away from a higher temperature substrate [10]. Plasma pulsing has also been shown to be capable of reducing particle formation and/or removing electrostatically trapped particles [11–14]. Silane containing plasmas for silicon amorphous film deposition are often diluted with hydrogen to improve film quality [15,16], a practice that has also been shown to inhibit particle formation [14,17]. As a side effect, hydrogen dilution can also decrease film deposition rates [18]. In spite of these techniques, particle contamination remains a significant problem and is made more challenging by the need to prevent

formation of particles less than 10 nm in diameter to meet current process requirements.

In this chapter, we discuss the application of a quartz crystal microbalance (QCM) impactor capable of detecting nanoparticles having sizes 10 nm or less under low pressure conditions. Although size information cannot be obtained directly from the diagnostic reported herein, there are significant benefits of using a single impaction stage including: high mass resolution, high mass sensitivity, low capital cost compared to other instruments, and low operating expenses. For applications such as monitoring dust contamination in microelectronic processing reactors, size information is not always important since the goal is often to suppress nanoparticle formation, or more specifically, have the mass density of the aerosol below a certain value defined by the process quality control constraints.

In spite of several studies related to the nucleation and formation of silicon nanoparticles in dilute silane plasmas, little focus has been given to suppressing or promoting particle formation by exploiting the transport of reactive silane radical species. Maemura et al. studied particle densities in a parallel plate plasma reactor at two different electrode spacings; however, the effects of electrode spacing on particle mass density were unclear [19]. Bhandakar et al. demonstrated that particle formation can be suppressed by increasing the Brownian diffusion of reactive species by increasing the bulk gas temperature [20].

In this work, a QCM impactor was used to study the effects of tube diameter, reactor pressure, and gas composition on particle formation (presented as a mass density of particles leaving the plasma reactor). Decreasing the discharge tube diameter inhibited particle formation as reactive species diffuse shorter distances on average to be lost to the reactor walls. Since diffusion coefficients scale inversely with pressure, to test the hypothesis we showed that increasing pressure can also promote particle formation by suppressing diffusive losses. As

hydrogen addition to the gas mixture is known to inhibit particle growth, hydrogen content in the reactor inlet was also varied to determine if the consequences of hydrogen content and tube diameter/operating pressure are cumulative. A 0-dimensional global plasma chemistry model was adapted to predict NP growth, and to provide further insights into silicon nanoparticle growth as a function of inlet gas composition and reactor diameter.

The experimental setup that the modelling results are based on is described in Section 3.2.1. the reaction mechanism used in the model is described in Section 3.2.2. Discussion of nanoparticle scaling as a function of plasma operating conditions is in Section 3.3. Concluding remarks are in Section 3.4.

3.2 Experimental and Computational Methods

To quantify the effects of pressure, reactor tube diameter, hydrogen content, and the silane fraction fed on NP nucleation, experiments were performed for two sets of conditions: constant pressure, and constant reactor tube diameter. For each of these cases, hydrogen content and the silane fraction were varied, however, the total molar flowrate was constant for all experiments. Particles generated in the plasma reactor were detected by the QCM impactor. Comparison of trends for NP production were made with results from the global plasma chemistry model.

3.2.1 Experimental Methods

The primary components of the experimental setup are the tubular plasma reactor and the QCM impactor, illustrated in Fig. 3.1. The plasma reactor consists of a 25 cm-long fused silica tube with two ring electrodes to produce a capacitively coupled plasma (CCP). Tubes having inner diameters of 1.0 cm, 1.7 cm, 2.2 cm, and 3.2 cm were investigated. The feed gas was 0.9% silane in helium and a balance gas of either pure argon, 10% hydrogen in argon, or pure hydrogen. The

total molar flowrate, controlled by flow controllers (MKS Instruments and Bronkhorst), of the feed gas was held constant at 52 standard cubic centimeters per minute (sccm). The reactor pressure was varied from 4.5 to 8.5 Torr by throttling the pump via a valve. A radio frequency (RF) 13.56 MHz AG0163 power supply with an AIT600 matching network (T&C Power Conversion) was used to supply the plasma reactor with 5 W of power, which was constant for all conditions. Ideally, average plasma parameters (e.g., electron temperature, ion density, bulk gas temperature) would be kept constant for all conditions; however, the measurement and maintenance of these parameters was beyond the scope of this work. Note that the measurement of plasma parameters for a silane plasma using Langmuir probe techniques [21] is made challenging due to silicon deposition fouling on the probe tips [22].

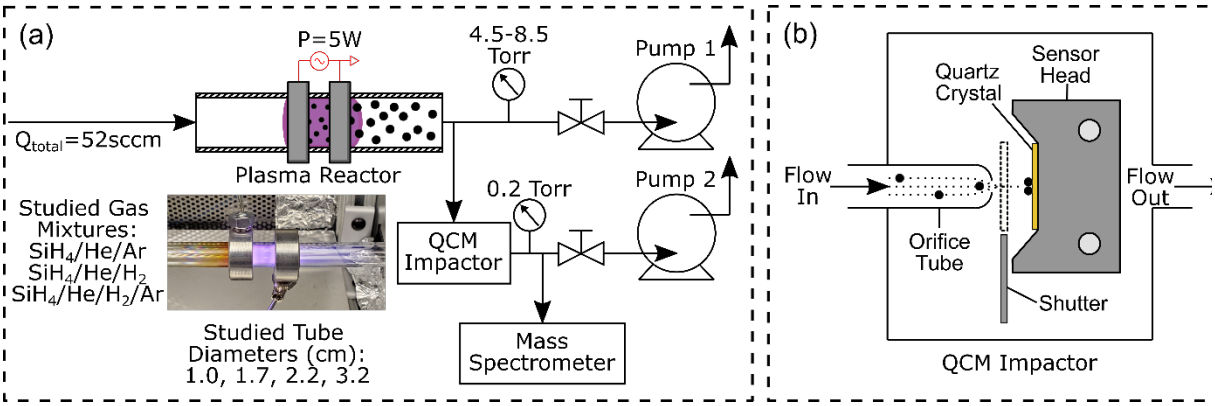

Figure 3.1. (a) Schematic of the experimental apparatus and (b) diagram of the QCM impactor.

Downstream of the plasma reactor, gas was diverted to the QCM impactor. The amount of gas diverted was not held constant due to the different reactor pressures and chemical composition. A 150 μm diameter orifice tube (Lenox Laser) was used to impact particles onto the quartz crystal (Telemark, part number 880-0201-3). Molar flowrates to the QCM were determined using software provided by the orifice manufacturer [23]. The pressure downstream of the orifice was held at 0.2 Torr.

For the conditions of this investigation, all particles, irrespective of size, are expected to impact onto the quartz crystal since the critical cutoff diameter of impaction, $d_{p,c}$, was always less than 1 Å (much smaller than any critical cluster size). As a result, the QCM measures the total aerosol mass current in the sample stream. The cutoff diameter of impaction is given by [24]:

$$d_{p,c} = \left(\frac{9\pi \cdot \mu \cdot D_O^3 \cdot Stk_C}{4 \cdot \rho_p \cdot Q \cdot C_C(P)} \right)^{0.5} \tag{3.1}$$

where μ is the dynamic viscosity of the gas, D_O is the diameter of the orifice, Stk_C is the critical Stokes number (0.24 for a circular orifice), ρ_p is the mass density of the particle material (i.e. silicon), Q is the volumetric flowrate through the orifice, and $C_C(P)$ is the Cunningham slip correction factor, which is dependent on pressure. Particles were assumed to stick to the QCM surface since the particles were small (< 10 nm) and thus the particles had a smaller kinetic energy in comparison to the adhesion energy [25,26]. Particle size was verified using a transmission electron microscope (TEM), and results can be found in section S.2 of the SI. To maintain constant impaction conditions, the orifice was cleaned between experiments using sonification in water for 5 minutes followed by blasting with pressurized air. The orifice was subsequently dried in a desiccator oven.

The quartz crystal was held by a sensor head (Telemark) equipped with a shutter. The resonance frequency of the quartz crystal was monitored using an OSC-100 oscillator (Inficon) and an FTM-2400 quartz crystal monitor (Kurt J. Lesker). The change in resonance frequency of the quartz crystal can be converted into a mass loading by using the Sauerbrey equation [27]:

$$\Delta m = -\Delta f \cdot \left(\frac{A \cdot (\rho_q \cdot \mu_q)^{0.5}}{2 \cdot f_0^2} \right) \tag{3.2}$$

where Δm is the change in the mass loading of the quartz crystal, Δf is the change in the quartz crystal resonance frequency, A is the effective crystal area, ρ_q is the density of the quartz crystal (2.65 $g \cdot cm^{-3}$), μ_q is the shear modulus of the quartz crystal ($2.95 \cdot 10^{11}$ $g \cdot cm^{-1} \cdot s^{-2}$), and f_0 is the resonant frequency of the fundamental mode of the quartz crystal (6 MHz). To avoid overloading, the quartz crystal was replaced whenever Δf > 40 Hz from its original value. The sampling procedure for the QCM is as follows: plasma ignition, opening the QCM shutter after 10 seconds, particle sampling for up to 120 seconds, closing the QCM shutter, turning the plasma off. Deposition rates were determined by fitting the linear response of the QCM. Deposition rates were then converted into particle mass densities by normalizing the deposition rates by the volumetric flowrate to the QCM.

Particles were impacted onto a small area at the center of the crystal. As a result, the calculated mass loading is expected to be overestimated by a constant factor if the effective crystal area is assumed to be that of the overlapping electrodes on the quartz crystal (0.33 cm^2, as determined from the electrode geometry shown in Fig. S.3 of the SI). This overestimate is due to the quartz crystal having a radially dependent mass sensitivity, with a maximum sensitivity at the center [34-36]. To account for this effect, the sensitivity of the QCM was determined as a function of radial distance from the center of the quartz crystal, r. To perform this calibration, a 200 $ng \cdot \mu L^{-1}$ solution of < 25 nm TiO_2 nanoparticles (Sigma-Aldrich, catalog number 637254) in deionized water (18.2 $M\Omega \cdot cm$) was prepared. QCM sensitivity as a function of r was determined by depositing 0.2 μL of the prepared solution at various locations for a series of quartz crystals. The water was left to evaporate at atmospheric conditions for 6 minutes, leaving behind a deposit of

TiO_2 nanoparticles of a known mass. QCM sensitivity was then calculated as the change in the quartz crystal resonance frequency over the mass loading. The positions of the deposits were measured from digital images of the quartz crystals. To avoid depositing over existing deposit and to simplify image processing, up to 4 depositions were performed in a line for each quartz crystal.

Downstream of the QCM, a quadrapole mass spectrometer (ExTorr Inc., Model XT300) was used to determine the amount of remaining silane. Ionization of the silane was performed by electron impact using an electron energy of 70 eV and a current of 2 mA. The $m / z = 31$ peak (corresponding to the mass-to-charge ratio of SiH_3^+, a dominant product of dissociative ionization of SiH_4) was normalized by the $m / z = 4$ peak (corresponding to helium) to account for small fluctuations of the reactor pressure upon plasma ignition and termination, which directly affected the flow to the mass spectrometer.

3.2.2 Computational Methods

GlobalKin, a 0-dimensional plasma chemistry model, was adapted for use in this work to predict NP growth. A detailed description of *GlobalKin* and the nanoparticle growth algorithm developed for this work can be found in Chapter 2.

Species and reactions used in the model for NP growth are listed in Table 3.1 and Table 3.2. Briefly, silane molecules undergo electron impact dissociation to form Si_xH_y radical species. A radical species is any Si_nH_m species where $m < 2n + 2$. Any species having $m = 2n + 2$ is a saturated silane species. Dissociation of silane molecules is produced by electron impact dissociative excitation and ionization, dissociative recombination, charge exchange, and excitation transfer from rare gas atoms. Si_nH_m radicals combine with each other or with saturated molecules to form higher order Si_nH_m species. This process continues until Si_nH_m clusters become large enough to be classified as nanoparticles. Here we classified a nanoparticle to be any Si_nH_m species

with $n \geq 13$. For example, the reaction

$$Si_3H_7 + Si_{11}H_{24} \rightarrow NP \tag{3.3}$$

produces a NP as the sum of the silicon atoms in the reactants exceeds 12.

Nucleation reactions, as in Eq. (3.3), initially produce and increase both the mass density and number density of NPs. Surface growth reactions, such as

$$SiH_3 + NP \rightarrow NP \tag{3.4}$$

add to the mass density of NPs while not adding to the number density of NPs. Coagulation reactions such as

$$NP + NP \rightarrow NP \tag{3.5}$$

decrease the number density of NPs while not changing the mass density. Neutral NPs were classified as being saturated or radicals, depending on the growth species.

When the precursor (or lower order Si_nH_m) species have been depleted due to surface deposition reactions, nanoparticles combine with each other in the coagulation reactions. Coagulation reactions will contribute no change to the particle mass density but will decrease the particle number density to yield particles with larger effective radius.

The choice to represent a NP as any Si_nH_m species having greater than 13 Si atoms was based in part on computational efficiency and part on the concept of "critical cluster size." As higher order Si_nH_m species are included in the mechanism, the number of reactions needed – and therefore the computational time required – to account for nucleation and coagulation grows rapidly. Here we take "critical cluster size" to mean the point at which a particle has reached a sufficiently large radius that growth is dominantly by surface processes (silane radicals sticking on the growing NP) and later by coagulation reactions (NP reacting with NP). Once the silane radicals have been depleted, growth is dominantly by coagulation. The cross sections for both

radical growth and coagulation increase as the number of Si atoms in the particle increases [28]. Optimization of the reaction mechanism used here has shown that the choice of 13 Si atoms to a NP enables representation of nucleation, growth and coagulation processes with relative computational efficiency on the timescales relevant in this system. Nucleation, growth and coagulation reactions occur simultaneously, though we expect the rate of coagulation to dominate as particles increase in size and silane radicals are depleted.

When nanoparticle number density in the plasma is high, they can carry both negative and positive charge [29,30]. Negative and positive nanoparticles are accounted for as separate species with independent mass densities. Negative and positive nanoparticles can interact with neutral nanoparticles through charge exchange or coagulation, or with each other through neutralization reactions. We assume that the elementary charge on the particles does not exceed ± 1. Previous work [31] has shown that this assumption is valid when the nanoparticle diameter is small.

3.3 Scaling of NP Nucleation and Growth

Experiments were performed to determine the effects of system parameters on particle formation. A detailed discussion on the development of the QCM impactor, including results from the validation and verification of the QCM can be found in the published version of this work (see footnote on page 39), but do not appear in this chapter. Following verification of the QCM impactor, the effects of pressure, hydrogen content, reactor tube diameter, and the silane fraction at the reactor inlet on particle formation were investigated using both experimental and computational methods.

3.3.1 The Effects of System Parameters on Particle Formation -Experimental

To relate the nucleation onset fraction to experimental parameters, particle mass density

(the mass deposition rate normalized by the volumetric flowrate to the QCM) was determined as a function of the silane fraction in the reactor inlet, reactor pressure, and hydrogen content, as shown in Fig. 3.2. For all cases, the mass density increased with increasing silane fraction at the reactor inlet. Intuitively, as more silane was fed into the reactor, more mass can be incorporated into particles. As pressure was increased at the same fraction of silane at the reactor inlet, particle mass density increased for all cases. The increase in mass density of the NPs agrees with the hypothesis that decreasing the diffusion coefficient of reactive silane radical species (by increasing the pressure) promotes particle formation over film deposition on the walls of the reactor. As the diffusion coefficient of reactive species is decreased and the reactor size is held constant, more radical species can be incorporated into particles before depositing on the walls since transport to the reactor walls is limited. Note that by the ideal gas law, increasing pressure will increase the silane mass density at the reactor inlet even if the fraction is the same.

When a 10% H_2 gas mixture was used in the inlet, shown in Fig. 3.2b, particle mass density generally increased compared to the pure argon case, shown in Fig. 3.2a. This result was surprising as hydrogen has been reported to suppress particle formation [14,17]. A moderate amount of H_2 in the balance gas appears to be disproportionately inhibiting film formation on the walls over particle growth for these conditions. Hydrogen radicals can deprotonate silane and other silyl species via hydrogen abstraction [32,33], and the resultant faster reaction kinetics are expected to promote particle formation over film growth due to diffusion to the walls.

This mechanism would require the increased rate of silane deprotonation by hydrogen radicals to be greater than the increase in conversion of reactive silyl species back into silane by hydrogen incorporation. Alternatively, a small to moderate amount of H_2 in the inlet flow may disproportionally inhibit film formation over particle formation by reducing the number of

potential reactive sites on the reactor walls. Upon increasing the hydrogen fraction from 10% H_2 to pure H_2, particle mass density in the effluent was decreased by over an order of magnitude (Figs. 3.2b-c). Particle formation is suppressed for high fractions of hydrogen in the balance gas. This effect will be later discussed in more detail.

Since the suppression of particle formation is important for a variety of industrial processes, the nucleation onset fraction was measured as a function of pressure and hydrogen content in the balance gas. The results are shown in Fig. 3.3. The nucleation onset fraction provides a minimum reactor inlet silane fraction above which particles can be detected with the QCM impactor. As the reactor pressure was increased, the nucleation onset fraction generally decreased. The effect of pressure was most significant when the balance gas was 10% H_2 where the nucleation onset fraction was reduced by a factor of 3 over a pressure range of 4.5 Torr to 8.5 Torr. However, this

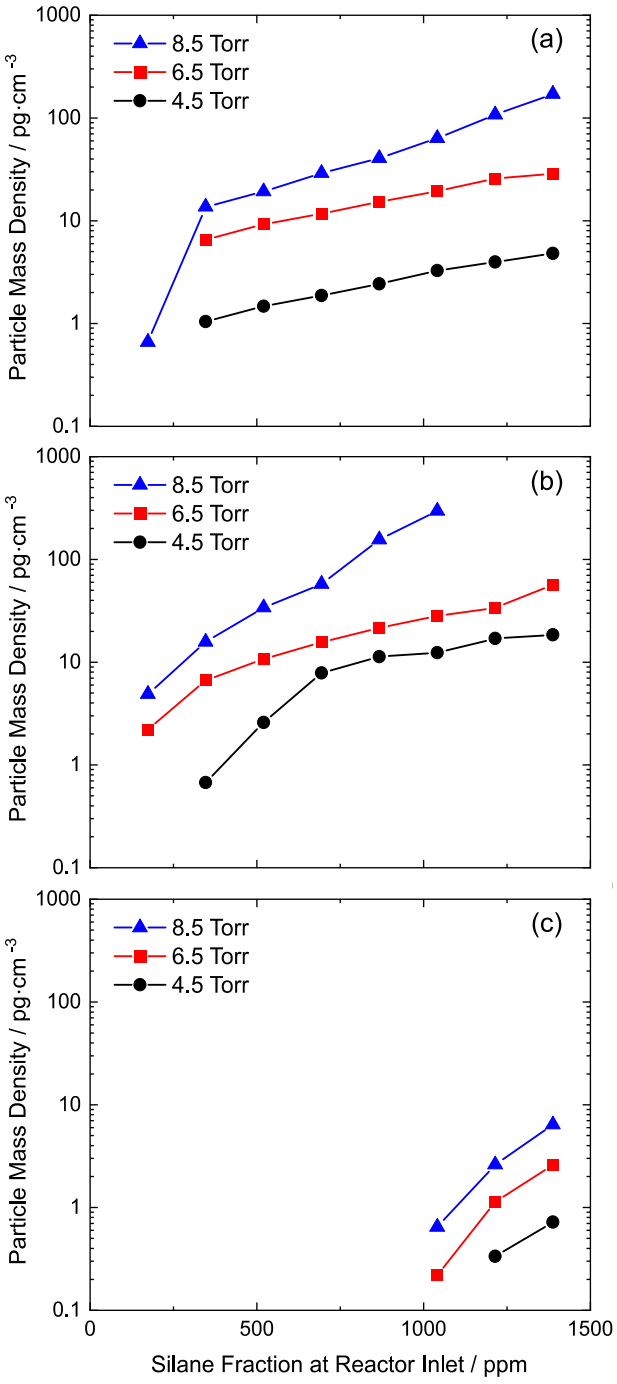

Figure 3.2. Particle mass density as a function of the silane fraction fed into the plasma reactor for various pressures at constant tube diameter given a balance gas of (a) pure Ar, (b) 10% H_2 in Ar, (c) pure H_2.

reduction was small considering that the increase in pressure results in an increase of the density of silane at the rector inlet by approximately a factor of 2. When a balance gas of pure H_2 was used, the nucleation onset fraction was larger and nearly constant over the pressure range that was investigated.

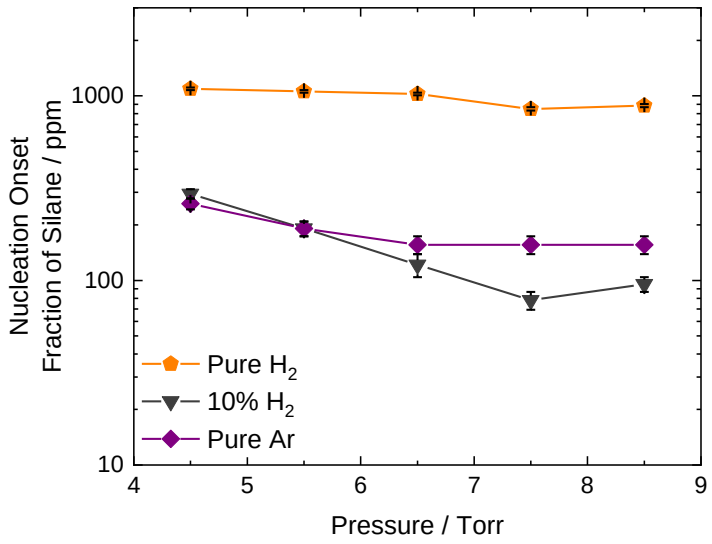

Figure 3.3. The nucleation onset fraction of silane as a function of reactor pressure at constant tube diameter for various balance gases. The bottom and top of the error bars represent the reactor inlet silane fractions at which the measured deposition rate was below and above the nucleation threshold respectively.

When the balance gas was switched to pure H_2, particle formation was greatly suppressed, as shown in Fig. 3.2c and Fig. 3.3. This result corroborates previous reports in the literature [14,17], and can be explained by the suppression of silane conversion into reactive species.

Silane conversion appears to be independent of tube diameter for our conditions as mass spectroscopy results for the 1.0 cm and 3.2 cm tubes were nearly identical. The timescale of silane conversion is expected to be much shorter than the gas residence time in the plasma reactor [34], while the observed film deposition onto the reactor walls was largely focused upstream or at the

powered electrode with little film deposition at or past the grounded electrode. As such, gas residence time is not expected to be an important parameter in determining eluted particle mass density, independent of reactor pressure and diameter, for our conditions. It would be ideal to have the capability to channel the silicon mass into either particle formation or film deposition, depending on the goal of the process, while maintaining a high precursor conversion. Varying reactor tube diameter appears promising to that end.

Particle mass density increased with tube diameter. To assess how the reactor tube diameter affects particle formation, particle mass density was measured as a function of the reactor inlet silane fraction at a constant reactor pressure of 6.5 Torr for various tube diameters, as shown in Fig. 3.4. Similar to the results shown in Fig. 3.2, particle mass density increased with increasing silane fraction at the reactor inlet for any given tube diameter. Upon increasing the tube diameter, particle mass density increased significantly for the pure Ar and 10% H_2 cases (over an order of magnitude when comparing the 1.0 cm tube mass densities to the 3.2 cm tube mass densities). These experiments were carried out at constant pressure and flow rate, and thus were free of artifacts due to changing silane mass density at the reactor inlet. This result is consistent with the

original hypothesis that smaller tubes will suppress particle formation due to higher rates of diffusion loss to the walls.

Particle mass densities were similar for the cases when the balance gas was Ar compared to 10% H_2 (all else kept constant). However, when the balance gas was switched to pure H_2, a significant decrease in particle mass densities occurred. For the pure H_2 case, particle mass density no longer increased with increasing tube diameter. High H_2 content may be lowering reaction rates such that deposition on the reactor walls is limited by kinetics rather than diffusion. This would explain why particle formation was suppressed (due to the lower concentrations of reactive species) and why the tube diameter becomes less relevant. As previously discussed, high H_2 content can suppress both particle and film formation on the walls of the tube. As such, the potential benefit of inhibiting particle formation is accompanied by reducing the film deposition

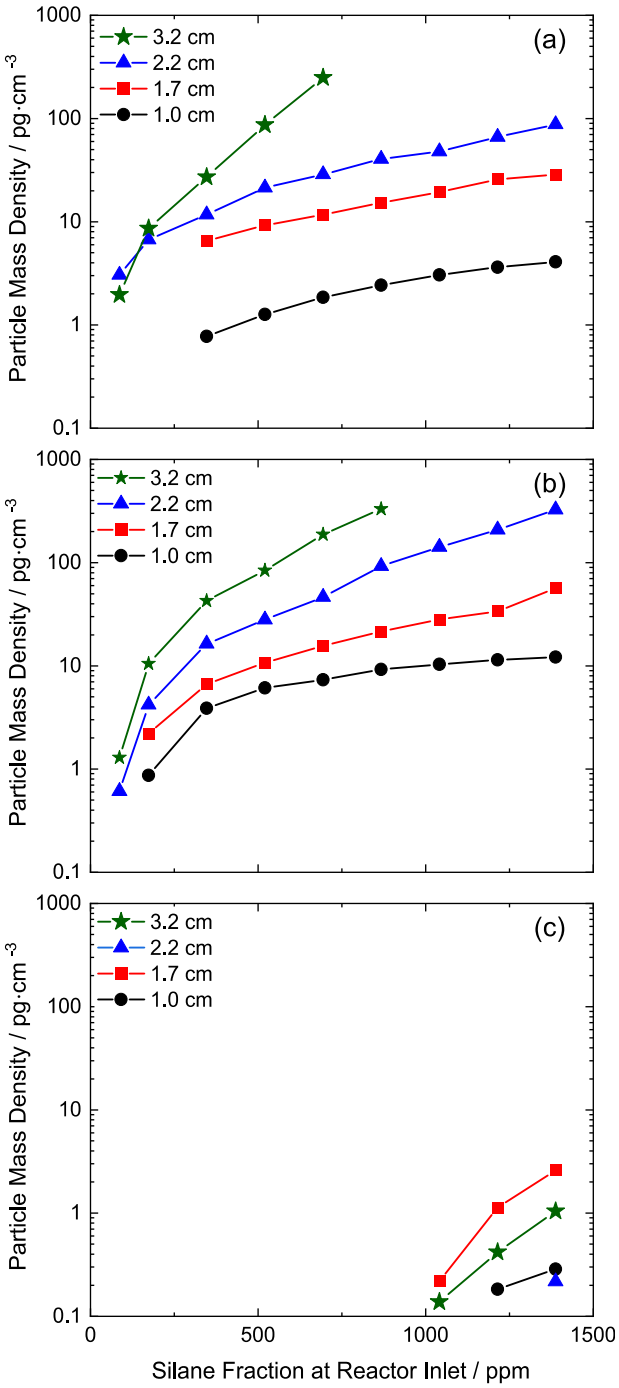

Figure 3.4. Mass deposition rate as a function of the reactor inlet silane fraction fed into the plasma reactor for various tube diameters at constant pressure given a balance gas of (a) pure Ar, (b) 10% H_2 in Ar, (c) pure H_2.

rate.

The results shown in Fig. 3.4 indicate that increasing reactor tube diameter can increase particle mass density when the background gas is Ar, while with a balance gas of pure H_2, the particle mass density is nominally independent of tube diameter. It is not immediately clear how the nucleation onset fraction of silane will be affected. As such, it is useful to express the nucleation onset fraction of silane as a function of reactor parameters for applications which focus on inhibiting particle formation. The nucleation onset fractions as a function of tube diameter given a balance gas of pure Ar, 10% H_2, and pure H_2 are shown in Fig. 3.5. For the pure argon case, increasing the tube diameter from 1.0 cm to 3.2 cm decreases the nucleation onset fraction by over an order of magnitude, a result explained by diffusion losses to the wall.

Upon switching to a balance gas of 10% H_2, increasing the tube diameter from 1.0 cm to 3.2 cm only decreased the nucleation onset fraction by a factor of 2, as hydrogen can suppress the effects of varying tube diameter by limiting reaction kinetics. This result may suggest that the deprotonation of silane radical species by hydrogen radicals was not significant compared to the insertion of hydrogen to convert reactive silane species back into silane species. As such, hydrogen may generally inhibit silane conversion, but disproportionally favor particle formation or film formation depending on the specific reactor conditions.

The nucleation onset fraction was significantly increased when the balance gas was switched to pure H_2, meaning particle nucleation was suppressed. The nucleation onset fraction appears to be largely independent of the tube diameter for a pure H_2 balance gas. Although varying H_2 content and varying the tube diameter appear to be useful parameters for suppressing or promoting particle formation, these effects cannot be combined to suppress particle formation. Although hydrogen may be required for some deposition processes to control film crystallinity

[15,16], for processes that do not require hydrogen, the use of small reactor sizes for deposition processes shows promise for inhibiting particle formation.

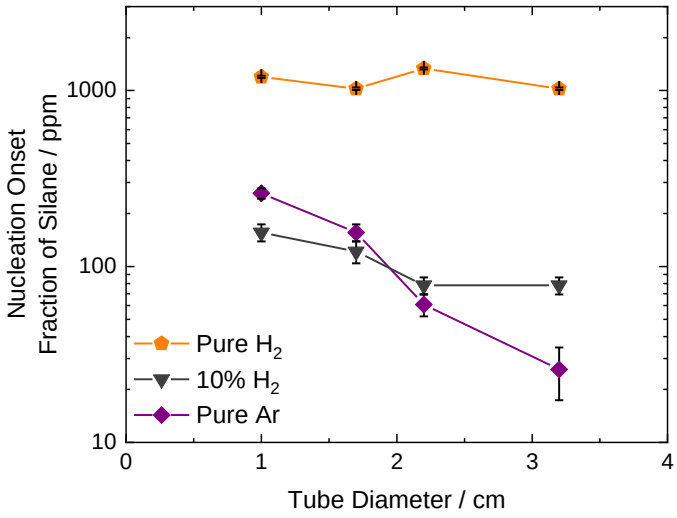

Figure 3.5 The nucleation onset fraction of silane as a function of reactor tube diameter for various balance gases. The reactor pressure was 6.5 Torr. The bottom and top of the error bars represent the reactor inlet silane fractions at which the measured deposition rate was below and above the nucleation threshold respectively.

3.3.2 The Effects of System Parameters on Particle Formation – Modelling

The computer model *GlobalKin* was used to further investigate the effects of changing reactor operating conditions on the nucleation and growth of silicon nanoparticles. The inlet gas mixture was flowed at 52 sccm with a small fraction (70-1000 ppm) of silane in argon through tubular reactors having varying diameters (1.0 cm, 1.7 cm, 2.2 cm, and 3.2 cm). The total RF power deposited and the pressure were held constant for all cases (5 W and 6.5 Torr).

The simulated mass densities and particle radii for the neutral NP (which had the largest density) as a function of inlet silane fraction are shown in Fig. 3.6 for all reactor diameters. The reactor outlet at which point these measurements were made is located 15 cm downstream of the

inlet and 10 cm downstream of the power deposition region. The experimental sampling site is 60 – 61 cm further downstream. NP losses occurring in the sampling line that connects the plasma reactor to the QCM and the collection efficiency of the QCM have not been accounted for in the model. The model results are a measure of the maximum NP production rates and expect to closely track the experimental measurements downstream.

The general trends from the model closely match the experimental results of increasing mass density with increasing silane fraction. For all conditions, silane was converted to reactive precursor species within a few cm of the flow entering the power deposition zone, allowing for particle nucleation to rapidly begin. This observation is consistent with the results shown in Fig. 3.5 which suggests that onset of nucleation occurs at an inlet fraction of 200 ppm of silane or less in pure argon for all reactor sizes. In nearly all cases, silane consumption exceeded 95%.

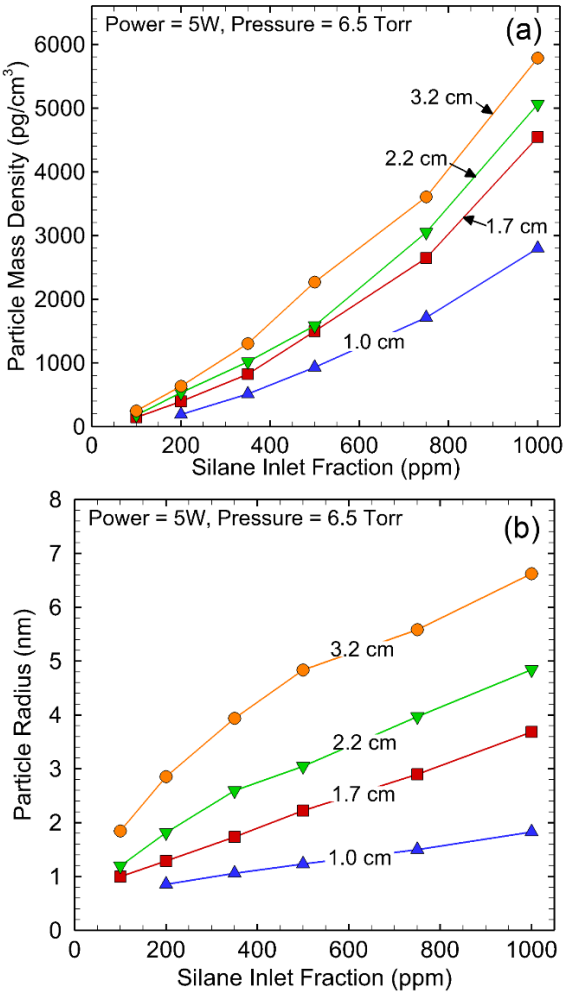

Figure 3.6. Particle mass density (a) and radius (b) predicted by *GlobalKin* as a function of silane inlet fraction in argon for different reactor diameters.

These results suggest that NP growth is reaction limited and transport dominated. Particle number density at the outlet is higher for low silane inlet fractions than with large silane fractions.

Inlet silane is depleted at roughly the same rate regardless of inlet silane fraction across all cases at the same reactor diameter. Nanoparticle number density increases in the plasma with increasing silane inlet fraction. However, at midrange silane inlet fractions (200 ppm for the 3.2 cm case) nanoparticle number density decreases downstream of the plasma as particles reach a critical cluster size and coagulate to form larger particles.

The model tracks a sequence of higher silane species and a single NP species, calculating the mass and radius of the NP species. Aside from the Si that may stick on the walls, the total mass (number) of Si atoms is conserved as a function of position. The distribution of that mass can be, for example, a larger density of smaller NPs or a smaller density of larger NPs. As long as there is a flux of silane radicals nucleating NPs at the smallest radius, the density of NPs increases while keeping the average size of the NP small. Once nucleation (the creation of new NPs) ceases due to the depletion of nucleating radicals, growth of NPs is dominated by coagulation ($NP + NP \rightarrow NP$), which reduces the number of NPs while increasing the radius of the remaining NP to conserve the total mass of Si. These processes are occurring simultaneously – though one process can dominate over another. In the low silane inlet fraction cases, the number density of particles downstream remains high. This indicates that the dominant process adding mass to the NPs is nucleation as opposed to coagulation. Nucleation will increase the particle number density by continually supplying small particles to the system while coagulation will decrease the number density as particles combine to create larger particles. The majority of the increase in NP diameter (while maintaining mass density constant) can be attributed to coagulation. These results suggest that not enough silane is available to generate a threshold value of reactive precursors for significant particle growth to the point that coagulation dominates before reactive precursors are lost to the wall or swept from the reactor by fluid flow.

A comparison of particle mass densities and radii across all reactor diameters at constant silane inlet fraction reinforces this observation. As reactor diameter decreases at constant inlet flow rate and pressure, the speed of the plug moving down the reactor increases. For comparison, the estimated plug speed in the 1.0 cm diameter reactor is about 150 cm/s whereas the estimated plug speed in the 3.2 cm reactor is 14 cm/s. The mass density of particles in all 3.2 cm cases is 2-3 times that in the 1.0 cm cases (3600 pg/cm^3 in the 3.2 cm reactor and 1700 pg/cm^3 in the 1.0 cm reactor at 500 ppm, for example). Due to the high rate of fluid flow in the 1.0 cm case, silane spends less time in the plasma region. However, the power deposition increases at the same rate, resulting in about the same dissociation fraction as in the 3.2 cm case. As noted above, decreasing the reactor diameter will also decrease the effective diffusion length to the walls. Modelling results suggest that particle growth can be suppressed by decreasing reactor diameter or by decreasing silane inlet fraction, consistent with the experimental results. Film formation is most likely suppressed by increasing reactor size and adjusting silane inlet fraction above the nucleation threshold to achieve a target particle size.

To demonstrate the potential consequences of sticking coefficients on nucleation and growth rates, two extremes were simulated with the model - a small tube (1 cm diameter) with zero and unity sticking coefficient for all radicals, and a large tube (3.2 cm diameter). The reactor conditions are a constant flow rate of 52 sccm, 5 W, 6.5 Torr and 350 ppm SiH_4. The results for particle mass density and particle radius as a function of reactor position are show in Fig. 3.7. For a diameter of 1 cm, there is a significant increase in particle radius and particle mass density from a sticking coefficient, s, of unity to s = 0. For a diameter of 3.2 cm, there is little change in particle radius. The particle mass density increases, though less appreciably than in the 1.0 cm case, downstream of the powered region. For a diameter of 1.0 cm, the more rapid rate of loss of radicals

to the walls with s = 1, even with a smaller residence time, results in lower net growth rates and smaller particles. For a diameter of 3.2 cm there is little change in the particle diameter between s=0 and s=1, as volumetric processes dominate the number densities of particle precursors and growth species in the plasma zone. However, downstream, after nucleation has occurred for both cases, the s=0 case produces a larger number density of smaller particles due to growth reactions of radicals onto the particles dominating over coagulation.

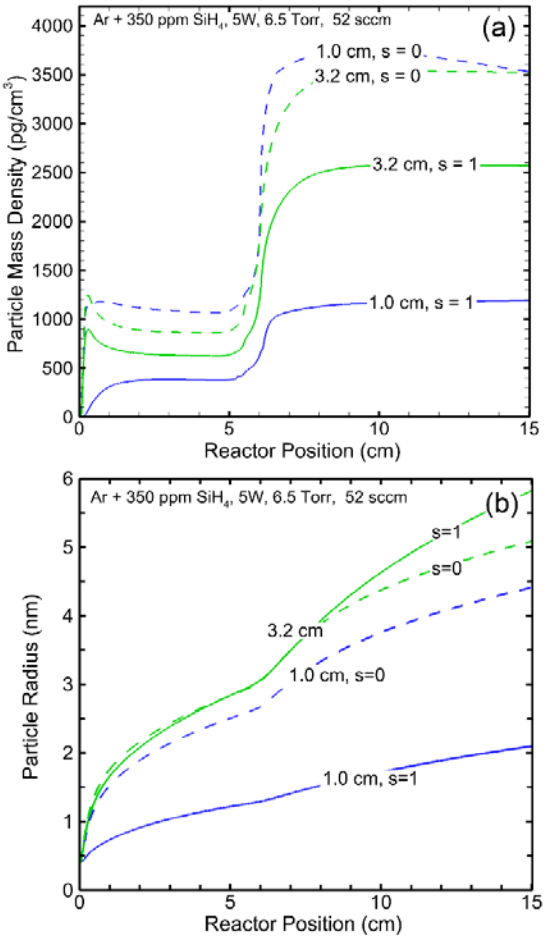

Figure 3.7 (a) Mass density and (b) Particle radius for tube diameters of 1.0 and 3.2 cm for two cases of the sticking coefficient for all silane radical species, s = 0 and s = 1.

3.4 Conclusions

In this work, a QCM impactor was used to measure particle mass densities from the effluent of a dilute silane plasma. Mass densities were determined as a function of the inlet silane fraction, gas composition, reactor pressure, and reactor tube diameter. Increasing the reactor tube diameter was shown to significantly increase particle mass density. Increasing the reactor pressure was also shown to increase particle mass density, though not as significantly as increasing the reactor tube diameter. Particle formation was greatly inhibited when pure H_2 was used as the balance gas. These results suggest that species diffusion to surfaces that act as sinks (e.g. reactor walls) plays a major role in determining whether film formation is favored over particle formation. Reactor conditions having high hydrogen fraction suppresses both film formation, and to a greater extent, particle formation.

Experimental and modeling results indicate that diffusion of radicals and their loss on the walls can be important with respect to NP formation. When varying the sticking coefficient of silicon precursor species on the reactor walls in the model, we see similar dependencies as experiments. These dependencies could be sensitive functions of reactor radius as sticking coefficients are likely a function of reactor radius. Changes in sticking coefficient at the reactor walls would be expected as the walls are subject to heating, ion bombardment, and photo desorption over the life of the reactor. As a film is deposited on the walls, sticking coefficients may change. Further studies are needed to fully parameterize these dependencies. Results from the model suggest that controlling particle growth and film formation is a delicate balance between controlling the particle growth regime (nucleation vs. coagulation) and fluid properties. Additionally, the model results suggest that reactor diameter (which also determines residence time for a given flow rate) should be tuned in combination with inlet gas composition to either

achieve a particle-free film, or particles of a specified size while also suppressing film formation on the reactor walls.

3.5 Tables

Table 3.1 Gas Phase Species Included in Plasma Chemistry Model

Argon Species

Ar(3*s*), Ar(1*s*$_2$), Ar(1*s*$_3$), Ar(1*s*$_4$), Ar(1*s*$_5$), Ar(4*p*), Ar(4*d*), Ar^+

Hydrogen Species[a]

H , H^*, H^+, H^-, H_2 , H_2^+, H_2^* , H_3^+, ArH^+

Silane and Silyl Species[b]

SiH, SiH_2, SiH_3, SiH_4, Si_2H_2, Si_2H_3, Si_2H_4, Si_2H_5, Si_2H_6, Si_nH_{2n+2}, Si_nH_{2n+1}, SiH^-, SiH_2^-, SiH_3^-, $Si_2H_3^-$, $Si_2H_4^-$, $Si_2H_5^-$, SiH_3^+, SiH_2^+

Nanoparticle Species[c]

NP, $NP^\bullet$, NP^+, NP^-

a) * denotes an excited state atom or molecule

b) Si_nH_{2n+2} and Si_nH_{2n+1} species included for $3 \leq n \leq 12$

c) $^\bullet$ denotes a nanoparticle radical. This reactive species is analogous to a Si_nH_{2n+1}.

Table 3.2 contains the nanoparticle growth reaction mechanism used in the model. The Ar/SiH_4 gas reaction mechanism is based on previous works [35,36]. Reaction rates for reactions involving NP have been estimated based on analogous reactions with Si_nH_{2n+2} and Si_nH_{2n+1} and on rates given in Ref.[34].

Table 3.2. Nanoparticle Growth Reaction Mechanism

Reaction		**Rate Coefficient[a]**
Nucleation[b]		
1	$Si_{12}H_{26} + SiH \rightarrow NP$	4.0×10^{-11}
2	$Si_{12}H_{26} + SiH_2 \rightarrow NP$	2.0×10^{-11}
3	$Si_{12}H_{26} + SiH_3 \rightarrow NP$	1.0×10^{-11}
4	$Si_{12}H_{26} + SiH_4 \rightarrow NP$	1.0×10^{-30}
5	$Si_{12}H_{26} + Si_2H_2 \rightarrow NP$	6.0×10^{-11}
6	$Si_{12}H_{26} + Si_2H_3 \rightarrow NP$	4.0×10^{-11}
7	$Si_{12}H_{26} + Si_2H_4 \rightarrow NP$	2.0×10^{-11}
8	$Si_{12}H_{26} + Si_2H_5 \rightarrow NP$	1.0×10^{-11}
9	$Si_{12}H_{26} + Si_2H_6 \rightarrow NP$	1.0×10^{-30}
10	$Si_{12}H_{25} + SiH \rightarrow NP$	2.67×10^{-11}
11	$Si_{12}H_{25} + SiH_2 \rightarrow NP$	1.0×10^{-11}
12	$Si_{12}H_{25} + SiH_3 \rightarrow NP$	2.67×10^{-11}
13	$Si_{12}H_{25} + SiH_4 \rightarrow NP$	1.0×10^{-13}
14	$Si_{12}H_{25} + Si_2H_2 \rightarrow NP$	1.0×10^{-11}
15	$Si_{12}H_{25} + Si_2H_3 \rightarrow NP$	2.67×10^{-11}
16	$Si_{12}H_{25} + Si_2H_4 \rightarrow NP$	2.0×10^{-11}
17	$Si_{12}H_{25} + Si_2H_5 \rightarrow NP$	2.67×10^{-11}
18	$Si_{12}H_{25} + Si_2H_6 \rightarrow NP$	1.0×10^{-13}
19	$Si_{11}H_{24} + Si_2H_2 \rightarrow NP$	6.0×10^{-11}

20	$Si_{11}H_{24} + Si_2H_3 \rightarrow NP$	4.0×10^{-11}
21	$Si_{11}H_{24} + Si_2H_4 \rightarrow NP$	2.0×10^{-11}
22	$Si_{11}H_{24} + Si_2H_5 \rightarrow NP$	1.0×10^{-11}
23	$Si_{11}H_{24} + Si_2H_6 \rightarrow NP$	1.0×10^{-30}
24	$Si_{11}H_{23} + Si_2H_2 \rightarrow NP$	6.0×10^{-11}
25	$Si_{11}H_{23} + Si_2H_3 \rightarrow NP$	2.67×10^{-11}
26	$Si_{11}H_{23} + Si_2H_4 \rightarrow NP$	2.0×10^{-11}
27	$Si_{11}H_{23} + Si_2H_5 \rightarrow NP$	2.67×10^{-11}
29	$Si_{11}H_{23} + Si_2H_6 \rightarrow NP$	1.0×10^{-13}
30[c]	$Si_nH_{2n+2} + Si_nH_{2n+1} \rightarrow NP$	1.0×10^{-11}
31[c]	$Si_nH_{2n+2} + Si_nH_{2n+2} \rightarrow NP$	1.0×10^{-30}
32[c]	$Si_nH_{2n+1} + Si_nH_{2n+1} \rightarrow NP$	2.67×10^{-11}
33[d]	$Si_nH_{2n+1} + SiH^- \rightarrow NP^-$	1.0×10^{-9}
34[d]	$Si_nH_{2n+1} + SiH_2^- \rightarrow NP^-$	1.0×10^{-9}
35[d]	$Si_nH_{2n+1} + SiH_3^- \rightarrow NP^-$	1.0×10^{-9}
36[d]	$Si_nH_{2n+1} + Si_2H_3^- \rightarrow NP^-$	1.0×10^{-9}
37[d]	$Si_nH_{2n+1} + Si_2H_4^- \rightarrow NP^-$	1.0×10^{-9}
38[d]	$Si_nH_{2n+1} + Si_2H_5^- \rightarrow NP^-$	1.0×10^{-9}
39[d]	$Si_nH_{2n+2} + SiH^- \rightarrow NP^-$	1.0×10^{-9}
40[d]	$Si_nH_{2n+2} + SiH_2^- \rightarrow NP^-$	1.0×10^{-9}
41[d]	$Si_nH_{2n+2} + SiH_3^- \rightarrow NP^-$	1.0×10^{-9}
42[d]	$Si_nH_{2n+2} + Si_2H_3^- \rightarrow NP^-$	1.0×10^{-9}
43[d]	$Si_nH_{2n+2} + Si_2H_4^- \rightarrow NP^-$	1.0×10^{-9}

44[d]	$Si_nH_{2n+2} + Si_2H_5^- \rightarrow NP^-$	1.0×10^{-9}
45	$Si_{12}H_{25} + SiH_2^+ \rightarrow NP^+$	1.0×10^{-10}
46	$Si_{12}H_{25} + SiH_3^+ \rightarrow NP^+$	1.0×10^{-10}
47	$Si_{12}H_{26} + SiH_2^+ \rightarrow NP^+$	1.0×10^{-10}
48	$Si_{12}H_{26} + SiH_3^+ \rightarrow NP^+$	1.0×10^{-10}
Charged Particle Reactions		
49	$e + NP \rightarrow NP^-$	1.0×10^{-8}
50	$H^- + NP \rightarrow NP^- + H$	3.0×10^{-10}
51	$Ar^+ + NP \rightarrow NP^+ + Ar$	3.0×10^{-10}
52	$ArH^+ + NP \rightarrow NP^+ + Ar + H$	3.0×10^{-10}
53	$H_2^+ + NP \rightarrow NP^+ + H_2$	3.0×10^{-10}
54	$H_3^+ + NP \rightarrow NP^+ + H_3$	3.0×10^{-10}
55	$H^+ + NP \rightarrow NP^+ + H$	3.0×10^{-10}
56	$Ar^+ + NP^- \rightarrow NP + Ar$	1.0×10^{-8}
57	$ArH^+ + NP^- \rightarrow NP + Ar + H$	1.0×10^{-8}
58	$H_2^+ + NP^- \rightarrow NP + H_2$	1.0×10^{-8}
59	$H_3^+ + NP^- \rightarrow NP + H_3$	1.0×10^{-8}
60	$H^+ + NP^- \rightarrow NP + H$	1.0×10^{-8}
61	$e + NP^+ \rightarrow NP$	1.0×10^{-7}
62	$H^- + NP^+ \rightarrow NP + H$	1.0×10^{-8}
Growth by Surface Deposition[e]		
63	$SiH^- + NP \rightarrow NP^-$	3.0×10^{-10}
64	$SiH_2^- + NP \rightarrow NP^-$	3.0×10^{-10}

65	$SiH_2^- + NP \rightarrow NP^-$	3.0×10^{-10}
66	$Si_2H_3^- + NP \rightarrow NP^-$	3.0×10^{-10}
67	$Si_2H_4^- + NP \rightarrow NP^-$	3.0×10^{-10}
68	$Si_2H_5^- + NP \rightarrow NP^-$	3.0×10^{-10}
69	$SiH_2^+ + NP \rightarrow NP^+$	3.0×10^{-10}
70	$SiH3^+ + NP \rightarrow NP^+$	3.0×10^{-10}
71	$SiH_2^+ + NP^- \rightarrow NP$	2.89×10^{-8}
72	$SiH3^+ + NP^- \rightarrow NP$	2.89×10^{-8}
73	$SiH^- + NP^+ \rightarrow NP$	1.0×10^{-8}
74	$SiH_2^- + NP^+ \rightarrow NP$	1.0×10^{-8}
75	$SiH_2^- + NP^+ \rightarrow NP$	1.0×10^{-8}
76	$Si_2H_3^- + NP^+ \rightarrow NP$	1.0×10^{-8}
77	$Si_2H_4^- + NP^+ \rightarrow NP$	1.0×10^{-8}
78	$Si_2H_5^- + NP^+ \rightarrow NP$	1.0×10^{-8}
79	$SiH + NP \rightarrow NP$	1.89×10^{-9}
80	$SiH_2 + NP \rightarrow NP$	1.32×10^{-9}
81	$SiH_3 + NP \rightarrow NP$	2.5×10^{-8}
82	$SiH_4 + NP \rightarrow NP$	1.0×10^{-30}
83	$Si_2H_2 + NP \rightarrow NP$	1.32×10^{-9}
84	$Si_2H_3 + NP \rightarrow NP$	6.0×10^{-10}
85	$Si_2H_4 + NP \rightarrow NP$	4.0×10^{-10}
86	$Si_2H_5 + NP \rightarrow NP$	4.0×10^{-10}
87	$Si_2H_6 + NP \rightarrow NP$	1.0×10^{-30}

88[f]	$Si_nH_{2n+1} + NP \rightarrow NP$	4.0×10^{-10}
89[f]	$Si_nH_{2n+2} + NP \rightarrow NP$	1.0×10^{-30}
90	$SiH + NP^- \rightarrow NP^-$	3.78×10^{-9}
91	$SiH_2 + NP^- \rightarrow NP^-$	2.64×10^{-9}
92	$SiH_3 + NP^- \rightarrow NP^-$	5.0×10^{-10}
93	$SiH_4 + NP^- \rightarrow NP^-$	1.0×10^{-30}
94	$Si_2H_2 + NP^- \rightarrow NP^-$	2.64×10^{-9}
95	$Si_2H_3 + NP^- \rightarrow NP^-$	1.2×10^{-9}
96	$Si_2H_4 + NP^- \rightarrow NP^-$	8.0×10^{-10}
97	$Si_2H_5 + NP^- \rightarrow NP^-$	8.0×10^{-10}
98	$Si_2H_6 + NP^- \rightarrow NP^-$	1.0×10^{-30}
99[f]	$Si_nH_{2n+1} + NP^- \rightarrow NP^-$	8.0×10^{-10}
100[f]	$Si_nH_{2n+2} + NP^- \rightarrow NP^-$	1.0×10^{-30}
101	$SiH + NP^+ \rightarrow NP^+$	3.78×10^{-9}
102	$SiH_2 + NP^+ \rightarrow NP^+$	2.64×10^{-9}
103	$SiH_3 + NP^+ \rightarrow NP^+$	5.0×10^{-10}
104	$SiH_4 + NP^+ \rightarrow NP^+$	1.0×10^{-30}
105	$Si_2H_2 + NP^+ \rightarrow NP^+$	2.64×10^{-9}
106	$Si_2H_3 + NP^+ \rightarrow NP^+$	1.2×10^{-9}
107	$Si_2H_4 + NP^+ \rightarrow NP^+$	8.0×10^{-10}
108	$Si_2H_5 + NP^+ \rightarrow NP^+$	8.0×10^{-10}
109	$Si_2H_6 + NP^+ \rightarrow NP^+$	1.0×10^{-30}
110[f]	$Si_nH_{2n+1} + NP^+ \rightarrow NP^+$	8.0×10^{-10}

111[f]	$Si_nH_{2n+2} + NP^+ \rightarrow NP^+$	1.0×10^{-30}
Agglomeration		
112	$NP + NP^+ \rightarrow NP^+$	1.0×10^{-9}
113	$NP + NP^- \rightarrow NP^-$	1.0×10^{-9}
114	$NP^- + NP^+ \rightarrow NP$	5.0×10^{-8}
115	$NP + NP \rightarrow NP$	1.0×10^{-9}
116	$NP^\bullet + NP^+ \rightarrow NP^+$	5.0×10^{-9}
117	$NP^\bullet + NP^- \rightarrow NP^-$	5.0×10^{-9}
118	$NP^\bullet + NP^\bullet \rightarrow NP$	1.0×10^{-8}
119	$NP^\bullet + NP \rightarrow NP$	5.0×10^{-9}

a) Reaction rates have units of $cm^3 \cdot s^{-1}$. A rate coefficient of 1×10^{-30} $cm^3 \cdot s^{-1}$ is intended to indicate no appreciable reaction.

b) Nucleation reactions resulting in $NP^\bullet$ are not shown. Nucleation of $NP^\bullet$ occurs by reactions 1-32 at half the given rate.

c) $7 \leq n \leq 12$

d) $11 \leq n \leq 12$

e) Growth reactions of $NP^\bullet$ are not shown. Growth of $NP^\bullet$ occurs by reactions 79-89 at half the given rate.

f) $3 \leq n \leq 12$

3.6 References

[1] Z. Kang, C. H. A. Tsang, N.-B. Wong, Z. Zhang and S.-T. Lee, J. Am. Chem. Soc. **129,** 12090 (2007).

[2] P. Lv, C. Xu and B. Peng, ACS Omega **5,** 6358 (2020).

[3] Z. Ni, S. Zhou, S. Zhao, W. Peng, D. Yang and X. Pi, Mater. Sci. Eng. R Reports **138,** 85 (2019).

[4] Y. Yang, W. Yuan, W. Kang, Y. Ye, Y. Yuan, Z. Qiu, C. Wang, X. Zhang, Y. Ke and Y. Tang, Nanoscale **12,** 7461 (2020).

[5] N. O'Farrell, A. Houlton and B. R. Horrocks, Int. J. Nanomedicine **1,** 451 (2006).

[6] O. I. Ksenofontova, A. V. Vasin, V. V. Egorov, A. V. Bobyl', F. Y. Soldatenkov, E. I. Terukov, V. P. Ulin, N. V. Ulin and O. I. Kiselev, Tech. Phys. **59,** 66 (2014).

[7] D. W. Cooper, Aerosol Sci. Technol. **5,** 287 (1986).

[8] M. P. Herrling and P. Rychen, Ultrapure Micro **1,** 34 (2017).

[9] G. S. Selwyn, J. Vac. Sci. Technol. B Microelectron. Nanom. Struct. Process. Meas. Phenom. **9,** 3487 (1991).

[10] G. M. Jellum, J. E. Daugherty and D. B. Graves, J. Appl. Phys. **69,** 6923 (1991).

[11] N. Kashihara, H. Setyawan, M. Shimada, Y. Hayashi, C. S. Kim, K. Okuyama and S. Winardi, J. Nanoparticle Res. **8,** 395 (2006).

[12] A. Bouchoule, A. Plain, L. Boufendi, J. P. Blondeau and C. Laure, J. Appl. Phys. **70,** 1991 (1991).

[13] Y. Watanabe, M. Shiratani and H. Makino, Appl. Phys. Lett. **57,** 1616 (1990).

[14] M. S. Masaharu Shiratani, S. M. Shinichi Maeda, K. K. Kazunori Koga and Y. W. Yukio Watanabe, Jpn. J. Appl. Phys. **39,** 287 (2000).

[15] U. Kroll, J. Meier, A. Shah, S. Mikhailov and J. Weber, J. Appl. Phys. **80,** 4971 (1996).

[16] A. Matsuda, J. Non. Cryst. Solids **59–60,** 767 (1983).

[17] Y. Kim, K. Koga and M. Shiratani, Curr. Appl. Phys. **20,** 191 (2020).

[18] S. Ben Amor, W. Dimassi, M. Ali Tebai and H. Ezzaouia, Phys. status solidi c **9,** 2180 (2012).

[19] Y. Maemura, H. Fujiyama, T. Takagi, R. Hayashi, W. Futako, M. Kondo and A. Matsuda, Thin Solid Films **345,** 80 (1999).

[20] U. Bhandarkar, U. Kortshagen and S. L. Girshick, J. Phys. D. Appl. Phys. **36,** 1399 (2003).

[21] N. B. Uner and E. Thimsen, Plasma Sources Sci. Technol. **27,** 074005 (2018).

[22] Q. Lin, X. Lin, Y. Yu, H. Wang and J. Chen, J. Appl. Phys. **74,** 4899 (1993).

[23] Orifice Calculator © Lenox Laser. https://lenoxlaser.com/resources/calculators/orifice-calculator/. Accessed 19 Oct. 2021.

[24] W. Hinds, *Aerosol Technology: Properties, Behavior, and Measurement of Airborne Particles*, John Wiley and Sons (1999).

[25] M. Ihalainen, T. Lind, A. Arffman, T. Torvela and J. Jokiniemi, Aerosol Sci. Technol. **48,** 31 (2014).

[26] M. J. Ellenbecker, D. Leith and J. M. Price, J. Air Pollut. Control Assoc. **30,** 1224 (1980).

[27] G. Sauerbrey, Zeitschrift fur Phys. **155,** 206 (1959).

[28] M. A. Olevanov, Y. A. Mankelevich and T. V. Rakhimova, J. Exp. Theor. Phys. **98,** 287 (2004).

[29] M. Vazquez-Pufleau, Y. Wang, P. Biswas and E. Thimsen, J. Chem. Phys. **152,** (2020).

[30] M. Gatti and U. Kortshagen, Phys. Rev. E - Stat. Nonlinear, Soft Matter Phys. **78,** 1

(2008).

[31] P. Agarwal and S. L. Girshick, Plasma Sources Sci. Technol. **21,** 055023 (2012).

[32] H. Zhuang, P. Lu, S. P. Lim and H. P. Lee, Langmuir **23,** 7392 (2007).

[33] P. Agarwal and S. L. Girshick, Plasma Chem. Plasma Process. **34,** 489 (2014).

[34] R. Le Picard, A. H. Markosyan, D. H. Porter, S. L. Girshick and M. J. Kushner, Plasma Chem. Plasma Process. **36,** 941 (2016).

[35] M. J. Kushner, J. Appl. Phys. **71,** 4173 (1992).

[36] J. Perrin, O. Leroy and M. C. Bordage, Contrib. to Plasma Phys. **36,** 3 (1996).

Chapter 4 A Reaction Mechanism for the Atmospheric Pressure Plasma Functionalization of Polystyrene[3]

Atmospheric pressure plasma jets (APPJs) are used to improve adhesive and hydrophilic properties of commodity hydrocarbon polymers such as polypropylene (PP), polyethylene (PE), and polystyrene (PS). These improvements largely result from adding oxygen functional groups to the surface. PS functionalization is of interest to producing high value biocompatible well-plates and dishes which require precise control over surface properties. In this paper, we discuss results from a computational investigation of APPJ functionalization of PS surfaces using $He/O_2/H_2O$ gas mixtures. A newly developed surface reaction mechanism for functionalization of PS upon exposure to these plasmas is discussed. A global plasma model operated in plug-flow mode was used to predict plasma produced species fluxes onto the PS surface. A surface site balance model was used to predict oxygen functionalization of the PS following exposure to the plasma and ambient air. We found that O-occupancy on the surface strongly correlates with the O-atom flux to the PS, with alcohol groups and crosslinked products making the largest contributors to total oxygen fraction. Free radical sites, such as alkoxy and peroxy, are quickly consumed in the post-plasma exposure to air through passivation and cross-linking. O-atoms fluences approaching 10^{17} cm^{-2} saturate the O-occupancy on the PS surface, creating functionality which is not particularly sensitive to moderated changes in operating conditions.

[3]Results discussed and portions of the text in this chapter have been previously published in J. Polito et. al, "Atmospheric Pressure Plasma Functionalization of Polystyrene", J. Vac. Sci. Technol. A 40, 043001 (2022). [Selected as an Editor's pick for J. Vac. Sci. Technol. Vol 40, Issue 4, Jul. 2022.]

4.1 Introduction

Low temperature plasmas are often used to improve the wettability and adhesive properties of saturated hydrocarbon polymers such as polyethylene (PET), polypropylene (PP), and polystyrene (PS) [1–5]. A common method for improving adhesion and wettability of a polymer utilizes oxygen containing plasmas to attach oxygen and oxygen containing functional groups to the polymer surface. The added oxygen content increases surface energy leading to more hydrophilic surfaces. Sources for plasma surface modification range from low pressure glow discharges [6–9] to atmospheric pressure dielectric barrier discharges (DBDs) or corona [10]. Low pressure systems are often used where UV light or high energy ions are important to the functionalization process while there is added cost for the associated vacuum processing. Atmospheric pressure DBDs, often sustained in ambient air having lower cost, are typically used for high volume functionalization of commodity polymers [11].

More recently, atmospheric pressure plasma jets (APPJs) have been adopted for surface functionalization of polymers [12,13]. APPJs typically consist of a rare gas (or rare gas mixture containing up to a few percent of an additive) flowing through a tubular plasma source into ambient air and onto the polymer surface. The plasma is produced in the tube with a pulsed voltage to generate a plume of plasma extending into the ambient air [14]. Other configurations confine the plasma to a flow channel using parallel radio frequency (RF) powered electrodes that largely confine the plasma to the device. Here the activated species in the plume consist dominantly of neutral radicals. Similar to DBDs, these systems offer advantages over low pressure discharges in that they do not require expensive vacuum equipment, allowing for larger volumes of polymer to be processed in either batch or continuous modes. The disadvantage of APPJs relative to DBDs sustained in air is that the APPJs typically require high flow rates of rare gases (and their associated

costs). APPJs tend to produce higher fluxes of reactive oxygen species (ROS) compared to DBDs sustained in air, which is advantageous for surface functionalization applications where improved hydrophilic and adhesive properties by addition of oxygen are desired.

Improving the wettability of polymers by addition of oxygen groups is of particular interest to the biological science and biomedical engineering communities. These communities often require polymeric materials to be in direct contact with living organisms. The oxygen functionality is used either directly (being more hydrophilic) or as a base for attaching more biologically active groups, such as amines. Surface characteristics that can influence cellular interactions with the polymer, such as surface energy and wettability, are important when choosing the polymer appropriate for the desired application [15,16]. PS is often used for cell culturing substrates (e.g., well-plates, petri dishes) due to its low toxicity and long shelf life of the plasma produced functionality after treatment [17,18].

The fixing of oxygen to a polymer surface improves wettability and adhesion by increasing the surface energy, thereby increasing hydrophilicity. APPJs consisting of Ar/O_2, Ar/H_2O, He/O_2, and N_2/O_2 gas mixtures, among others, have been used for polymer modification with varying success of increasing hydrophilicity [19–21]. Water contact angle measurements that relate the angle of water spreading on the polymer surface with surface energy through Young's equation are the most common method for determining the degree of functionalization that has occurred on a polymer surface after plasma treatment [2,22]. Decreases in contact angle correlate to an increase in wettability and are thought to be due to the addition of alcohol, carbonyl, ketone, and aldehyde functional groups. These groups have been experimentally characterized on the surface of plasma treated PS by x-ray photoelectron spectroscopy (XPS) measurements [23–27]. While water contact angle measurements and XPS measurements independently confirm that plasma treated

PS has some degree of functionalization, there is no formulaic relationship between the measured contact angle and amount of each functional group on the surface after plasma treatment. This lack of direct correlation makes optimization of the functionalization process more difficult. Computational modelling, when paired with experimental measurements, can be a useful tool in determining the chemistry of a plasma treated polymer surface.

Several models have addressed plasma functionalization of polymers, but they are largely limited to PP due to its wide industrial use and relatively simple monomer unit. Wang et. al related contact angle and XPS measurements to functional groups on a PP surface after treatment by an atmospheric pressure air DBD [28]. Their regressive model was able to predict changes in contact angle as a function of percentage of O atoms on the PP surface for their DBD conditions. A robust method for predicting surface functionalization is to couple a plasma chemistry model that predicts fluxes to surfaces with a surface site balance model that predicts the evolution of surface properties. The functionalization of PP has been modelled with this technique using fluid and global model techniques [29–31]. These models predicted the fractional occupation of functional groups on the PP surface as functions of plasma operating conditions on rough and smooth surfaces.

While these models have the potential to be extended to investigate plasma functionalization of other commodity polymers, little of this work has been done. As polymer monomer units become more complex, the reaction mechanisms for functionalization of the polymers become increasingly unclear. For example, the presence of aromatic rings in the monomer units of polymers such as PS and polycarbonate raise issues of steric hindrance and reactivity of the aromatic ring compared to other sites on the polymer backbone. Investigations have addressed how aromatic compounds such as benzene or toluene interact in plasmas [32–34]. Work has been also been done to predict final configurations of oxygen functional groups on a

modified PS surface using density functional theory (DFT) and ab initio molecular dynamics (MD) techniques [35]. However, these works have not yet been expanded to a complete reaction mechanism for plasma functionalization of polymers containing aromatic rings, such as PS.

In this chapter, a reaction mechanism for the functionalization of PS by a He/O_2 APPJ is proposed. Results are discussed from a computational investigation of coupled global plasma chemistry and surface-site-balance models using this reaction mechanism for surface functionalization of PS after APPJ treatment and post-treatment exposure to ambient air. The global model is used in a plug-flow mode to provide the plasma produced reactive species that exit the reactor, mix with ambient air and impinge upon a flat PS surface. A surface site balance model is used to track changes in fractional occupancy of surface groups due to gas-surface and surface-surface reactions. The plasma treated surface is then exposed to ambient humid air to simulate short-term aging of the functionalized surface. The functionalization of the PS in terms of fractional occupancy of oxygen on the surface as function of power, gas composition, and humidity are discussed. We found that parameters affecting O production, such as power and inlet gas composition, offer the largest degree of control for optimizing the O-occupancy on the PS surface. We predict that alcohol and crosslinked groups make up the largest contribution of O-containing functional groups on the PS surface after APPJ treatment and exposure to ambient air.

The surface reaction mechanism is discussed in Section 4.2. Base case plasma properties and parametric studies examining the change in oxygen content on the PS surface are discussed in Sections 4.3 and 4.4. Concluding remarks are in Section 4.5.

4.2 Surface Reaction Mechanism

PS is a saturated hydrocarbon polymer whose monomer unit contains an aromatic benzene ring (denoted with subscript b in the following), two H atoms at secondary-sites (denoted with

subscript 2), and an H atom at a tertiary site (denoted with subscript 3). (See Fig. 4.1.) Commercially available PS is atactic, meaning its monomer units are configured randomly such that there is an equal likelihood for any of the four groups to be oriented towards the surface of the material. However, the benzene ring is physically larger than the neighboring sites which may result in the benzene ring obscuring neighboring sites as a form of steric hindrance. The density of PS surface sites in the model is initialized as 10^{15} cm^{-2}, in agreement with available molecular dynamics data and reported values for other polymeric materials [30,36]. The density of benzene sites, N_b, is initially 0.5×10^{15} cm^{-2}. The initial surface densities for the secondary and tertiary H atoms are $N_2 = N_3 = 0.25 \times 10^{15}$ cm^{-2}.

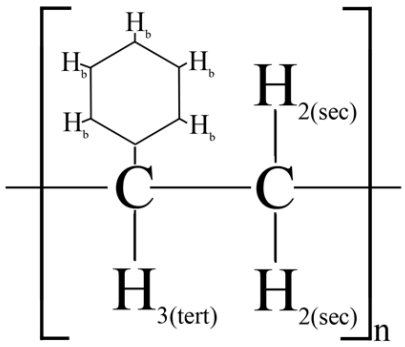

Figure 4.1. Polystyrene monomer unit.

The model includes 71 gas-phase species and 33 surface species. The gas-phase species included in the model are listed in Table 4.1. The gas-phase reaction mechanism for a He/O_2 atmospheric plasma has been discussed in detail in prior work [29,30]. In short, atomic oxygen is produced primarily through electron impact dissociation of O_2 (neutral and dissociative attachment) and by dissociative Penning reactions with excited states of He. O atoms are consumed dominantly through three body collisions with O_2 to form ozone, O_3. O_2 is also electronically excited by collisions with electrons to form $O_2(^1\Delta)$ and $O_2(^1\Sigma)$. If water vapor is present in the plasma, H_2O is dissociated by electron impact to form OH and H, and by Penning reactions with excited states of He. Reactions of O_3 with H lead to formation of OH while reactions of O_3 with OH lead to formation of HO_2. Positive ions, O^+, O_2^+, and H_2O^+ are produced by electron impact ionization of O, O_2, and H_2O, by charge exchange from He^+ and He_2^+, and by Penning

reactions with excited states of helium. Formation of negative ions is dominated by three body electron attachment to O_2 to form O_2^- at atmospheric pressure. The plasma produced ion densities in the system are 2-3 orders of magnitude lower than the neutral plasma produced reactive oxygen species (ROS). The gas-phase species in the model that can react with the PS to promote oxidation are: O_2^* (sum of electronically excited states of O_2), O_3, O, H, OH, and HO_2.

As PS and PP share the same monomer units except for one group, the surface reaction mechanism closely follows that for the functionalization of PP previously discussed in Ref. [29]. Changes were made to the mechanism to account for reactions with the benzene ring in PS rather to the methyl group in PP in the polymer monomer unit. Some values of reaction probabilities have been adjusted from those discussed in Ref. [29] as discussed below. The full gas-surface reaction mechanism is listed in Table 4.2. In several cases, reaction probabilities between gas phase and surface resident species were approximated by analogy to gas phase reactions. For example, H abstraction from benzene in the gas phase has a rate coefficient of k. The rate coefficient was normalized by the gas kinetic rate coefficient k_0, representing the fastest possible rate of reaction. The probability of reaction is then $p = k/k_0$. This probability was then assigned to the analogous surface reaction of a gas phase species abstracting an H atom from the aromatic ring in the PS backbone. These probabilities would be further de-rated by steric hindrances. The analogous gas phase reactions that were used to estimate gas-surface reaction probabilities are in Table 4.3.

Oxidation of the PS surface is a three-step mechanism that begins with the abstraction of hydrogen from the polymer chain to form an alkyl radical site or from the benzene ring to form a phenyl radical site. Reactivity of the surface sites scale with the activation energy required to remove the H atom at that site such that the probabilities of reaction scale as $p(H_{tert}) > p(H_{sec}) >$

p(H_R) (See Fig. 4.1). After H abstraction, gas-phase species (O, O_2, O_3, O^*, OH) react with the surface radical sites to form oxygen containing radical sites or terminate the site by formation of alcohol, aldehyde, or hydroperoxyl functional groups.

Etching of the PS surface was not included in this mechanism. Low molecular weight materials on the polymer surface after plasma treatment are indicative of polymer etching [44,45]. However, even under low pressure conditions where ion fluxes to the surface were high, significant amounts of low molecular weight materials were not found on the PS surface after plasma exposure for times less than one hour [37,38]. Recently, the etching probabilities for APPJ-produced O, H, and OH radical species incident onto a PS surface have been reported [39,40]. The etching rate due to OH was reported to be the highest with a probability on the order of 10^{-2} for an Ar/H_2O plasma with OH radical density of 10^{14} cm^{-3}, suggesting that the removal of one C atom occurs for every 100 OH radicals [39]. PS etching was highly sensitive to the oxygen content in the environment between the reactor outlet and the PS surface [41]. In cases where the plasma jet was not shielded and the local oxygen concentration was that of ambient air, etching was much less significant than in cases where the plasma jet was shielded. This result was likely a consequence of consumption of O and OH. The system under study is not shielded and has an OH flux to the surface on the order of 10^{14} cm^{-2} s^{-1}, 3-4 orders of magnitude smaller than the flux of OH reported in Ref. [39]. We expect etching to be negligible for our system.

Chain scission, or the breakings of bonds in the middle of a polymer chain, has also been neglected in this mechanism. Chain scission has been shown to occur in studies of the plasma treatment of polymers such as PP, PE, and PMMA; however chain scission has not been observed in treatment of PS having no prior oxidations [38,42,43]. Experiments of PS treated by a low pressure Ar/O_2 plasma determined that PS is prone to chain scissions after oxidation, or treatment

times much greater than those addressed here [25]. The lack of chain scissions in plasma treated PS is thought to be due to the presence of the benzene ring, which stabilizes the PS backbone by trapping and redistributing energy [3]. There still remains the possibility that chain scissions could occur at the end of the polymer chain where the trapping and redistribution of energy by the benzene ring may not be as pronounced. We have assumed that chain ends do not make up a significant portion of our sample and have neglected chain scission.

Cross-linking occurs when a surface radical site on one polymer chain reacts with a radical site on another polymer chain as a form of lowering surface energy. Cross-linking has been shown to occur on the surface of plasma treated PP and PS, and can contribute to increased surface adhesion and wettability [43–45]. A cross-linking mechanism has been included as a means of terminating radical sites and so stabilize the surface functionalization against further aging. In the proposed mechanism, cross-linking is allowed between two peroxy radical sites or between phenoxy sites. While cross-linking may occur during plasma treatment, we expect the majority of cross-linking to occur in the post-treatment exposure to ambient air where fluxes of reactive species to the surface, and therefore termination of radical sites by those species, is less likely.

The aging of plasma treated polymers is a well-known phenomenon. Aging is an evolution of the surface properties after plasma treatment over a period of minutes to many days or weeks [39,46]. For example, air plasma treatment of polypropylene increases surface oxygen content and reduces the water contact angle as an indication of making the surface more hydrophilic [47]. Following plasma treatment, the water contact angle will increase from its minimum post-treatment value. The cause of aging is poorly known, and may be attributed to slow reactions between surface species that reduce the exposure of oxygen groups on the surface, reactions with the ambient air, and release of treatment induced stress on the surface which rotates

oxygen groups away from the surface [42,43]. Post-exposure of the PS with ambient air is included in this model to account for these effects.

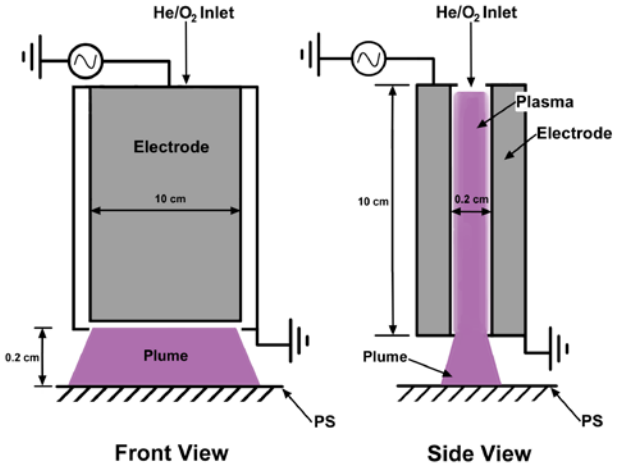

Figure 4.2. Front and side view of plasma head geometry used in model. A He/O_2 mixture at atmospheric pressure is flowed between parallel plate electrodes separated by 2 mm, with the plume flowing into ambient air.

4.3 Base Case Plasma Properties

The plasma device investigated here is based on commercial plasma sources used to functionalize polymers for biotechnology applications. A schematic of the reactor geometry used in the model is shown in Fig. 4.2. For the base case, 45 slm (standard liters/min) SLM of a He/O_2=98/2 gas mixture with a water vapor impurity of 10 ppm flows into the top of a plasma head at atmospheric pressure. The gas mixture flows between a set of electrodes having length 10 cm, width 10 cm, and separation of 0.2 cm. The power deposition is 210 W which we assume produces a uniform discharge over the electrode area. The gas flow exits the plasma head through a slot located 10 cm from the inlet and mixes with humid air ($N_2/O_2/H_2O$ = 77.5/20/2.5) in a 2 mm gap between the plasma head and the PS surface. The rate of diffusion of air into the plasma plume

is approximated as 1% of the inlet flowrate based on 2-dimensional computational fluid dynamics modeling.

Densities of gas phase species for the base case conditions are shown in Fig. 4.3. The base case conditions yield a plasma with an electron density, n_e , on the order of 10^{10} cm^{-3} and an average electron temperature, Te , of 2.5 eV which is consistent with reported values for rf-driven APPJs [48–50]. While not shown in Fig. 4.3a, the gas temperature increases down the length of the reactor from 300 K to about 312 K before decreasing to 300 K in the air gap. (With the narrow electrode gap, the heat conduction to the walls of the discharge, held at 300 K, is efficient.) O_2^*, O_3, and O are the primary ROS exiting the reactor to mix with air. O_2^* (5×10^{16} cm^{-3}) and O (3×10^{15} cm^{-3}) are formed with high densities downstream as electronic excitation and electron impact dissociation of O_2 are the main sources of energy dissipation in this system. O_3 (1.6×10^{16} cm^{-3}) is formed dominantly through three-body collisions between O and O_2. O_3 is formed at the same rate as O near the top of the reactor before reaching a steady state value that is constrained by the low mole fraction of O_2. Significant densities of H (2×10^{13} cm^{-3}) and OH (2×10^{13} cm^{-3}) are produced by electron impact dissociation of H_2O, and excitation transfer from He^*,

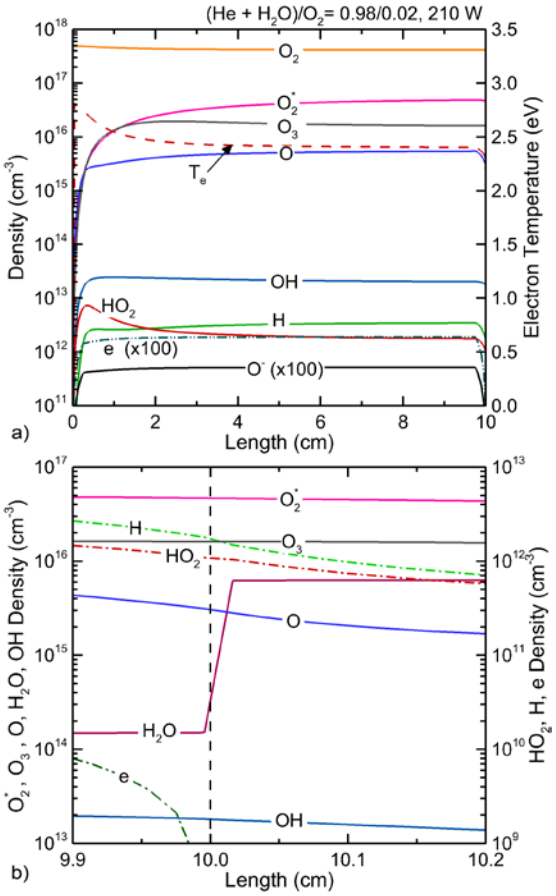

Figure 4.3. Base case plasma properties (Pressure = 1 atm, $He/O_2/H_2O$= 98/2/10 ppm Power = 210 W, Gap = 2 mm, Ambient air = $N_2/O_2/H_2O$ = 78/20/2). a) On the reactor and b) in the gap between the plasma head and the PS surface.

as a result of the water impurity. HO_2 (2×10^{13} cm^{-3}) is produced as a product of reactions of OH with O_3 and H_2 with O_2. The O density decreases in the air gap after exiting the reactor due to reactions with H_2O and H_2O dissociation products to form more energetically favorable molecular species OH, H_2, O_2, and H_2O.

The resulting functionalization of the PS surface by these ROS fluxes is shown in Fig. 4.4a. The PS surface was exposed to the plasma plume for 12 seconds, which corresponds to a polymer web speed of 10 cm/min for this configuration. After plasma treatment, the PS surface is exposed to ambient air for 200 seconds. (The entire post-treatment time is not shown in Fig. 4.4a.) Exposure to ambient air serves mainly to terminate any free radical sites left on the PS surface after contact with the plasma, thereby stabilizing the surface. Changes in surface functionality due to exposure to ambient air occur only over the first 20 seconds after the plasma is turned off, at which time steady state oxygen fractional occupancy is achieved. Plasma treated PS has been shown to maintain stability for up to 1 year [18]. We consider the steady state fractional occupancy of oxygen achieved after the first 20 seconds of post-treatment to be the final stable configuration of the modified polymer.

Total oxygen fractional occupancy on the PS surface shown in Fig. 4.4 increases linearly from zero to 50% over the first half of the 12 second treatment time, with a more gradual increase to about 56% oxygen occupancy occurring in the latter half of treatment time. The alcohol functional group makes the largest contribution to the total O-occupancy, accounting for 48% of the total O-occupancy when the final, stable configuration is achieved, or 86% of the total O-occupancy. The surface functionalization is dominantly initiated by H abstraction from the surface to form alkyl radical sites by the high flux of plasma-produced O to the surface, with secondary contributions by OH,

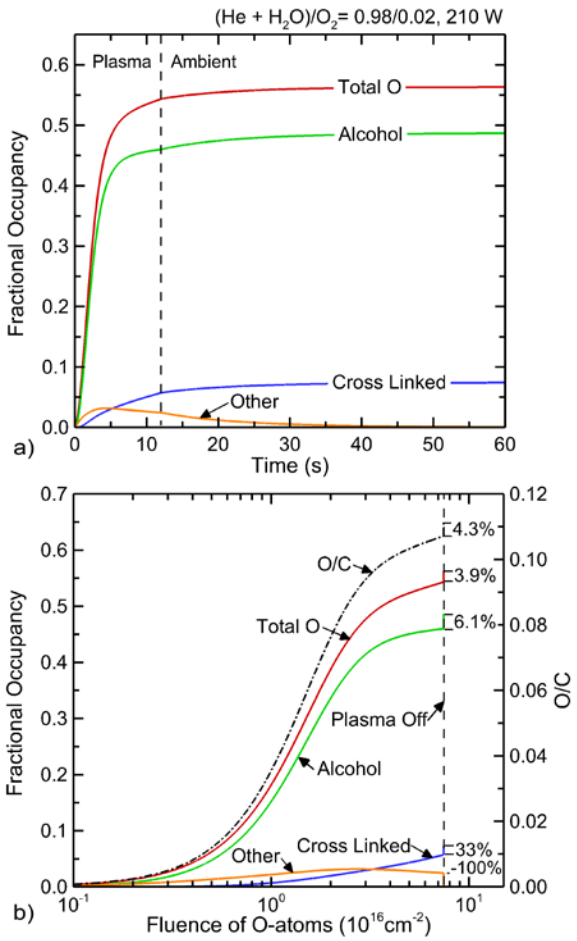

Figure 4.4. Base case fractional occupancy of O- containing functional groups on PS surface after plasma treatment and exposure to air. a) Occupancy as a function of time for a plasma treatment time of 12 s and post-treatment time until 60 s). b) Occupancy and O/C ratio as a function of O-atom fluence. Tick-marks and percentage after plasma turn-off denote the change in occupancy (or O/C ratio) during the post-plasma exposure to air.

$$O + R_n - H \rightarrow OH + R_n\text{–}\bullet \quad (4.1)$$

$$OH + R_n - H \rightarrow H_2O + R_n\text{–}\bullet \quad (4.2)$$

where Rn is the PS monomer unit, with n = 2 for the secondary H site, 3 for the tertiary H site and b for the benzene ring.

There are three pathways for alcohol group formation after surface functionalization is initiated.

$$OH + R_n – • \rightarrow R_n –OH, \ n=2,3 \quad (4.3)$$

The first consists of addition of OH formed as either plasma produced ROS or as a product of H abstraction to an alkyl radical site (Eq. 4.3). In the second pathway, O and O_3 react with an alkyl site to form an alkoxy radical site. The alkoxy radical site can then abstract an H from a neighboring site.

$$O + R_n –• \rightarrow R_n – O•, \ n=1,2,b \quad (4.4)$$

$$R_n – O• + R_m – H \rightarrow R_n– OH + R_m –•, \ n,m=1,2,b \quad (4.5)$$

Finally, addition of O_2 to an alkyl site, results in the formation of a peroxy group. The peroxy group undergoes reaction with OH to form an alcohol group and O_2.

$$O_2 + R_n –• \rightarrow R_n – OO•, \ n=1,2,b \quad (4.6)$$

$$OH + R_n – OO• \rightarrow R_n –OH + O_2, \ n=1,2 \quad (4.7)$$

In the first half of the plasma treatment period, the next largest contributor to total oxygen coverage is the “other” group, comprised mostly of unterminated alkoxy radical sites. The next most abundant site is cross-linked products. Addition of O_2 to an alkyl site can also result in the formation of a peroxy group, which can participate in reactions with other peroxy groups to form cross-linked products.

$$R_n – OO• + R_n – OO• \rightarrow R_n – OO – R_n + O_2, \ n=1,2,b \quad (4.8)$$

In the latter half of the plasma treatment time the “other” group begins to decrease as peroxy sites are terminated by these cross-linking reactions. Steady state total oxygen occupancy is approached as the formation of the alcohol group slows down in the latter half of the treatment time. When the plasma is turned off, total oxygen occupancy increases slightly to approach the steady state value of 56% as the remaining radical sites are terminated (dominantly the alkoxy

sites) in favor of a stable surface configuration. These base case results are consistent with experimental XPS measurements, which suggest that groups containing the C-O bond (alcohol or ether groups) make the largest contribution to total oxygen fraction on the surface of plasma treated PS [26,38,51].

The oxygen occupancy on polymer films is often expressed as the O/C (oxygen-to-carbon) ratio, a value typically produced by XPS measurements. The O/C ratio was estimated for our results as a function of O-fluence to the PS surface, and is shown in Fig 4.4b. It is important to note that our estimation of the O/C ratio may be lower than that given by XPS measurements. Real samples will have some degree of surface roughness after functionalization, which will increase the surface area available for measurements by XPS. The treated "sample" in our case is perfectly flat. As the O-fluence approaches its maximum value (7×10^{16} cm^{-2}) near the end of the plasma treatment time, the O/C ratio on the surface approaches a steady state value of 11%. The trends in O/C estimated here are consistent with experimentally determined O/C from XPS measurements resulting from low pressure plasma treated PS over similar ranges of O-fluence [52]. The saturation in O/C is a consequence of the low reactivity of the aromatic ring compared to the alkane components and the propensity for cross-linking.

The fluence of O-atoms to the surface terminates when the plasma is turned off (or surface is removed from the plasma plume). The surface continues to evolve by, for example, abstraction of H from surface sites by peroxy groups and passivation of free radical sites by ambient O_2. The evolution of the surface composition post-plasma exposure is indicated by the double lines labeled with the percentage increase in Fig. 4.4b. An increase in O-coverage of 3.9% occurs with post-plasma exposure, largely attributable to the formation of alcohol groups (6.1%) and crosslinked

products (33%). This increase in part comes from a decrease in the coverage of alkoxy and peroxy groups of essentially 100%.

4.4 Scaling of O-Occupancy on PS

In this section, the dependence of O-occupancy of the PS surface will be discussed while varying the distance between the plasma source and surface, O_2 mole fraction in the inlet flow, and humidity in the ambient.

4.4.1 Plasma Source to PS Surface Distance

One of the process variables in PS functionalization is the distance between the plasma head and the PS surface. Since this is a remote plasma source, the plasma itself will not be altered and so the flux of reactive species leaving the plasma source does not directly depend on the source-surface distance. However, during the additional flow time to reach the surface, reactions occur in the plume, including reactions with the ambient air diffusing into the plume. The gap was varied between 1 and 20 mm to investigate how these changes in chemistry due to air diffusion into the plume effect the surface functionality.

The densities of gas phase species in the gap between the plasma source and PS surface, for gap distances of 1 mm, 5 mm, 10 mm, and 20 mm are shown in Fig. 4.5a-d. The fractional occupancy of oxygen containing groups on the PS surface after 12 seconds of plasma treatment and 200 seconds of post-treatment air exposure are shown in Fig. 4.6. As the gap increases from 1 mm to 20 mm the density of O reaching the PS surface decreases from 1×10^{15} cm^{-3} to 8×10^{14} cm^{-3} while the O_3 density decreases from 2×10^{16} cm^{-3} to 1×10^{16} cm^{-3}. O atoms are consumed by reactions with O_2 to produce O_3 and with water vapor to form OH. Total O-occupancy decreases with increasing gap distance from 56% at 2 mm to about 45% at 20 mm. Alcohol is the

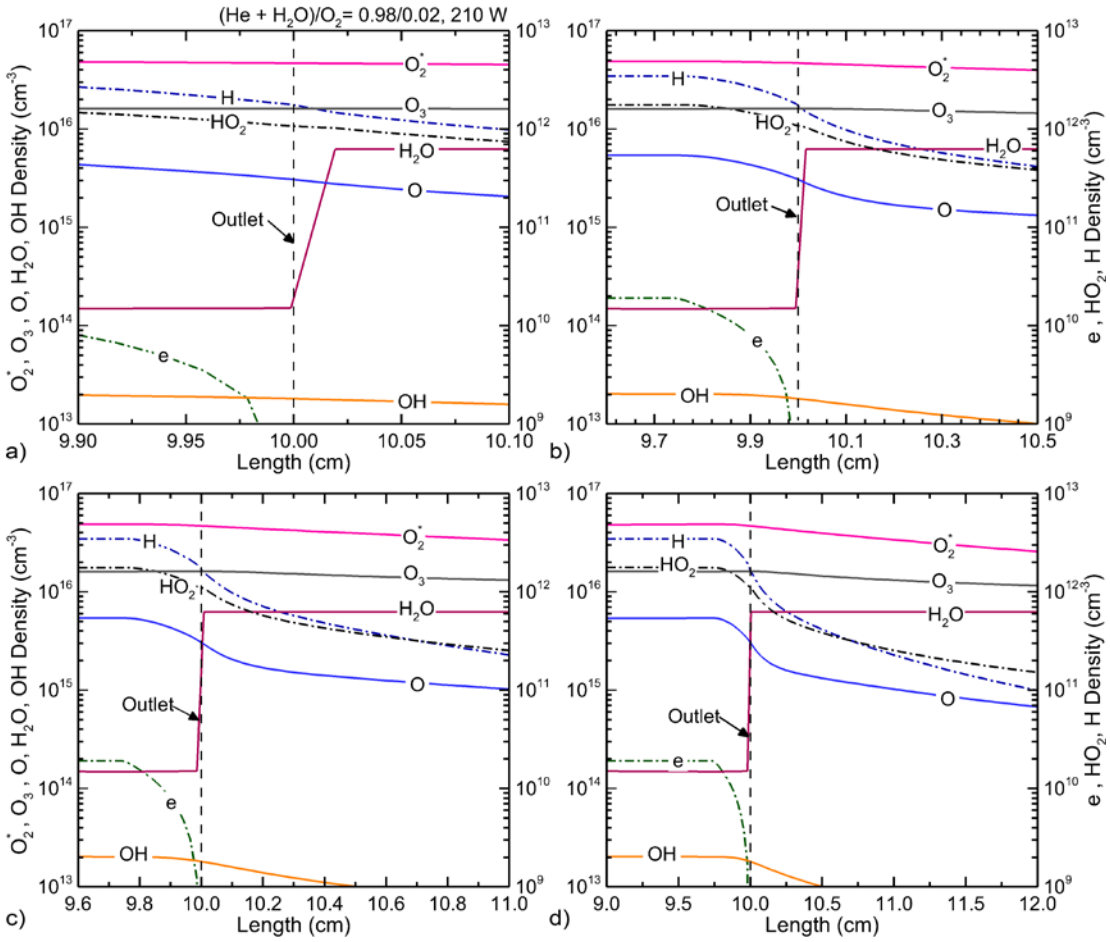

Figure 4.5. Gas phase species densities in the gap between the plasma head and the PS surface as a function of gap distance. a) 1 mm, b) 5 mm, c) 10 mm, d) 20 mm. The densities of O_2*, O_3, O, H_2O and OH are shown on the left scale. The densities of e and HO_2 are shown on the right scale.

dominant functional group formed on the PS surface for all gap distances, though the alcohol fraction decreases from 48% at 2mm to 43% at 20 mm. The decrease in alcohol group can be attributed to a decrease in OH from about 2×10^{13} cm^{-3} to about 8×10^{12} cm^{-3} from 1 mm to 20 mm. The decrease in total oxygen occupancy on the PS surface with increase in gap from 1 mm to 20 mm implies that O may be the most important gas-phase species for functionalizing the PS. However, for these conditions, the fluence of O-atoms is in the saturation regime for all gaps.

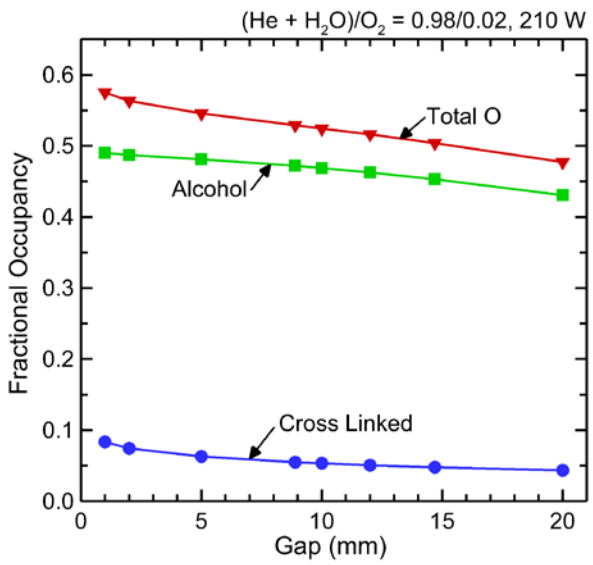

Figure 4.6. Fractional occupancy of oxygen containing functional groups on the PS surface as a function of gap distance of the plasma head from the surface for power of 210 W. Plasma treatment time is 12 s and post-treatment exposure to air is 200 s.

4.4.2 Mole Fraction of Oxygen in Inlet Flow

The inlet mole fraction of oxygen in the He/O2 mixture was varied from 0 to 10% to determine the consequences on the fractional occupancy of O on the PS surface after treatment. Water impurity was not included in the inlet for these cases to isolate the effects of changing the oxygen content on the end functionalization. O-occupancy using the base case power of 210 W is shown in Fig. 4.7a for the inlet mole fraction O_2 of 0 to 10 percent. The densities of O and O_3 at the surface for this range of mole fraction of O_2 are shown in Fig. 4.7b. The addition of even a small amount of O_2 (0.05%) is enough to produce significant O-occupancy (>50%) on the plasma treated PS surface. As the inlet O_2 is increases from 0.05% to 1% there is a local maximum of 62.5% O-occupancy that occurs at 0.3% O_2 inlet fraction. When the inlet O_2 is increases from 0.3% to 1%, the total O-occupancy decreases to 58% and continues to slowly decrease as the O_2 fraction increases to 3%. At O_2 inlet fractions higher than 3%, the total O-occupancy begins to fall off more steeply, from about 54% at 3% O_2 to 38% at 10% O_2.

These trends are largely attributable to the O-atom flux to the surfaces as a function of O_2 inlet fraction. The increase in O-atom density simply results from the increase in O_2 fraction. The rapid decrease in O-atom density at higher O_2 fraction results from the onset of O_3 formation with

the higher O_2 mole fraction, increasing to in excess of 10^{17} cm^{-3} at 10% inlet fraction. H abstraction from the PS backbone is the initiating event in PS functionalization. O-atoms will abstract H from the backbone whereas O_3 does not. Conversion of O to O_3 decreases the rate of initialization of PS functionalization.

The trends in total O-occupancy can be attributed to the dependence of the dominant oxidation products on O_2-fraction. From 0.3% to 1% O_2 fraction, the alcohol content is nearly constant (49-50%) while the cross-linked products decrease from 12% to 9%. With there being no OH production in the gas phase, the =C-OH alcohol bonding results dominantly from H abstraction by peroxy groups (Eq. 4.7). The increase in cross products results from an increase in generation of peroxy groups with the larger flux of O_2, which then leads to cross-linking (Eq. 4.8).

At low O_2 fractions, power is dissipated in the form of electron impact

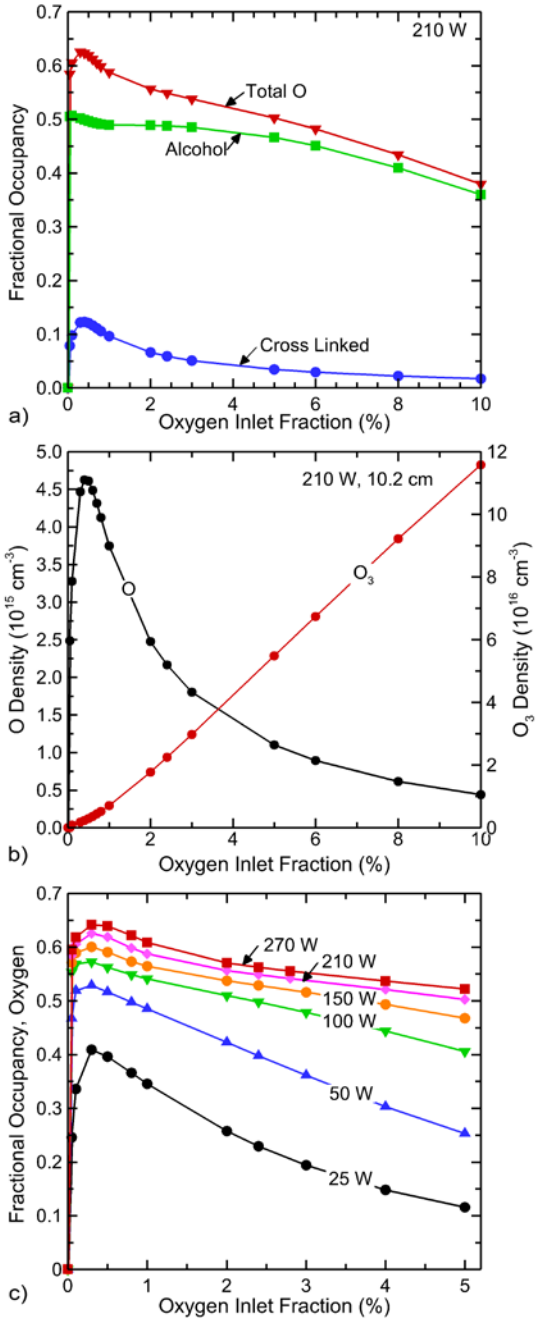

Figure 4.7. Processing parameters as a function of O_2 fraction in the inlet flow (without H_2O impurity). a) Fractional occupancy of oxygen containing functional groups on the PS surface for RF power of 210 W. b) Density of O-atoms and O_3 for 210 W. c) Total fractional occupancy of oxygen for different RF powers.

reactions to predominantly form O atoms, by direct electron impact on O_2, by dissociative excitation transfer from excited states of He and by dissociative recombination of O_2^+. With a small inlet fraction of O_2, the generation of O atoms is limited by the availability of O_2. In fact, the majority of the O_2 can be completely dissociated. With the increase in O_2 inlet fraction, the O-atom density at the surface of the PS has a maximum value of 4.5×10^{15} cm^{-3} at an inlet O_2-fraction of about 0.4%, as shown in Fig. 4.7b, which also corresponds to the local maximum in total O-occupancy on the PS surface. As the inlet mole fraction of O_2 increases, more pathways for non-dissociative power dissipation become available in the form of vibrational, rotational, and non-dissociative electronic excitation, which results in a decrease in the O flux to the substrate. The rapid decrease in O-atom density at higher O_2 fraction also results from the onset of O_3 formation with the higher O_2 mole fraction, increasing to in excess of 10^{17} cm^{-3} at 10% inlet fraction.

After a critical mole fraction of O_2 (0.8% for this case), O_3 becomes the dominant ROS. O initiates PS functionalization by abstracting H from the surface, but is unable to also passivate the newly formed alkyl site to form alkoxy. O_2 can passivate the alkyl site in the absence of adequate O to form peroxy sites, but these sites preferentially combine to form stabilizing cross-linked products. This reaction pathway would account for the smaller decrease in cross-linked products compared to the decrease in alcohol groups when O_3 dominates the ROS fluxes. Alkyl sites that have been passivated by O to form alkoxy sites propagate the initial functionalization step by abstracting H from neighboring sites to form the alcohol group, in effect resulting in the possibility for two H abstractions for every O atom.

These trends suggest that the operating point that yields the highest degree of functionalization under these conditions is that which produces the highest O density (and flux) and the lowest O_3 density. If the O density has the largest effect on the final functionalization of

the PS, it can also be concluded that H abstraction by ROS is the rate limiting step in the functionalization mechanism. Finite rates of H abstraction and passivation between O and O_3 can always be overcome by increasing the ROS fluence to the point that the saturation regime is approached (Fig. 4b). That is the case for powers > 100-150 W for our conditions. The oxygen fraction (up to 5%) that yields the maximum O surface coverage is nearly independent of powers above 100-150 W as shown in Fig. 4.7c. For lower powers (< 100 W), the functionalization is not saturated and there is increasing sensitivity of O surface coverage to O_2 inlet fraction. As shown in Fig. 4.9c, when not saturated (powers of 25 W and 50 W), the decrease in O-atom flux and increase in O_3 flux with increasing O_2 inlet fraction produces a significant decrease in O surface coverage.

4.4.3 Water Vapor Mole Fraction

The most rapid H abstraction from the PS backbone to initiate functionalization occurs by the OH radical. There is some logic to having water vapor in the inlet flow to provide a flux of OH to the PS surface, while also producing other reactive oxygen species (ROS) [59,60]. Water vapor in the inlet flow was varied as a fraction of the sum of H_2O +O_2, r = $[H_2O]/([H_2O] + [O_2])$. The water concentration r was varied from 0 to 100 for inlet gas compositions, $He/(H_2O + O_2)$ = 99.95/0.05,99.5/0.5, 99/1. The inlet fractions of $H_2O + O_2$ (0.05% - 1%) were chosen based on our results and studies by others that suggest that the maximum densities of ROS are produced when $H_2O + O_2$ composes 1% or less of the inlet flow [19,53].

Plasma properties for $[H_2O] + [O_2]$ = 1.0% and r = 0.09, 0.9 and 0.99 are shown in Fig. 8. The delivery of ROS to the substrate is maximum at low inlet H_2O concentrations (r < 0.1) due to a higher rate of dissociation of O_2 and the presence of H from dissociation of H_2O that acts as a reducing species. As the inlet H_2O concentration increases from r = 0.09 to 0.99, there is a decrease

in O density at the surface from 1×10^{15} cm^{-3} to 3×10^{13} cm^{-3} while the total OH density at the outlet changes little (6×10^{13} cm^{-3} to 5.4×10^{13} cm^{-3}). OH and O can both be produced as dissociation products of H_2O, though OH formation occurs at a higher rate. When the inlet H_2O concentration increases beyond r = 0.9, OH is more abundant than O at the reactor outlet, though OH is depleted more quickly in the air gap so that a higher flux of O ultimately reaches the surface. O_3 also decreases (4×10^{15} cm^{-3} to 9×10^{11} cm^{-3}) with increasing H_2O inlet fraction. A decrease in O_3 density corresponds with the decrease in O_2 fraction in the inlet thereby reducing the likelihood of 3-body reactions.

The fractional occupancies of O-containing functional groups on the PS surface after treatment with plasmas having differing concentrations of water vapor for an inlet flow of ($H_2O + O_2$) =

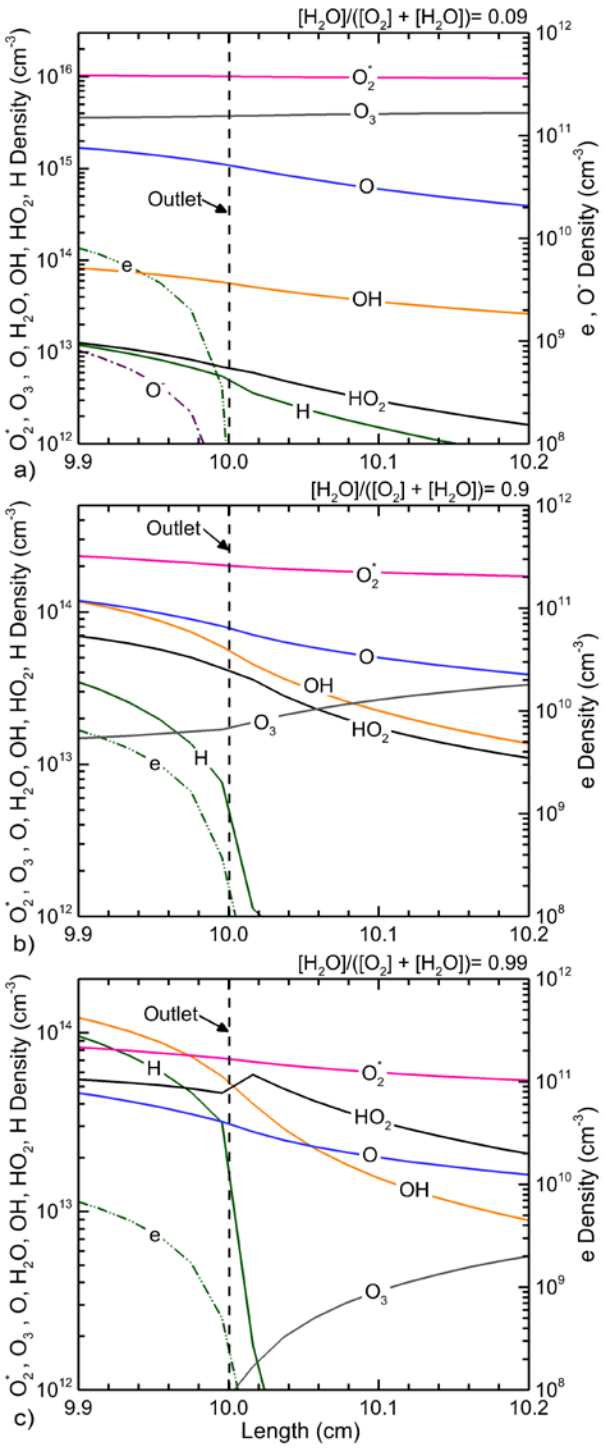

Figure 4.8. Gas phase species densities at the out and across the gap for $He/O_2/H_2O$ plasma where the fraction of $[H_2O] + [O_2]$ is held constant at 1% for different ratios of inlet H_2O fraction, $r = [H_2O]/([O_2] + [H_2O])$. a) r = 0.09, b) 0.90, and c) 0.99.

0.05, 0.5 and 1% are shown in Fig. 4.9. The general trend is decreasing O-occupancy with increasing inlet water vapor concentration. Increasing r (larger H_2O fraction) results in a decrease in total O-occupancy that also corresponds to a change in the dominant functional group from alcohol to cross-linked products. For low values of (H_2O + O_2), the decrease in O-occupancy is nearly linear with the decrease in O_2 in the flow (increasing r). For larger values of (H_2O + O_2), O-occupancy is fairly constant until r = 0.5, and nearly constant as a function of (H_2O + O_2). Both of these trends indicate operation in a saturated regime. The one exception is the transition from no water in the flow (r = 0) to a finite amount (r = 0.01) where the O-occupancy decreases, for example, from 0.62 to 0.55. The introduction of OH into the flow to the substrate ultimately leads to lower O-occupancy.

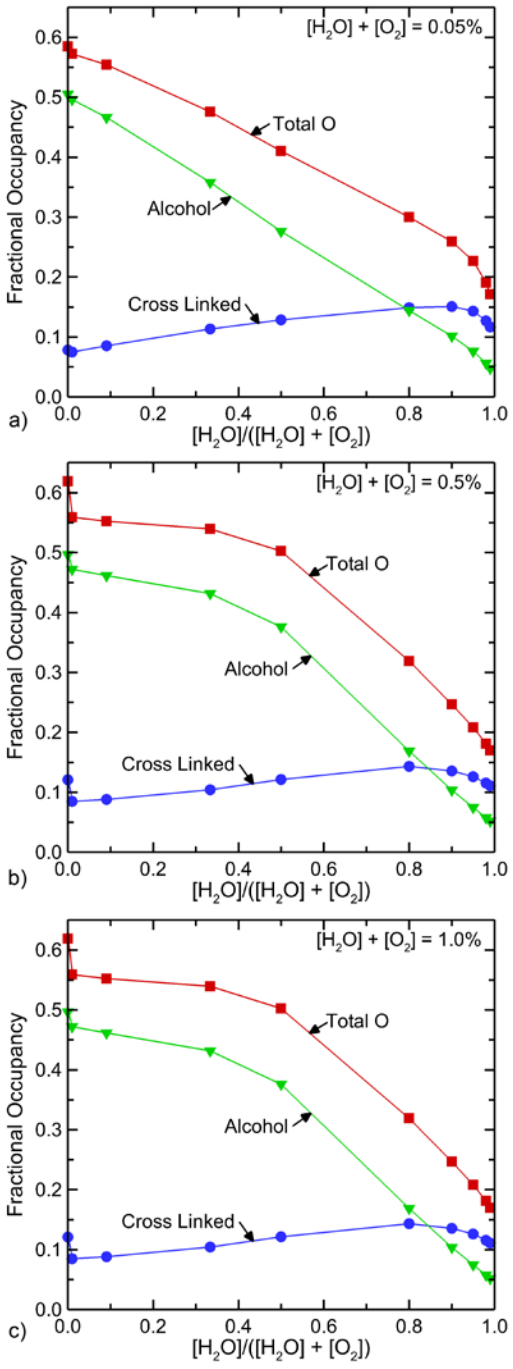

Figure 4.9. Fractional occupancy of oxygen containing functional groups on the PS surface after plasma treatment and exposure to air as a function of ratio of H_2O to O_2 and total mole fraction of H_2O + O_2 in the inlet gas. Plasma treatment time = 12 s, Post-treatment time = 200 s. a) H_2O + O_2 = 0.5% , b) H_2O + O_2 = 0.8 %, c) H_2O + O_2 = 1.0%.

The change in dominant functional group at large r is due to the decrease in O-fluence with the decrease in O_2 fraction. The density of O at the substrate is 3.9-4.9 $\times 10^{14}$ cm^{-3} for r = 0.1, and 3.5-4.2 $\times 10^{13}$ cm^{-3} for r = 0.9 The density at the substrate of OH varies by less than a factor of 2 for all conditions (except for r = 0), clustered about 2 $\times 10^{13}$ cm^{-3}, as production of OH at low r is buoyed by reactions of $O(^1\Delta)$ with H_2O. At high r and large total mole fraction of (H_2O + O_2), the flux of OH to the substrate is power limited, as the H_2O is not depleted in the gas phase. The major change in densities at the substrate is in the O_3 concentration, increasing from 9 $\times 10^{12}$ cm^{-3} [r=0.9, (H_2O + O_2)=0.05%] to 4 $\times 10^{15}$ cm^{-3} [r=0.1, (H_2O + O_2) =1%].

For conditions where the OH fluxes dominate over other ROS, the OH initiates H abstraction from the PS with a higher probability than O, and so O occupancy should increase with increasing OH fluxes. However, the alkyl sites so produced are converted to peroxy sites by O_2 faster than they can be converted to alkoxy sites by the low O-fluence. Although there is an increase in alkoxy formation by increasing fluxes of O_3, the decrease in O-fluence dominates. These peroxy sites preferentially cross-link, effectively terminating the reaction. Crosslinking decreases the number of surface sites available for functionalization (two sites are terminated for every crosslink) and leads to a lower total O-occupancy. Significant lowering of the O-fluence effectively eliminates a reaction pathway for alcohol formation (H abstraction of neighboring sites by alkoxy group). PS functionalization for these conditions is dominated by the O-atom fluence. Water vapor in the inlet shows promise for fine tuning the fractional coverage of desired functional groups if the goal is not necessarily maximizing the O-coverage. Trends in O-coverage as a function of H_2O inlet concentration are the same regardless of the total gas composition for He rich cases.

4.4.4 Relative Humidity in Ambient Air

Water vapor in the inlet flow can have a significant effect on surface functionalization due to the resulting change in density and mole fractions of OH, O and O_3. Water vapor in the ambient air that diffuses into the plasma plume, and in the post-treatment environment, has little effect on the functional groups on the PS surface. The fractional occupancy of functional groups on the PS surface as a function of the percent H_2O in the ambient air was varied from 0 to 10% while having no H_2O in the inlet flow to enable evaluation of the effects of water vapor in the ambient air on the end functionalization. As H2O fraction in the ambient increases for powers in the saturation regime, there was little change in the surface oxygen coverage. The most likely outcome of passivating free radical sites on the PS surface is formation of peroxy by the far more abundant O_2. As such, the water vapor in the ambient has little influence on the final passivation products. Control of plasma-produced ROS has the greatest leverage for controlling the functionalization of the PS surface with plasma jets compared to controlling the ambient conditions.

4.5 Conclusions

A reaction mechanism for the surface functionalization of PS by a He/O_2 atmospheric pressure plasma jet was developed and implemented in a 0-dimensional, plug-flow global plasma chemistry model to predict fluxes of gas-phase species onto the PS surface. A surface site balance model was used to predict changes in the PS surface due to gas-phase and surface-surface reactions during plasma treatment and post-treatment exposure to the ambient. Fractional occupancy of oxygen on the PS surface was quantified as a function of plasma operating conditions. Results from this investigation suggest that alcohol functional groups and cross-linked products are the largest contributors to the oxygen-functionalization of the plasma treated PS, consistent with experimental measurements for similar conditions. The high fraction of cross-linked products may

explain the lack of long-term post-treatment changes in surface properties (as represented, for example, by change in water contact angle) that otherwise occurs with other plasma treated polymers such as polypropylene. Control of the O-atom flux to the surface is the dominant factor in determining the degree of oxygen functionalization with hydrogen abstraction from the PS backbone being the rate limiting step in the PS functionalization. Tuning of that functionalization, that is adjusting the proportion of different functional groups, can be achieved by controlling the water vapor content in the inlet flow to the plasma.

The O-atom coverage and functionality can be made less sensitive to operating conditions by using powers and O_2 inlet fractions that correspond to the saturation regime. Saturation in O-atom coverage and products occurs for O-atom fluences approaching 10^{17} cm^{-2}. With O-atom fluences below saturation, the O-coverage logically decreases, but more importantly the system becomes more sensitive to changes in power, impurities, O_2 inlet fraction, post-plasma exposure and the value of fluence itself. Obtaining reproducible results with a minimum of post-plasma change in properties will likely require operating at or near the saturation regime.

4.6 Tables

Table 4.1 Gas Phase Species Included in Plasma Chemistry Model

Hydrogen Species [a, b]

H , H^*, H^+, H^-, H_2 , $H_2(r)$, $H_2(v)$, H_2^+, H_2^* , H_3^+

Oxygen Species [a, b]

O_2 , $O_2(r)$, O_2 (v) , O_2^* , $O_2(^1S)$, O_2^+ , O_2^- , O, O^*, O^+ , O^- , O_3, O_3^* , O_3^- , O_4^+

Nitrogen Species [a, b]

N_2 , $N_2(r)$, $N_2(v)$, N_2^* , N_2^+ , N_3^+ , N_4^+ , N , N^* , N^+

Helium Species [a]

He , He^+ , He , $He_2(^1S)$, $He_2(^3P)$, $He_2(^1P)$, $He(^3P)$, $He(^3S)$, He_2^* , He_2^+

Heterogenous Species [a,b]

OH , OH^* , OH^- , H_2O , $H_2O(v)$, H_2O^+ , HO_2 , H_2O_2 , H_3O^+ , NO, NO_2 , NO_2^+, NO_2^-, NO_3 ,

NO_3^-, N_2O , $N_2O(v)$, NH, HNO, HNO_2 , HNO_3 , HNO_4 , $H_4O_2^+$, $H_2O_3^+$, $H_5O_2^+$, HeH^+

a) * denotes an excited state atom or molecule

b) *(r)* and *(v)* denote rotationally and vibrationally excited molecules, respectively

Table 4.2 Surface Reaction Mechanism

Surface species			
$R_n - H$ (b = benzene ring, 2= secondary, 3= tertiary) $R_n -•$ $R_n - O•$ $R_n - OO•$ $R_n - OH$ $R_n - OOH$ $HR_n = O$ $R_n - OO - R_n$ $R_n - O - R_n$		PS backbone Alkyl Alkoxy Peroxy Alcohol Hydroperoxide Carbonyl Crosslink Product Crosslink Product	
	Reaction	Probability or reaction rate coefficient[a]	Comments
	Gas-phase Surface Reactions		
1	$O + R_3 - H \rightarrow OH + R_3 -•$	5×10^{-3}	c
2	$O + R_2 - H \rightarrow OH + R_2 -•$	5×10^{-4}	c
3	$O + R_b - H \rightarrow OH + R_b -•$	3.31×10^{-4}	b
4	$OH + R_3 - H \rightarrow H_2O + R_3 -•$	0.5	c
5	$OH + R_2 - H \rightarrow H_2O + R_2 -•$	0.5	c
6	$OH + R_b - H \rightarrow H_2O + R_b -•$	6.61×10^{-3}	b
7	$HO_2 + R_3 - H \rightarrow H_2O_2 + R_3 -•$	5×10^{-5}	c

8	$HO_2 + R_2 – H \rightarrow H_2O_2 + R_2 –•$	5×10^{-5}	c
9	$O + R_3 –• \rightarrow R_3 – O•$	0.5	c
10	$O + R_2 –• \rightarrow R_2 – O•$	0.5	c
11	$O + R_b –• \rightarrow R_b – O•$	1.0	b
12	$O_2 + R_3 –• \rightarrow R_3 – OO•$	2×10^{-3}	c
13	$O_2 + R_2 –• \rightarrow R_3 – OO•$	4.4×10^{-4}	c
14	$O_2 + R_b –• \rightarrow R_b – OO•$	5.83×10^{-2}	b
15	$O_3 + R_3 –• \rightarrow R_3 – OO• + O_2$	1.0	c
16	$O_3 + R_2 –• \rightarrow R_2 – OO• + O_2$	0.5	c
17	$O_3 + R_b –• \rightarrow R_b – OO• + O_2$	1.0	b
18	$O + R_b – O• \rightarrow R_b – OO•$	0.626	b
19	$NO + R_3 – O• \rightarrow R_3 –• + NO_2$	0.1	c
20	$NO + R_2 – O• \rightarrow R_2 –• + NO_2$	0.1	c
21	$NO + R_b – O• \rightarrow R_b –• + NO_2$	3.6×10^{-2}	b
22	$O + R_3 – OH \rightarrow R_3 –O• + OH$	7.5×10^{-4}	c
23	$OH + R_3 – OH \rightarrow R_3 –O• + H_2O$	8.2×10^{-3}	c
24	$OH + R_b – OH \rightarrow R_b –O• + H_2O$	2.18×10^{-2}	b
	Surface- Surface reactions		
25	$R_3 – OO• + R_3 – H \rightarrow R_3 – OOH + R_3 –•$	5.5×10^{-16}	c
26	$R_2 – OO• + R_2 – H \rightarrow R_2 – OOH + R_2 –•$	5.5×10^{-16}	c
27	$R_b – OO• + R_3 – H \rightarrow R_b – OOH + R_3 –•$	5.5×10^{-17}	e
28	$R_b – OO• + R_2 – H \rightarrow R_b – OOH + R_2 –•$	1.1×10^{-18}	e
29	$R_3 – O• + R_3 – H \rightarrow R_3 – OH + R_3 –•$	2×10^{-14}	c

30	$R_3 – O• + R_2 – H \rightarrow R_3 – OH + R_2 –•$	4×10^{-14}	c
31	$R_3 – O• + R_b – H \rightarrow R_3 – OH + R_b –•$	2×10^{-16}	c, d
32	$R_2 – O• + R_3 – H \rightarrow R_2 – OH + R_3 –•$	2×10^{-14}	c
33	$R_2 – O• + R_2 – H \rightarrow R_2 – OH + R_2 –•$	4×10^{-14}	c
34	$R_2 – O• + R_b – H \rightarrow R_2 – OH + R_b –•$	4×10^{-16}	c, d
35	$R_b – O• + R_3 –H \rightarrow R_b – OH + R_3 –•$	7.5×10^{-14}	c, d
36	$R_b – O• + R_2 –H \rightarrow R_b – OH + R_2 –•$	7.5×10^{-14}	c, d
37	$R_2 – O• + R_3 – OOH \rightarrow R_2 – OH + R_3 – OO•$	1×10^{-20}	c
38	$R_2 – O• + R_2 – OOH \rightarrow R_2 – OH + R_3 – OO•$	1×10^{-20}	c
39	$R_b –• + R_3 –H \rightarrow R_b – H + R_3 –•$	7×10^{-14}	d
40	$R_b –• + R_2 –H \rightarrow R_b – H + R_2 –•$	7×10^{-14}	d
41	$R_b –• + R_2 –OH \rightarrow R_b – H + R_2 –O•$	1×10^{-14}	d
42	$R_b –• + R_3 –OH \rightarrow R_b – H + R_3 –O•$	1×10^{-14}	d
	Cross Linking reactions[g]		
43	$R_b – O• + R_b – O• \rightarrow R_b – OO – R_b$	3×10^{-11}	f
44	$R_n – OO• + R_m – OO• \rightarrow R_n – OH + HR_m= O + O_2$	2.4×10^{-14}	f
45	$R_n – OO• + R_n – OO• \rightarrow R_n – OO – R_n + O_2$	4×10^{-14}	f
46	$R_n – OO• + R_m – OO• \rightarrow R_n – OO – R_m + O_2$	1×10^{-14}	f
	Gas-phase termination reactions		
47	$H + R_3 –• \rightarrow R_3 – H$	0.2	c
48	$H + R_2 –• \rightarrow R_2 – H$	0.2	c
49	$H + R_b –• \rightarrow R_b – H$	1.0	b

50	$HO_2 + R_b – \bullet \rightarrow R_b – OOH$	1.0	b
51	$OH + R_3 – OO\bullet \rightarrow R_3 – OH + O_2$	5×10^{-5}	c
52	$OH + R_2 – OO\bullet \rightarrow R_2 – OH + O_2$	5×10^{-5}	c
53	$OH + R_b – O\bullet \rightarrow R_b – OOH$	9.29×10^{-12}	b
54	$HO_2 + R_3 – OO\bullet \rightarrow R_3 – OOH + O_2$	5×10^{-5}	c
55	$HO_2 + R_2 – OO\bullet \rightarrow R_2 – OOH + O_2$	5×10^{-5}	c
54	$HO_2 + R_3 – O\bullet \rightarrow R_3 – OH + O_2$	0.50	b
55	$HO_2 + R_2 – O\bullet \rightarrow R_2 – OH + O_2$	0.50	b
56	$OH + R_3 – \bullet \rightarrow R_3 – OH$	1×10^{-5}	c
57	$OH + R_2 – \bullet \rightarrow R_2 – OH$	1×10^{-5}	c

Table 4.3 Analogous Gas Phase Reactions for Surfaces Reaction Mechanisms

	Reaction in Table 2	Analogous Reaction	Rate Coefficient ($cm^3\ s^{-1}$)	Source
	Gas-Phase Surface Reactions			
3	$O + R_b - H \rightarrow OH + R_b -\bullet$	Benzene + OH → Phenyl + H_2O	6.61×10^{-15}	[39], est
6	$OH + R_b - H \rightarrow H_2O + R_b -\bullet$	Benzene + OH → Phenyl + H_2O	6.61×10^{-15}	[39]
11	$O + R_b -\bullet \rightarrow R_b - O\bullet$	Estimated as gas kinetic.	1×10^{-10}	[29], est
14	$O_2 + R_b -\bullet \rightarrow R_b - OO\bullet$	Phenyl + $O_2 \rightarrow C_6H_5OO\bullet$	5.83×10^{-12}	[40]
17	$O_3 + R_b -\bullet \rightarrow R_b - OO\bullet + O_2$	Estimated as gas kinetic.	1×10^{-10}	[29], est
18	$O + R_b - O\bullet \rightarrow R_b - OO\bullet$	$C_6H_5O + O\bullet \rightarrow C_6H_5OO\bullet$	6.26×10^{-13}	[41]
21	$NO + R_b - O\bullet \rightarrow R_b -\bullet + NO_2$	C_6H_5O + NO → products	1.80×10^{-12}	[42]
24	$OH + R_b - OH \rightarrow R_b - O\bullet + H_2O$	Phenol + OH → C_6H_5O + H_2O	2.18×10^{-12}	[39]
	Surface- surface reactions			
41	$R_b -\bullet + R_2 - OH \rightarrow R_b - H + R_2 - O\bullet$	C_2H_5OH + Phenyl → Benzene + CH_3CH_2O	1.0×10^{-14}	[43]
42	$R_b -\bullet + R_3 - OH \rightarrow R_b - H + R_3 - O\bullet$	C_2H_5OH + Phenyl → Benzene + CH_3CH_2O	1.0×10^{-14}	[43]
	Gas-phase termination reactions			
49	$H + R_b -\bullet \rightarrow R_b - H$	Phenyl + H → Benzene	1.63×10^{-10}	[44]
53	$OH + R_b - O\bullet \rightarrow R_b - OOH$	$C_6H_5O + OH \rightarrow C_6H_5OOH$	9.29×10^{-22}	[45]
54	$HO_2 + R_3 - O\bullet \rightarrow R_3 - OH$	$CH_3O + HO_2 \rightarrow CH_3OH + O_2$	4.7×10^{-11}	[48]
55	$HO_2 + R_2 - O\bullet \rightarrow R_2 - OH$	$CH_3O + HO_2 \rightarrow CH_3OH + O_2$	4.7×10^{-11}	[48]

4.7 References

[1] S. Guruvenket, G. M. Rao, M. Komath and A. M. Raichur, Appl. Surf. Sci. **236,** 278 (2004).

[2] Y. Tamada and Y. Ikada, Polymer (Guildf). **34,** 2208 (1993).

[3] E. M. Liston, L. Martinu and M. R. Wertheimer, J. Adhes. Sci. Technol. **7,** 1091 (1993).

[4] L. Carrino, G. Moroni and W. Polini, J. Mater. Process. Technol. **121,** 373 (2002).

[5] J. Meichsner, M. Nitschke, R. Rochotzki and M. Zeuner, Surf. Coatings Technol. **74–75,** 227 (1995).

[6] M. R. Sanchis, O. Calvo, O. Fenollar, D. Garcia and R. Balart, J. Appl. Polym. Sci. **105,** 1077 (2007).

[7] H. R. Yousefi, M. Ghoranneviss, A. R. Tehrani and S. Khamseh, Surf. Interface Anal. **35,** 1015 (2003).

[8] U. Schulz, P. Munzert and N. Kaiser, Surf. Coatings Technol. **142–144,** 507 (2001).

[9] M. Lehocký, H. Drnovská, B. Lapčíková, A. M. Barros-Timmons, T. Trindade, M. Zembala and L. Lapčík, Colloids Surfaces A Physicochem. Eng. Asp. **222,** 125 (2003).

[10] I. Novák, V. Pollák and I. Chodák, Plasma Process. Polym. **3,** 355 (2006).

[11] Y. Kusano, J. Adhes. **90,** 755 (2014).

[12] M. J. Shenton and G. C. Stevens, J. Phys. D. Appl. Phys. **34,** 2761 (2001).

[13] X. Lu, M. Laroussi and V. Puech, Plasma Sources Sci. Technol. **21,** (2012).

[14] A. Schütze, J. Y. Jeong, S. E. Babayan, J. Park, G. S. Selwyn and R. F. Hicks, IEEE Trans. Plasma Sci. **26,** 1685 (1998).

[15] N. Gomathi, A. Sureshkumar and S. Neogi, **94,** 1478 (2008).

[16] S. Yonson, S. Coulombe, V. Léveillé and R. L. Leask, J. Phys. D. Appl. Phys. **39,** 3508

(2006).

[17] P. K. Chu, J. Y. Chen, L. P. Wang and N. Huang, Mater. Sci. Eng. R Reports **36,** 143 (2002).

[18] O. M. Ba, P. Marmey, K. Anselme, A. C. Duncan and A. Ponche, Colloids Surfaces B Biointerfaces **145,** 1 (2016).

[19] P. Luan, V. S. S. K. Kondeti, A. J. Knoll, P. J. Bruggeman and G. S. Oehrlein, J. Vac. Sci. Technol. A **37,** 031305 (2019).

[20] A. Vesel, R. Zaplotnik, G. Primc and M. Mozetič, Polymers (Basel). **12,** (2020).

[21] Y. Ren, C. Wang and Y. Qiu, Surf. Coatings Technol. **202,** 2670 (2008).

[22] N. De Geyter, R. Morent and C. Leys, Surf. Interface Anal. **40,** 608 (2008).

[23] L. Lianos, D. Parrat, T. Q. Hoc and T. M. Duc, J. Vac. Sci. Technol. A Vacuum, Surfaces, Film. **12,** 2491 (1994).

[24] T. H. Chen, F. Y. Chung, W. F. Jiang and C. Huang, Vacuum **186,** 110069 (2021).

[25] R. W. Paynter and H. Benalia, J. Electron Spectros. Relat. Phenomena **136,** 209 (2004).

[26] E. H. Lock, D. Y. Petrovykh, P. Mack, T. Carney, R. G. White, S. G. Walton and R. F. Fernsler, Langmuir **26,** 8857 (2010).

[27] K. Fricke, K. Duske, A. Quade, B. Nebe, K. Schroder, K. D. Weltmann and T. Von Woedtke, IEEE Trans. Plasma Sci. **40,** 2970 (2012).

[28] C. Wang and X. He, Surf. Coatings Technol. **201,** 3377 (2006).

[29] A. N. Bhoj and M. J. Kushner, J. Phys. D. Appl. Phys. **40,** 6953 (2007).

[30] R. Dorai and M. J. Kushner, J. Phys. D. Appl. Phys. **36,** 666 (2003).

[31] A. N. Bhoj and M. J. Kushner, J. Phys. D. Appl. Phys. **39,** 1594 (2006).

[32] J. . Stille, R. . Sung and J. Vander Kooi, J. Org. Chem **1065,** 3116 (1965).

[33] H. Sekiguchi, M. Ando and H. Kojima, J. Phys. D. Appl. Phys. **38,** 1722 (2005).

[34] J. F. Rabek and B. Ranby, J Polym Sci Part A-1 Polym Chem **12,** 295 (1974).

[35] R. C. Longo, A. Ranjan and P. L. G. Ventzek, ACS Appl. Nano Mater. **3,** 5189 (2020).

[36] J. J. Végh and D. B. Graves, Plasma Process. Polym. **6,** 320 (2009).

[37] NIST Chemical Kinetics Database

[38] J. Park, L. Wang and M. C. Lin, Int. J. Chem. Kinet. **36,** 49 (2004).

[39] R. Knispel, R. Koch, M. Siese and C. Zetzsch, Ber. Bunsenges. Phys. Chem. **94,** 1375 (1990).

[40] T. Yu and M. C. Lin, J. Am. Chem. Soc. **116,** 9571 (1994).

[41] G. Da Silva and J. W. Bozzelli, J. Phys. Chem. A **112,** 3566 (2008).

[42] S. C. Xu and M. C. Lin, J. Phys. Chem. B **109,** 8367 (2005).

[43] J. Park, Z. F. Xu, K. Xu and M. C. Lin, Proc. Combust. Inst. **34,** 473 (2013).

[44] L. B. Harding, Y. Georgievskii and S. J. Klippenstein, J. Phys. Chem. A **109,** 4646 (2005).

[45] M. Batiha, A. H. Al-Muhtaseb and M. Altarawneh, Int. J. Quant. Chem. **112,** 848 (2012).

[46] R. Atkinson, D. L. Baulch, R. A. Cox, J. . Crowley, R. F. Hamspon, R. G. Hynes, M. E. Jenkin, M. J. Rossi and J. Troe, Atmos. Chem. Phys. **6,** 3625 (2006).

[47] Q. F. Wei, Mater. Charact. **52,** 231 (2004).

[48] E. Assaf, C. Schoemaecker, L. Vereecken and C. Fittshchen, Phys. Chem. Chem. Phys. **20,** 10660 (2018).

[49] P. Luan and G. S. Oehrlein, J. Phys. D. Appl. Phys. **51,** (2018).

[50] R. M. France and R. D. Short, Langmuir **14,** 4827 (1998).

[51] F. M. Petrat, D. Wolany, B. C. Schwede, L. Wiedmann and A. Benninghoven, Surf. Interface Anal. **21,** 274 (1994).

[52] V. S. S. K. Kondeti, Y. Zheng, P. Luan, G. S. Oehrlein and P. J. Bruggeman, J. Vac. Sci. Technol. A **38,** 033012 (2020).

[53] S. J. Moss, A. M. Jolly and B. J. Tighe, Plasma Chem. Plasma Process. **6,** 401 (1986).

Chapter 5 Reaction Mechanisms for Plasma Modification of Organic Molecules in Solution[4]

Mechanisms for the cold atmospheric plasma (CAP) treatment of cells in solution are needed for more optimum design of plasma devices for wound healing, cancer treatment, and bacterial inactivation. However, the complexity of organic molecules on cell membranes makes understanding mechanisms that result in modifications (i.e., oxidation) of such compounds difficult. As a surrogate to these systems, a reaction mechanism for the oxidation of cysteine in CAP activated water was developed and implemented in a 0-dimensional (plug-flow) global plasma chemistry model with the capability to address plasma-liquid interactions. Reaction rate coefficients for organic reactions in water were estimated based on available data in the literature or by analog to gas-phase reactions. The mechanism was validated by comparison to experimental mass-spectrometry data for COST-jets sustained in He/O_2, He/H_2O and $He/N_2/O_2$ mixtures treating cysteine in water. Results from the model were used to determine the consequences of changing COST-jet operating parameters, such as distance from the substrate and inlet gas composition, on cysteine oxidation product formation. Results indicate that operating parameters can be adjusted to select for desired cysteine oxidation products, including nitrosylated products

[4] Results discussed and portions of the text in this chapter have been previously published in J. Polito, et. al. "Reaction Mechanism for Atmospheric Pressure Plasma Treatment of Cysteine in Solution," *J. Phys. D. Appl. Phys.* 56, 395205 (2023).

5.1 Introduction

Cold atmospheric pressure plasmas (CAPs) have potential applications in plasma medicine including cancer treatment [1,2], chronic wound healing [3], disinfection [4,5], and medical device decontamination [6]. A variety of well-characterized CAP devices have been used for plasma medical applications, including dielectric barrier discharges (DBDs), atmospheric pressure plasma jets (APPJs), and plasma needles [7–10]. These devices are either "touching", in which the plasma is in direct contact with the target, or "non-touching" in which reactive species generated in the plasma transport across a non-powered region to reach the target. Plasma jet devices for biomedical applications are generally sustained in either argon or helium with additives or impurities (i.e., air, oxygen, water) that result in generation of reactive oxygen and nitrogen species (RONS) in the plasma.

The RONS produced in these plasma jets include the some of the same RONS involved in biological processes in living organisms where they play an active role in redox biology [11]. RONS, generated by CAP or a living system, are known to affect proteins [12] particularly proteins with the thiol (-SH)-containing amino acid cysteine which is prone to oxidation and nitrosylation [13,14] The low molecular weight protein glutathione (GSH), for example, is the major cellular cysteine-containing protein participating in cellular redox reactions [15]. Crucial biological processes involve the thiol redox state. The inflammatory extracellular signaling protein high mobility group box 1 (HMGB1), for example, contains three redox-sensitive cysteine residues [16]. Depending on the dynamic redox state of each of the cysteine residues, the protein fulfills different functions. The consequences of plasma treatment of proteins *in vivo* could be, to a certain extent, transported or preserved via thiol group oxidation [17]. Oxidative modifications of biomolecules have the potential to modulate and control downstream physiological processes [18].

Cystine (RSSR), a commonly found product after plasma treatment, contains a disulfide bridge, a key structural element essential for protein structure and function [19]. Cystine is a sensitive sensor of the redox state of a cell [19] which can be further oxidized or nitrosylated. These molecules can lead to bioactive derivates that have anti-proliferative effects on cancer cells [20], playing a role in the nitric oxide pathway with implications for wound healing, cancer biology, and cardiac functioning [21–23]. A range of products, including non-stable transient products, can be found after plasma treatment [14,21]. Bioactive reactive sulfur species (RSS) (e.g., cyst(e)ine sulfoxides and cysteine-S-sulfonate) have the potential to influence cellular redox balance [20,24].

Given the large number of in-solution RONS produced by CAP, and the many reactions that may occur with living cells, isolating specific reaction pathways is challenging [25,26]. The amino acid cysteine has been used in studies of CAP interacting with water-based solutions as a surrogate for biological models, due to its amino, carboxyl, and thiol groups that are common in biological macromolecules, and cell membranes in particular [21,27–29], and the biological relevance of the molecule, as discussed above. Developing mechanisms for in-solution interactions of RONS with simpler amino acids provides a baseline for understanding such interactions with living cells.

Developing an in-solution reaction mechanism for CAP produced RONS interactions with cysteine will benefit from a combined experimental and computational approach. Cysteine interactions with RONS have been modeled by Lackmann et al. [30] using molecular dynamics (MD) simulations. The MD simulations included interactions of reactants that may be produced by two plasma jet sources, the kINPen sustained in argon [31] and the COST-jet sustained in helium/argon mixtures [32]. Cysteine oxidation was initiated by OH_{aq} or NO_{aq} at the thiol (-SH)

site on the cysteine molecule. (The subscript "aq" denotes an in-solution species, to differentiate from their gas phase analogues.) Interactions with H_2O_{2aq}, O_{2aq}, and O_{3aq} were also addressed, but were found to be less important than interactions with OH_{aq} and NO_{aq} on the short timescales that could be addressed with MD ($\leq$ 10 ps). A detailed mechanism was produced, which included branching ratios of cysteine oxidation products formed after interactions of cysteine or cysteine intermediate products with RONS. However, due to the computational limitations of MD, longer timescale interactions on the order of seconds or minutes could not be resolved.

Computational models with ability to address timescales consistent with experimental treatment times (seconds to minutes) would aid in further understanding of plasma-assisted modifications of organic molecules in solutions. Recent measurements have shown that atomic O_{aq} is one of the most abundant ROS produced by CAP sources sustained in mixtures containing oxygen impurities, and so its interactions with organic molecules should also be considered [33,34].

In this chapter, we discuss results from computational and experimental investigations in which we propose a reaction mechanism for the COST-jet treatment of cysteine in water solutions. A 0-dimensional (0D) global plasma chemistry model was used in a plug-flow mode to simulate the gas-phase reactive species densities and fluxes that come into contact with ambient air in the gap between the reactor outlet and continue to the liquid surface. The gas-phase fluxes impinge on a 1 mm thick solution of cysteine in water. A liquid reaction mechanism that accounts for transport across the gas-liquid interface and liquid-phase reactions was coupled to the gas phase plasma-chemistry model, providing densities of in-liquid species after plasma treatment. The reaction mechanism was validated with experimental mass spectroscopy measurements from the He/O_2 and He/H_2O COST-jet treatment of cysteine in a water solution. Experiments were also

performed for solutions treated by the COST-jet sustained in $He/N_2/O_2$ to produce nitrosylated cysteine products, in addition to oxidation products. The results from the model were used to investigate reaction pathways and mechanisms responsible for the production of cysteine oxidation products as a function of plasma operating parameters including distance between the reactor outlet and the liquid surface, oxygen inlet flow rate, and nitrogen inlet flow rate. Results indicate that some degree of control over the formation of specific products can be achieved by leveraging these plasma parameters.

The experimental methods used to investigate $He/N_2/O_2$ COST-jet treatment of cysteine in solution are described in Section 5.2. The cysteine reaction mechanism is discussed in Section 5.3. A comparison of the model results against experimental data for validation of the reaction mechanism is contained in Section 5.4. Plasma and liquid properties produced by the model for base-case conditions are in Section 5.5. Results, including comparison of the model with experimental mass spectroscopy measurements are discussed in Section 5.6. Conclusions are in Section 5.7.

5.2 Description of the Experiments

5.2.1 Plasma Source

The experiments utilize the atmospheric pressure COST reference microplasma jet (the COST-jet), which has been previously described in detail by Golda et al [32]. The COST-jet is a capacitively coupled plasma that operates at a frequency of 13.56 MHz. The source has two 30 mm long electrodes positioned 1 mm apart, resulting in an active plasma region measuring 1 mm $\times$ 1 mm $\times$ 30 mm. Helium was used as the primary inlet gas. Experiments used for validation of the model kept a total gas flow of 1 slm for the two gas mixtures of He/H_2O = 99.75/0.25 and

He/O_2 = 99.4/0.6. For the He/H_2O mixture, dry helium was passed through a bubbler before being mixed with additional dry helium downstream to produce the desired mole fractions. To reduce impurities, the helium and oxygen (research grade ARC3 PurityPlus 5.0) were delivered through stainless steel tubing. The nitrogen containing gas mixture for the base case was $He/N_2/O_2$ = 99.0/0.8/0.2. The power deposition was kept constant at 750 ± 10 mW and was continuously monitored with integrated current and voltage probes.

5.2.2 Sample Treatment

To investigate the consequences of plasma treatment of biologically important molecules, the amino acid cysteine was used as a surrogate. The L-form of cysteine was sourced from Alfa Aeasar (L-Cysteine A10435, ⩾98%) and dissolved in HPLC (high performance liquid chromatography) grade water to a final concentration of 100 μg/ml. One milliliter of these solutions was then transferred to 12-well plates producing a solution depth of 1 mm and exposed to the COST-jet effluent at a gap distance of 4 mm. For each gas mixture, control samples were also taken where the cysteine solution was only exposed to the respective gas flow without igniting the plasma for a duration equal to the maximum treatment time used. All experiments were performed in triplicate.

5.2.3 Mass Spectrometry

The chemical changes that occurred in cysteine due to plasma treatment were experimentally analyzed using mass spectrometry (MS). 100 μL of each 1 ml sample was transferred to an autosampler vial. A UPLC-MS/MS method was used, utilizing a Thermo Vanquish LC instrument (Thermo Fisher Scientific) coupled to a Thermo Orbitrap Exploris 480 mass spectrometer (Thermo Fisher Scientific) with a heated electrospray ionization (HESI) source.

Chromatographic separation was accomplished with a Waters BEH Amide column (2.1 x 100mm, 1.8 μM) that was maintained at 45°C. A linear gradient of mobile phase A (H_2O + 0.1% FA [formic acid]) and mobile phase B (MeCN + 0.1% FA) was used: 0-0.1 min (99% B, 0.4 ml/min), 0.1-7 min (99-30% B, 0.4 ml/min), 7-10 min (99% B, 0.4 ml/min). Samples were analyzed as 2 μL injections in positive ion mode (spray voltage 3.5 kV, vaporizer temperature 350°C, ion transfer tube temperature °C, sheath gas 50 a.u., sweep gas 1 a.u., and aux gas 10 a.u.) with a mass range of m/z 60-1000. Mass spectrometer 1 (MS1) data were collected with a resolving power of 60,000 and an automatic gain control (AGC) target of 1 x 10^{-6}. Mass spectrometer 2 (MS2) data were collected with a resolving power of 30,000, cycle time of 0.6 s, and stepped higher-energy collision dissociation (HCD) energy of (30, 50, 150 eV). The raw data were imported into Skyline, an open-source MS analysis software package [35], for peak integration and selection using targeted data processing.

5.3 Reaction Mechanism

The gas-phase mechanism for a $He/O_2/N_2$ atmospheric pressure plasma has been discussed in detail in previous works [37,39,40]. Briefly, electron impact dissociation of O_2, N_2, and H_2O (when a water impurity is included in the inlet) are responsible for generating some RONS (e.g., O, OH) and the reactive products needed to form other RONS.

$$e + O_2 \longrightarrow O + O + e \tag{5.1}$$

$$e + N_2 \longrightarrow N + N + e \tag{5.2}$$

$$e + H_2O \longrightarrow OH + H + e \tag{5.3}$$

$$e + H_2O \longrightarrow H + H + O + e \tag{5.4}$$

$$e + H_2O \longrightarrow H_2 + O + e \tag{5.5}$$

Electron energy is primarily lost through inelastic collisions that produce electronically, rotationally, or vibrationally excited states of O_2, N_2, and H_2O ($O_2(r)$, $O_2(v)$, O_2^*, $O_2(^1S)$, $N_2(r)$, $N_2(v)$, N_2^*, $H_2O(v)$). Electronically excited states of N_2 (N_2^*) are dissociatively quenched by O_2 to produce O atoms, and participate in reactions with O to form NO. O_3 is formed as a result of three-body reactions of O and O_2. The 79 gas-phase species included in this work are listed in Table 5.2. As is common in modeling of complex plasma chemistry, excitation to several excited states is lumped into producing a single state, here denoted with *, which is usually the lowest lying state with the longest lifetime. This practice acknowledges that higher excited states will relax or be quenched on times shorter than those of interest. Typically, only the lowest lying, metastable states survive in the plume to reach the liquid.

Every gas-phase species has a liquid-phase counterpart. The liquid-phase mechanism has been discussed previously in Refs. [36] and [41]. Neutral species from the gas-phase solvate into the liquid-phase according to Henry's law as described in Chapter 2.1.4. Henry's law constants that are used to determine the probability a gas-phase species will solvate are listed in Table 5.1. Reactive neutrals can combine in the liquid to form more stable molecules (e.g., OH_{aq}, H_2O_{2aq}, O_{3aq}, HNO_{3aq}, NO_{3aq}). Solvated RONS and RONS produced by plasma-assisted liquid reactions react with organic molecules in the liquid to produce oxidated and nitrosylated organic products.

Cysteine is an organic compound containing a carboxyl group (-COOH), an amine group ($-NH_2$), and a thiol group (-SH). (See Fig. 5.1.) The cysteine reaction mechanism includes 17 cysteine-derived species and 40 liquid-phase reactions of RONS with cysteine. The reaction mechanism and reaction rate coefficients used in this work are listed in Table 5.3. Only reactions with the thiol group of the cysteine molecule are considered in this work. The sulfur atom in the

thiol group is highly reactive in comparison to the other parts of the cysteine molecule, leading to preferential interaction of RONS with the thiol site [21,29]. The presence of the carboxyl group leads to resonance stabilization of the cysteine molecule which contributes to a reduction in reactivity at sites other than the thiol site [42].

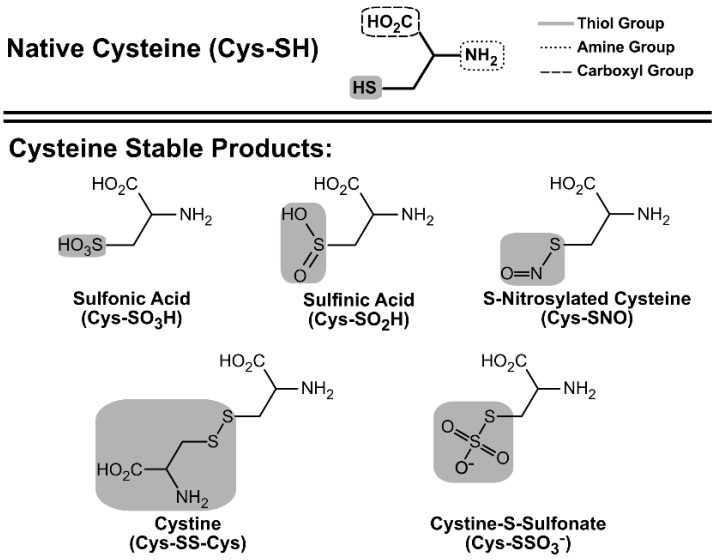

Figure 5.1. Molecular structure of native cysteine and its stable oxidation products.

Similar to the gas-phase oxidation of long-chain alkanes [43], the liquid-phase oxidation of the cysteine thiol site can be considered a three-step mechanism. Oxidation begins with abstraction of the H atom from the thiol site by O_{aq}, O^-_{aq}, OH_{aq}, OH^-_{aq}, or HO_{2aq} to form a thiol radical site. Reactions of RONS at the thiol radical site result in short-lived intermediate products that can undergo rearrangement or subsequent reactions with RONS to form stable oxidation products. In this work an oxidation product is considered stable when its lifetime is long enough to enable experimental detection [30]. We consider cysteine sulfenic acid (Cys-SO_2H), cysteine sulfonic acid (Cys-SO_3H), cysteine-S-sulfonate (Cys-SSO_3^-), cystine (Cys-S-S-Cys), and nitrosylated cysteine (Cys-SNO) to be stable compounds. The structures of these molecules are shown in Fig. 1. (Since Cys- species only exist in solution, the "aq" suffix will not be used in the following text.)

The reaction mechanism of RONS with cysteine shown in Table 5.3 was initially based on molecular dynamics simulations by Lackmann et. al [30]. Reaction rate coefficients for oxidations

of organic molecules in solution are largely unavailable and so have been estimated based on analogous gas-phase reactions of RONS with alkanes taken from the NIST Chemical Kinetics Database [44]. In the few cases where they are available, reaction rate coefficients of RONS with the native cysteine molecule were taken from the NIST Solutions database [45]. Reaction rate coefficients have been adjusted to account for differences in the interactions of molecules in the liquid-phase rather than the gas-phase and to achieve consistency with experiments. In general, gas-phase reaction rate coefficients produced shorter times for cysteine depletion and oxidation in the liquid-phase than observed experimentally. These smaller rate coefficients in large part reflect transport limits in the liquid compared to the gas phase.

5.4 Validation of the Reaction Mechanism

Stapelmann et. al [46] tracked several COST-jet produced ROS from the gas-phase to the liquid phase to predict their impact on the modification of cysteine molecules in a water solution. Mass spectrometry was used to show trends in depletion of the native cysteine and formation of cysteine-derived oxidation products in heavy water ($H_2{}^{18}O$) over five minutes of plasma treatment for two gas mixtures, He/O_2 = 99.4/0.6 and He/H_2O = 99.75/0.25. The gas mixtures were chosen to control the dominant plasma-produced ROS (O in He/O_2; OH and H_2O_2 in He/H_2O) fluxes to the liquid. The stable cysteine oxidation products considered were cysteine-S-sulfonate (Cys-SSO_3H), cysteine sulfenic acid (Cys-SO_2H), and cysteine sulfonic acid (Cys-SO_3H). The combination product cystine (Cys-S-S-Cys) was also measured. The authors found significant differences in the reaction pathways between treating the solution with the COST-jet sustained in He/O_2 and He/H_2O. Treatment with the COST-jet using the He/O_2 mixture resulted in preferential formation of irreversible oxidation products (i.e., Cys-SO_3H) while treatment by the COST-jet using the He/H_2O mixture favored reversible oxidation products (i.e, Cys-SO_2H). The authors

attributed the difference in product formation to the origin of the ROS responsible for the modification. ROS known in redox biology, like OH in the He/H_2O mixture, caused more reversible oxidation products while ROS unknown to nature, i.e. O in the He/O_2 mixture, caused irreversible reaction products.

5.4.1 He/O2 and He/H2O COST-jet Treatment

Results from the Stapelmann et al. study [46] have been reproduced in this section to provide validation for the reaction mechanism discussed in Section IV. The mass spectrometry-produced peak intensity measurements for cysteine-derived oxidation products formed over a five-minute treatment period by exposure to the effluent from COST-jets sustained in He/O_2 and He/H_2O which are shown alongside model-produced densities in Fig. 5.2 and Fig. 5.3. Values have been normalized to one to provide a more direct comparison of the trends in product formation over time between the experiments and the model. The model uses the same reaction mechanism as discussed in Section 5.3. Only the gas composition has been adjusted to match the gas composition used in the experiments.

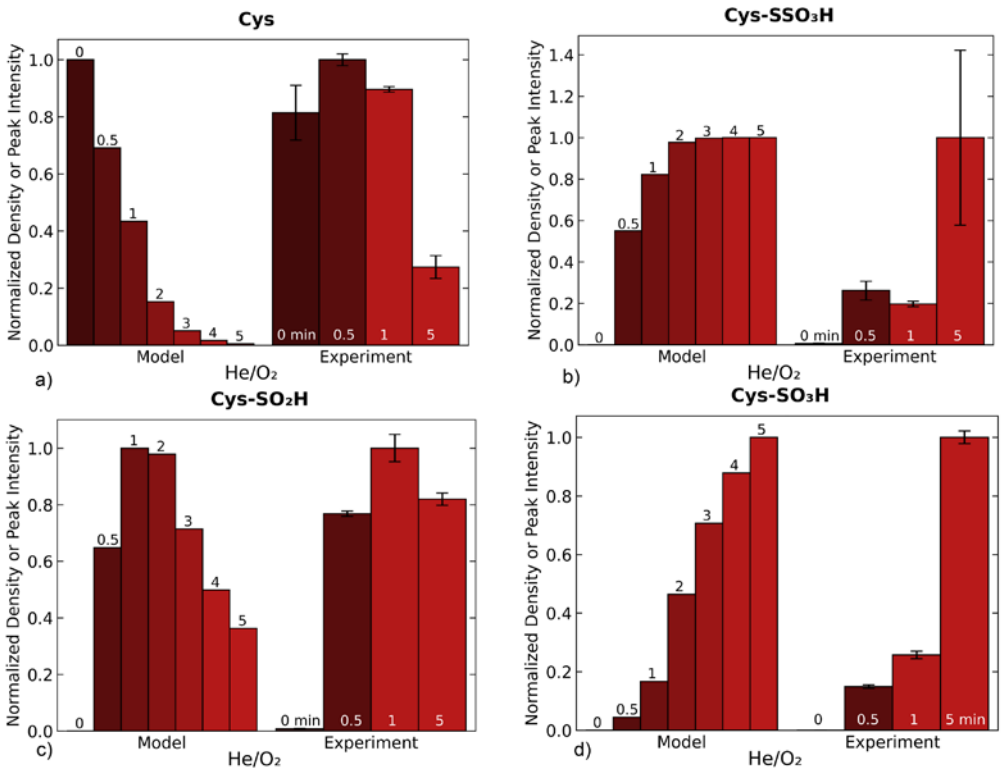

Figure 5.2. Comparison of trends in (a) native cysteine depletion and(b-d) cysteine oxidation product formation between model and experiments for the COST-jet treatment using a He/O_2 = 99.4/0.6 gas mixture as a function of plasma exposure time. Values (model-predicted number density or mass spectrometry-produced peak intensity) have been normalized to 1.

Overall, trends predicted by the model are in good agreement with the measured values. For treatment of cysteine using the COST-jet sustained in He/O_2 (Fig. 5.2), cysteine is significantly depleted after five minutes of plasma treatment as H is abstracted from the thiol group by ROS (O_{aq}, OH_{aq}, $HO_{2,aq}$) to form thiol radical sites. Thiol radical sites are converted to intermediate oxidation products by subsequent reactions with ROS. Intermediate products can then be converted to stable oxidation products by reactions with RONS or with reactions involving O_{2aq}. The reaction mechanism relating the formation pathways of the cysteine oxidation products to the fluences of plasma-produced RONS is discussed in Section 5.6.

Cys-S-SO_3H and Cys-SO_3H (irreversible oxidation products) are preferentially produced

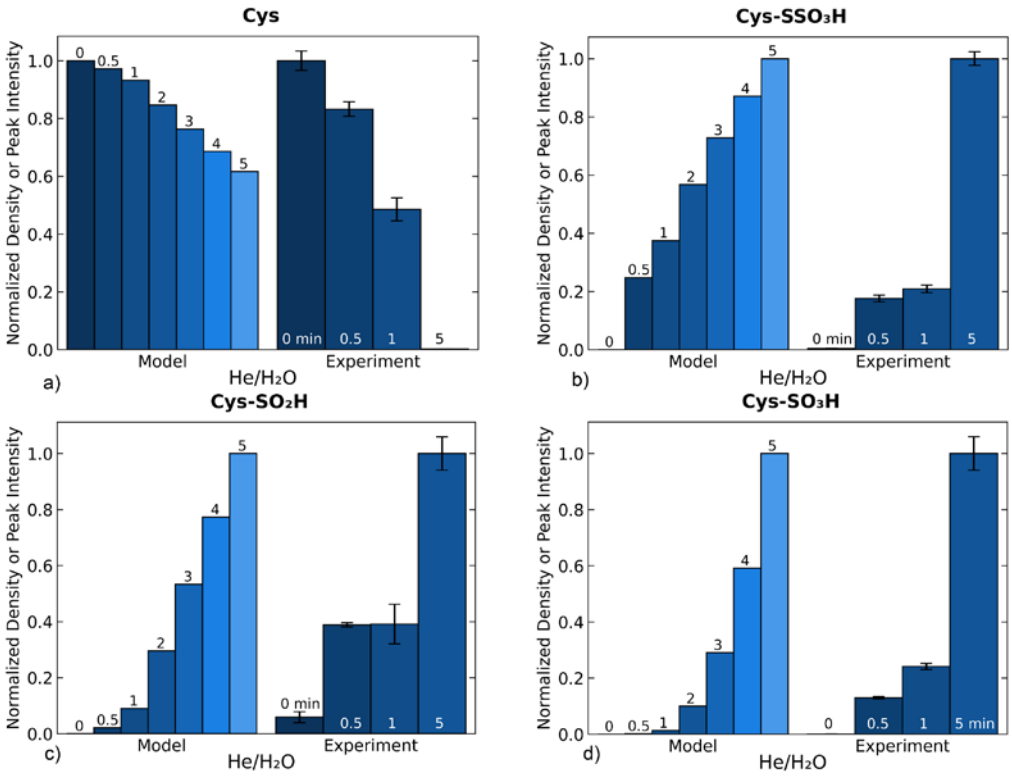

Figure 5.3. Comparison of trends in (a) native cysteine depletion and (b-d) cysteine oxidation product formation between model and experiments for the COST-jet sustained in a He/H_2O = 99.75/0.25 gas mixture as a function of plasma exposure time. Values (model-predicted number density or mass spectrometry-produced peak intensity) have been normalized to 1.

after 2-3 minutes of plasma treatment, which is consistent with the results by Stapelmann et al. [39]. The model also accurately predicts the trend in generation of Cys-SO_2H, which forms over the first minute of plasma treatment, then is depleted over the next four minutes as Cys-SO_2H is converted to Cys-SO_3H by reactions with solvated ROS.

When exposed to the COST-jet sustained in He/H_2O, Cys-SO_3H and Cys-S-SO_3H are also formed, though neither are formed preferentially. Unlike treatment by the COST-jet sustained in He/O_2, where Cys-SO_2H is eventually depleted, Cys-SO_2H forms continuously when using the He/H_2O mixture. This result indicates that a higher fluence of plasma-produced ROS, O in particular, is needed to promote conversion to Cys-SO_3H. The fluences of RONS required to

produce cysteine oxidation products are discussed in Section VII. Though not shown in Fig. 5.3, cystine (Cys-S-S-Cys) is preferentially formed by treatment with the COST-jet sustained in He/H_2O. Hydrogen is abstracted from the thiol (-SH) site of the cysteine molecule to create a thiol radical site. In the absence of significant densities of ROS, and especially at early treatment times, two thiol sites will react to form Cys-S-S-Cys.

5.5 Base Case Plasma and Liquid Species Properties

The reactor configuration used for the results in this section is based on the experimental setup discussed in Section 5.2. The COST-jet sustained in He/O_2 has been extensively characterized [32]. Typical O atom densities for 0.2-1.0% O_2 admixtures have been reported to be between 1 and 3×10^{15} cm^{-3} while O_3 densities increase from 1×10^{14} cm^{-3} to 1×10^{15} cm^{-3} as the percent of O_2 increases [47–49]. The COST-jet is most often operated in a power range between a few hundred milliwatts and a few watts, which yields electron densities on the order of a few times 10^{10} cm^{-3} [50].

The model considers the radio-frequency (RF) powered, 1 atm COST-jet operated in $He/N_2/O_2$ mixtures with a constant power of 750 mW. The base case is 1010 sccm of a feed gas consisting of $He/N_2/O_2$ = 99/0.8/0.2 with a 1 ppm water impurity. The gas flows through the top of the reactor and moves vertically down the length of the reactor (3 cm) and across the gap between the reactor and liquid (4 mm). The gap between the powered and grounded electrode is 1 mm and the width of the electrodes is 1 mm, yielding a plasma with a cross-sectional area of 1 mm^2. The plasma is assumed to be uniform over the electrode cross-sectional area. There is a 4 mm gap between the reactor outlet and the liquid surface in which the reactor effluent comes into contact with ambient air. In this plug flow approach, the entrainment of ambient air into the effluent is approximated by adding humid air ($N_2/O_2/H_2O$ = 79/20/1) with a flow rate of 10 sccm

into the mixture as the gas exits the discharge channel.

The treated liquid is a 1 mm thick solution of water containing 100 µg/ml cysteine (5×10^{17} cm^{-3} cysteine molecules). The liquid initially has a pH = 7 and is initially saturated with atmospheric gases.

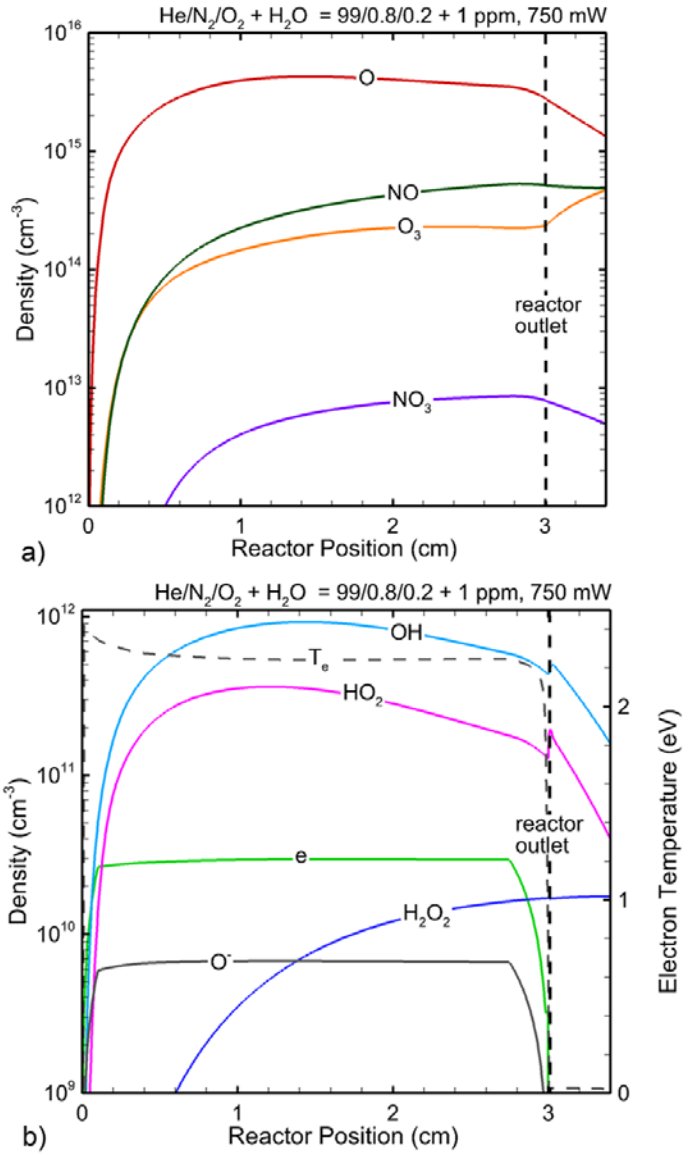

Figure 5.4. Base case plasma properties for COST-jet operating in 1010 sccm $He/N_2/O_2$ = 99/0.8/0.2 with 750 mW power deposition. (a) ROS and RNS. (b) Electron temperature and density, and ROS.

5.5.1 Plasma Properties

The densities of gas phase species predicted by the model for the base case conditions are shown in Fig. 4. The average electron density in the plasma channel predicted by the model is 3 × 10^{10} cm^{-3} and the average electron temperature is 2.2 eV. (Here, electron temperature is 2/3 of the average electron energy, obtained from the electron energy distribution that in most cases is non-Maxwellian.) These values are consistent with experimentally measured values for the COST-jet sustained in He/O_2 [50]. RONS including O, O_3, NO, OH, and HO_2 are produced in the powered region and exit the reactor at 3.0 cm to mix with ambient air in the gap above the liquid. Atomic oxygen is formed predominantly through electron impact dissociation of molecular oxygen or through dissociative excitation transfer of O_2 or excited state O_2 with excited state N_2. The predicted atomic oxygen density (4 × 10^{15} cm^{-3}) is consistent with experimentally reported values of atomic oxygen measured in the He/O_2 COST-jet [48,49]. O_3 (2 × 10^{14} cm^{-3}) is formed primarily through three-body reactions of O and O_2. The predominant nitrogen-containing RONS is NO (4 × 10^{14} cm^{-3}). NO is formed primarily through electron impact excitation of molecular nitrogen (N_2^*), followed by reaction with O to produce N^* and NO. OH (8 × 10^{11} cm^{-3}), HO_2 (2 × 10^{11} cm^{-3}), and H_2O_2 (1 × 10^{10} cm^{-3}) are produced in the plasma region as a result of the small water

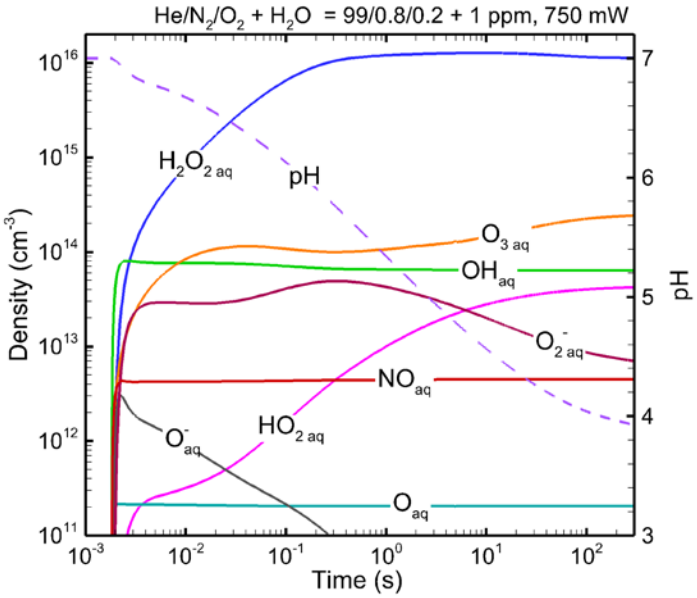

Figure 5.5. Base case aqueous densities for COST-jet operating in 1010 sccm $He/N_2/O_2$ = 99/0.8/0.2, 750 mW treating a 100 µg/ml cysteine (5 × 10^{17} cm^{-3} cysteine molecules) solution.

impurity in the feed gas.

The densities of OH and HO_2 increase at the reactor outlet as the plasma effluent comes into contact with humid air, then decrease in the air gap due to interactions with each other to form H_2O and O_2. O_3 also increases in the air gap as O is consumed in three-body reactions with O_2 whose density increases in the effluent due to mixing with the ambient air. The maximum reactivity that can be produced in the liquid due to gas phase RONS is ultimately a function of the fluence of the RONS incident onto the liquid surface over the time of exposure. Fluence (molecules/cm^2) is the time integral of the flux (molecules/cm^{-2}-s). The maximum density of RONS in the liquid is dependent upon the flux ($cm^{-2}s^{-1}$) of gas phase RONS delivered to the liquid surface integrated over time, or the fluence (cm^{-2}), of gas-phase RONS. The fluences of gas phase RONS onto the water that correspond to the densities shown in Fig. 4 for our conditions after five minutes of plasma treatment are: 1.4×10^{13} cm^{-2} H_2O_2, 5.0×10^{13} cm^{-2} HO_2, 2.6×10^{14} cm^{-2} OH, 9.1×10^{14} cm^{-2} O_3, 3.6×10^{17} cm^{-2} NO, and 4.8×10^{18} cm^{-2} O.

5.5.2 Liquid RONS Production

Densities of aqueous species produced during five minutes of treatment by the COST-jet sustained in $He/O_2/N_2$ are shown in Fig. 5.5. Plasma produced RONS solvate into the liquid according to the Henry's Law equilibrium constants (i.e., species having higher Henry's law constants will solvate more readily than those with lower Henry's law constants). Solvation is primarily responsible for the production of reactive aqueous neutrals such as OH_{aq}, NO_{aq}, and O_{aq}. Solvation and subsequent saturation of OH_{aq}, NO_{aq}, and O_{aq} occur quickly (about 2 ms) after liquid exposure to the plasma effluent while other species such as H_2O_{2aq}, O_{3aq}, and HO_{2aq} require longer exposure (0.5 s – 1 min) to saturate. Species, that as a result of aqueous reactions, become supersaturated will desolvate into the gas phase. In addition to solvation, H_2O_{2aq} and O_{3aq} are

formed through aqueous reactions of solvated ROS.

$$OH_{aq} + OH_{aq} \rightarrow H_2O_{2aq} \quad (5.6)$$

$$HO_{2aq} + HO_{2aq} \rightarrow H_2O_{2aq} \quad (5.7)$$

$$H_3O^+_{aq} + HO^-_{2aq} \rightarrow H_2O_{2aq} + H_2O_{aq} \quad (5.8)$$

$$HO^-_{2aq} + H_2O_{aq} \rightarrow H_2O_{2aq} + OH^-_{aq} \quad (5.9)$$

$$H_{aq} + HO_{2aq} \rightarrow H_2O_{2aq} \quad (5.10)$$

$$O_{aq} + O_{2aq} \rightarrow O_{3aq} \quad (5.11)$$

H_2O_{2aq} and O_{3aq} are considered long-lived species as they are relatively stable (thermal decay occurs, but on timescales longer than the studied treatment time). Long-lived species can produce more reactive products over their lifetimes, either in reactions with other RONS or by slow-decay processes.

(H)NO_x species are some of the most abundant plasma-produced RONS that solvate into the liquid. The dominant gas phase RONS are NO (5×10^{14} cm^{-3}) and HNO_2 (8×10^{12} cm^{-3}). NO_{aq} and NO_{2aq} reach saturation within milliseconds of treatment time. NO_{xaq} species undergo reactions with H_2O_{aq} to form HNO_{xaq}, which hydrolyzes to form $H_3O^+_{aq}$.

$$NO_{x,aq} + H_2O_{aq} \rightarrow HNO_{xaq} + OH_{aq} \quad (5.12)$$

$$HNO_{xaq} + H_2O_{aq} \rightarrow H_3O^+_{aq} + NO^-_{xaq} \quad (5.13)$$

The increase in $H_3O^+_{aq}$ results in a decrease of the model-predicted pH from 7 to 3.9 over the course of the five-minute treatment for the COST-jet sustained in He/O_2/N_2, whereas mixtures not containing N_2 tend to produce smaller changes in pH [51,52]. Cysteine is stable within the pH range studied in this work and so pH does not play a direct role in the modification of the cysteine molecule [53]. However, the pH tolerances of the target molecule and surrounding system should

be taken into consideration when designing plasma devices for biological treatments.

5.6 Formation of Cysteine Oxidation Products

In this section, the model-predicted densities of cysteine oxidation products after plasma treatment will be discussed while varying the gap distance between the reactor exit and the liquid and the inlet gas composition. A comparison between model results and experimental mass spectroscopy measurements will be presented to motivate the addition of N_2 to the gas inlet.

5.6.1 Base Case Modifications to Native Cysteine

Plasma jets in general, and the COST-jet in particular, potentially offer precise control over RONS delivered to a target by varying the inlet gas composition [54,55]. For example, addition of N_2 to the COST-jet sustained in He/O_2 increases the flux of plasma-produced $(H)NO_x$ species reaching the liquid while decreasing the inventory of O_3 formed in the plasma. However, the effects of plasma-produced $(H)NO_x$ on the modification of biological targets in plasma treated solutions is still unclear. Experiments described in Section 5.2 were performed to help illuminate the consequences of N_2 addition to the inlet gas on cysteine oxidation product formation. Mass spectrometry was performed and used for further validation of the reaction mechanism for the tri-gas conditions. Normalized model-produced densities of cysteine and several oxidation products for the base case discussed in Section 5.5 are shown in Fig. 5.6 alongside normalized mass spectrometry peak intensity measurements from experiments also performed under the base case conditions in Fig. 5.6.

The model-produced aqueous number densities of cysteine and its stable derivatives are shown in Fig. 5.7 as a function of plasma treatment time. The model predicts major cysteine depletion occurs after 10-20 seconds of plasma treatment. The model is initialized with the only

organic molecule in the water being cysteine while the experiments naturally include cystine or other unstable products that may revert back to cysteine as a result of plasma treatment. This likely explains the differences in the severity of depletion of the native cysteine between the model and the experiments. Cystine (Cys-S-S-Cys) and Cys-SSO_3H are the first stable products to form with significant number densities ($> 10^8$ cm^{-3}).

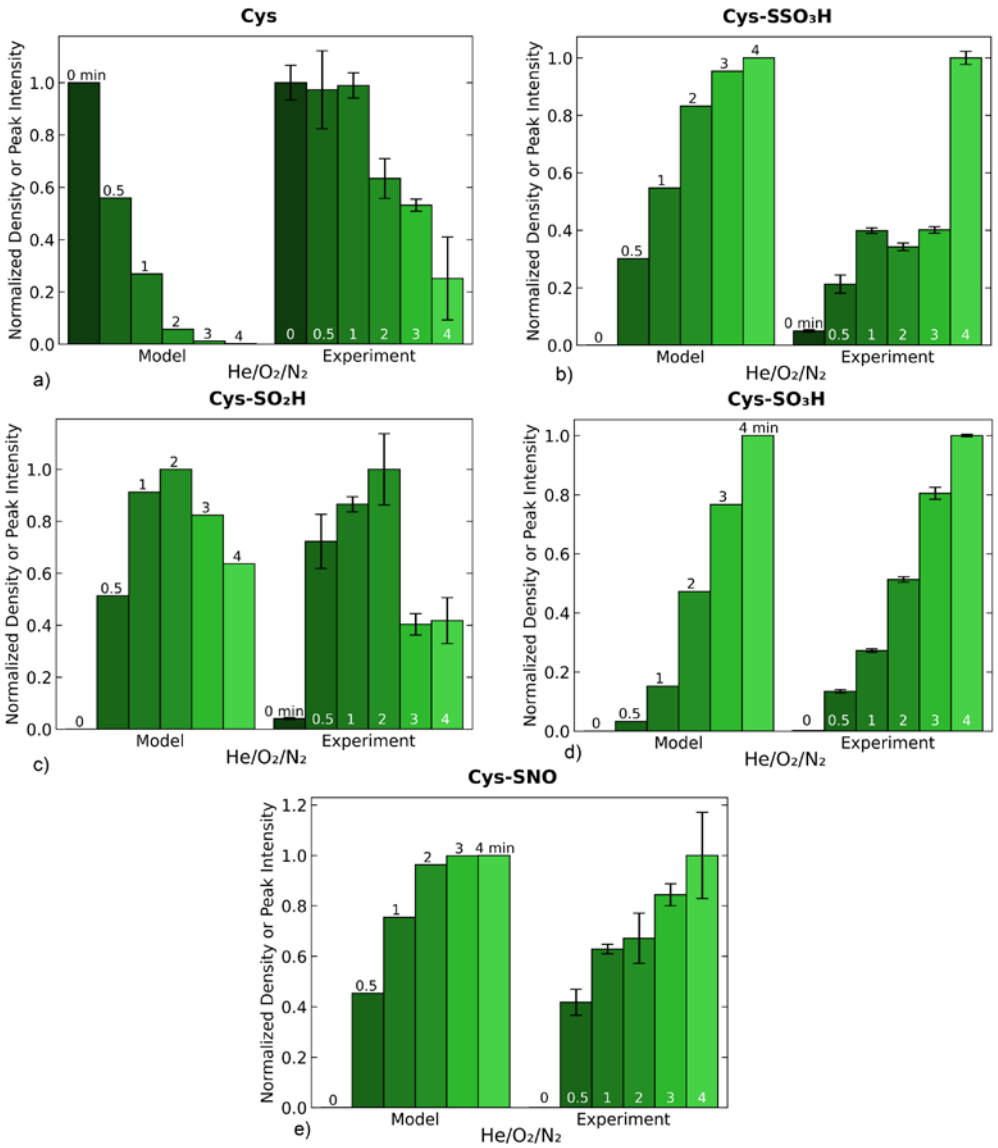

Figure 5.6. Comparison of trends in cysteine oxidation product formation between model and experiments for the treatment by the COST-jet sustained in $He/N_2/O_2$ = 99/0.8/0.2 gas mixture as a function of exposure time. Values (model-predicted number density or mass spectrometry-produced peak intensity) have been normalized to 1.

Short-lived O and OH solvate into the liquid and their in-water densities reach saturation within a few ms. These saturation values are not a classical Henry's law equilibrium but rather an equilibrium between the rates of solvation of these species (a source) and their reaction with the organic molecules in solution (a sink). These ROS abstract H atoms from the cysteine thiol (-SH)

group to form thiol radicals. Cystine initially forms from two thiol radicals, as densities of RONS, including negative ions and long-lived species such as H_2O_{2aq}, O_{3aq}, HO_{2aq}, and NO_{xaq} increase by solvation or through aqueous reactions;

$$Cys + O_{aq} \rightarrow Cys - S^{\bullet} + OH_{aq} \tag{5.14}$$

$$Cys + OH_{aq} \rightarrow Cys - S^{\bullet} + H_2O_{aq} \tag{5.15}$$

$$Cys + HO_{2aq} \rightarrow Cys - S^{\bullet} + H_2O_{2aq} \tag{5.16}$$

$$Cys - S^{\bullet} + Cys - S^{\bullet} \rightarrow Cys - S - S - Cys \tag{5.17}$$

Within the first few milliseconds of plasma treatment, Cys-SSO_3H also becomes a major product.

Several mechanisms for the formation of Cys-SSO_3H from cysteine have been proposed [56,57]. The formation of Cys-SSO_3H may occur through cleavage of the SH group by radical attack and subsequent oxidations by SH-derived species (e.g., $SO_2^-{}_{aq}$, $SO_3^-{}_{aq}$) at the radical site, or through the cystine oxidation-reduction cycle. The mechanism for Cys-SSO_3H formation in this work is based on that proposed by Wende et. al [25]. Cys-SSO_3H is represented in the mechanism as Cys-SSO_3^-, which is conventional in oxidation-reduction chemistry. We assume that Cys-SSO_3^- and Cys-SSO_3H are quickly reversible in solution and use the two representations interchangeably from this point forward. The Wende mechanism suggests that in addition to abstracting H from the thiol group, O_{aq} and OH_{aq} may also remove the entire SH moiety from the cysteine molecule. SH undergoes a replacement reaction with O_{2aq} to form $SO_2^-{}_{aq}$, which participates in charge exchange with O_{2aq} to form SO_{2aq}. $SO_{2\,aq}$ then hydrolyzes with H_2O_{aq} to form $HSO_3^-{}_{aq}$.

$$Cys + OH_{aq} \rightarrow Cys^{\bullet}(-2H) + SH + H_2O_{aq} \tag{5.18}$$

$$Cys + O_{aq} \rightarrow Cys^{\bullet}(-2H) + SH + OH_{aq} \tag{5.19}$$

$$SH + O_{2aq} \rightarrow SO^-_{2\,aq} + H^+_{aq} \tag{5.20}$$

$$SO^{-}_{2\,aq} + O_{2aq} \rightarrow SO_{2aq} + O^{-}_{2aq} \quad (5.21)$$

$$SO_{2aq} + H_2O_{aq} \rightarrow HSO^{-}_{3aq} + H^{+}_{aq} \quad (5.22)$$

$$Cys + HSO^{-}_{3aq} \rightarrow Cys - SSO^{-}_{3} + H_{2aq} \quad (5.23)$$

$$Cys - S - S - R + HSO^{-}_{3aq} \rightarrow Cys - SSO_3^{-} + Cys^{\bullet}(-H) \quad (5.24)$$

After about 4 ms, $HSO_3^-{}_{aq}$ forms with high enough number density (a few times 10^{10} cm^{-3}) to produce Cys-SSO_3H through reaction with either cysteine or Cys-S-S-Cys. Cys-SSO_3H is the primary stable oxidation product for the first 20 seconds of plasma treatment, after which production of sulfonic acid (Cys-SO_3H) dominates.

While Cys-SSO_3H and cystine are being formed, the first oxidation state of the thiol radical, sulfenic acid (Cys-SOH), is formed through a direct reaction involving OH_{aq} or a series of indirect reactions involving both OH_{aq} and O_{3aq}. The density of O_{3aq} saturates about ten times more slowly than OH, which saturates within 2 ms, as aqueous reactions contribute to the accumulation of O_{3aq}. O_3 has a saturated aqueous density of around 1×10^{14} cm^{-3} while OH has a saturated aqueous density of around 7×10^{13} cm^{-3}. A density of 2×10^{8} cm^{-3} Cys-SOH forms by the time the density of OH_{aq} has reached saturation, after which the rate of formation of Cys-SOH briefly matches the rate of

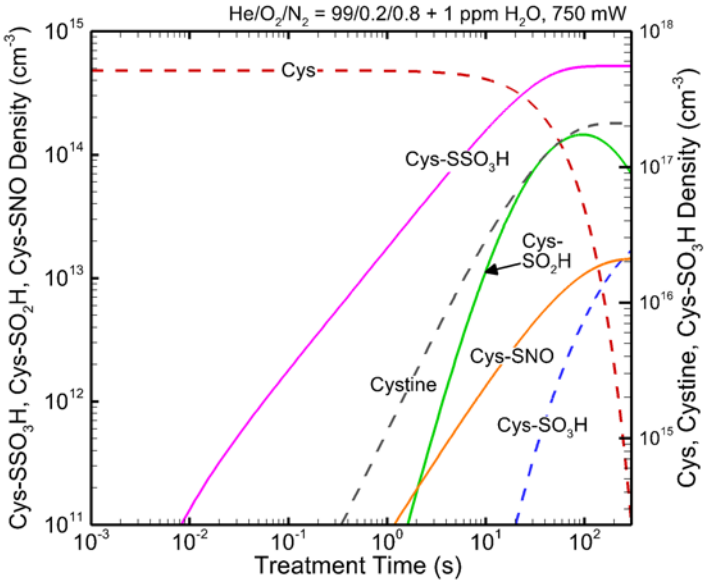

Figure 5.7. Model-produced number densities of cysteine oxidation products as a function of COST-jet treatment time for the base case conditions. 1010 sccm $He/N_2/O_2$ = 99/0.8/0.2, 750 mW.

accumulation of O_{3aq} (from 2 – 20 ms).

At early treatment times (< a few ms), before saturation of most other RONS, the direct pathway to Cys-SOH formation (Eq. 5.2) is likely dominant. Direct OH_{aq} addition to cysteine is slow compared to the formation of the Cys-SOH_2 intermediate and most other competing reactions that also consume OH_{aq}. At later times, when most other RONS are saturated, the indirect pathway for Cys-SOH formation is likely dominant.

$$Cys - S^{\bullet} + OH_{aq} \rightarrow Cys - SOH \tag{5.25}$$

$$Cys + OH_{aq} \rightarrow Cys - SOH_2 \tag{5.26}$$

$$Cys - SOH_2 + O_{3aq} \rightarrow Cys - SOH + O_{2aq} + OH_{aq} \tag{5.27}$$

Cys-SOH forms continuously for the first 1.5 minutes of treatment time before depletion starts to occur faster than formation as Cys-SOH is converted to more stable, higher oxidation products.

Conversion from Cys-SOH to sulfinic acid (Cys-SO_2H) requires the addition of OH_{aq} to Cys-SOH to form the intermediate product Cys-$S(OH)_2$. Subsequent reactions with O_{aq}, O^-_{aq}, OH_{aq}, or O_{2aq} convert the Cys-$S(OH)_2$ to Cys-SO_2H.

$$Cys - SOH + OH_{aq} \rightarrow Cys - S(OH)_2 \tag{5.28}$$

$$Cys - S(OH)_2 + O_{aq} \rightarrow Cys - SO_2H + OH_{aq} \tag{5.29}$$

$$Cys - S(OH)_2 + O^-_{aq} \rightarrow Cys - SO_2H + OH^-_{aq} \tag{5.30}$$

$$Cys - S(OH)_2 + OH_{aq} \rightarrow Cys - SO_2H + H_2O_{aq} \tag{5.31}$$

$$Cys - S(OH)_2 + O_{2aq} \rightarrow Cys - SO_2H + HO_{2aq} \tag{5.32}$$

Significant quantities of Cys-SO_2H form within 20 ms of the start of plasma treatment. Cys-SO_2H accumulates over the first two minutes of plasma treatment before conversion to Cys-SO_3H overtakes Cys-SO_2H production through reaction of Cys-SO_2H with O_{aq}, OH_{aq}, O_{2aq}, or

H_2O_{2aq}.

$$Cys - SO_2H + O_{aq} \rightarrow Cys - SO_3H \quad (5.33)$$

$$Cys - SO_2H + OH_{aq} \rightarrow Cys - SO_3H + H_{aq} \quad (5.34)$$

$$Cys - SO_2H + O_{2aq} \rightarrow Cys - SO_3H + O_{aq} \quad (5.35)$$

$$Cys - SO_2H + H_2O_{2aq} \rightarrow Cys - SO_3H + H_2O_{aq} \quad (5.36)$$

After 20 s of plasma treatment, Cys-SO_3H becomes the predominant stable oxidation product over Cys-SSO_3H. The model-predicted density of Cys-SO_3H after 5 minutes of plasma treatment is 2.4×10^{16} cm^{-3} and the density of Cys-SSO_3H after 5 minutes of plasma treatment is 5.2×10^{14} cm^{-3}. Cys-SO_3H is not an easily reversible product. In living organisms, formation of Cys-SO_3H is irreversible, though formation of Cys-SO_2H and Cys-SOH can be reversed [27,58]. This reversibility of lower oxidation states may contribute to lower densities of Cys-SOH and Cys-SO_2H in the experiments, especially at longer treatment times and under anaerobic conditions.

The oxidation of cysteine appears to be limited both by the step-wise nature of its oxidation pathways and by the hydrogen abstraction step. The hydrogen abstraction step is dependent on the solvation of fluxes of gas phase O and OH into the liquid. Cysteine oxidation product formation sensitivity to RONS production will be discussed in the following subsections.

5.6.2 Air Gap

The distance between the reactor outlet and the liquid surface can be used as a control parameter to tune the flux of RONS reaching the liquid. The gap is adjusted in the model by extending the length over which plug flow is calculated after power is turned off at the end of the 3 cm electrode length. To emulate ambient air mixing, air is introduced to the plasma effluent at 3 cm with a flow rate that is 1% of the total inlet flowrate. Increasing the gap increases the amount

of mixing between the COST-jet's effluent and the ambient air. The fluence of gas phase species onto the liquid and number densities of aqueous cysteine oxidation products after five minutes of treatment with the COST-jet sustained in the $He/N_2/O_2$ mixture are shown in Fig. 5.8. The densities of the aqueous species are normalized by their values for a gap of 10 mm to emphasize the trends with gap.

As the gap increases, the final number density of the cysteine increases (from 1×10^{13} cm^{-3} when the gap is 1 mm to 1×10^{16} cm^{-3} when the gap distance is 10 mm). This corresponds to a reduction in cysteine depletion from nearly 100% with a 1 mm gap to 49% for a gap of 10 mm. As the gap increases, air entrainment into the plasma effluent also increases. The fluence of plasma-produced short lived RONS onto the liquid decreases as reactive

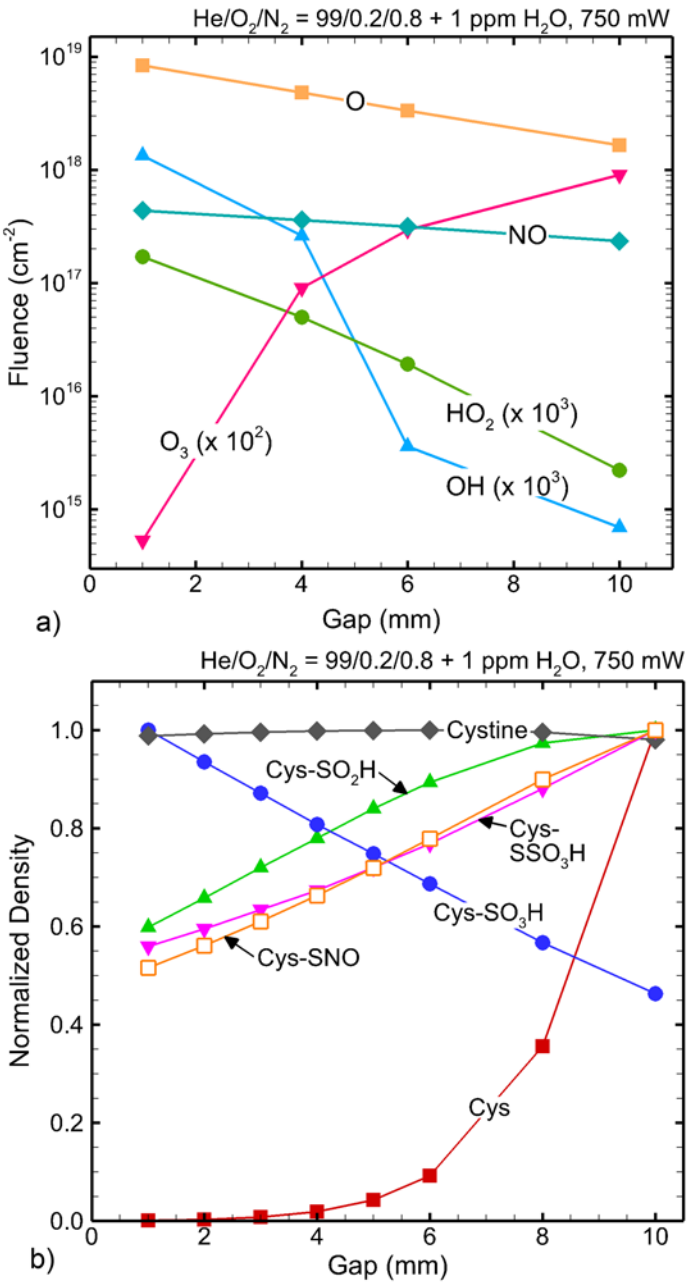

Figure 5.8. Reactant properties as a function of gap between nozzle and liquid. a) Fluences of select RONS onto the liquid and b) normalized cysteine oxidation product densities after five minutes of plasma treatment by driven the COST-jet sustained in $He/N_2/O_2$.

species are converted into more stable species in the air gap. The fluence of short-lived RONS such as O that are primarily produced in the plasma are more sensitive to changes in the gap. There are less dramatic decreases in aqueous number densities as the gap increases for RONS that can be replenished by aqueous reactions, such as O_{3aq} and OH_{aq}. Increasing the gap from 1 mm to 10 mm results in a five times reduction in saturated O_{aq} density from 3.5×10^{11} cm^{-3} to 7×10^{10} cm^{-3}, whereas the reduction in OH_{aq} is only two times, from 8.6×10^{13} cm^{-3} to 3.6×10^{13} cm^{-3}. The O_{3aq} density is transient, and does not reach saturation, but has maximum values at the end of treatment time (3.6×10^{14} cm^{-3} for a 1 mm gap and 2×10^{14} cm^{-3} for a 10 mm gap). O_3 solvates into the liquid, but O_{3aq} can also be generated by aqueous reaction (Eq.5.11). O_{3aq} is consumed by reaction with intermediate cysteine oxidation products (reactions 13, 15, and 22 in Table 5.3) or by charge exchange with negative ions (Eq. 5.37) faster than it is produced by reactions with aqueous ROS for the first 6 - 7 seconds of plasma treatment time.

$$O_{3aq} + O_{2aq}^{-} \rightarrow O_{3aq}^{-} + O_{2aq} \tag{5.37}$$

The rate of consumption of O_{3aq} gradually decreases over the remaining treatment time (as intermediate cysteine products are converted to higher oxidation states) while the rate of production due to aqueous reactions is nearly constant (as O_{aq} and O_{2aq} saturate). At the end of the plasma treatment time, the rate of O_{3aq} production by aqueous reaction is nearly double the rate of $O_{3,aq}$ consumption. With the gas phase density of O_3 above the water being 5×10^{14} cm^{-3}, and a Henry's law constant of 0.3, the saturated aqueous density is 1.5×10^{14} cm^{-3}. So the in liquid production of O_{3aq} produces slightly super-saturated conditions that result in the desolvation of O_{3aq}.

Trends in oxidation resulting from varying gap can be extended to understanding the hierarchy of RONS' importance in the production of cysteine oxidation products. As the gap

increases from 1 mm to 10 mm, the final number density of Cys-SSO_3H increases from 4×10^{14} cm^{-3} to 8×10^{14} cm^{-3}, Cys-SO_2H increases from 5×10^{13} cm^{-3} to 9×10^{13} cm^{-3}, and Cys-SNO increases from 1×10^{13} cm^{-3} to 2×10^{13} cm^{-3}. The final number density of Cys-SO_3H decreases from 3×10^{16} cm^{-3} to 1×10^{16} cm^{-3}. Cys-SSO_3H formation requires O_{aq} or OH_{aq} for H abstraction, but subsequent reaction steps are driven by O_{2aq}. There is little change in the O_{2aq} density as gap distance increases due to its saturation, indicating that a reduction in short-lived aqueous ROS favors Cys-SSO_3H formation.

While not shown in Fig. 5.8, as it is not considered a stable product, the final number density of Cys-SOH also increases from 5×10^{15} cm^{-3} at 1 mm gap to 2×10^{16} cm^{-3} at 10 mm gap, though more Cys-SOH is produced in the 1 mm case than in the 10 mm case for the first 110 seconds of plasma treatment. The formation of Cys-SOH enables pathways to formation of higher order oxidation products. Cys-SOH formation is dependent on OH_{aq} and O_{3aq} (Eqs. 5.26-5.28) while its conversion to Cys-SO_2H requires O_{aq}, O^-_{aq}, OH_{aq}, or O_{2aq} (Eqs. 5.29-5.33). Further conversion to Cys-SO_3H (Eqs. 5.34-5.37) requires O_{aq}, OH_{aq}, O_{2aq}, or H_2O_{2aq}. H_2O_{2aq} is a long-lived aqueous species whose saturated number density decreases from 1×10^{16} cm^{-3} to 7×10^{15} cm^{-3} as the gap increases from 1 mm to 10 mm.

As the fluences of short-lived ROS onto the liquid decrease with increasing gap, the formation of Cys-SOH and Cys-SO_2H, the first and second oxidation states, are not particularly sensitive to reduction of O_{aq}. However, as Cys-SO_2H fails to be converted to Cys-SO_3H at larger gaps, formation of the third oxidation state does become sensitive to O_{aq} concentration, H_2O_{2aq} concentration, or both. Based on gas phase analogues and agreement with experiment, the reaction rate coefficient of H_2O_{2aq} with Cys-SO_2H (Eq. 5.36) is 3-6 orders of magnitude smaller than reactions of Cys-SO_2H with other ROS (O_{aq}, OH_{aq}). As a result, Cys-SO_3H formation is likely

most sensitive to the O_{aq} density. However, as Cys-SO_3H is the most abundant oxidation product under all conditions, fluences of O on the order of a few times 10^{18} cm^{-2} are sufficient to promote full oxidation. Further studies are needed to decouple the effects of short-lived and long-lived species on the formation of the Cys-SO_3H.

Cys-SNO formation is dependent on the presence of NO_{aq}. As the gap increases from 1 mm to 10 mm, there is a small increase in the saturated density of NO_{aq} from 4×10^{12} cm^{-3} to 5×10^{12} cm^{-3} though the fluence of NO decreases (from 4×10^{17} cm^{-2} at 1 mm to 2×10^{17} cm^{-2} at 10 mm). Higher air entrainment in the larger gap leads to conversion of NO to HNO_x in reactions with H and a third body. HNO_x hydrolyzes after solvation to regenerate NO_{aq} (Eqs. 5.12-5.13), which contributes to the slight rise in NO_{aq} density as the air gap increases. As the increase in NO_{aq} concentration between the smaller and larger gap is not large, it is more likely that as the gap increases, the reduction in O, OH, and NO fluences, and the resulting aqueous ROS concentrations, contribute to a decrease in competition for reactions at the thiol radical site and a higher rate of formation of Cys-SNO. These trends suggest that increasing the air gap could be a control mechanism if nitrosylated cysteine is the desired product.

Cystine is the only stable product that is not significantly affected by changing the gap. Cystine forms quickly after initial H abstraction from the thiol group (Eq. 5.14-5.16), which indicates that the flux of RONS from the plasma to the liquid is sufficient to initiate cysteine oxidation for all gaps. This result suggests that fluences of RONS on the order of 10^{18} cm^{-2} are greater than needed to promote H abstraction , though the percentage depletion of the initial cysteine molecule may decrease at larger gaps. As such, gap size can be used as a control parameter to select for desired cysteine oxidation products. However, if complete conversion of native cysteine to oxidized products is desired, gap size may not be the most effective operating

parameter.

5.6.3 Oxygen Inlet Flowrate

To determine the consequences of ROS fluxes produced by the He/N_2/O_2 CO ST-jet on the formation of cysteine oxidation products, the inlet mole fraction of oxygen was varied while keeping the inlet mole fraction of nitrogen (f_{N2} = 0.8%) and the total inlet flow rate (1010 sccm) constant. The gas-phase densities of a selection of RONS as a function of position in the reactor (and gap) are shown in Fig. 5.9 for oxygen inlet flow rates from 1 – 30 sccm, corresponding to O_2 mole fractions of 0.1% – 3%.

As oxygen inlet flow rate increases from 1 sccm (f_{O2} = 0.1%) to 8 sccm (f_{O2} = 0.8%) there is an increase in gas-phase RONS production. O and NO have maximum densities of 5.6 × 10^{15} cm^{-3} and 6 × 10^{14} cm^{-3} for f_{O2} = 0.1%. For O_2 inlet mole fractions higher than 0.1%, the densities of O and NO begin to decrease as O is consumed by three-body reactions in favor of O_3 production. There is a monotonic increase

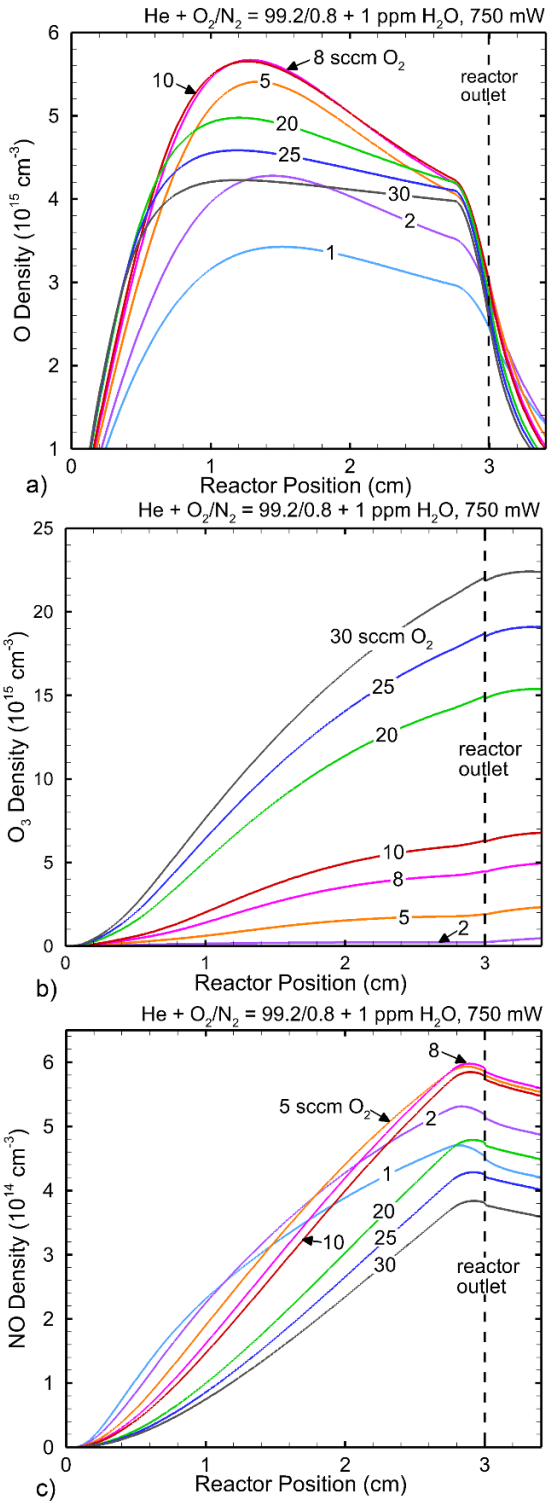

Figure 5.9. Densities of plasma-produced RONS as a function of O_2 position in the reactor and gap, and O_2 flow rate. a) O, b) O_3 and c) NO.

in O_3 production as O_2 inlet flow rate increases. As the level of water impurity is kept constant, the amount of OH produced in the gas-phase is not greatly affected.

The smallest density of O is produced when the inlet oxygen mole fraction is $f_{O2} = 0.1\%$ and the smallest density of NO is produced when $f_{O2} = 3\%$. At low flow rates under low power conditions where the fractional dissociation of O_2 is low, there is simply not enough O_2 in the inlet to produce high densities of O. At high inlet O_2 fractions, the consumption of O by three-body processes competes with the consumption of O by reactive nitrogen species to form NO. To maximize both O and NO production in the gas phase, the inlet O_2 fraction must be high enough to produce sufficient O by dissociation, but low enough so that losses of O to O_3 are not dominant.

Although the highest density of O is produced in the gas-phase when the O_2 inlet mole fraction is $f_{O2} = 0.8\%$, the highest density of O_{aq} (2×10^{11} cm^{-3}) occurs when the O_2 inlet fraction is $f_{O2} = 0.2\%$. For these conditions, O_2 mole fractions higher than 0.2% result in significant consumption of O in favor of O_3 production in the air gap. The highest densities of OH_{aq} (6.4×10^{13} cm^{-3}) and H_2O_{2aq} (1.1×10^{16} cm^{-3}) are also produced at 0.2% inlet O_2. Losses of NO are not as large as loss of O in the air gap and so the highest NO_{aq} density (5.5×10^{12} cm^{-3}) occurs at $f_{O2} = 0.8\%$, when the gas-phase NO production is highest.

Fluences after five minutes of plasma treatment of select RONS that are responsible for the formation of cysteine oxidation products are shown in Fig. 5.10a for different inlet O_2 fractions. The densities of cysteine and its oxidation products after five-minutes of plasma treatment are shown in Fig. 5.10b. As O_2 inlet fraction increases, depletion of cysteine decreases from over 99% at the lowest O_2 fraction to about 84% at the highest O_2 fraction. Low O_2 inlet fractions yield higher fluences of RONS (O_{aq}, OH_{aq}, HO_{2aq}) that contribute to hydrogen abstraction from the thiol site (Eqs. 16-18). As the O_2 inlet fraction increases from 0.1% to 3%, the fluence of atomic O

decreases from 4.7×10^{18} cm^{-2} to 2.9×10^{18} cm^{-2} as O is consumed in favor of O_3. The maximum O fluence is 4.8×10^{18} cm^{-2} at f_{O2} = 0.2%. OH and HO_2 have maximum fluences of 1.5×10^{15} cm^{-2} and 1.7×10^{14} cm^{-2} for f_{O2} = 0.1%.

As O_2 inlet fraction increases from 0.1% to 0.8%, the fluence of O_3 increases by three orders of magnitude (2.5×10^{14} cm^{-2} to 1.9×10^{17} cm^{-2}) as increased density of O_2 leads to increased O_3 formation through three-body processes. At the same time, fluences of HO_2 and OH also suffer 2-3 orders of magnitude decreases. HO_2 is formed predominantly by third-body assisted reactions of H with O_2 in the gas phase. OH is formed predominantly in the gas-phase by single replacement reactions of HO_2 with O. As O_2 inlet increases and O and O_2 are depleted by O_3 production, HO_2 and OH production also decrease. Increasing O_2 inlet fraction has little effect on

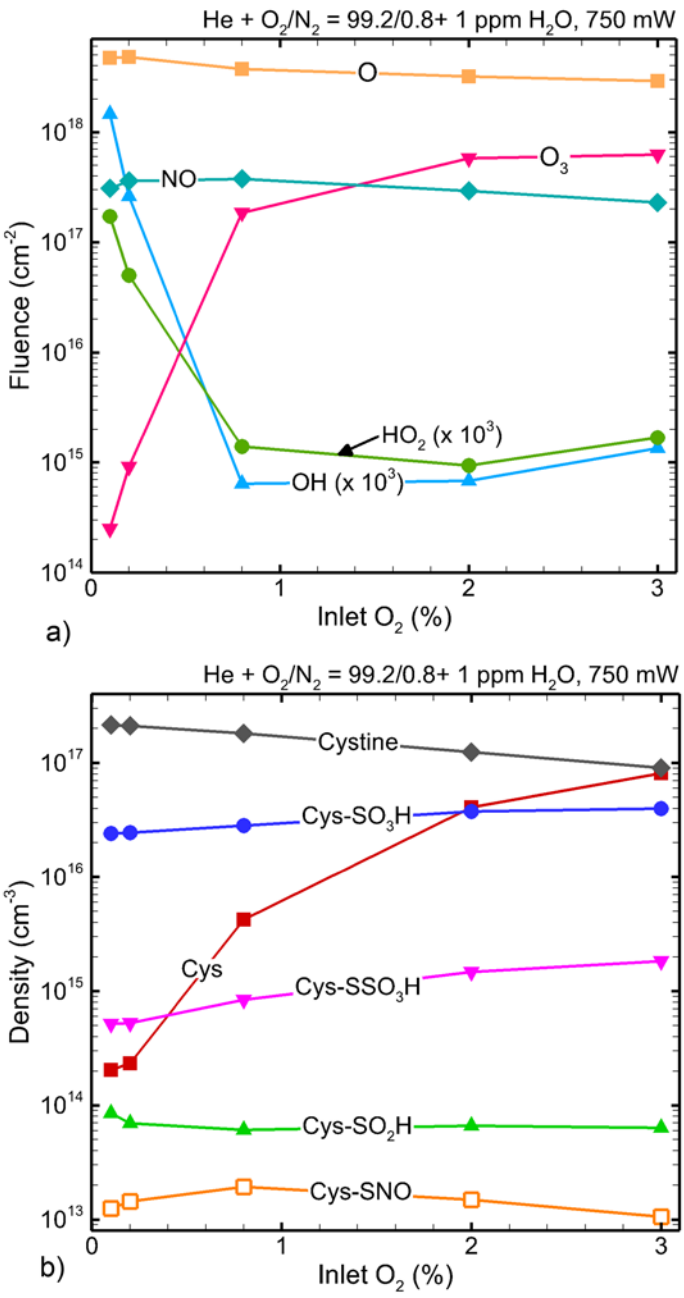

Figure 5.10. Reactant properties as a function of O_2 inlet fraction after five minutes of treatment by COST-jet sustained in He/N_2O_2. a) Fluences of select ROS into liquid and b) cysteine oxidation products.

the fluence of NO (3.1×10^{17} cm^{-2} at 0.1% O_2 and 2.3×10^{17} cm^{-2} at 3% O_2), which indicates that the production of NO is limited by the inlet fraction of N_2 under these low power conditions.

With an increase in O_2 inlet fraction, the fluence of O_3 onto the liquid increases. There is a higher rate of formation of Cys-SOH through the intermediate product Cys-SOH_2, which regenerates O_{2aq} and OH_{aq} from O_{3aq} (Eq. 5.27). OH_{aq} converts Cys-SOH to Cys-SO_2H (Eq. 5.28). When the fluence of OH to the liquid decreases (with increasing O_2 inlet fraction), Cys-SOH is not converted to Cys-SO_2H as readily. However, OH fluences of at least 6×10^{11} cm^{-2} are sufficient to promote formation of the second oxidation state with densities on the order of 10^{14} cm^{-3}.

Though there is a decrease in Cys-SO_2H production from the lowest inlet O_2 fraction to the highest, there is an increase in final Cys-SO_3H density (2.4×10^{16} cm^{-3} at f_{O2} = 0.2% to 3.9×10^{16} cm^{-3} at f_{O2} = 3%). Though the fluence (and aqueous production) of O and OH suffer at high O_2 inlet fractions, Cys-SO_2H can also be converted to Cys-SO_3H by O_{2aq} and H_2O_{2aq} (Eqs. 5.36-5.37). Increasing O_2 inlet fraction will monotonically increase O_2 fluence and decrease H_2O_2 fluence. Though the fluences of O, OH, and H_2O_2 are reduced, the increase in O_2 fluence and subsequent increase in generation of O_{2aq} is sufficient to sustain conversion to the final oxidation product. ROS (O_{aq}, OH_{aq}) that originate in the liquid rather than the plasma have some contribution to the formation of Cys-SO_3H [46].

The Cys-SSO_3H formation pathway also requires O_{2aq} (Eqs. 5.18-5.24). As the densities of other aqueous RONS (O_{aq}, OH_{aq}) decrease with increasing inlet O_2, formation of Cys-SSO_3H becomes more viable due to increasing densities of O_{2aq}. Reduction in RONS concentrations also reduces competition between reactions resulting in thiol radical sites (Eqs. 5.14-5.16) and reactions of the native cysteine molecule to form cystine (Eq. 5.17). The final density of Cys-SSO_3H is 5.2

$\times 10^{14}$ cm^{-3} for f_{O2} = 0.2% and 1.8×10^{15} cm^{-3} for f_{O2} = 3%.

As Cys-SNO formation is dependent upon NO_{aq} (reaction 36 in Table 5.3), production of Cys-SNO is expected to be highest when the NO_{aq} production is highest (f_{O2} = 0.8%, when the NO fluence is also highest). The final Cys-SNO density is 1.9×10^{13} cm^{-3} when f_{O2} = 0.8% and 1.4×10^{13} cm^{-3} when f_{O2} = 0.2% (base case conditions). Cys-SNO production suffers at higher O_2 inlet fractions, though it is not as greatly affected by increasing O_2 flow rate as other oxidation products. This lack of sensitivity results from the fluence of NO not being as greatly affected by changing O_2 inlet fraction when the N_2 inlet fraction is held constant. As the rate coefficient for the formation of Cys-SNO at a thiol radical site is 2-3 orders of magnitude smaller than the rate coefficient of other oxidation products with the thiol radical site (reaction 36 in Table 5.3), increased Cys-SNO production likely requires NO fluences to be orders of magnitude higher. However, NO fluences on the order of a few times 10^{17} are sufficient to produce Cys-SNO with densities on the order of 10^{13} cm^{-3}.

Cystine production is reduced as inlet O_2 increases (2.1×10^{17} cm^{-3} f_{O2} = 0.1% to 9×10^{16} cm^{-3} at f_{O2} = 3%). At f_{O2} = 0.2%, when O_{aq} and OH_{aq} densities are highest (and O fluence is highest), thiol radical production occurs most readily by reaction of cysteine with O_{aq} and OH_{aq} (Eqs.5.14 and 5.15). When densities of thiol radical sites are high, the fast conversion of two thiol radical sites to cystine occurs more quickly than other ROS can react to form oxidation products (Eq. 5.17). When fluences of ROS are reduced, the production of cystine decreases. Less RONS are available to participate in H abstraction, resulting in a lower density of thiol radical sites. Competition between RONS reactions that form oxidation products and the near immediate reaction of two thiol radical sites to form cystine is reduced due to the lower density of thiol radical sites. More thiol radical sites can be oxidized. The production of Cys-SO_3H is increased due to

the increase in O_{2aq} discussed above, though depletion of the native cysteine molecule is reduced at higher O_2 inlet fractions. Total fluences of H-abstracting RONS on the order of 10^{18} cm^{-2} are sufficient to promote H-abstraction that results in at least 84% depletion of the native cysteine molecule.

Control of hydrogen abstraction from cysteine is critical if oxidation products are preferred over the formation of cystine. If full conversion of the cysteine to oxidation products is desired, lower fluences of plasma-produced RONS for longer treatment times may be preferable. If nitrosylated products are also desired, the gas-phase production of NO should be maximized while also controlling the rate of thiol radical site formation.

5.6.4 Nitrogen Inlet Fraction

N_2 inlet fraction was varied (f_{N2}, from 0% – 5%) while holding the O_2 inlet fraction (f_{O2} = 0.2%) and the total inlet flow rate (1010 sccm) constant to investigate the consequences of RNS production on cysteine oxidation product formation. Of special interest here is the formation of the nitrosylated product, Cys-SNO. Maximizing NO additions to organic molecules may be desirable for applications in wound healing and cancer treatment. For example, the presence of NO during wound treatment lowers risk of infection and wound complication by promoting increased cell motility, providing anti-bacterial effects, and influencing gene regulation [59]. Final fluences of select RONS that contribute to the formation of cysteine oxidation products as a function of inlet N_2 fraction are shown in Fig. 5.11a. The final densities of cysteine oxidation products as a function of f_{N2} are shown in Fig. 5.11b.

Increasing the N_2 flow rate while holding the O_2 flow rate constant increases the density of NO_x species produced in the gas phase and decreases the fluence of ROS (O, OH, HO_2) onto the liquid. O is consumed by NO_x formation while formation of HO_2 and OH require O, O_2, and H_2O

dissociation products such as H. Under low power conditions, O_2 and N_2 will be preferentially dissociated over H_2O. The maximum density of gas-phase NO produced is about 5×10^{14} cm^{-3} for f_{N2} = 1% or higher. Increasing the N_2 fraction beyond 1% does not result in significant increases in the NO density when the O_2 inlet fraction is held constant at f_{O2} =0.2%. The fluence of NO to the liquid is also not terribly sensitive to f_{N2} (around 3×10^{18} cm^{-2} for all f_{N2}). At this flow rate, production of NO is limited by power and the production of O atoms and not the availability of N_2. The production of the Cys-SNO product is also not significantly increased for N_2 inlet fractions higher than 1%. The maximum Cys-SNO density after five minutes of plasma treatment is $1.5 – 1.6 \times 10^{13}$ cm^{-3}.

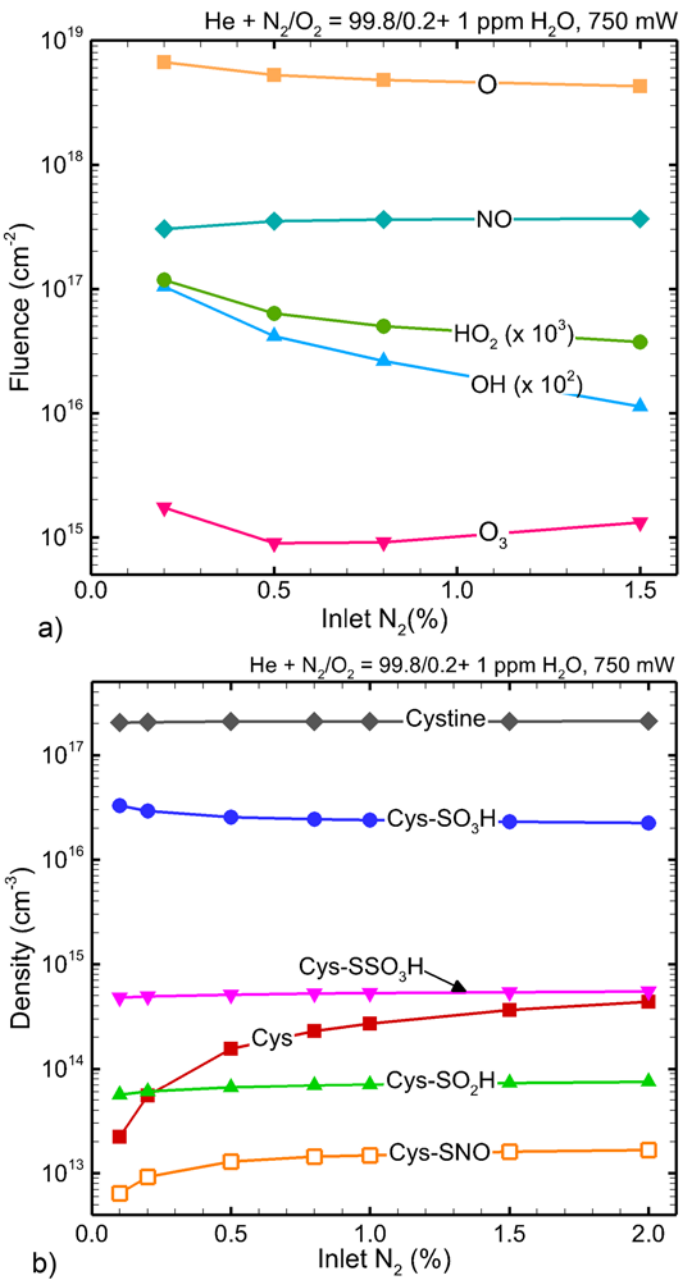

Figure 5.11. Reactant properties as a function of N_2 inlet fraction after five minutes of treatment by COST-jet sustained in He/N_2O_2. a) Fluences of select ROS into liquid and b) cysteine oxidation products.

Varying N_2 inlet fraction while holding O_2 inlet fraction constant results in more depletion

of the native cysteine molecule than when O_2 inlet fraction is varied. Varying N_2 inlet fraction results in near complete depletion of the native cysteine molecule for all N_2 inlet fractions, whereas only 84% of the cysteine molecule was depleted for large values of f_{O2}. When N_2 inlet fraction is varied with the O_2 inlet fraction being low, the production of O_3 by three-body processes does not deplete O. The fluence of O_3 stays low (around 10^{15} cm^{-2}) while the fluences of O, OH, and HO_2 remain high enough (5-6 × 10^{18} cm^{-2}) that hydrogen abstraction from the thiol group (Eqs. 16-18) dominates. The high density of thiol radical sites promotes rapid formation of cystine, resulting in a near constant density of cystine (1 × 10^{17} cm^{-3}) regardless of the N_2 inlet fraction. Since the fluences of ROS remain high as the inlet N_2 increases, and formation of oxidation products Cys-SO_2H, Cys-SO_3H, and Cys-SSO_3H depend only on ROS, not RNS, the final densities of these products are not sensitive to varying N_2 inlet fraction at constant O_2. The variation in these species is 6-7 × 10^{13} cm^{-3} Cys-SO_2H, 2-3 × 10^{16} cm^{-3} Cys-SO_3H, and 5 × 10^{14} cm^{-2} Cys-SSO_3H over the range of f_{N2} when there is 0.2% O_2 in the inlet.

Increasing f_{N2} beyond 0.2% does not result in a significant change in Cys-SNO production, as the fluence of NO (3 × 10^{18} cm^{-2}) is limited by the O_2 inlet fraction. As discussed in the previous section, NO fluences on the order of a few times 10^{17} cm^{-2} result in Cys-SNO densities on the order of 10^{13} cm^{-3}. Higher production of Cys-SNO requires higher NO fluence. Higher NO fluence could potentially be achieved by adjusting the N_2 inlet fraction and the O_2 inlet fraction together.

5.7 Conclusions

A reaction mechanism for the CAP treatment of cysteine in water was developed and applied to the investigation of cysteine oxidation and production of nitrosylated products using a global plasma- and liquid-chemistry model. The reaction mechanism was validated against experimental data for COST-jets sustained in He/H_2O and He/O_2 treating cysteine in water. Both

gas mixtures result in depletion of the native cysteine molecule while promoting full oxidation to Cys-SO_3H. As the presence of NO and its incorporation into oxidation products is often desirable for wound treatment applications, experiments that treated cysteine solution with a COST-jet sustained in He/N_2/O_2 mixtures were performed. Small amounts of nitrosylated Cys-SNO are formed with He/H_2O and He/O_2 due to mixing of the effluent of the COST-jet with the ambient air. Experimental results showed that the nitrosylated Cys-SNO product is produced in much higher quantities after treatment using the He/N_2/O_2 mixture due to the controlled and larger production of NO_x.

The validated reaction mechanism and model were used to investigate reaction pathways and mechanisms contributing to the oxidation of cysteine by the COST-jet sustained in He/N_2/O_2 mixtures. Results indicate that some selectivity over some oxidation products can be achieved through changing plasma operating parameters such as gap distance and inlet gas flow rate of O_2 and N_2. The oxidation of the cysteine molecule is sensitive to the gas-phase production of ROS responsible for the initiating hydrogen abstraction step. If the flux of ROS to the liquid is too high, hydrogen abstraction occurs too quickly and formation of cystine dominates over formation of oxidation products. If the Cys-SNO product is desired, the inlet fraction of N_2 should be increased though tuning other operating parameters (i.e., rf power, total flow rate) may be more effective in selecting for the nitrosylated product.

Only reactions at the cysteine thiol (-SH) site were considered in this work, as the thiol site is the most reactive site on the cysteine molecule. However, hydrogen abstraction can occur at the amino site, along the alkane backbone, or at the carboxyl site as well. Future work should consider whether contributions from these sites also play important roles in the oxidation of the cysteine molecule, as these groups are common in living organisms. Oxidation at sites other than the thiol

site on other molecules will contribute to, for example, bacterial inactivation due to oxidative stress.

Cell media solutions usually contain an array of organic and inorganic molecules (i.e., vitamins, proteins) that also likely consume plasma-produced RONS, and with which cysteine derived radical species may react. The fundamental processes discussed in this investigation of RONS reacting with cysteine would be components of that larger, more complex reaction mechanism. We expect that initiating reactions of RONS with other organic molecules will be similar to those discussed here for cysteine. The greatest uncertainty is then reactions of those activated molecules with other organic molecules, leading to structures analogous to cystine or cross-linked-like molecules.

5.8 Tables

Table 5.1 Henry's Law Constants

Species	Dimensionless Henry's law constant	Comments
H, H^*	6.48×10^{-3}	a, b
H_2, $H_2(r)$, $H_2(v)$, H_2^*	1.80×10^{-2}	a
OH, $OH(A^2\Sigma)$	6.20×10^{2}	a
HO_2	1.32×10^{5}	
H_2O_2	1.92×10^{6}	
O_2, $O_2(v)$, $O_2(r)$, $O_2(^1S)$	3.24×10^{-2}	a
O, O^*	2.00×10^{1}	c
O_3, O_3^*	3.00×10^{-1}	a
N_2, $N_2(r)$, $N_2(v)$, N_2^*, N, N^*	1.60×10^{-2}	a, b
He, $He(2^1S)$, $He(2^3S)$, $He(2^3P)$, $He(2^1P)$, He(3P), He(3S), He_2^*	9.42×10^{-3}	a, b
NO	4.40×10^{-2}	
NO_2	2.80×10^{-1}	
NO_3	4.15×10^{1}	
N_2O, $N_2O(v)$	5.99×10^{-1}	a
N_2O_3	6.00×10^{2}	
N_2O_4	3.69×10^{1}	
N_2O_5	4.85×10^{1}	
NH	1.47×10^{3}	d
HNO_2, HNO	1.15×10^{3}	a
HNO_3	4.80×10^{6}	
HNO_4	3.47×10^{6}	

a) Value corresponds to the first species in the list. Other species assumed to have the same Henry's law constant.
b) Excited states rapidly quench to ground state in water. Henry's law saturation is not expected.
c) Adjusted from Ref. 36 for consistency with experimental measurements of atomic O density in liquid for similar COST-jet systems [48,49].
d) Approximated as NH_3.

Table 5.2 Gas Phase Species Included in Plasma Chemistry Model

Hydrogen Species [a,b]

H , H^* , H^+ , H^- , H_2 , $H_2(r)$, $H_2(v)$, H_2^+ , H_2^* , H_3^+

Oxygen Species [a, b]

O_2 , $O_2(r)$, O_2 (v) , O_2^* , $O_2(^1S)$, O_2^+ , O_2^- , O , O^* , O^+ , O^- , O_3 , O_3^* , O_3^- , O_4^+

Nitrogen Species [a, b]

N_2 , $N_2(r)$, $N_2(v)$, N_2^* , N_2^+ , N_3^+ , N_4^+ , N , N^* , N^+

Helium Species [a]

He , He^+ , He , $He(2^1S)$, $He(2^3S)$, $He(2^3P)$, $He(2^1P)$, $He(3P)$, $He(3S)$, He_2^*

Heterogenous Species [a,b]

OH , OH^* , OH^- , H_2O , $H_2O(v)$, H_2O^+ , HO_2 , H_2O_2 , H_3O^+ , NO , NO^+, NO_2 , NO_2^+, NO_2^-, NO_3 , NO_3^- , N_2O , $N_2O(v)$, N_2O_3 , N_2O_4 , N_2O_5 , NH , HNO , HNO_2 , HNO_3 , HNO_4 , $H_4O_2^+$, $H_2O_3^+$, $H_5O_2^+$, $H_2NO_2^+$, $H_4NO_3^+$, $H_6NO_4^+$, H_2NO^+ , HeH^+

a * denotes an excited state atom or molecule

b *(r)* and *(v)* denote rotationally and vibrationally excited molecules, respectively

Table 5.3 Cysteine Liquid Reaction Mechanism

Cysteine Species	
Cys-SH	Cysteine
Cys-S•	Thiol radical
Cys=S	Cys(-2H), intermediate product. Reconfiguration of S after H abstraction.
Cys-SOH	Sulfenic acid
Cys- SO_2H	Sulfinic acid
Cys-SO_3H	Sulfonic acid
Cys- $S(OH)_2$	Intermediate product. 2 OH additions to S after H abstraction.
Cys- SOH_2	Intermediate product. Direct OH addition to SH group.
Cys-S=O	Intermediate product. O double bonded to S after H abstraction.
Cys-S-S-Cys	Cystine
Cys-SONO	Double bonded O, N double bonded O addition to S after H abstraction
Cys-SNO	N double bonded O addition to S after H abstraction
Cys-S-S•	Product of radical attack on cystine
Cys•(-2H)	Product of radical attack on cystine
Cys-S-S-O_2	Intermediate product in the formation of Cysteine-S-Sulfonate
Cys-S-S-O_3^-	Cysteine-S-Sulfonate
SH	Abstracted thiol group

	Reaction	Reaction rate coefficient[a]	Comments
	Initiation reactions		
1	$OH_{(aq)} + Cys\text{-}SH \rightarrow H_2O_{(aq)} + Cys\text{-}S•$	1.68×10^{-17}	b
2	$HO_{2(aq)} + Cys\text{-}SH \rightarrow H_2O_{2(aq)} + Cys\text{-}S•$	5.65×10^{-16}	b
3	$OH_{(aq)} + Cys\text{-}SH \rightarrow H_2O_{(aq)} + SH + Cys•(-2H)$	1.00×10^{-18}	est.
4	$O_{(aq)} + Cys\text{-}SH \rightarrow OH_{(aq)} + SH + Cys•(-2H)$	2.00×10^{-18}	est.
5	$O_{(aq)} + Cys\text{-}SH \rightarrow OH_{(aq)} + Cys\text{-}S•$	1.68×10^{-15}	b
6	$O^-_{(aq)} + Cys\text{-}SH \rightarrow OH^-_{(aq)} + Cys\text{-}S•$	1.68×10^{-20}	est.
	Intermediate product formation		
7	$O_{(aq)} + Cys\text{-}S• \rightarrow O_{(aq)} + Cys=S$	5.60×10^{-13}	est.

8	$O^-_{(aq)}$ + Cys-S• → $O^-_{(aq)}$ + Cys=S	5.60×10^{-20}	est.
9	$OH_{(aq)}$ + Cys-S• → $OH_{(aq)}$ + Cys=S	5.60×10^{-14}	b
10	$OH^-_{(aq)}$ + Cys-S• → $OH^-_{(aq)}$ + Cys=S	5.60×10^{-20}	est.
11	$O_{2(aq)}$ + Cys-S• → $O_{2(aq)}$ + Cys=S	4.68×10^{-15}	b
12	$O_2^-{}_{(aq)}$ + Cys-S• → $O_2^-{}_{(aq)}$ + Cys=S	1.00×10^{-20}	b
13	$O_{3(aq)}$ + Cys-S• → $O_{2(aq)}$ + Cys-S=O	8.31×10^{-16}	b
14	$OH_{(aq)}$ + Cys-S• → Cys-SOH_2	2.80×10^{-17}	b
15	$O_{3(aq)}$ + Cys-SOH_2 → $H_2O_{(aq)}$ + $O_{2(aq)}$ + Cys-S=O	2.08×10^{-16}	b
16	$OH_{(aq)}$ + Cys-SOH → Cys-$S(OH)_2$	5.60×10^{-17}	b
17	$OH_{(aq)}$ + Cys-S-S-Cys → $OH_{(aq)}$ + Cys-S• + Cys-S-S•	2.00×10^{-15}	est.
18	$SO_{2(aq)}$ + Cys-S• → Cys-S-S-O_2	3.49×10^{-13}	b
19	$NO_{(aq)}$ + Cys-S=O → Cys-SONO	5.00×10^{-19}	est.
	Sulfenic acid formation		
20	$H_2O_{2(aq)}$ + Cys-SH → $H_2O_{(aq)}$ + Cys-SOH	4.68×10^{-22}	est.
21	$OH_{(aq)}$ + Cys-S•→ $OH_{(aq)}$ + Cys-SOH	5.60×10^{-13}	b
22	$O_{3(aq)}$ + Cys-SOH_2→ $O_{2(aq)}$ + $OH_{(aq)}$ + Cys-SOH	6.23×10^{-16}	b
	Sulfinic acid formation		
23	$O_{(aq)}$ + Cys-$S(OH)_2$ → $OH_{(aq)}$ + Cys-SO_2H	1.12×10^{-15}	est.
24	$O^-_{(aq)}$ + Cys-$S(OH)_2$ → $OH^-_{(aq)}$ + Cys-SO_2H	1.12×10^{-18}	est.
25	$OH_{(aq)}$ + Cys-S=O → $OH_{(aq)}$ + Cys-SO_2H	1.00×10^{-17}	b
26	$OH_{(aq)}$ + Cys-$S(OH)_2$ → $H_2O_{(aq)}$ + Cys-SO_2H	1.12×10^{-17}	est.
27	$O_{2(aq)}$ + Cys-$S(OH)_2$ → $HO_{2(aq)}$ + Cys-SO_2H	4.68×10^{-17}	est.
	Sulfonic acid formation		
28	$O_{(aq)}$ + Cys-SO_2H → $H_{(aq)}$ + Cys-SO_3H	5.60×10^{-14}	est.
29	$OH_{(aq)}$ + Cys-SO_2H → $H_{(aq)}$ + Cys-SO_3H	5.60×10^{-15}	b
30	$O_{2(aq)}$ + Cys-SO_2H → $O_{(aq)}$ + Cys-SO_3H	4.68×10^{-17}	b
31	$H_2O_{2(aq)}$ + Cys-SO_2H → $H_2O_{(aq)}$ + Cys-SO_3H	4.68×10^{-20}	b
	Cystine formation		
32	Cys-S• + Cys-S• → Cys-S-S-Cys	1.00×10^{-10}	b
	Cystine-S-sulfonate formation		

33	$HSO_3^-{}_{(aq)}$ + Cys-S-S-Cys → Cys-SH + Cys-S-S-O_3^-	1.00×10^{-18}	est.
34	$HSO_3^-{}_{(aq)}$ + Cys-S-S-Cys → $H_{2(aq)}$ + Cys-S-S-O_3^-	1.00×10^{-15}	est.
35	$OH_{(aq)}$ + Cys-S-SO_2 → $H^+{}_{(aq)}$ + Cys-S-S-O_3^-	1.00×10^{-15}	est.
	Cysteine-SNO formation		
36	$NO_{(aq)}$ + Cys-S• → Cys-SNO	5.60×10^{-19}	est.
	Additional reactions		
37	$O_{2(aq)}$ + SH → $SO_2^-{}_{(aq)}$ + $H^+{}_{(aq)}$	1.24×10^{-11}	b
38	$H_2O_{2(aq)}$ + SH → $HO_{2(aq)}$ + $H_2S_{(aq)}$	5.00×10^{-15}	b
39	Cys•(-2H) + SH + $H_{(aq)}$ → Cys	1.00×10^{-35}	est.
40	Cys•(-2H) + H_2S → Cys	1.00×10^{-15}	est.

a) Reaction rate coefficients have units of cm^3/s.

b) Reaction rate is approximated from an analogous gas-phase reaction with a long chain alkane from the NIST database [44] or from analogous reactions in solution from the NIST solutions [45] database and adjusted to match experimental measurements.

5.9 References

[1] J. Schlegel, J. Köritzer and V. Boxhammer, Clin. Plasma Med. **1,** 2 (2013).

[2] M. Keidar, A. Shashurin, O. Volotskova, M. Ann Stepp, P. Srinivasan, A. Sandler and B. Trink, Phys. Plasmas **20,** (2013).

[3] A. Kramer, J. Lademann, C. Bender, A. Sckell, B. Hartmann, S. Münch, P. Hinz, A. Ekkernkamp, R. Matthes, I. Koban, I. Partecke, C. D. Heidecke, K. Masur, S. Reuter, K. D. Weltmann, S. Koch and O. Assadian, Clin. Plasma Med. **1,** 11 (2013).

[4] N. Kaushik, S. Mitra, E. J. Baek, L. N. Nguyen, P. Bhartiya, J. H. Kim, E. H. Choi and N. K. Kaushik, J. Adv. Res. **43,** 59 (2023).

[5] M. K. J. Nicol, T. R. Brubaker, B. J. Honish, A. N. Simmons, A. Kazemi, M. A. Geissel, C. T. Whalen, C. A. Siedlecki, S. G. Bilén, S. D. Knecht and G. S. Kirimanjeswara, Sci. Rep. **10,** 1 (2020).

[6] C. A. J. Van Gils, S. Hofmann, B. K. H. L. Boekema, R. Brandenburg and P. J. Bruggeman, J. Phys. D. Appl. Phys. **46,** (2013).

[7] K. D. Weltmann, E. Kinde, T. Von Woedtke, M. Hähnel, M. Stieber and R. Brandenburg, Pure Appl. Chem. **82,** 1223 (2010).

[8] J. Winter, K. Wende, K. Masur, S. Iseni, M. Dünnbier, M. U. Hammer, H. Tresp, K. D. Weltmann and S. Reuter, J. Phys. D. Appl. Phys. **46,** (2013).

[9] G. Fridman, M. Peddinghaus, H. Ayan, A. Fridman, M. Balasubramanian, A. Gutsol, A. Brooks and G. Friedman, Plasma Chem. Plasma Process. **26,** 425 (2006).

[10] S. Reuter, T. Von Woedtke and K. D. Weltmann, J. Phys. D. Appl. Phys. **51,** (2018).

[11] D. B. Graves, J. Phys. D. Appl. Phys. **45,** (2012).

[12] T. Von Woedtke, A. Schmidt, S. Bekeschus, K. Wende and K.-D. Weltmann, In Vivo

(Brooklyn). **33,** 1011 (2019).

[13] E. Takai, T. Kitamura, J. Kuwabara, S. Ikawa, S. Yoshizawa, K. Shiraki, H. Kawasaki, R. Arakawa and K. Kitano, J. Phys. D. Appl. Phys. **47,** (2014).

[14] J.-W. Lackmann, G. Bruno, H. Jablonowski, F. Kogelheide, B. Offerhaus, J. Held, V. Schulz-von der Gathen, K. Stapelmann, T. von Woedtke and K. Wende, PLoS One **14,** e0216606 (2019).

[15] H. Sies, Free Radic. Biol. Med. **27,** 916 (1999).

[16] H. Yang, P. Lundbäck, L. Ottosson, H. Erlandsson-Harris, E. Venereau, M. E. Bianchi, Y. Al-Abed, U. Andersson and K. J. Tracey, Mol. Med. **27,** 58 (2021).

[17] T. Heusler, G. Bruno, S. Bekeschus, J.-W. Lackmann, T. von Woedtke and K. Wende, Clin. Plasma Med. **14,** 100086 (2019).

[18] K. Wende, Z. Nasri, J. Striesow, M. Ravandeh, K.-D. Weltmann, S. Bekeschus and T. von Woedtke, in 2022 IEEE International Conference on Plasma Science (ICOPS) 1 (IEEE, 2022).

[19] L. B. Poole, Free Radic. Biol. Med. **80,** 148 (2015).

[20] G. I. Giles, M. J. Nasim, W. Ali and C. Jacob, Antioxidants **6,** 1 (2017).

[21] G. Bruno, T. Heusler, J. W. Lackmann, T. von Woedtke, K. D. Weltmann and K. Wende, Clin. Plasma Med. **14,** 100083 (2019).

[22] A. A. Ali, J. A. Coulter, C. H. Ogle, M. M. Migaud, D. G. Hirst, T. Robson and H. O. McCarthy, Biosci. Rep. **33,** (2013).

[23] C. Belge, P. B. Massion, M. Pelat and J. L. Balligand, Ann. N. Y. Acad. Sci. **1047,** 173 (2005).

[24] C. E. Paulsen and K. S. Carroll, Chem. Rev. **113,** 4633 (2013).

[25] K. Wende, G. Bruno, M. Lalk, K. D. Weltmann, T. Von Woedtke, S. Bekeschus and J. W. Lackmann, RSC Adv. **10,** 11598 (2020).

[26] K. Wende, T. Von Woedtke, K. D. Weltmann and S. Bekeschus, Biol. Chem. **400,** 19 (2018).

[27] F. Kogelheide, K. Kartaschew, M. Strack, S. Baldus, N. Metzler-Nolte, M. Havenith, P. Awakowicz, K. Stapelmann and J. W. Lackmann, J. Phys. D. Appl. Phys. **49,** (2016).

[28] I. Sremački, G. Bruno, H. Jablonowski, C. Leys, A. Nikiforov and K. Wende, Plasma Sources Sci. Technol. **30,** (2021).

[29] H. J. Forman, M. Maiorino and F. Ursini, Biochemistry **49,** 835 (2010).

[30] J. W. Lackmann, K. Wende, C. Verlackt, J. Golda, J. Volzke, F. Kogelheide, J. Held, S. Bekeschus, A. Bogaerts, V. Schulz-Von Der Gathen and K. Stapelmann, Sci. Rep. **8,** 1 (2018).

[31] S. Bekeschus, A. Schmidt, K. D. Weltmann and T. von Woedtke, Clin. Plasma Med. **4,** 19 (2016).

[32] J. Golda, J. Held, B. Redeker, M. Konkowski, P. Beijer, A. Sobota, G. Kroesen, N. S. J. Braithwaite, S. Reuter, M. M. Turner, T. Gans, D. O'Connell and V. Schulz-Von Der Gathen, J. Phys. D. Appl. Phys. **49,** (2016).

[33] S. Reuter, K. Niemi, V. Schulz-Von Der Gathen and H. F. Döbele, Plasma Sources Sci. Technol. **18,** (2009).

[34] S. Reuter, J. Winter, A. Schmidt-Bleker, D. Schroeder, H. Lange, N. Knake, V. Schulz-Von Der Gathen and K. D. Weltmann, Plasma Sources Sci. Technol. **21,** (2012).

[35] K. J. Adams, B. Pratt, N. Bose, L. G. Dubois, L. St. John-Williams, K. M. Perrott, K. Ky, P. Kapahi, V. Sharma, M. J. Maccoss, M. A. Moseley, C. A. Colton, B. X. Maclean, B.

Schilling and J. W. Thompson, J. Proteome Res. **19,** 1447 (2020).

[36] A. M. Lietz and M. J. Kushner, J. Phys. D. Appl. Phys. **49,** 425204 (2016).

[37] J. Kruszelnicki, A. M. Lietz and M. J. Kushner, J. Phys. D. Appl. Phys. **52,** (2019).

[38] A. Stancampiano, P. E. Bocanegra, S. Dozias, J. M. Pouvesle and E. Robert, Plasma Sources Sci. Technol. **30,** (2021).

[39] A. N. Bhoj and M. J. Kushner, J. Phys. D. Appl. Phys. **39,** 1594 (2006).

[40] R. Dorai and M. J. Kushner, J. Phys. D. Appl. Phys. **36,** 666 (2003).

[41] W. Tian and M. J. Kushner, J. Phys. D. Appl. Phys. **47,** (2014).

[42] S. Wenske, J. W. Lackmann, L. M. Busch, S. Bekeschus, T. von Woedtke and K. Wende, J. Appl. Phys. **129,** (2021).

[43] J. Polito, M. Denning, R. Stewart, D. Frost and M. J. Kushner, J. Vac. Sci. Technol. A **40,** 1 (2022).

[44] NIST Chemical Kinetics Database

[45] NDRL/NIST Solution Kinetics Database on the Web

[46] K. Stapelmann, B. Myers, M. H. Quesada, E. Lenker and P. J. Ranieri, J. Phys. D. Appl. Phys. **54,** (2021).

[47] D. Ellerweg, J. Benedikt, A. von Keudell, N. Knake and V. Schulz-von der Gathen, New J. Phys. **12,** 013021 (2010).

[48] D. Steuer, I. Korolov, S. Chur, J. Schulze, V. Schulz-Von Der Gathen, J. Golda and M. Böke, J. Phys. D. Appl. Phys. **54,** (2021).

[49] B. Myers, E. Barnat and K. Stapelmann, J. Phys. D. Appl. Phys. **54,** (2021).

[50] J. Golda, F. Kogelheide, P. Awakowicz and V. S. Von Der Gathen, Plasma Sources Sci. Technol. **28,** (2019).

[51] T. R. Brubaker, K. Ishikawa, H. Kondo, T. Tsutsumi, H. Hashizume, H. Tanaka, S. D. Knecht, S. G. Bilén and M. Hori, J. Phys. D. Appl. Phys. **52,** (2019).

[52] H. Xu, C. Chen, D. Liu, W. Wang, W. Xia, Z. Liu, L. Guo and M. G. Kong, Plasma Sci. Technol. **21,** (2019).

[53] K. Abe, H. Kondo and S. Arai, Agric. Biol. Chem. **51,** 2763 (1987).

[54] A. Schmidt-Bleker, R. Bansemer, S. Reuter and K. D. Weltmann, Plasma Process. Polym. **13,** 1118 (2016).

[55] P. Preissing, I. Korolov, J. Schulze, V. Schulz-Von Der Gathen and M. Böke, Plasma Sources Sci. Technol. **29,** (2020).

[56] J. L. Bailey and R. D. Cole, J. Biol. Chem. **234,** 1733 (1959).

[57] J. B. Kohl, A. T. Mellis and G. Schwarz, Br. J. Pharmacol. **176,** 554 (2019).

[58] R. L. Levine, L. Mosoni, B. S. Berlett and E. R. Stadtman, Proc. Natl. Acad. Sci. U. S. A. **93,** 15036 (1996).

[59] C. V. Suschek and C. Opländer, Clin. Plasma Med. **4,** 1 (2016).

Chapter 6 A Hierarchal Model for Bacterial Cell Inactivation in Solution by Direct and Indirect Treatment Using Cold Atmospheric Plasmas[5]

Cold atmospheric plasma (CAP) devices have shown promise for a variety of plasma medical applications including wound healing and bacterial inactivation often contained in liquids. In the latter application, plasma-produced reactive oxygen and nitrogen species (RONS) interact with and damage bacterial cells, though the mechanism by which cell damage occurs is unclear. Computational models can help elucidate relationships between plasma-produced RONS and cell killing by enabling direct comparison between dissimilar plasma devices and by examining the effects of changing operating parameters in these devices. In biological applications, computational models of plasma-liquid interactions would be most effective in design and optimization of plasma devices if there is a corresponding prediction of the biological outcome. In this chapter, we propose a hierarchal model for planktonic bacterial cell inactivation by plasma produced RONS in liquid. The reaction mechanism for plasma induced modification of cysteine (Chapter 5) was extended to provide a basis for cell killing by plasma-produced RONS. Results from the model are compared to literature to provide proof of concept. Differences in time to bacterial inactivation as a function of plasma operating parameters including gas composition and plasma source configuration are discussed. Results indicate that optimizing gas-phase reactive nitrogen species (RNS) production may be key in the design of plasma devices for disinfection.

[5] Results discussed and portions of the text in this work were submitted as J. Polito and M. J. Kushner "A Hierarchal Model for Bacterial Cell Inactivation in Solution by Direct and Indirect Treatment Using Cold Atmospheric Plasmas," to *J. Phys D: Appl Phys.* on 14 March 2024.

6.1 Introduction

Cold atmospheric plasmas (CAP) can provide a non-invasive source of reactive oxygen and nitrogen species (RONS) for a variety of plasma medical and agricultural applications. Current uses of CAP include cancer therapy [1,2], wound healing [3,4], surface sterilization [5,6], air purification [7,8], and food sanitation [9,10]. CAP is particularly promising for plasma medical applications, in particular medical instrument sterilization and wound disinfection, as the plasma efficiently kills bacteria while minimizing damage to the treated surface or detrimentally affecting the patient.

Several CAP sources have been investigated for plasma medical applications, including a variety of atmospheric pressure plasma jet (APPJ) sources [11,12]. APPJs can be classified as indirect (non-touching) sources in which the plasma is not in contact with the target or as direct (touching) sources in which the plasma is in contact with the target (Figure 6.1). An example of an indirect APPJ is the COST-Jet [13] where the applied electric field is perpendicular to the gas flow, producing a confined plasma and largely neutral plume carrying activated species to the surface. An example of a direct APPJ is the kINPen [4] where the electrode configuration enables propagation of ionization wave through the gas plume. The proximity of the exit of the APPJ to the surface then determines whether the APPJ is touching or not touching. Typically, these APPJ sources are operated in a carrier gas such as argon or

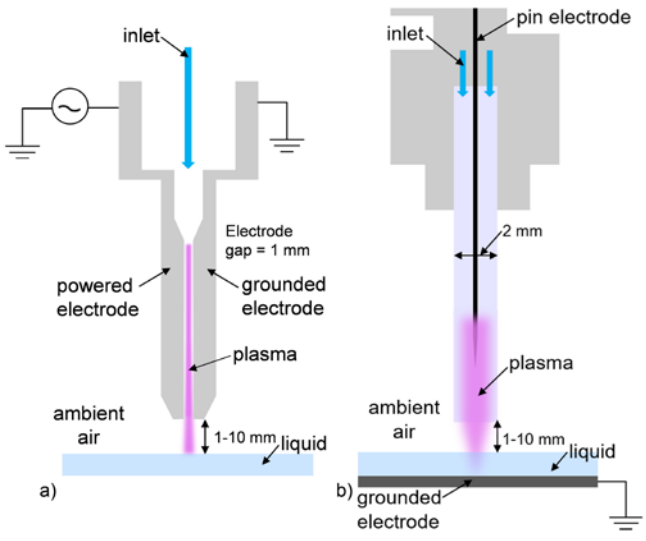

Figure 6.1. Example of a) an indirect (non-touching) plasma source and b) a direct (touching) plasma source.

helium containing few percent mixtures of air, water, or oxygen to generate RONS in the gas-phase. Further reactions and RONS production can occur as the rare-gas jet mixes with the ambient air.

Often, the biological target is covered by a layer of liquid or is contained in solution, as in planktonic bacteria. Both types of sources are efficient at generating RONS in the gas-phase which can solvate into the liquid-phase to produce important antibacterial RONS such as OH_{aq}, H_2O_{2aq}, NO_{3aq}^-, and $ONOO_{aq}^-$. These species are produced either by the direct solvation of plasma produced species or by subsequent reactions in the liquid.

Many plasma configurations have been studied independently as sources for bacterial inactivation, however there are few direct comparisons between devices. In some studies, direct and indirect treatment are compared using the same device. For example, Yahaya et. al studied the direct and indirect bactericidal effects of a dielectric barrier discharge by comparing the kill curves of cells exposed directly to the plasma versus those exposed to plasma activated water (PAW) [14]. They found that, while both direct and indirect treatment resulted in reduction of cell viability, direct treatment was more effective and was about fifteen times faster. Others have studied indirect plasma treatment by allowing the plasma effluent (plasma-produced RONS) to come into contact with solution containing bacterial cells. Van Gils et. al investigated inactivation of the drug-resistant bacteria *Pseudomonas aeruginosa* in solution by argon APPJ. They found that a 6-log reduction in cell viability was achievable after about 3 minutes of treatment [15].

Researchers have reported the time for bacterial inactivation using direct plasma configurations to be on the order of 3-5 minutes [16], whereas bacterial inactivation using indirect plasma configurations occurs on the order of 10 minutes or longer [17]. Shorter time for bacterial inactivation using direct sources is likely partly due to the additional delivery of photons and ions

to the liquid surface, which leads to higher generation of RONS by liquid-phase reactions than when indirect sources are used. The time to inactivation will also depend on plasma operating parameters such as power, gas composition, and distance from the target, as well as the initial bacteria concentration.

The precise mechanisms of bacterial inactivation by plasma-produced RONS are still unclear. In general, plasma-induced bacterial inactivation is thought to be due to apoptosis through oxidative stress [12,18,19]. Reactions of plasma-produced RONS with organic molecules on the cell membrane result in interruptions to cell signaling pathways. Damage to the membrane itself or to cell signaling pathways results in excessive uptake of reactive oxygen species (ROS) into the cell body. High concentrations of ROS such as O and OH in the cell body result in reduced functionality of vital cell processes, and eventually leads to cell death.

Determining the mechanism for bacterial inactivation is further complicated in many applications by the bacteria being in a liquid or cell culture medium. For example, plasma devices have been used to reduce bacterial load in severe burn wounds, which are often coated with thin layers of fluid [20,21]. The presence of a liquid layer, whether produced by the host organism, or in experiments where cells are cultured in solution containing nutrients, affects both the generation and consumption of plasma-produced RONS. The effects of the components of the solution must be considered when determining, for example, the dose of bactericidal RONS necessary to achieve the desired outcome.

Computer models can help elucidate the mechanism of bacterial inactivation by plasma-produced RONS by enabling comparison between plasma source configurations, gas compositions, power profiles, or other operating conditions that may be difficult to experimentally compare side-by-side. To date, models have characterized plasma-production of RONS and

delivery of those RONS to the target [22,23] and have predicted post-treatment modifications of key amino acids [24,25], but little work has been done to represent the mechanism by which RONS interact with large organic molecules or cells in wet conditions. Previous work has shown success in approximating reaction rates of organic molecules in solution by starting from analogous gas-phase reaction rates of RONS with long-chain alkanes [26]. Since cells membranes are, at the most basic level, surfaces made of organic molecules, it follows that a first approximation to determine a reaction mechanism for RONS with cells may be to start with previous mechanisms for RONS with organic molecules.

In this chapter, we discuss results from a plasma chemistry and plasma liquid interaction model (*GlobalKin*), and a hierarchical cell death model to describe trends in planktonic cell death resulting from CAP treatment. A mechanism based on CAP treatment of cysteine was adjusted for consistency with cell kill curves in the literature, and proposed to represent reaction rates for RONS interactions with planktonic bacteria cells in the hierarchical cell death model. Results for time to bacterial inactivation as a function of plasma operating parameters such as gas composition and plasma source configuration are discussed and compared to results from the literature to provide proof of concept. Model results are consistent with the literature and indicate that bacterial inactivation efficiency is higher in systems that generate more reactive nitrogen species (RNS) in the gas phase. The hierarchal cell eath model developed for this chapter is discussed in Section 6.2. The base case plasma properties are discussed in Section 6.3. Parametric studies of plasma treatment of planktonic bacteria are discussed in Section 6.4 and concluding remarks are in Section 6.5.

6.2 Hierarchal Model for Cell Death

In this section, a hierarchal approach for predicting cell death as a result of exposure to a

plasma is discussed. The hierarchal model was implemented in *Globalkin* (described in Chapter 2). *GlobalKin* was operated in plug-flow mode and gas-phase fluxes calculated by *GlobalKin* were provided to the liquid module to predict liquid-phase densities after 12 minutes of plasma exposure time.

The experimental observation is that planktonic bacterial cell death does not begin immediately upon application of the plasma to the solution or growth media. Rather, there is an induction time during which assays show that although cells may be stressed, they are in large part alive [27,28]. Only after a critical treatment time do cells begin to die. Since reactions of cells with liquid-phase RONS would presumably begin as soon as the solution is activated by the plasma, these observations imply that cell death results from the accumulation of damage, where here damage is defined in the most general way as cells not being healthy. As the cells accumulate damage as a result of reactions with RONS, the cells become stressed. After accumulating a critical amount of damage, the cells die. When removing the source of damage and stress (e.g., turning off the plasma), some fraction of the less stressed or damaged cells may recover to be healthy. Some fraction of the more stressed or damaged cells will die.

A hierarchal reaction mechanism was developed to describe cell death in solution as a result of plasma-produced-RONS delivery to a liquid surface. The hierarchal model is based on any single cell accumulating a critical amount of damage by a sequence of reactions with RONS whereby a healthy cell becomes progressively more stressed or sick. When a critical amount of damage has been accumulated, the cell is declared to be dead. Table I contains the reaction mechanism that describes this process.

A typical bacterium is a few microns in diameter and 4-5 microns long. With a surface site density of 10^{15} cm^{-2}, there are about 10^8 sites on the cell membrane that contain functionalities

(e.g., -H, -NH_2, -OH, -O) that are susceptible to attack by RONS. The sequential set of reactions that transition a healthy cell to a sick (or stressed) cell to a dead cell is based on reactions of RONS with these surface functionalities. Modifications of organic molecules, such as proteins, on the cell membrane, may result in changes to cell signaling, motility, or regulatory function that can lead to expedited cell death [12]. Reaction rates for this mechanism were estimated based on rates of hydrogen abstraction from the small organic molecule cysteine by RONS.

Cysteine contains biologically relevant functionalities (-SH, -NH_2, -COOH, -H) and is often used in biological models to quantify complex reaction pathways [29]. Previous work established a reaction mechanism for plasma-assisted modifications of cysteine in solution that was in good agreement with experimental data [26]. Only rates for hydrogen abstraction were considered, as the hydrogen abstraction step was determined to be the rate limiting step in the modification of the cysteine molecule. Based on the cysteine mechanism, O_{aq}, O_{aq}^-, OH_{aq}, OH_{aq}^-, HO_{2aq}, and H_2O_{2aq} are the ROS allowed to interact with the cell in solution and result in damage. (The aq suffix denotes an aqueous species.) Reactions with NO_{aq}, NO_{2aq}^-, NO_{3aq}^-, and $ONOO_{aq}^-$ were also included as these species have been shown to be important for wound healing and for bacterial inactivation [30,31]. Rates for cell interaction with RONS were adjusted from those published in Ref. [26] to be consistent with timescales for achieving bacterial cell inactivation reported in the literature. In particular, studies by Van Gils et. al [15] and Chandana et. al [16] were most influential in determining rates of reactions and time to cell killing.

In practice, cells are plated in solution containing cell media or broth which provides key nutrients for keeping cells alive. Cell media or broth consists of vitamins, proteins, and other organic matter that can scavenge or produce RONS. In the model, the growth medium is not accounted for as a separate species. Instead, we consider one colony forming unit (CFU) to

approximate a cell plus its associated media.

In the hierarchical cell reaction mechanism, an individual cell undergoes a series of sequential reactions with RONS that progressively damage the cell. The health of the cell is classified by how many sequential interactions it has undergone. Based on the typical size and surface site density of a planktonic cell such as *Pseudomonas aeruginosa*, we assume our idealized cell to have 10^8 reaction sites. A cell is classified as being no longer viable when 10% of those sites have undergone reaction with RONS, or 10^7 discrete reactions have taken place. That is C_0 (a healthy cell) reacts with a RONS species to become a damaged cell C_1. The now damaged cell C_1 reacts with a RONS species to become a damaged cell C_2. For a real cell, this sequence would occur 10^7 times until the cell is classified as being dead. As it is impractical to track the 10^7 discrete events for one individual cell that are required to declare the cell dead, 20 sequential generations of increasingly damaged cells were tracked. The 20^{th} generation of the cell is considered dead. The consumption of RONS is accelerated by the ratio of the number of discrete reactions required to kill a cell (10^7) to the number of generations of the model cells (20) to approximate reaction rates with real cells. A set of "ghost" reactions in which consumption of RONS does not result in cell damage are included to reflect the actual RONS consumption. Rates of RONS consumption are assumed to be slower for cells that are more damaged, as the number of reactive sites decreases. An example of the populations of the cell death model as a function of treatment time, including all 20 generations of sequentially damaged cells is shown in Figure 6.2a. These results are for the base case plasma treatment with a remote, non-touching plasma source, and will be discussed in more detail below.

In experiments, following plasma treatment some fraction of damaged cells can recover and become healthy cells, while a fraction of treated, but still alive cells is irreparably damaged

and will eventually die. In this work, the successive cell generations of damaged cells are divided into three groups. The first group (generation C_0 to generation C_6) is classified as being healthy. The second group (generation C_7 to generation C_{13}) is classified as being sick, and the last third (generation C_{14} to generation C_{20}) are cells that will die in the short term. Cells C_{20} are immediately dead. (See Figure 6.2b).

Most experimental measurements of cell viability occur over the long term by re-plating the CFUs and assessing reproduction of those cells. Healthy cells reproduce. Over this longer assessment period, we assume that the heavily damaged cells die as do a fraction of the sick cells. To achieve consistency with times for cell death reported in the literature, we estimated that 60% of the sick population will recover and classified this population as being alive, while 40% of the sick population will not recover and is classified as dead. In the discussion that follows we classify as

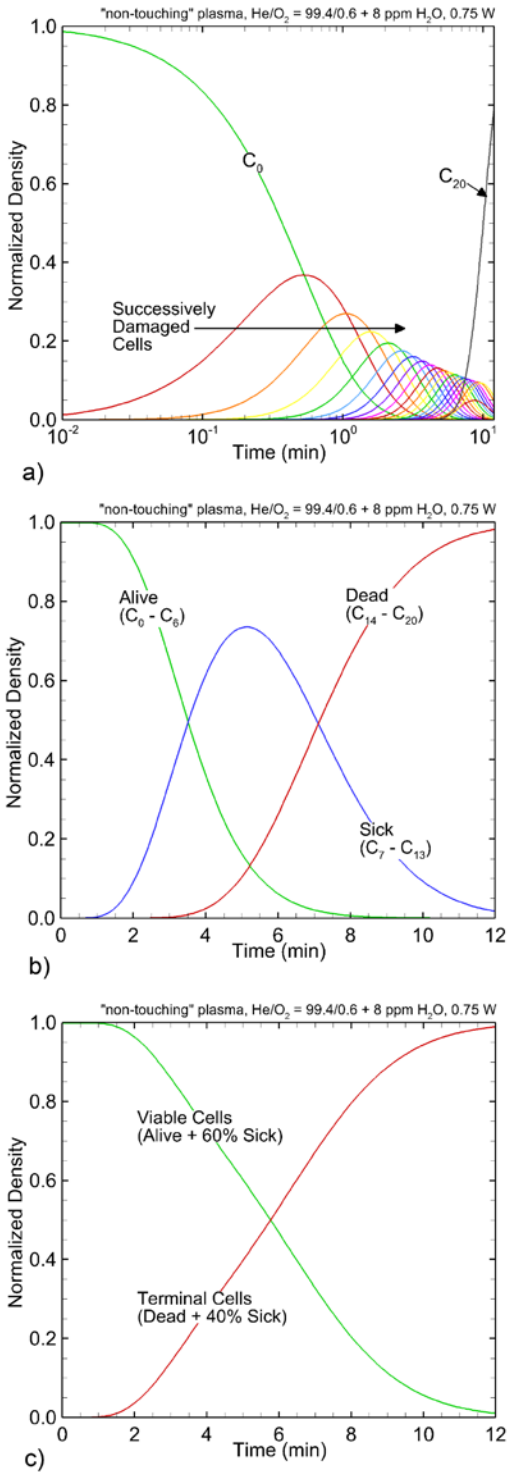

Figure 6.2. Results from the cell death model including a) 20 generations of damaged CFU, b) division of generations into alive, sick, and dead, and d) estimate of viable/terminal cell populations. Initial CFU concentration = 10^7 cm^{-3}.

being *viable* the healthy population plus 60% of the sick population. We classify as being *terminal* the heavily damaged and dead population plus 40% of the sick population (Figure 6.2c). The estimation that 60% of the sick population recovers while only 40% is terminal is intended to account for long time periods between treatment and measurement that often occur under experimental conditions in which the healthy cell population may reproduce.

6.3 Base Case Plasma and Liquid Properties

The base case uses an indirect (non-touching) source patterned after the COST-jet (Figure 6.1a). The plasma chamber consists of two 1 mm wide by 3 cm long rectangular electrodes spaced 1 mm apart. One electrode is powered by 750 mW of constant RF power while the other electrode is grounded. Inlet gases consist of 1000 sccm of a He/O_2 = 99.4/0.6 mixture containing 8 ppm of water impurity flowing from the top of the reactor and plasma is generated between the two electrodes. The plasma is assumed to be uniform over the 1 mm^2 cross sectional-area. The outlet of the plasma source is at 3 cm where plasma

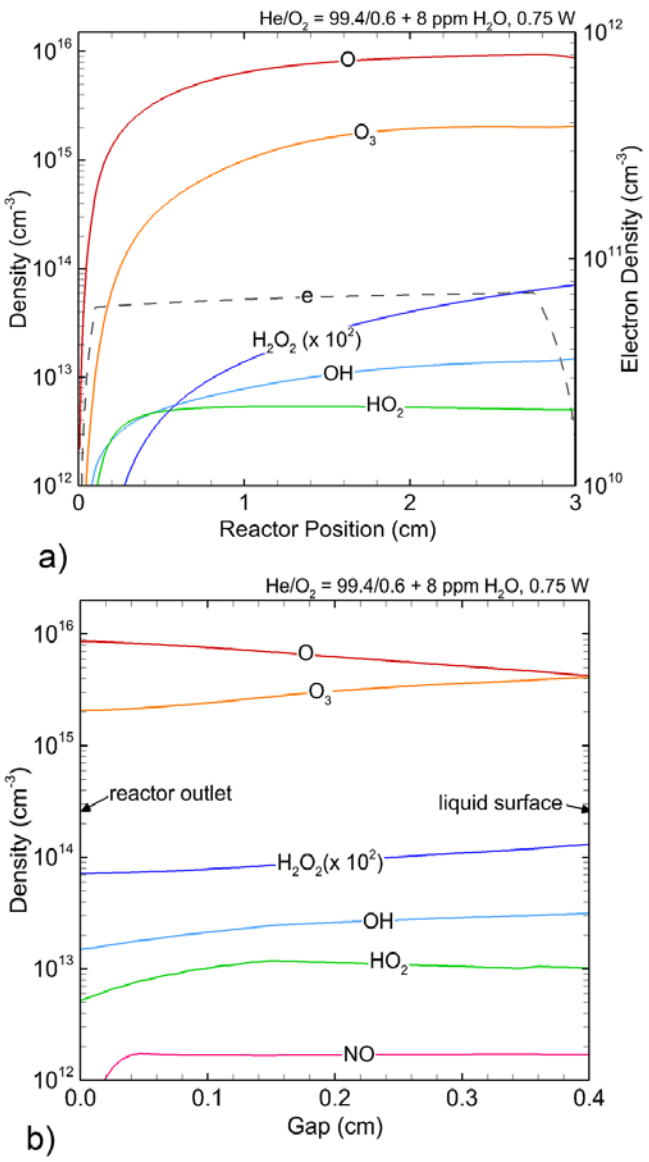

Figure 6.3. Gas-phase species production for the indirect plasma source a) in the reactor and b) in the air gap between the reactor outlet and liquid surface.

effluent flows out of the source and mixes with ambient humid air ($N_2/O_2/H_2O$ = 78/20/2). The effluent is exposed to the ambient air over a gap distance of 4 mm before coming into contact with the liquid surface. The liquid surface is exposed to the plasma effluent for up to 12 minutes. The treated liquid is 1 ml of water. An initial concentration of CFU in the water is not included in the base case so that RONS delivery to the liquid can be evaluated independently of the presence of organic material.

The gas phase production of selected RONS in the plasma source and in the gap between the reactor outlet and liquid surface are shown in Figure 6.3. The model predicts an electron density of 6.8×10^{10} cm^{-3} in the plasma source which is consistent with experimental measurements of the helium COST-jet, which is reported to be on the order of a few times 10^{10} cm^{-3} when the power is a few hundred milliwatts to a few watts [13]. Production of atomic O (7.9×10^{15} cm^{-3}) is also consistent with literature values, which is reported to be on the order of a few times 10^{15} cm^{-3} [32].

ROS such as HO_2, OH and H_2O_2 are formed in the powered region of the plasma source as a result of the water impurity. Water is dissociated by electron impact and heavy particle dissociative excitation transfer (DET) to form OH and HO_2. H_2O_2 is formed through reaction of H_2O dissociation products.

$$e + H_2O \rightarrow OH + H + e \tag{6.1}$$

$$He^* + H_2O \rightarrow He + OH^+ + H + e \tag{6.2}$$

$$He_2^* + H_2O \rightarrow 2He + OH^+ + H + e \tag{6.3}$$

$$He^* + H_2O \rightarrow He + OH^* + H \tag{6.4}$$

$$He_2^* + H_2O \rightarrow 2He + OH^* + H \tag{6.5}$$

$$HO_2 + HO_2 \rightarrow H_2O_2 \tag{6.6}$$

$$HO_2 + H_2O \rightarrow H_2O_2 + OH \tag{6.7}$$

As the plasma effluent exits the powered region and comes into contact with ambient air, electron impact ionization and excitation essentially cease. There is some small production of O, H and OH due to due to dissociative recombination of O_2^+ and H_2O^+, but this additional contribution is small compared to the O, H and OH already contained in the flow. NO_x species are then formed in the air gap. NO_x is formed through reaction of nitrogen dissociation products and plasma produced ROS. However, since no N-containing species flowed through the plasma, the production of RNS is nominal. RONS produced in the powered region and in the air gap impinge upon the liquid surface and solvate into the liquid as described above. The production of select liquid-phase RONS are shown in Figure 6.4 as a function of plasma exposure time.

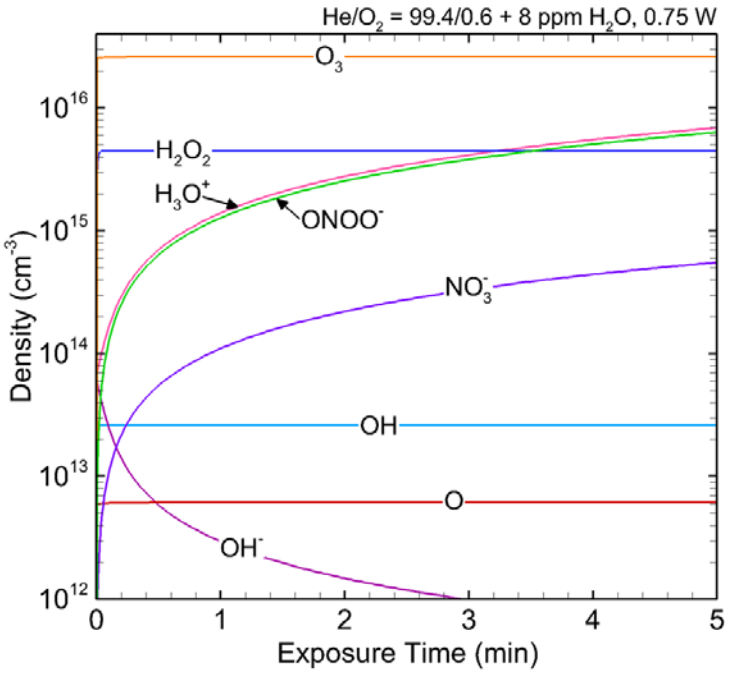

Figure 6.4. Liquid species production as a function of plasma exposure time using the indirect plasma source. There are no CFU in the liquid.

Species with moderate Henry's law coefficients (e.g. O and OH) solvate and quickly come to equilibrium, whereas species with low Henry's law coefficients (e.g. NO, O_3) solvate less readily. Production of long-lived species such as H_2O_{2aq} and O_{3aq} is due partially to solvation and partially to liquid-phase reaction of solvated ROS.

$$O_{aq} + O_{2aq} \rightarrow O_{3aq} \tag{6.8}$$

$$HO_{2aq} + HO_{2aq} \rightarrow H_2O_{2aq} \tag{6.9}$$

$$OH_{aq} + OH_{aq} \rightarrow H_2O_{2aq} \tag{6.10}$$

O_{3aq} (2.5×10^{16} cm^{-3}) and H_2O_{2aq} (4.5×10^{15} cm^{-3}) are the most abundant RONS produced in the liquid under these conditions at early treatment times. At later treatment times, reactions of solvated RNS with ROS contribute to an increase in peroxynitrite ($ONOO_{aq}^-$) and nitrate (NO_{3aq}^-). Peroxynitrite ($ONOO_{aq}^-$) is formed as a product of $O_{2}^-{}_{aq}^-$ and NO_{aq}.

$$O_{2aq}^- + NO_{aq} \rightarrow ONOO_{aq}^- \tag{6.11}$$

The $ONOO_{aq}^-$ concentration increases relative to H_2O_{2aq} concentration, and exceeds the concentration of H_2O_{2aq} after about 3.5 minutes of liquid exposure to the plasma effluent. This long time for buildup of the long lived $ONOO_{aq}^-$ is due to the low plasma production rate of RNS. The efficiency of the plasma to preferentially produce some RONS over others contributes to differences in times to achieve bacterial inactivation, as will be discussed in the following section.

6.4 Onset to Cell Death

The base case for assessing the onset of cell death is the He/O_2 = 99.4/0.6 gas mixtures whose plasma activated gas phase and liquid phase densities were discussed in the prior section. Detailed cell viability curves for the He/O_2 base case are shown in Figure 6.2 for an initial CFU concentration of 1×10^7 cm^{-3}. Cell killing does not begin immediately. Instead, there is a

delayed onset to cell killing that corresponds to the time for RNS species such as $ONOO^-_{aq}$ and NO^-_{3aq} to begin to approach their saturation limit in solution (a little over 1 minute). Nearly 100% of the CFU are classified as being alive for over 1 minute of exposure time (Figure 2b). It then follows that the mechanism for cell death is most sensitive to the rates chosen for reactions with RNS species (reactions7-10 in Table 1). Increases in the rate coefficients for RNS reactions with CFUs resulted in times to cell death that were too short for non-touching configurations. Using the classification scheme described above, 50% of the cells are viable after 6 minutes of exposure and 50% are terminal. After 12 minutes of exposure, 99% of cells are classified as terminal.

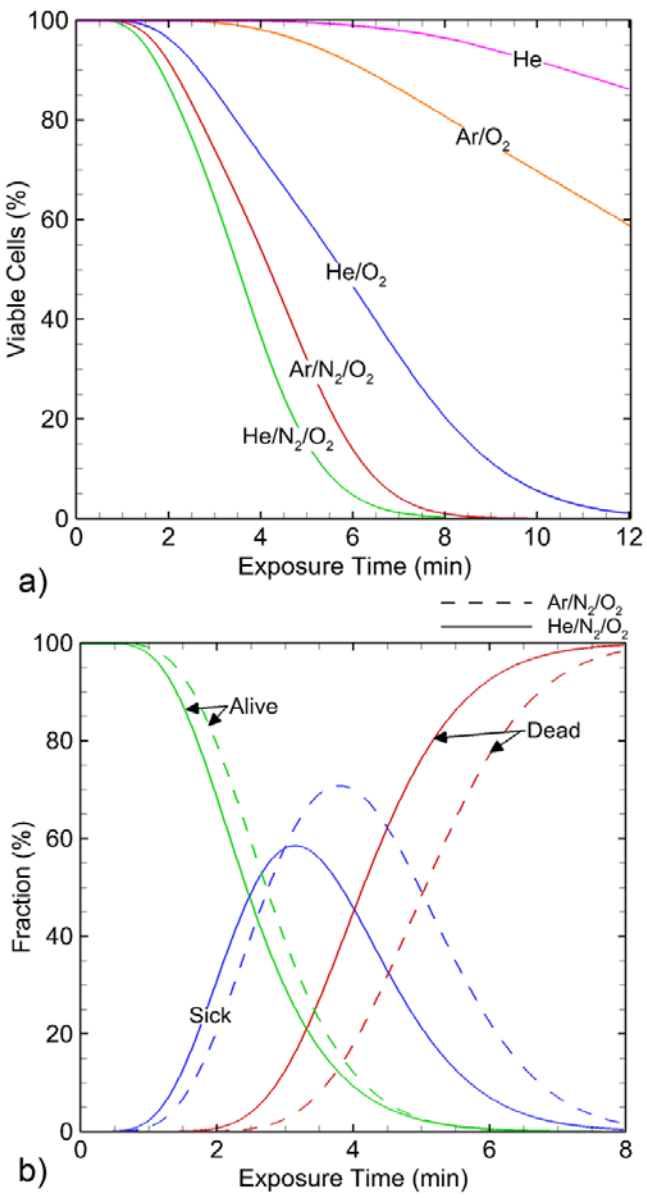

Figure 6.5. Cell viability over time for different inlet plasma gas compositions using the indirect plasma source: a) He, Ar/O_2 = 99.4/0.6, He/O_2 = 99.4/0.6, $Ar/N_2/O_2$ = 99/0.8/0.2, $He/N_2/O_2$ = 99/0.8/0.2 and b) fraction of viable, damaged, and terminal cells for the two tri-gas compositions.

6.4.1 Cell Killing as a Function of inlet Gas Composition

Changing the inlet plasma gas composition is a direct method to alter the composition of

RONS interacting with the target and can be valuable for isolating the effects of specific RONS on cell death. Often, it is impractical to greatly alter the plasma gas composition experimentally, as small changes to the device configuration may, for example, alter plasma impedance and power matching. Parametric studies on gas mixtures using models can provide guidance for designing or optimizing experimental devices.

Cell viability after 12 minutes of plasma treatment time was evaluated using five inlet gas compositions: He, He/O_2 = 99.4/0.6, Ar/O_2 = 99.4/0.6, $He/N_2/O_2$ = 99/0.8/0.2, $Ar/N_2/O_2$ = 99/0.8/0.2. All compositions consisting of one or two gasses include a water impurity of 8 ppm. The tri-gas mixtures include a water impurity of 25 ppm. The choice of how much water impurity to include was based on ongoing modelling efforts for matching OH and H_2O_2 production in the COST-jet using He, He/O_2, and $He/N_2/O_2$ mixtures. The power was held constant at 750 mW for all gas compositions. The gap between the reactor outlet and the liquid surface was 4 mm and the initial CFU concentration was 1×10^7 cm^{-3} for all cases. CFU viability for all gas compositions over the 12-minute treatment period is shown in Figure 5a

Based on the hierarchal cell death model, for otherwise constant conditions, the tri-gas mixtures are the most efficient at cell killing, with nearly all cells killed after 8 minutes of treatment time. The cases in which O_2 (with H_2O impurity) was the only additive required an additional 4 minutes (He/O_2) or more (Ar/O_2) to produce similar reductions in viability. These results are consistent with those reported in literature for a similar plasma configuration. Chandana et. al changed the gas composition in a touching APPJ to treat *E. Coli* under wet conditions [16]. They found that the addition of air as an impurity in both helium and argon plasmas reduced cell viability more efficiently than air, argon, or helium only plasmas. The effectiveness of the tri-gas cases can be attributed to the production of NO_x species in the plasma. NO_x delivery to the liquid results in

formation of HNO_{xaq} which hydrolyzes to form $H_3O_{aq}^+$ and NO_{xaq}^- and lowers the pH of the solution.

$$NO_{xaq} + H_2O_{aq} \rightarrow HNO_{aq} + OH_{aq} \quad (6.12)$$

$$HNO_{xaq} + H_2O_{aq} \rightarrow H_3O_{aq}^+ + NO_{xaq}^- \quad (6.13)$$

Common bacteria such as *P. aeruginosa* and *E. Coli* are viable over a wide range of pH, so the decrease in solution pH alone cannot explain the efficiency of nitrogen-containing plasmas for cell killing [33,34]. However, the reactive nitrogen species (RNS) NO_{2aq}^-, NO_{3aq}^-, $ONOO_{aq}^-$ are able to damage the CFU in our mechanism. Studies suggest that plasma-produced H_2O_{2aq} works in synergy with NO_{xaq}, in part via the formation of $ONOO_{aq}^-$, to increase the efficiency of cell killing [30]. It then follows that $He/N_2/O_2$ would be more efficient at cell killing than $Ar/N_2/O_2$ for our conditions, as the helium mixture produces double the gas-phase RNS as the argon mixture. For example, the density of NO delivered to the liquid surface is 5.9×10^{13} cm^{-3} for the helium mixture while 3×10^{13} cm^{-3} NO is delivered to the liquid surface for the argon mixture. These RNS solvate into the liquid and contribute to the formation of NO_{xaq}^- and $ONOO_{aq}^-$, which then damage the cells. The fractions of cells that are alive, sick, or dead for the $He/N_2/O_2$ and $Ar/N_2/O_2$ mixtures are shown in Figure 5b. Onset to cell death requires nearly one more minute of plasma exposure with the argon mixture compared to the He mixture, which is a direct consequence of the lower RNS production in the argon mixture.

The mixtures that contain only O_2 also produce cell killing, though these mixtures are less efficient at cell killing than those containing O_2 and N_2. For gas mixtures containing only rare gas and oxygen, NO_x species are only formed in significant amounts in the gap between the reactor outlet and the liquid surface as plasma-produced radicals react with N_2 in the air. Little NO_x is produced for these conditions as there is little direct dissociation of N_2 by electron impact or

dissociative excitation transfer. Therefore, cell killing is largely due to reactive oxygen species (ROS) in these cases. More OH and H_2O_2 are delivered to the liquid surface in the argon-oxygen mixture than in the helium-oxygen mixture (1.7×10^{13} cm^{-3} OH and 2.8×10^{12} cm^{-3} H_2O_2 in argon; 1.1×10^{13} cm^{-3} OH and 3.6×10^{11} H_2O_2 in helium). DET from the argon metastable is more efficient at dissociating water than the helium metastable [35,36].

More O_3 is also formed in the argon mixture compared to the He mixtures (1.5×10^{16} cm^{-3} in argon, 1.8×10^{15} cm^{-3} in helium). However, in the hierarchal cell death mechanism, O_3 does not directly impact cell viability and in previous studies was found to hinder modifications of organic molecules in solution [26]. The helium mixture is more efficient at producing atomic O, which both interacts directly with the CFU and contributes to the formation of other RONS in the air gap and in the liquid-phase after solvation. (8.2×10^{15} cm^{-3} O is delivered to the liquid surface in helium, 2.4×10^{15} cm^{-3} O is delivered to the liquid surface in argon.) The ability of the helium mixture to more efficiently dissociate O_2 to O, combined with the lower production of O_3, contributes to a higher rate of cell killing than in the argon mixture for this plasma source configuration, even though the gas-phase production of OH and H_2O_2 is less in the argon mixture.

Results from the model suggest that non-touching configurations that minimize O_3 production while maximizing O production may be optimal for cell killing when nitrogen is not included in the gas mixture. Cell killing is most efficient when ROS and RNS are formed in the plasma and can work synergistically to damage cells. The hierarchal model is able to capture trends for reduction in cell viability when the inlet gas composition is changed.

6.4.2 Cell Killing as a Function of Plasma Source Configuration

Cell viability for different gas mixtures was discussed for *non-touching* conditions. For these conditions, the plasma is well confined between the electrodes and does not extend

downstream. The plasma produced reactants in the plume that reach the liquid consist dominantly of neutral species. The opposite extreme in plasma source design is a *touching* configuration, in which the active plasma extends from the plasma source to (and touches) the surface of the liquid. Investigations of cell viability for a *touching* source that is approximately based on the kINPen [4,37] (Figure 1b) were performed to compare to the *non-touching* configuration. The *touching* configuration consists of a 1 cm long plasma zone in the actual source with a plasma plume that extends beyond the source by 4 mm to touch the liquid. Of the 750 mW total power deposition, about 89% is deposited in the plasma source.

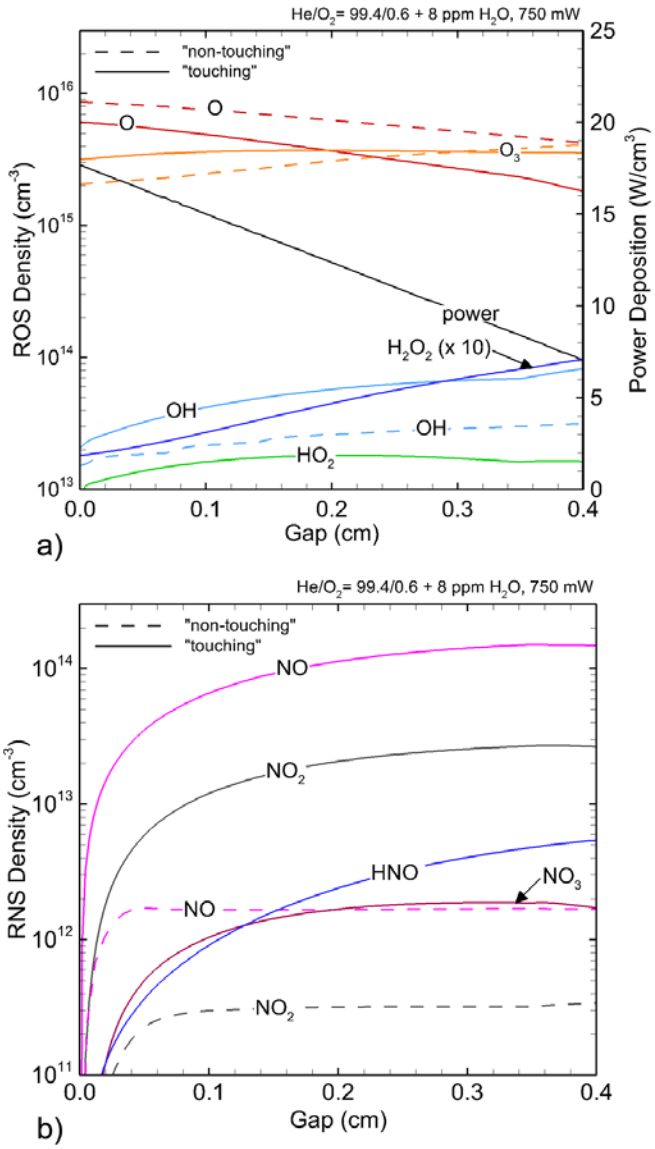

Figure 6.6. Reactive species density in the air gap for "touching" and "non-touching" plasma source configurations. a) ROS and b) RNS.

The remainder of the power is expended in the gap, with the profile as a function of position shown in Figure 6.6. The power is non-zero at the liquid surface.

Plasma forms inside the source and extends across the 4 mm air gap to impinge upon the liquid surface. Unlike in the non-touching configuration, the ambient air diffusing into the plume

can participate in electron impact and ion collisional processes that can lead to higher production of RONS in the air gap. The production of select RONS in the air gap is shown in Figure 6.6. For the same power deposition, the touching configuration is more effective overall at producing key cell killing RONS in the gas phase such as OH, H_2O_2, and NO. Densities of these species increase across the air gap in the touching case as a result of the power expended in the gap that allows for continued electron impact processes. In the non-touching case, the production of these species stagnates as reactive neutrals are consumed in reactions with the ambient air.

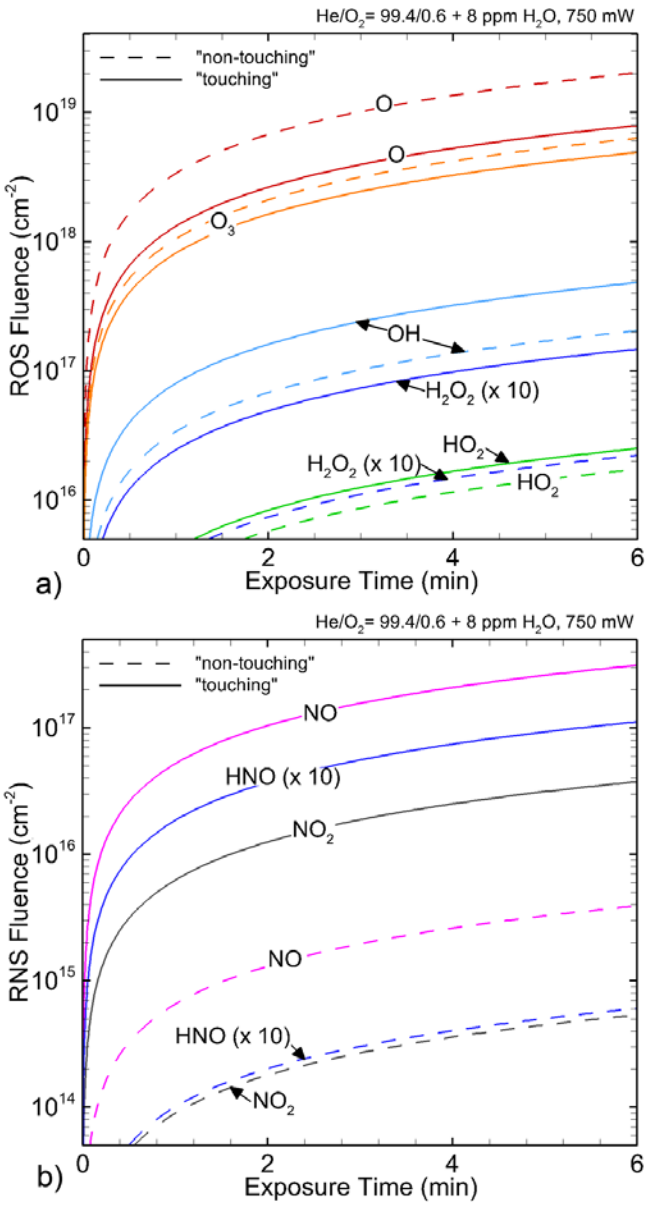

Figure 6.7. Comparison of fluence of gas-phase a) ROS and b) RNS to the liquid surface over time in touching and non-touching configurations.

The density of H_2O_2 increases by nearly an order of magnitude in the air gap while the increase in OH and HO_2 is less pronounced (a few times the density at the exit of the plasma source). The densities at the surface of the liquid are 9.7×10^{12} cm^{-3} for H_2O_2, 8.2×10^{13} cm^{-3} for OH, and 1.6×10^{13} cm^{-3} for HO_2 in the touching configuration. These densities in the non-touching configuration are 1.3×10^{12} cm^{-3} for H_2O_2, 3.1×10^{13} cm^{-3} for OH, and 1.0×10^{13}

for HO_2. In both configurations the density of O decreases across the air gap as three-body reactions involving O_2 convert O to O_3. In the touching configuration, the density of O_3 increases in the air gap from 3.1×10^{15} cm^{-3} at the exit of the plasma source to about 3.6×10^{15} cm^{-3} at the liquid surface. This is a less pronounced increase than in the non-touching configuration where the density of O_3 is 2.0×10^{15} cm^{-3} at the reactor outlet and 4.1×10^{15} cm^{-3} O_3 at the liquid surface. In the touching configuration, O is more efficiently converted to NO_x products rather than O_3, as shown in Figure 6.6b. The touching plasma is able to deliver 1.5×10^{14} cm^{-3} NO, 2.7×10^{13} cm^{-3} NO_2, 1.7×10^{12} cm^{-3} NO_3, and 5.4×10^{12} cm^{-3} HNO to the liquid surface. The densities of these same species at the liquid surface in the non-touching configuration are two orders of magnitude lower.

The delivery of the fluxes of plasma produced species to the liquid integrated over time, or the fluence, aligns with the production of gas-phase species. Fluences are shown in Figure 6.7. Higher gas-phase production and delivery to the surface of most RONS by the touching plasma generally leads to higher production of liquid-phase RONS than the non-touching plasma. RONS concentrations in the liquid as a result of the two plasma configurations are shown in Figure 6.8.

Both plasma configurations generate similar concentrations of H_2O_{2aq} and OH_{aq}, however, the touching configuration generates significantly more HO_{2aq}. The touching plasma produces 3.8×10^{15} cm^{-3} H_2O_{2aq}, 1.8×10^{13} cm^{-3} OH_{aq}, and 5.7×10^{13} cm^{-3} HO_{2aq} while the non-touching plasma generates 4.5×10^{15} cm^{-3} H_2O_{2aq}, 2.6×10^{13} cm^{-3} OH_{aq}, and 2.4×10^{11} cm^{-3} HO_{2aq}. The high generation rate of HO_{2aq} for the touching source is largely due to the high rate of generation of HNO and NO_3 in the air gap. These species then solvate into the liquid. NO_{3aq} reacts with H_2O_{2aq} and HNO_{aq} reacts with O_{2aq} to generate HO_{2aq} in solution.

$$H_2O_{2aq} + NO_{3aq} + H_2O_{aq} \rightarrow HO_{2aq} + NO_{3aq}^{-} + H_3O_{aq}^{+} \tag{6.14}$$

$$HNO_{aq} + O_{2aq} \rightarrow HO_{2aq} + NO_{aq} \quad (6.15)$$

The reaction with NO_{3aq} results in a higher rate of in-solution consumption of H_2O_{2aq} than in the non-touching configuration. Higher generation and delivery of HNO_x and other RNS by the touching plasma leads to nearly two orders of magnitude higher production of aqueous RNS than the non-touching plasma. The touching configuration produces 1.9×10^{12} cm^{-3} NO_{aq}, 4.5×10^{12} cm^{-3} NO_{2aq}, 9.5×10^{12} cm^{-3} NO_{2aq}^-, 1.1×10^{17} cm^{-3} NO_{3aq}^-, and 4.9×10^{17} cm^{-3} $ONOO_{aq}^-$.

The combined effects of higher HO_{2aq} and aqueous RNS generation contributes to nearly two times faster cell killing by the touching plasma. Viability as a function of treatment time for an initial density of 1×10^7 cm^{-3} CFU is shown in Figure 6.9. The touching plasma kills > 99.9% CFUs after 6 minutes of exposure while the non-touching plasma requires nearly 12 minutes to achieve the same result. Time for cell killing is consistent with reports by Van Gils et. al., Chandana et. al., and Deng et.al for time to bacterial inactivation for similar touching and non-touching systems [15–17].

Similar to the non-touching cases

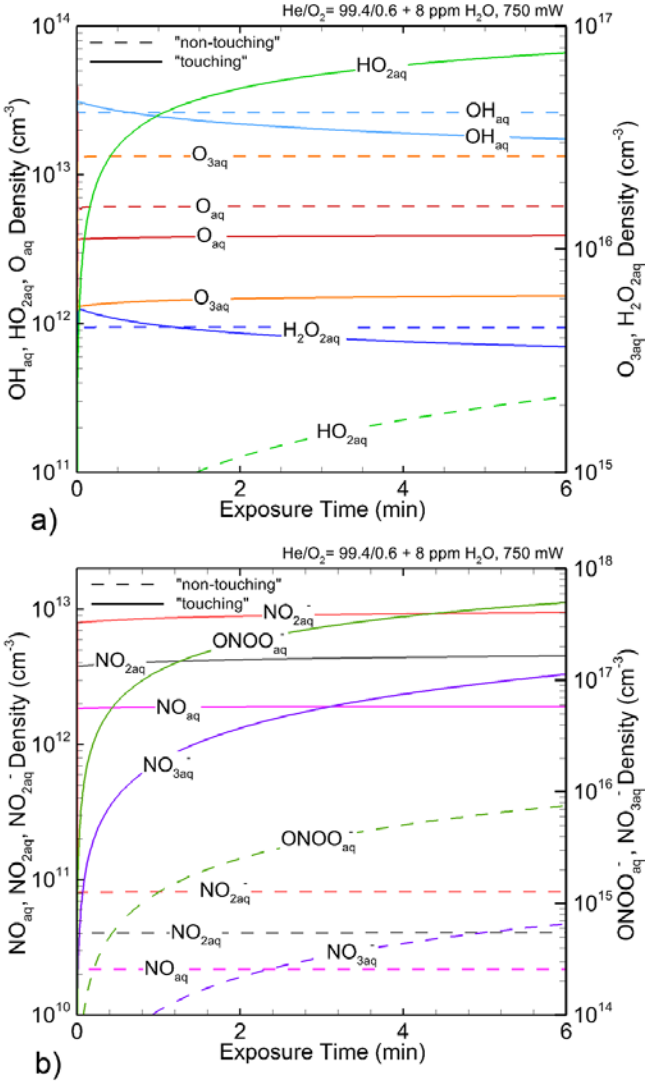

Figure 6.8. Densities of liquid-phase ROS (a) and RNS (b) over time for touching and non-touching configurations.

where higher gas-phase production of RNS led to more efficient cell killing, the improved killing efficiency of the touching plasma is due in part to its enhanced ability to produce RNS in the air gap. However, this is likely not the only explanation for its experimentally observed higher efficiency. For example, it has been shown that the electrical properties of touching plasmas may interrupt cellular redox pathways, in turn affecting the electrical properties of the biological target and creating a feedback loop between the plasma and the cells [38]. While cell charging is beyond the scope of the current investigation, the effects that the biological target has on the plasma (e.g., electrical properties, RONS production by the target) should be evaluated and considered in future models for holistic plasma device design.

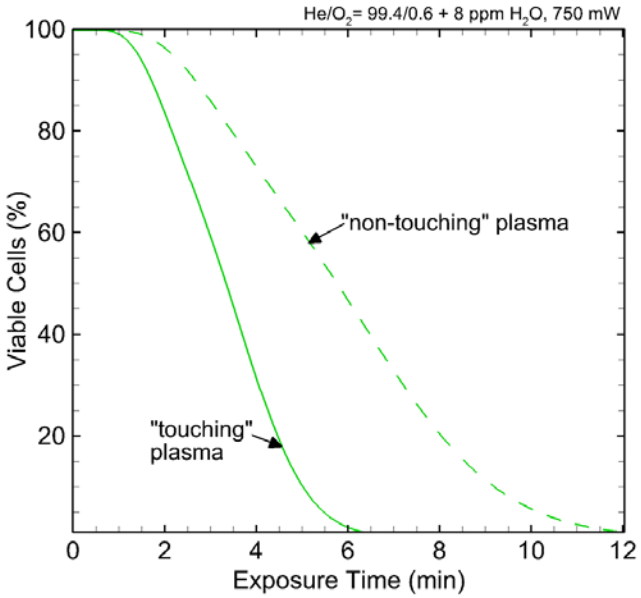

Figure 6.9. CFU viability as a function of plasma exposure time for two plasma source configurations ("touching" vs. "non-touching").

6.4.3 Cell Killing as a Function of the Air Gap for the Touching Plasma

Production of RNS is a direct consequence of air entrainment in the air gap for APPJ configurations where nitrogen is not included in the gas inlet. Touching configurations are more effective at producing RNS in the air gap, as plasma extends into the air gap and allows for continued production of reactive species by electron impact processes. However, more air entrainment does not necessarily correspond to more effective bacterial inactivation. To investigate these issues, the length of the air gap in the model for the touching plasma was varied

between 1 mm and 10 mm. The spatial slope of the power in the gap as shown in Figure 6.6a was held constant, so shorter gaps had larger power at the surface of the liquid. Air entrainment was also adjusted between 2% of the gas inlet flow for a 1 mm gap and 9.5% for a 10 mm gap. The gas inlet flow conditions (He/O_2 = 99.4/0.6 + 8 ppm H_2O, 1010 sccm) and total power deposition (750 mW) were held constant. The reactor geometry is the same as discussed in the previous section and the initial CFU concentration was 10^7 cm^{-3}.

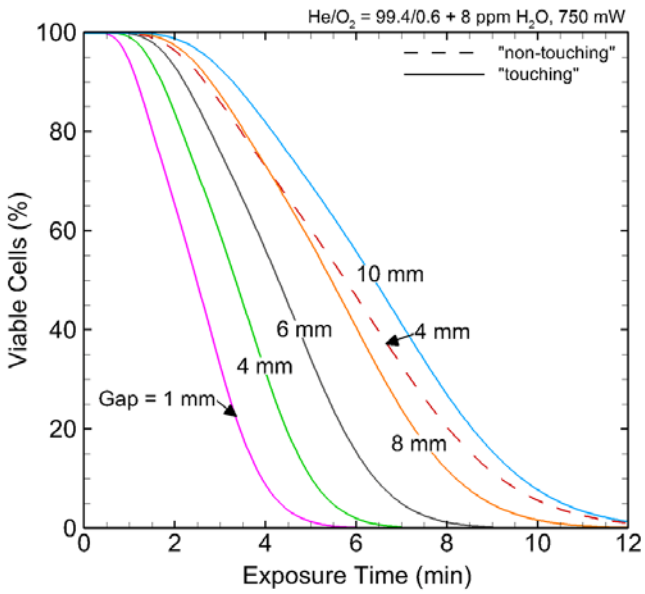

Figure 6.10. CFU viability as a function of plasma source distance from the liquid surface (air gap).

Cell viability over a 12 minute plasma exposure time for air gaps between 1 mm and 10 mm is shown in Figure 6.10. The viability curve for the non-touching base case (air gap = 4 mm) is also shown for comparison. The touching plasma is effective for bacterial inactivation when the air gap is between 1 mm and 10 mm with a decreasing efficiency for increasing air gap. The time to achieve 1% viability is about 5.5 minutes with a 1 mm gap and 12.5 minutes with the 10 mm gap. Fluxes of gas-phase RONS to the liquid surface are shown in Figure 6.11a. The time to reduce cell viability by 80% as a function of air gap is shown in Figure 6.11b. The corresponding concentrations of select liquid-phase ROS and RNS produced by these fluxes at the time when CFU viability has been reduced by 80% are shown in Figure 6.12.

In general, smaller air gaps produce higher fluxes of gas-phase ROS and lower fluxes of gas-phase RNS to the liquid surface than larger air gaps. The exceptions are the fluxes of O_3 and

H_2O_2. The 1 mm gap delivers fluxes of 1.3×10^{16} cm^{-2} s^{-1} O_3 and 1.2×10^{13} cm^{-2} s^{-1} H_2O_2 to the liquid surface while the 10 mm gap delivers fluxes of 1.7×10^{16} cm^{-2} s^{-1} O_3 and 8.5×10^{13} cm^{-2} s^{-1} H_2O_2. The flux of O_3 in the 10 mm gap is higher than in the non-touching base case (1.8×10^{13} cm^{-2} s^{-1}). As O_3 does not directly contribute to cell killing while consuming O (which does contribute to cell-killing), the high O_3 delivery to the liquid surface resulting from larger air gaps likely contributes to less efficient cell killing. NO flux has the greatest increases between the 1 mm gap and the 2 mm gap before reaching a maximum in the 6 mm gap and decreasing gradually at larger gaps. The NO fluxes are 2.5×10^{14} cm^{-2} s^{-1} for the 1 mm gap, increasing to 8.9×10^{14} cm^{-2} s^{-1} for the 6 mm gap, and decreasing to 7.3×10^{14} cm^{-2} s^{-1} for the 10 mm gap. Although H_2O_2 delivery is greatest with the largest air gaps, the corresponding decrease in HO_2 (9.4×10^{13} cm^{-2} s^{-1} for 1 mm and 7.8×10^{12} cm^{-2} s^{-1} for 10 mm gap) and O delivery (5.6×10^{16} cm^{-2} s^{-1} for 1 mm and 3.7×10^{15} cm^{-2} s^{-1} for 10 mm) results in an overall lower production of liquid phase ROS and longer times to cell killing with the larger air

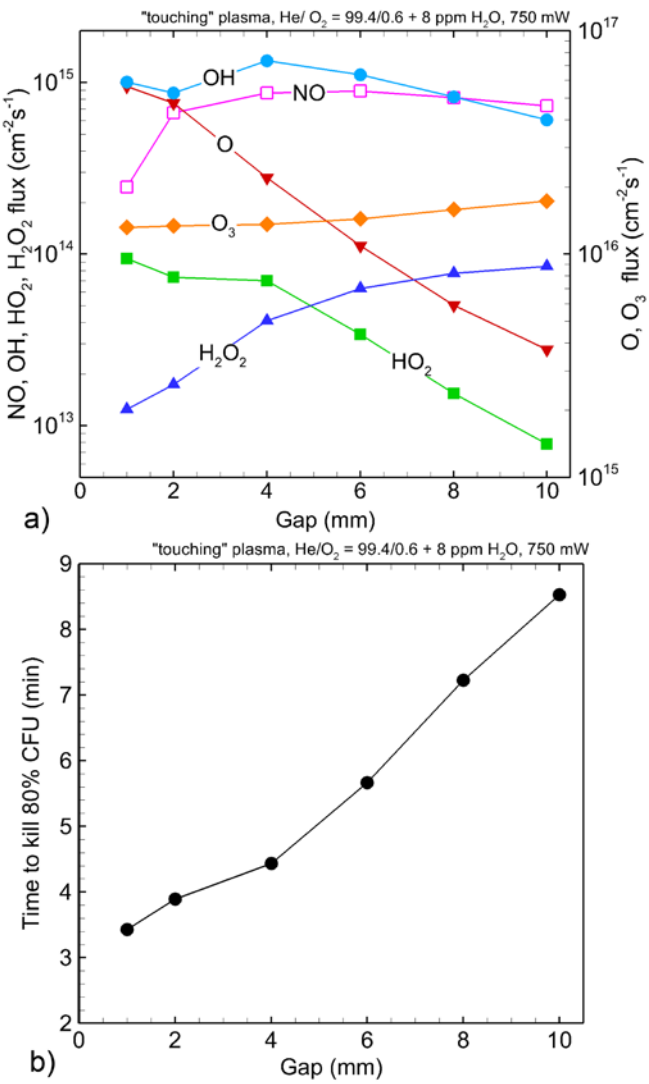

Figure 6.11. Reactant properties as a function of the air gap. a) Gas-phase RONS fluxes to the liquid surface. b) Time required for fluxes to reduce CFU viability by 80%.

gaps. The 1 mm air gap achieves 80% reduction in CFU viability 2.5 times faster than the 10 mm air gap as a consequence of these trends in fluxes of RONS in the air gap.

At the time of 80% cell killing, the NO_{xaq} concentrations are highest for larger gaps as a consequence of there being longer exposure times. There are 4.9×10^{11} cm^{-3} NO_{aq}, 1.9×10^{12} cm^{-3} $NO_2^-{}_{aq}$, and 5.7×10^{15} cm^{-3} $NO_3^-{}_{aq}$ for a gap of 1 mm at the time of 80% cell killing – 3.5 min. For a gap of 10 mm and killing time of 8.5 min, these concentrations are 1.9×10^{12} cm^{-3} NO_{aq}, 2×10^{13} cm^{-3} $NO_2^-{}_{aq}$, and 4.4×10^{17} cm^{-3} $NO_3^-{}_{aq}$. These higher concentrations of NO_{xaq} at the time of 80% cell killing are due in part to higher fluxes of H_2O_2. H_2O_2 solvates and produces $NO_3^-{}_{aq}$ through Reaction 14. Although the NO_{xq} concentrations increase with larger air gaps, the $ONOO^-{}_{aq}$ concentration at the time of 80% cell killing is nearly constant for air gaps between 4 mm and 10 mm (about 4×10^{17} cm^{-3}), which may indicate that this density of $ONOO^-{}_{aq}$ is critical for cell killing. Producing this concentration of $ONOO^-{}_{aq}$ requires an air gap large enough that air entrainment produces sufficient RNS flux. $ONOO^-{}_{aq}$ is dominantly produced in the liquid by reactions between $O_2^-{}_{aq}$ and NO_{aq} (Eq. 6.11). Smaller gaps can achieve the critical $ONOO^-{}_{aq}$ density at short times due to higher power at the liquid surface, which contributes to a higher flux of $O_2^-{}_{aq}$ onto the liquid surface. However, $ONOO^-{}_{aq}$ production is likely limited by the flux of NO, which does not change significantly when the air gap is between 4 mm and 10 mm.

Larger air gaps produce lower ROS fluxes and higher RNS fluxes onto the liquid surface. As a result, aqueous ROS concentrations at the time of 80% cell killing are lower with larger air gaps. The concentrations of ROS such as O_{aq} are diminished at larger air gaps as gas phase O is converted to O_3 or NO_x before reaching the liquid surface, while H_2O_{2aq} decreases at longer treatment times as it is consumed in reactions with NO_{xaq}. For example, when CFU viability has been reduced by 80%, there is 2.2×10^{13} cm^{-3} O_{aq} and 2.6×10^{16} cm^{-3} H_2O_{2aq} for a gap of 1 mm. For a gap of 10 mm these concentrations are 4.9×10^{11} cm^{-3} O_{aq} and 4.3×10^{16} cm^{-3} H_2O_{2aq}. Lower ROS fluxes result in longer time to ROS accumulation to achieve critical densities for cell killing.

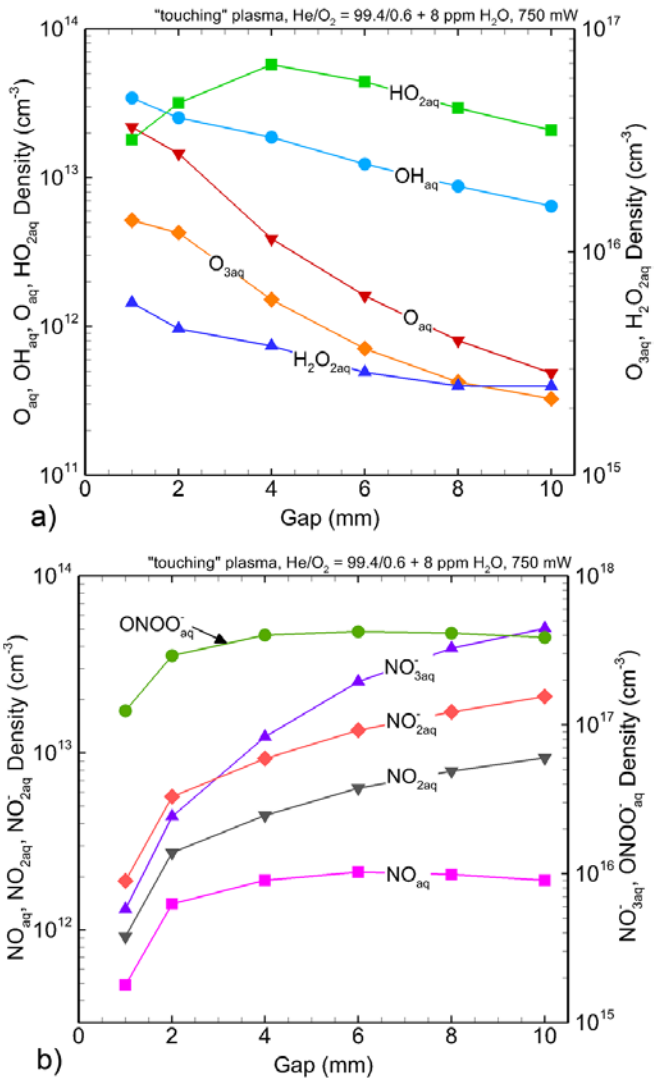

Figure 6.12. Liquid-phase ROS (a) and RNS densities to achieve 80% reduction in CFU viability.

If RNS such as $ONOO^-_{aq}$ were solely responsible for cell killing, then smaller gaps (where fluxes of RNS are lower) should be less efficient at cell killing than larger gaps. Results indicate that a balance of ROS and RNS delivery is needed to maximize the efficiency of plasma systems for bacterial inactivation. Configurations (such as the non-touching plasma) that contribute primarily ROS fluxes and liquid-phase ROS are not as effective as systems that can produce both

ROS and RNS in the liquid-phase. Configurations that maximize RNS fluxes while minimizing ROS fluxes (such as the touching plasma with 10 mm air gap) are the least efficient. Configurations that produce large densities of O_3 in the gas-phase are also not ideal. Results reinforce the importance of considering both ROS and RNS production (in both the gas and liquid phases) when designing devices for bacterial inactivation.

6.5 Conclusions

A hierarchal mechanism for reaction of RONS with bacterial cells in plasma activated solutions was proposed as an evaluator for cell viability. The mechanism, based on reactions for modification of cysteine in solution, was implemented in a global plasma chemistry model to describe relationships between plasma operating parameters and time to bacterial inactivation. The mechanism was normalized to be consistent with times for bacterial inactivation reported in the literature for similar operating conditions. The consequences of inlet gas composition in a non-touching plasma source indicated that a nitrogen addition to the inlet rare gas resulting in non-negligible production of RNS that solvate into solution leads to more rapid bacterial inactivation than only an oxygen addition. Inactivation times for a touching plasma source configuration were compared to the non-touching configuration using the same gas composition, power, and distance from the target. The touching plasma was twice as efficient at bacterial inactivation as the non-touching plasma in spite of similar ROS production in the gas-phase. However, the touching plasma produced 100 times more RNS in the air gap between the outlet of the plasma source and the liquid surface than the non-touching plasma. When the length of the air gap was varied in the touching configuration to maximize RNS delivery to the surface, cell killing became less efficient, indicating that production of both ROS and RNS are important to consider when designing effective plasma systems for bacterial inactivation.

Although the model discussed in this chapter makes several simplifying assumptions (such as neglecting reactions of RONS with the cell growth medium), the capability was demonstrated to reproduce trends for bacterial inactivation reported in the literature across a range of plasma operating parameters and plasma devices. The current model is limited to planktonic bacterial cells that are free to move about in the solution. The mechanism may not be valid for treatment of eukaryotic cells, which are more complex than bacterial cells. Jablonowski et. al observed, similarly to the findings in this chapter, that bacterial cell inactivation was most effective when plasma-produced ROS and RNS fluxes were delivered to the surface, but that eukaryotic cells (such as mammalian cancer cells) were less affected by the plasma activated species produced by the same gas mixture [39]. Eukaryotic cells are also often plated at the bottom of a well plate or petri dish and covered by a thin layer of solution. Needed improvements to the model to address these conditions would be adding capability to have stationary cells under the liquid layer, which would enable probable mechanisms for eukaryotic cell killing to be investigated more accurately.

6.6 Tables

Table 6.1 CFU Plasma Deactivation Reaction Mechanism

	Reaction	Reaction rate Coefficient (cm^3/s)
	Cell death reactions[a]	
1	$CFU_i + O_{aq} \rightarrow CFU_{i+1}$	1.68×10^{-15}
2	$CFU_i + O^-_{aq} \rightarrow CFU_{i+1} + e_{aq}$	1.68×10^{-20}
3	$CFU_i + OH_{aq} \rightarrow CFU_{i+1}$	1.68×10^{-17}
4	$CFU_i + OH^-_{aq} \rightarrow CFU_{i+1} + e_{aq}$	1.91×10^{-20}
5	$CFU_i + H_2O_{2aq} \rightarrow CFU_{i+1} + H_2O_{aq}$	4.98×10^{-18}
6	$CFU_i + HO_{2aq} \rightarrow CFU_{i+1}$	5.65×10^{-16}
7	$CFU_i + NO_{aq} \rightarrow CFU_{i+1}$	8.00×10^{-15}
8	$CFU_i + NO^-_{2aq} \rightarrow CFU_{i+1} + e_{aq}$	5.60×10^{-22}
9	$CFU_i + NO^-_{3aq} \rightarrow CFU_{i+1} + e_{aq}$	5.60×10^{-22}
10	$CFU_i + ONOO^-_{aq} \rightarrow CFU_{i+1} + e_{aq}$	5.60×10^{-22}
	Ghost reactions[b,c,,d,e,f,g]	
11	$CFU_j + O_{aq} \rightarrow CFU_j$	2.52×10^{-09}
12	$CFU_j + O^-_{aq} \rightarrow CFU_j + e_{aq}$	2.52×10^{-14}
13	$CFU_j + OH_{aq} \rightarrow CFU_j$	2.52×10^{-11}
14	$CFU_j + OH^-_{aq} \rightarrow CFU_j + e_{aq}$	2.87×10^{-14}
15	$CFU_j + H_2O_{2aq} \rightarrow CFU_j + H_2O_{aq}$	7.02×10^{-14}
16	$CFU_j + HO_{2aq} \rightarrow CFU_j$	8.48×10^{-10}
17	$CFU_j + NO_{aq} \rightarrow CFU_j$	4.00×10^{-09}
18	$CFU_j + NO^-_{2aq} \rightarrow CFU_j + e_{aq}$	8.40×10^{-14}
19	$CFU_j + NO^-_{3aq} \rightarrow CFU_j + e_{aq}$	8.40×10^{-14}
20	$CFU_j + ONOO^-_{aq} \rightarrow CFU_j + e_{aq}$	8.40×10^{-14}
21	$CFU_k + O_{aq} \rightarrow CFU_k$	2.52×10^{-12}
22	$CFU_k + O^-_{aq} \rightarrow CFU_k + e_{aq}$	2.52×10^{-17}
23	$CFU_k + OH_{aq} \rightarrow CFU_k$	2.52×10^{-14}

24	$CFU_k + OH^-_{aq} \rightarrow CFU_k + e_{aq}$	2.87×10^{-17}
25	$CFU_k + H_2O_{2aq} \rightarrow CFU_k + H_2O_{aq}$	7.02×10^{-17}
26	$CFU_k + HO_{2aq} \rightarrow CFU_k$	8.48×10^{-13}
27	$CFU_k + NO_{aq} \rightarrow CFU_k$	4.00×10^{-10}
28	$CFU_k + NO^-_{2aq} \rightarrow CFU_k + e_{aq}$	8.40×10^{-12}
29	$CFU_k + NO^-_{3aq} \rightarrow CFU_k + e_{aq}$	8.40×10^{-12}
30	$CFU_k + ONOO^-_{aq} \rightarrow CFU_k + e_{aq}$	8.40×10^{-12}
31	$CFU_l + O_{aq} \rightarrow CFU_l$	2.52×10^{-09}
32	$CFU_l + O^-_{aq} \rightarrow CFU_l + e_{aq}$	2.52×10^{-15}
33	$CFU_l + OH_{aq} \rightarrow CFU_l$	2.52×10^{-13}
34	$CFU_l + OH^-_{aq} \rightarrow CFU_l + e_{aq}$	2.87×10^{-15}
35	$CFU_l + H_2O_{2aq} \rightarrow CFU_l + H_2O_{aq}$	7.02×10^{-14}
36	$CFU_l + HO_{2aq} \rightarrow CFU_l$	8.48×10^{-13}
37	$CFU_l + NO_{aq} \rightarrow CFU_l$	4.00×10^{-11}
38	$CFU_l + NO^-_{2aq} \rightarrow CFU_l + e_{aq}$	8.40×10^{-13}
39	$CFU_l + NO^-_{3aq} \rightarrow CFU_l + e_{aq}$	8.40×10^{-13}
40	$CFU_l + ONOO^-_{aq} \rightarrow CFU_l + e_{aq}$	8.40×10^{-13}
41	$CFU_m + O_{aq} \rightarrow CFU_m$	2.52×10^{-10}
42	$CFU_m + O^-_{aq} \rightarrow CFU_m + e_{aq}$	2.52×10^{-16}
43	$CFU_m + OH_{aq} \rightarrow CFU_m$	2.52×10^{-14}
44	$CFU_m + OH^-_{aq} \rightarrow CFU_m + e_{aq}$	2.87×10^{-16}
45	$CFU_m + H_2O_{2aq} \rightarrow CFU_m + H_2O_{aq}$	7.02×10^{-15}
46	$CFU_m + HO_{2aq} \rightarrow CFU_m$	8.48×10^{-13}
47	$CFU_m + NO_{aq} \rightarrow CFU_m$	4.00×10^{-12}
48	$CFU_m + NO^-_{2aq} \rightarrow CFU_m + e_{aq}$	8.40×10^{-14}
49	$CFU_m + NO^-_{3aq} \rightarrow CFU_m + e_{aq}$	8.40×10^{-14}
50	$CFU_m + ONOO^-_{aq} \rightarrow CFU_m + e_{aq}$	8.40×10^{-14}
51	$CFU_n + O_{aq} \rightarrow CFU_n$	2.52×10^{-11}
52	$CFU_n + O^-_{aq} \rightarrow CFU_n + e_{aq}$	2.52×10^{-17}
53	$CFU_n + OH_{aq} \rightarrow CFU_n$	2.52×10^{-15}

54	$CFU_n + OH^-_{aq} \rightarrow CFU_n + e_{aq}$	2.87×10^{-17}
55	$CFU_n + H_2O_{2aq} \rightarrow CFU_n + H_2O_{aq}$	7.02×10^{-16}
56	$CFU_n + HO_{2aq} \rightarrow CFU_n$	8.48×10^{-14}
57	$CFU_n + NO_{aq} \rightarrow CFU_n$	4.00×10^{-12}
58	$CFU_n + NO^-_{2aq} \rightarrow CFU_n + e_{aq}$	8.40×10^{-17}
59	$CFU_n + NO^-_{3aq} \rightarrow CFU_n + e_{aq}$	8.40×10^{-17}
60	$CFU_n + ONOO^-_{aq} \rightarrow CFU_n + e_{aq}$	8.40×10^{-17}
71	$CFU_x + O_{aq} \rightarrow CFU_x$	2.52×10^{-13}
72	$CFU_x + O^-_{aq} \rightarrow CFU_x + e_{aq}$	2.52×10^{-18}
73	$CFU_x + OH_{aq} \rightarrow CFU_x$	2.52×10^{-15}
74	$CFU_x + OH^-_{aq} \rightarrow CFU_x + e_{aq}$	2.87×10^{-18}
75	$CFU_x + H_2O_{2aq} \rightarrow CFU_x + H_2O_{aq}$	7.02×10^{-18}
76	$CFU_x + HO_{2aq} \rightarrow CFU_x$	8.48×10^{-14}
77	$CFU_x + NO_{aq} \rightarrow CFU_x$	4.00×10^{-13}
78	$CFU_x + NO^-_{2aq} \rightarrow CFU_x + e_{aq}$	8.40×10^{-18}
79	$CFU_x + NO^-_{3aq} \rightarrow CFU_x + e_{aq}$	8.40×10^{-18}
80	$CFU_x + ONOO^-_{aq} \rightarrow CFU_x + e_{aq}$	8.40×10^{-18}

a) $0 \leq i \leq 20$
b) $0 \leq j \leq 3$
c) $4 \leq k \leq 7$
d) $8 \leq l \leq 11$
e) $12 \leq m \leq 15$
f) $16 \leq n \leq 19$
g) $x = 20$

6.7 References

[1] M. Keidar, A. Shashurin, O. Volotskova, M. Ann Stepp, P. Srinivasan, A. Sandler and B. Trink, Phys. Plasmas **20,** (2013).

[2] D. B. Graves, Plasma Process. Polym. **11,** 1120 (2014).

[3] A. Kramer, J. Lademann, C. Bender, A. Sckell, B. Hartmann, S. Münch, P. Hinz, A. Ekkernkamp, R. Matthes, I. Koban, I. Partecke, C. D. Heidecke, K. Masur, S. Reuter, K. D. Weltmann, S. Koch and O. Assadian, Clin. Plasma Med. **1,** 11 (2013).

[4] S. Bekeschus, A. Schmidt, K. D. Weltmann and T. von Woedtke, Clin. Plasma Med. **4,** 19 (2016).

[5] N. Kaushik, S. Mitra, E. J. Baek, L. N. Nguyen, P. Bhartiya, J. H. Kim, E. H. Choi and N. K. Kaushik, J. Adv. Res. **43,** 59 (2023).

[6] M. K. J. Nicol, T. R. Brubaker, B. J. Honish, A. N. Simmons, A. Kazemi, M. A. Geissel, C. T. Whalen, C. A. Siedlecki, S. G. Bilén, S. D. Knecht and G. S. Kirimanjeswara, Sci. Rep. **10,** 1 (2020).

[7] K. Urashima, IEEE Open J. Nanotechnol. **3,** 159 (2022).

[8] J.-S. Jung and J.-G. Kim, J. Electrostat. **86,** 12 (2017).

[9] A. Sakudo, Y. Yagyu and T. Onodera, Int. J. Mol. Sci. **20,** 5216 (2019).

[10] V. Scholtz, J. Pazlarova, H. Souskova, J. Khun and J. Julak, Biotechnol. Adv. **33,** 1108 (2015).

[11] J. Šimončicová, S. Kryštofová, V. Medvecká, K. Ďurišová and B. Kaliňáková, Appl. Microbiol. Biotechnol. **103,** 5117 (2019).

[12] J.-W. Lackmann and J. E. Bandow, Appl. Microbiol. Biotechnol. **98,** 6205 (2014).

[13] J. Golda, J. Held, B. Redeker, M. Konkowski, P. Beijer, A. Sobota, G. Kroesen, N. S. J.

Braithwaite, S. Reuter, M. M. Turner, T. Gans, D. O'Connell and V. Schulz-Von Der Gathen, J. Phys. D. Appl. Phys. **49,** (2016).

[14] A. G. Yahaya, T. Okuyama, J. Kristof, M. G. Blajan and K. Shimizu, Molecules **26,** 2523 (2021).

[15] C. A. J. Van Gils, S. Hofmann, B. K. H. L. Boekema, R. Brandenburg and P. J. Bruggeman, J. Phys. D. Appl. Phys. **46,** (2013).

[16] L. Chandana, C. J. Sangeetha, T. Shashidhar and C. Subrahmanyam, Sci. Total Environ. **640–641,** 493 (2018).

[17] X. Deng, J. Shi and M. G. Kong, IEEE Trans. Plasma Sci. **34,** 1310 (2006).

[18] H. Zhang, C. Zhang and Q. Han, Appl. Microbiol. Biotechnol. **107,** 5301 (2023).

[19] L. Wang, C. Xia, Y. Guo, C. Yang, C. Cheng, J. Zhao, X. Yang and Z. Cao, Future Microbiol. **15,** 115 (2020).

[20] M. A. Oliver, L. K. Hussein, E. A. Molina, J. W. Keyloun, S. M. McKnight, L. M. Jimenez, L. T. Moffatt, J. W. Shupp and B. C. Carney, Burns (2024).

[21] B. Boekema, M. Stoop, M. Vlig, J. van Liempt, A. Sobota, M. Ulrich and E. Middelkoop, Appl. Microbiol. Biotechnol. **105,** 2057 (2021).

[22] W. Ning, H. Shang, Y. Ji, R. Li, L. Zhao, X. Huang and S. Jia, High Volt. **8,** 326 (2023).

[23] A. M. Lietz and M. J. Kushner, J. Phys. D. Appl. Phys. **49,** 425204 (2016).

[24] G. Bruno, T. Heusler, J. W. Lackmann, T. von Woedtke, K. D. Weltmann and K. Wende, Clin. Plasma Med. **14,** 100083 (2019).

[25] P. Attri, J. Han, S. Choi, E. H. Choi, A. Bogaerts and W. Lee, Sci. Rep. **8,** 10218 (2018).

[26] J. Polito, M. J. Herrera Quesada, K. Stapelmann and M. J. Kushner, J. Phys. D. Appl. Phys. **56,** 395205 (2023).

[27] A. Mai-Prochnow, A. B. Murphy, K. M. McLean, M. G. Kong and K. (Ken) Ostrikov, Int. J. Antimicrob. Agents **43,** 508 (2014).

[28] O. Lunov, V. Zablotskii, O. Churpita, A. Jäger, L. Polívka, E. Syková, A. Dejneka and Š. Kubinová, Biomaterials **82,** 71 (2016).

[29] J. W. Lackmann, K. Wende, C. Verlackt, J. Golda, J. Volzke, F. Kogelheide, J. Held, S. Bekeschus, A. Bogaerts, V. Schulz-Von Der Gathen and K. Stapelmann, Sci. Rep. **8,** 1 (2018).

[30] P.-M. Girard, A. Arbabian, M. Fleury, G. Bauville, V. Puech, M. Dutreix and J. S. Sousa, Sci. Rep. **6,** 29098 (2016).

[31] S. Arndt, P. Unger, E. Wacker, T. Shimizu, J. Heinlin, Y. F. Li, H. M. Thomas, G. E. Morfill, J. L. Zimmermann, A. K. Bosserhoff and S. Karrer, PLoS One **8,** 1 (2013).

[32] B. Myers, E. Barnat and K. Stapelmann, J. Phys. D. Appl. Phys. **54,** (2021).

[33] A. Tsuji, Y. Kaneko, K. Takahashi, M. Ogawa and S. Goto, Microbiol. Immunol. **26,** 15 (1982).

[34] A. R. Tuttle, N. D. Trahan and M. S. Son, Curr. Protoc. **1,** (2021).

[35] D. X. Liu, P. Bruggeman, F. Iza, M. Z. Rong and M. G. Kong, Plasma Sources Sci. Technol. **19,** (2010).

[36] Y. Du, G. Nayak, G. Oinuma, Z. Peng and P. J. Bruggeman, J. Phys. D. Appl. Phys. **50,** 145201 (2017).

[37] S. Reuter, T. Von Woedtke and K. D. Weltmann, J. Phys. D. Appl. Phys. **51,** (2018).

[38] J. Sutter, J. Brettschneider, S. Mamchur, F. Krebs, S. Gershman and V. Miller, Plasma **6,** 577 (2023).

[39] H. Jablonowski, M. A. C. Hänsch, M. Dünnbier, K. Wende, M. U. Hammer, K.-D.

Weltmann, S. Reuter and T. von Woedtke, Biointerphases **10,** (2015).

Chapter 7 Summary and Future Work

In this dissertation, mechanisms for plasma interactions with complex surfaces and molecules were developed and used in a 0D computational plasma chemistry model to better understand relationships between plasma operating conditions and the desired modification of the complex target. Results from the models inform plasma reactor and device designs that can optimize the outcome of several existing or emerging commercial systems.

7.1 Summary

In Chapter 1, an overview of LTPs was given. Applications that involve plasma interactions with complex surfaces and molecules including plasma nanoparticle synthesis, plasma functionalization of polymers, and plasma medical device design were discussed.

In Chapter 2, the 0D plasma chemistry model *GlobalKin* was described in detail. The plug-flow approach was introduced as a mode of operation of *GlobalKin* that provides a quasi 1D description of plasma properties. An algorithm to predict nanoparticle nucleation and growth trends in flowing plasmas and its implementation into *GlobalKin* was also discussed.

In Chapter 3, the *GlobalKin* nanoparticle growth algorithm was used to elucidate trends in silicon nanoparticle nucleation and growth in a low-pressure flowing plasma. A reaction mechanism that considers nucleation, surface growth, and coagulation reactions for silicon nanoparticles was proposed. Results from the model were compared to experiments that used a novel Quartz Crystal Microbalance (QCM) impactor to collect particle mass density data as a function of inlet gas composition, reactor diameter, and reactor pressure. Trends from the model

agreed well with the experimental results and suggested that control of the nanoparticle growth regime (nucleation or coagulation) can be achieved by tuning the inlet gas flowrate together with the reactor diameter.

In Chapter 4, a reaction mechanism for the atmospheric pressure plasma functionalization of polystyrene (PS) was proposed. Reaction rate coefficients for gas-phase ROS interactions with functional groups on the PS backbone were estimated based on analogous gas-phase reactions with long-chain alkanes. *GlobalKin* provided fluxes of gas-phase species to the PS surface and a surface site balance model was used to predict changes in functionality at the PS surface after treatment by a He/O_2 APPJ in contact with humid air. Results for the final functionality of the PS surface agreed well with experimental XPS results cited in the literature. Results suggested that the degree of O-occupancy on the PS surface is highly sensitive to the flux of O atoms delivered to the surface. Plasma operating parameters that can be adjusted to adjust the O-atom flux include inlet gas composition and power. Results also suggested that finer control of O-occupancy is achievable when the O-atom fluence is less than 10^{17} cm^{-2}, or below saturation.

In Chapter 5, the mechanism for PS functionalization was adjusted and extended to predict modifications of cysteine in solution. Cysteine was chosen as a surrogate molecule for more complex biological systems, as it contains the thiol group (-SH) which is crucial to many biological processes. The mechanism was validated against experiments that exposed cysteine in water to the plasma effluent of the COST-jet sustained in He/O_2 or He/H_2O. Both the model and the experiments showed depletion of the cysteine molecule and the oxidation of the thiol group to SO_3 after plasma treatment. Experiments were also performed with the COST-jet sustained in $He/N_2/O_2$, which resulted in the formation of nitrosylated cysteine products. Leveraging the validated model against the experiments allowed detailed discussion of the reaction mechanisms

responsible for the production of oxidated and nitrosylated cysteine products as a result of plasma treatment. Results indicated that the control of the functionality on the treated cysteine molecule can be achieved by altering the flux of RONS to the liquid surface by changing inlet gas composition or distance of the reactor outlet from the surface.

In Chapter 6, the work done in understanding the mechanisms responsible for modifications to the cysteine molecule were leveraged to produce a hierarchal model for bacterial cell inactivation in solution by touching and non-touching APPJs. In Chapter 5, cysteine modification was shown to be limited by hydrogen abstraction. The mechanism for planktonic cell death in solution was based on hydrogen abstraction from the cysteine molecule and adjusted to achieve consistency for times to bacterial cell inactivation reported in literature. Comparison of times to cell death as a function of inlet gas composition and plasma configuration were discussed. The model allowed for comparison of times to bacterial inactivation as a result of treatment by two dissimilar plasma devices, which is difficult to achieve experimentally. Results indicated that plasma production of both ROS and RNS are required to achieve optimum bacterial inactivation. Optimal plasma operating conditions were also discussed.

7.2 Implications

LTPs continue to gain traction as reactive chemistry sources for various applications, especially those involving complex organic compounds and living organisms. Better understanding of how the plasma interacts with the target molecule or surface to achieve the desired outcome is necessary for designing and optimizing plasma devices. Computational modelling can be used as a tool in designing these devices, but complete validated reaction mechanisms for plasma interactions with complex surfaces and molecules, especially those containing organic functionality, have been largely unavailable. The work discussed in this

dissertation represents a contribution to the low temperature plasma field in the form of validated reaction mechanisms for plasma interactions with silicon nanoparticles, polymer surfaces, and organic molecules in solution that increase our understanding of how reactivity produced from a plasma can add commercial value to or promote modifications that induce desired effects on complex targets. Modelling results lead to recommendations for plasma operating conditions that can improve or optimize plasma device design.

The growth regime of silicon nanoparticles (nucleation or coagulation) grown in a low-pressure flowing plasma was shown to be sensitive to the reactor diameter and inlet flow rate. The reactor diameter affected the amount of precursor material lost to the walls, which can be controlled to some extent by changing the flow rate. The results suggested that control of particle suppression or growth can be achieved by tuning the reactor diameter in combination with the inlet gas composition.

The addition of O-functionality to a dry PS surface was shown to be sensitive to the flux of plasma produced O-atoms. Results suggested that alcohol functional groups and cross-linked products made the largest contribution to the O-functionalization of PS after plasma treatment. Adjusting the proportion of different functional groups on the PS surface can be achieved through changing the fraction of water vapor or O_2 in the inlet.

The reaction pathways responsible for producing oxidation productions on APPJ treated cysteine in solution were discussed. Nitrosylated cysteine products were only observed when RNS species were produced in the plasma. The end functionality of APPJ treated cysteine in solution can be adjusted by changing the fraction of O_2 and N_2 in the inlet.

The hierarchal model for cell death allowed time to bacterial inactivation to be compared between two dissimilar plasma devices. This study showed that bacterial inactivation is sensitive

to RNS production. The most efficient treatment systems were those that produced both ROS and RNS in the plasma. The time to bacterial inactivation can be optimized by changing inlet gas composition, distance from the substrate, or plasma device configuration.

The mechanisms discussed in the latter half of this dissertation are most relevant to the field of plasma medicine. While plasma-water interactions have been studied extensively, plasma interactions with solutions containing organic compounds are less well understood. Development and validation of a mechanism for the plasma treatment of cysteine in solution elucidated some of the reaction pathways that are most important for plasma interactions with organic molecules in solution. Knowledge gained in the cysteine study can be leveraged in studying how plasma interacts with more complex targets, such as cells, as shown in Chapter 6. Better understanding of plasma interactions with biological targets, such as bacteria or cancer cells, is necessary for defining key characteristics of plasma medical devices (e.g., plasma dose, treatment time) that are necessary for federal approval and clinical use.

The validated reaction mechanisms discussed in this dissertation have been used to provide suggestions for optimizations to plasma device design that will increase selectivity or efficiency in systems that involve plasma interactions with complex surfaces and molecules. The models and mechanisms discussed in this work can be adjusted or extended to inform future studies on plasma interactions with other complex molecules.

7.3 Future Work

Validated reaction mechanisms for plasma interactions with complex molecules and surfaces are necessary for improving modelling capabilities to assist with cost-efficient plasma device design. However, development of mechanisms for complex systems is largely hindered by

lack of data for validation. Intentional design of experiments meant to aid in reaction mechanism development is an area that can be extended upon in future work.

With experimental data available for validation, the mechanisms reported herein can be extended to other similar molecules, or those that may differ in functionality from those reported on in this dissertation. For example, polycarbonate is a widely used commercial polymer whose backbone contains some of the same functionality as PS. Reactions can be added or deleted from the PS mechanism to describe possible reactions with polycarbonate backbone. Similarly, the reaction mechanism for cysteine in solution can be extended to other organic molecules in solution to better suit the desired application.

The plasma-liquid mechanisms described in this dissertation make a major assumption in that the organic molecule or cell is always contained in pure liquid water. In experimental conditions, the solution is rarely pure water. In cell experiments, the solution often contains proteins, vitamins, and other organic material that acts as the "cell food." More work needs to be done to understand how the "cell food", or cell media, acts as a source or sink of plasma-produced RONS. Intentional design of experiments that expose cell media to the plasma and include time-dependent measurements of pH and RONS content would enable development of a reaction mechanism to describe the behavior of the cell media in the absence of cells. Repeating the same experiments when cells are present in solution would enable development of a reaction mechanism for cell death in cell media, rather than in water. Both mechanisms would provide valuable knowledge that would allow more accurate models, more efficient plasma device design, and faster commercialization of plasma medical devices.

Furthermore, the model for bacterial inactivation is currently limited to planktonic bacterial cell death and does not describe plasma interactions with stationary cells at the bottom of a well

plate or petri dish that are covered with a layer of liquid. Capability could potentially be added to *GlobalKin* to treat stationary cells by executing a surface kinetic model after the liquid model. However, this method would require a description of the interface between the liquid and the cell surface as well as the ability to track reactive species fluxes through the liquid layer and may be better suited to a 2D model. The model for bacterial inactivation discussed in Chapter 6 can potentially be extended to other, more complex cells, though extensive validation would be needed. The behavior of cells exposed to plasma differs by cell type, line, and shape. Therefore, with appropriate experimental data available for validation, mechanisms can be developed that are specific to each cell type or line.